COMPLEMENTARY RFID TAG ANTENNAS

BY

CHUKWUDI ANSELM DIUGWU

A THESIS SUBMITTED FOR THE DEGREE OF DOCTOR OF PHILOSOPHY AT THE UNIVERSITY OF KENT, CANTERBURY

2007

The only man I know who behaves sensibly is my tailor;
he takes my measurements anew each time he sees me.
The rest go on with their old measurements and expect me to fit them.

-George Bernard Shaw

To the Sons and Daughters of Ishialogo

Abstract

This thesis is mainly concerned with the investigation of a systematic approach to selecting tag antennas whose electromagnetic properties are compatible with the platforms on which they are supported and the immediate environment in which they are to be operated. The work is divided into three parts. The first two explore the design and optimisation of Radio Frequency Identification (RFID) tag antennas: firstly, in this section, behaviour of an electric dipole is explored. Secondly, a novel dual band Slot Patch Antenna (SPA) antenna is designed and developed, which employs various resonant slots to perturb the tuning and impedance of a conventional slotline. The third investigates its operation within a roll cage.

Complementary dipole and Slot Patch Antennas (SPA) are investigated to obtain a range of options on antenna configurations that, at certain selected frequency bands, give optimum interaction with the antenna support material. This requires that the regions of Perfect Electric Conductor (PEC) and free space dielectric substrate in both antennas be interchanged. The antennas are truncated of the otherwise infinite perfect electric conductor and dielectric substrate.

The radar cross sections (RCS) are predicted under various load conditions and orientations when the models are illuminated with plane wave. The convergence of this method has been found to depend on the load conditions and the substrate thickness and permittivity. The RCS at boresight is found to depend on the radiating elements. The effects of various possible mounting platforms are predicted.

The feasibility of reading tags through wire meshes such as those on a roll cage is investigated. The cages, of various mesh sizes, exhibit transmission responses characterised by frequency spacing of approximately half the first resonant frequency. The insertion loss is found to decrease with increasing mesh size. Also, the standing waves inside the cage exhibit nulls whose voltage standing wave ratio (v.s.w.r.) decreases with increasing mesh sizes. The distance, or range, over which the tag surveillance operates, is approximated in proportion to the amplitude of the standing wave at the position of the tag with peaks and nulls occurring at every half wavelength. The effects on the read range of either electromagnetic absorber or scatterer packing the space with the roll cage are also investigated.

Acknowledgements

I would like to express my profound gratitude to my academic supervisor Dr. John Batchelor for facilitating my entry into his research group and also for his support and rigorous academic guidance throughout my research.

I would also like to express my sincere appreciation to Dr. Arthur Drinkwater for making very remarkable comments on the work. I would also like to thank Prof. Richard Langley and Emeritus Prof. Mohamed Sobhy for their early contributions.

I would like to thank Martin Fogg of the RF Tag Ltd., Oxford for collaboration and the provision of testing instruments. Without his valuable help, completion of this work would not have been possible.

I would also like to thank in a special way Nigel Simpson, Simon Jakes, Clive Birch, and Terry Rockhill for helps with fabrications; to Julian Lucas, Dan Hook and Paul Sinnock for support with IT.

I wish to thank my friends Emma Ossai, Br. Larence Ezilo, Fr. Peter Geldard, Mattew, Charan, Jonathan, Jean-Baptiste, Emeka, Agu, Uche, Fredie and Benito for their well-wishes and encouragements.

I would like to thank my parents Crescent and Mary, my wife Chibuogwu, my Uncle James, my brothers Okechukwu and Ikechukwu, my sister Chinyere and my children Beluchi, Nwomiko and Kamlota whose love and patient understanding gave me the encouragement to complete my Ph.D.

Publications arising from this work

1 C. A. Diugwu, J. C. Batchelor and R. J. Langley, "Investigation into the Effects of Human Interaction with a Passive RFID Tag Antenna," *IEE PREP 2004*, Hertford, UK.

2 C. A. Diugwu, J. C. Batchelor, R. J. Langley, and M Fogg: Planar Antenna for Passive Radio Frequency Identification [RFID] Tags, 2004 *IEEE AFRICON. 7th AFRICON conf. In Africa IEEE*, 2004, vol. 1, pp. 21-24, ISBN 0 947974 33 4

3 C. A. Diugwu, J. C. Batchelor, R. J. Langley, "On The Behaviour of Linear Dipole Antennas with Application to Passive Radio Frequency Identification Tags Operating at 869 MHz," *IEE 2003 LCS Proced.* pp.53-56, ISBN 0-9538863-4-4

4 C.A. Diugwu, J.C. Batchelor and R.J. Langley: Dual-band RFID Tag Antenna, IEEE LAPC conf. In Loughborough UK, 2005, pp. 225-228

5 Diugwu, C.A and Batchelor, J.C., "Analysis of the surface current distributions in a dual band planar antenna for passive RFID tag'" in *Proc., IEEE AP-S Int. Symp.* vol. 3A, July 2005 pp.459 - 462

6 C.A. Diugwu and J.C. Batchelor: "Electromagnetic Field Distributions in a Wire Grid Enclosure for RFID Application," in *Proc., IEEE AP-S Int. Symp.* and USNC/URSI National Science Meeting, July 2006, pp. 3233-3236

7 C.A. Diugwu, J.C., "Batchelor Dual-band Antenna for Passive RFID Tags," SAIEE, Africa Research Journal, *Inc. Trans. of the SAIEE*, vol. 97, no. 3, September 2006.

8 C.A. Diugwu, J.C. Batchelor, and M Fogg, "Field distribution and RFID reading within metallic roll cage," *Electr. Letters*, vol. 42 no. 23, 2007

9 C. Diugwu and J. C. Bachelor, "Complementarity in the optimisation of RFID slot and patch tag antennas," in *Proc., IEEE AP-S Int. Symp.* and USNC/URSI National Science Meeting, June 2007, Honolulu, Hawaii, USA

10 C. Diugwu and J. C. Bachelor, "Complementarity in the optimisation of RFID dipole tag antennas," in *Proc., IEEE AP-S Int. Symp.* and USNC/URSI National Science Meeting, June 2007, Honolulu, Hawaii, USA

Contents

CHAPTER 1

INTRODUCTION

1.1 Motivation and Objectives

Research in automatic identification both to ensure improved security and personal safety is currently receiving significant interest. There have been recommendations to tag objects right from the start of a production stage in order to be able to trace them through a process chain [1.1]. The expectation is for a low cost tag that will enable the identification, tracking and location of objects anywhere in the world through the inter-operability of communication systems.

Radio frequency identification (RFID) will be one of the most exciting features of the next generation of auto-ID systems. Response to the increasing demand will be met through improvement in identification efficiency through diversification scheme and advances in antenna techniques [1.2].

This thesis considers at certain RFID frequency bands the selection of antennas whose electromagnetic properties are compatible with the objects to be tagged. By systematically adopting the principle of complementarity in tag antenna design [1.3], the options of creating tags for objects whose outer surface offers various compositions of support materials in the UHF and microwave regime are increased. Here complementarity also creates a choice for the use of cross polarised field pattern, wherein a patch electric field and magnetic field are substantially orthogonal to the slot electric field and magnetic field.

The immediate environment in which tags operate is another important consideration. Identification of a normal tag is often constrained when placed behind screened surfaces such as roll cage grids. Normally roll cage grids are frequency selective surfaces (FSS)

[1.4], [1.5] and if properly designed, would pass fields at tag frequency while stopping standing waves. Thus, issues concerning the transmissivity of roll cage wire mesh surfaces surrounding the tag as well as the feasibility of reading within roll cages will be presented.

This Chapter presents the mechanism of RFID systems in Section 1.1; a review of related past works is presented in Section 1.2; the factors that are militating against the read range of a tag and hence motivating this research are discussed in Section 1.3. The chapter concludes with a comprehensive summary in Section 1.4.

1.2 The RFID mechanism

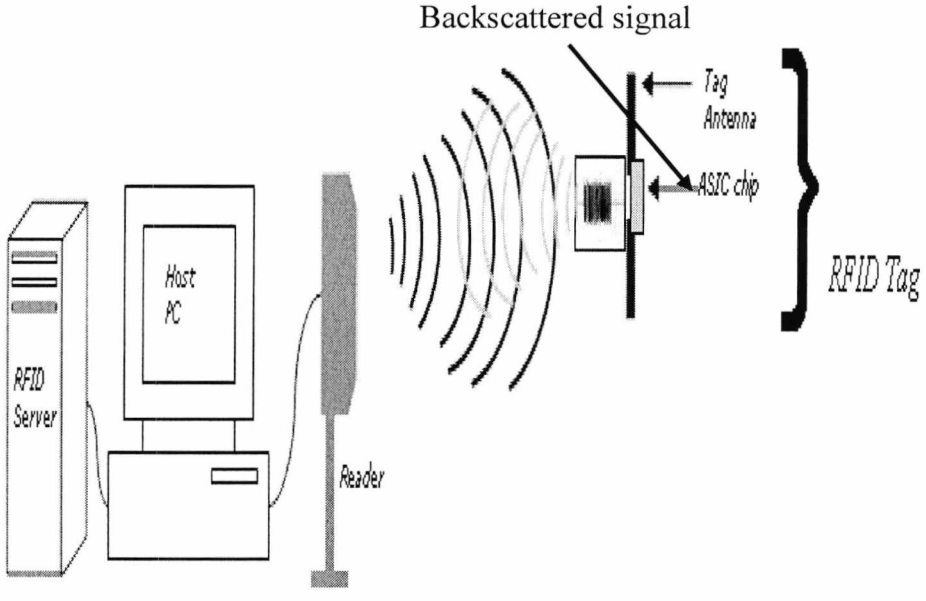

Fig. 1.1: An overall diagram of the typical RFID system

Figure 1.1 presents the overall identification system which consists of the tag, the reader and the data management system. This thesis is primarily concerned with developing tag antenna solutions. The tag is made up of an integrated circuit and antenna which, when attached to an object, is capable of receiving, holding and transmitting information related to the object. The process begins with the reader antenna transmitting a continuous wave (CW) that interacts with the tag attached to an object which then returns a modulated signal to the reader. Thus, the tag and hence the object can be tracked at any points on its journey. An introduction to and analysis of tag antennas can be found in [1.6], [1.7].

1.3 A review of previous work on this subject

Stockman's classic work on reflected power communication methods [1.8] still has significant research interest, resulting in a myriad of publications on the subject. In reference [1.9], Landt reported on RFID timeline including the development of long-range transponder systems of the well-known "identification, friend, or foe" (IFF) type for aircrafts. In contrast to the long range transponder, Harris developed the radio transmission systems with modulated passive responder [1.10]. In related work, Harrington studied the electromagnetic theory techniques and measurement for loaded scaterers [1.11], [1.12]. Although these early works arise out of experience with radar systems, they illustrate remarkable foresight and indeed have proved of value in the development of more recent systems.

The sensormatic and checkpoint Electronic Article Surveillance (EAS) was developed in 1969. This technology employed an only 1-bit tag which meant that only the presence or absence of a tag was detected. It should be recalled that at this time the size of the antenna for multi-bit tags was as large as $32\,cm \times 12\,cm$. The development in auto-ID systems had accelerated in the 1970s thereby increasing potential application areas. Consequently, Alfred Koelle working with Steven Depp and Robert Freyman had developed short range radio telemetry for electronic identification using modulated backscatter [1.13]. This innovation marked the beginning of the use of completely

passive tags. Read ranges of the order of tens of metres were achieved at the expense of large antenna size. The promise of automatic vehicle identification was reported in reference [1.14].

The spread of RFID was very rapid in the 1980s; for example with the introduction of electronic toll collection [1.15]. The quest for miniaturisation led to the use of the Electric Erasable Programmable Memory (EEPROM) which is a compact non-volatile memory. With this and other related advances, multi-tagging across different business types was achieved. Nonetheless, the engineering complexity of the chip technology continued to increase in the 1990s resulting in the development of microwave Schottky diodes that were constructed on a conventional Complementary Metal Oxide Semiconductor (CMOS) integrated circuit. From this followed the fabrication of a single integrated circuit for application in the microwave region. ASIC chips (also known as transponders) are now fabricated using surface acoustic waves (SAW) devices as tuning elements in the microwave operating frequency range [1.16], [1.17].

A tag can be distinguished as either active or passive [1.18]. An active tag requires the inconvenience of a battery but offers good sensitivity and transmit power. A passive tag uses an antenna to take power from the interrogating signal and thereby circumvents the problem of designing a separate power supply. In practical systems, the energy transferred to the chip in the second method is sometimes suboptimal. The ideal performance requires that the antenna should have an impedance at the operating frequency equal to the complex conjugate of the chip's impedance, [1.19]. Consequently, any means of improving matching will enhance performance.

The mere fact that a passive tag relies on an antenna to power-up obviously imposes a set of strict criteria on the choice and construction the antenna. In a conventional RF circuit, the antenna is connected to the signal processing unit by a transmission line. This mechanism increases losses. However, with the recent advances in planar antenna technology, it is now possible to fully integrate antennas with these RF components on the same board and thus significantly reduce the losses. The ease with which integration

can be achieved depends on the type and geometry of the tag antenna. Designs with Planar Inverted-F Antennas (PIFAs) for application to metallic objects have been reported [1.20] but integrating such antennas with ICs is often cumbersome. Thus, this thesis is concerned with uniplanar antennas for passive RFID tags. In order to facilitate tag creation, Rao *et al.* introduced a design guide in which the practicality of a folded dipole antenna was demonstrated [1.21].

1.4 Electromagnetic compatibility (EMC) considerations

Electromagnetic compatibility constrains both the operating frequency and power of an RFID system. With these constraints in mind, and given the need to recognize tags wherever they might be, the RFID designer must develop support for diversity techniques (multiple frequencies and dual or circular polarisations). Furthermore, the capacity of a single element printed antenna must be increased by using techniques of widebanding, dual-banding, and frequency or polarisation diversifications. In [1.22], wideband operation was reported which uses tuning stub to cause perturbation. Optimisation can also be achieved at any given frequency by varying the radiation characteristics of the antenna device to realise broad-band operation with circularly polarised fields [1.23]. Besides wide banding, antenna capacity can be increased by dual banding and in particular through exciting further available modes within the antenna structure. Recent designs include [1.24] which exploits orthogonal-modes to achieve dual band operation.

Size reduction is a very crucial factor in realising tag antenna requirements; with the result that miniaturisation techniques must be borne in mind early in the design stage. In order to realise smaller antennas, different methods have been proposed such as lossy dielectrics, meander lines and the use of shorting pins or active elements. Applying meander line techniques implies manipulating the field distribution within the antenna. Surface currents can be manipulated using bent dipoles or mender-line dipoles [1.25]. Size reduction can also be achieved using higher permittivity substrate at a financial, efficiency and bandwidth cost. Although much work has been published on the above

antenna techniques, very little literature seems to be available on the benefit of complementary planar antenna solutions for RFID applications.

Furthermore, the antenna characteristic can then be continuously adapted to the environmental conditions using an active circuit which maximises signal reception by creating peaks in antenna gain in the direction of arrival of the signals. But this is an expensive option so as far as tagging is concerned and for this reason, frequency diversity that enables operation within nulls is preferred.

The environment in which a tag operate can constitute a problem; for instance, transmitting signals through enclosures, specifically wire mesh roll cages that often surround the tag. Although the main function of roll cages is to physically secure objects while making then visually accessible, multiple reflections may arise from the surface of the cage and cause standing waves which can degrade the tag reception. The system is then suboptimal if this remains unchecked. Any means to predict or avoid sitting a tag in the nulls of standing waves increases reliability. For this reason, it is of great interest to study transmission of a typical reflective surface, that is, roll cages. A related work by Casey which involves the study of electromagnetic field shielding properties of wire mesh screen was reported in [1.26].

The era of study of extra-ordinary transmission through subwavelength holes in metallic films started with Ebbesen [1.27]. Transmission is enhanced by multiple reflections on walls which exhibit resonances in line with the lattice sizes and periodicity of the grid. In references [1.28] the study of the resonance-induced wave penetrating through electromagnetic opaque object which is analogous to a planar metal grid surface was reported. Also, the pioneering contribution of [1.29] on closely spaced elements gave insight into using array elements as a form of frequency selective surface, in which the perfect conductors act as a band pass and band stop respectively. This was formulated as a solution to an optimisation problem. Following this publication, and other works van der Molen et al. [1.30], the ability of a surface to discriminate certain frequencies was firmly established as an optimisation solution. Nevertheless, this kind of research is still

immature as far as RFID systems are concerned since the operational constraints within such enclosed surface has not been fully studied.

1.5 The Scope of this Project

The challenge of producing a reliable RFID system requires consideration of the following aspect of the antenna subsystem.

(i) The antenna must be low profile;

(ii) In order to satisfy the constraints imposed by electromagnetic compatibility (EMC) antenna must possess multi-functional characteristics in the RFID designated bands;

(iii) Antenna must be matched to non-50Ω and complex impedance chip while fulfilling cost and fabrication requirements;

(iv) Antenna must be insensitive to the platform on which it is mounted (which may include metal or glass containing liquid);

(v) Tagged cartons may be contained within metal sided roll cages for distribution;

(vi) The detection of antennas in a metal screened cavity is difficult due to fundamental electromagnetic limitations.

(vii) Antennas having a wide 3dB beamwidth and an efficient radiation response are needed to achieve depth of resolution of the target;

(viii) The physics behind the scattering problem is complicated due to the large number of parameters affecting the interaction between the electromagnetic field and current generated in the complex configuration of conducting metals and dielectric. Modelling techniques however play an important role in beginning to understand the electromagnetic wave propagation in the metal or dielectric environment.

1.6 Thesis Overview

This thesis introduces and methodically investigates novel passive uniplanar antennas for use in RFID tags. Electromagnetic simulation of these devices along with integrating them to the ASIC chip is a great challenge in RFID engineering. The target problem in this project is take advantage of complementary configurations in tag design for different material surfaces. Certain selected frequency bands are considered and some of the ways in which interaction with supporting materials can be optimised by introducing a choice of complementary antenna solutions are investigated.

The thesis has a total of seven chapters of which the four main chapters have been published. Chapter 2 presents some basic theoretical analysis of antennas, tags and the Radio frequency (RF) coupling mechanisms. Also included in this chapter is overview of the electromagnetic simulator, CST Microwave Studio and the tag measurements systems.

In Chapter 3 consideration are made at certain selected frequency bands, the strategy for tag antenna optimisation by considering the interaction of the choice of electric dipole or its complementary configuration magnetic dipole with the type of support materials. Besides, this chapter provides support of some of the concepts introduced in Chapter 2.

Chapter 4 introduces a novel dual band Slot Patch Antenna (SPA) design for application with passive RFID tags. Various configurations of slotted patches are studied in the context of creating a tag. Parametric studies and optimisation processes are investigated. The effect of field polarisations and radar cross section analysis of the antenna effects different materials on the antenna are presented along with read measurements of a tag fabricated using the SPA.

Chapter 5 explores complementarity in the optimisation of RFID tag antennas in order to increase the options of mounting antennas on different surfaces; hence a Complementary Patch Antenna (CPA), which is the inverted shape of the SPA antenna studied in chapter

4, is presented. A comprehensive parametric study is undertaken. Presented also in this chapter is the field polarisations and radar cross section analysis of the antenna. The effects of different materials on the antenna are presented along with read measurements of a tag fabricated using the CPA.

Chapter 6 investigates the feasibility of reading tags through wire meshes such as those of a roll cage. The influence of wire mesh size on the transmission responses of the roll cages is investigated. The standing wave profile within the structure is analysed. Results of reading tags inside the enclosure are presented.

In Chapter 7 a summary of the thesis is given along with conclusions and recommendations for future work in this topic.

1.7 References

[1.1] EPC Global, "Specification for air interface: EPC Radio frequency identification protocols, Class-1 Gneration-2 UHF RFID, Protocol communications at 860 MHz – 960 MHz," Version 1.0.9, 2005

[1.2] S. Sarma, D. L. Brock, and K. Ashton, "The networked physical world – proposal for engineering the next generation computing, commerce and automatic identification. Technical Report MIT-AUTOID-WH-001, MIT Auto-ID Center, 2000.

[1.3] G.H. Owyang and Ronold King, "Complementarity in the Study of Transmission Lines," IRE Transactions on Microwave Theory and Techniques, pp.172-180, March 1960.

[1.4] E.A. Parker, A.N. El Sheikh and A.C. de C. Lima, "Convoluted frequency selective array elements derived from linear and crossed dipoles," IEE, Proceedings-H, Vol. 140 No 5, pp.378-380, October 1993.

[1.5] B.M. Cahill and E.A. Parker, "Field switching in an enclosure with active FSS screen," IEE, Electronics Letters, Vol.37, No 4, pp.244-245, February

2001.

[1.6] K. Finkenzeller, "RFID handbook: fundamental and application in contact smart cards and identification," John Wiley & Sons England, 2003.

[1.7] P. Sorrells, "Passive RFID Basic", Microchip Technology Inc., AN680, DS00680B, 1998.

[1.8] Stockman Harry, "Communication by Means of Reflected Power", Proceedings of the IRE, pp 1196-1204, October 1948.

[1.9] Landt, J., "The history of RFID," Potentials, IEEE, Volume 24, Issue 4, Oct.-Nov. 2005 Page(s):8 - 11

[1.10] Harris, D. B.; "Radio transmission systems with modulatable passive responder", US Patent 2,927,321, March 1, 1960.

[1.11] Harrington, R. F., "Field measurements using scatterers", 1963-1964

[1.12] Harrington, R. F, "Theory of loaded scatterers", 1963-1964

[1.13] Baldwin, H., Depp, S., Koelle, A. and Freyman, R.; "Interrogation and detection system", US Patent 4,075,632, Feb 21, 1978.

[1.14] Hauslen, R. A., "The promise of automatic vehicle identification", IEEE Trans. On Vehicular Technology, Vol. VT-26, No 1, Feb 1977, pp 30-38.

[1.15] P. Blythe, "RFID for road tolling, road-use pricing and vehicle access control," *IEE Colloquium Dig. RFID Technology*, Doc. no. 19990675, Oct 1999, 8/1-8/16.

[1.16] Andreas Hierlemann and Henry Baltes, "CMOS-based chemical microsensors," *Analyst*, 2003, **128**, 15–28

[1.17] Ivan D. Avramov, "The RF-Powered Surface Wave Sensor Oscillator—A Successful Alternative to Passive Wireless Sensing," *IEEE Trans. on Ultrasonics, Ferroelectrics, and Frequency Control*, vol. 51, no. 9, September 2004, p.1148-1156

[1.18] I. D. Robertson and I. Jalaly, "RFID tagging explained," *IEE Engineer*, vol.1, no. 01, pp. 20-23, Feb 2003.

[1.19] Rao, K.V.S.; Lam, S.F.; Pillai, V.; Martinez, R.; Heinrich, H.; "Power

reflection coefficient analysis for complex impedances in RFID tag design," Microwave Theory and Techniques, IEEE Transactions on, Volume 53, Issue 9, Sept. 2005 Page(s):2721 - 2725

[1.20] Hirovnen, M.; Persula, P.; Jaakkola, K.; Laukkanen, K.; "Planar inverted-F antenna for radio frequency identification," Electronic Letter Vol. 40, Issue 14, 2004, pp. 848 – 850.

[1.21] Rao, K.V.S.; Nikitin, P.V.; Lam, S.F.; 'Antenna design for UHF RFID tags: a review and a practical application', *Antennas and Propagation*, IEEE Transactions on Volume 53, no. 12, Dec. 2005 pp. 3870 - 3876

[1.22] Horng-Dean Chen, "Broadband CPW-Fed Square Slot Antennas With a Widened Tuning Stub," *IEEE Trans. Antennas Propag*, vol. 51, no.8, Aug., 2003 p.1982-1986

[1.23] Hani A. Ghali, and Tarek A. Moselhy, "Broad-Band and Circularly Polarized Space-Filling-Based Slot Antennas" *IEEE Trans. Microw. Theory Tech.*, vol. 53, no. 6, Jun. 2005

[1.24] C.A. Diugwu, J.C., "Batchelor Dual-band Antenna for Passive RFID Tags," SAIEE, Africa Research Journal, *Inc. Trans. of the SAIEE*, vol. 97, no. 3, September 2006.

[1.25] Thomas. J. Warnagiris and Thomas. J. Minardo, "Performance of a Meandered Line as an Electrically Small Transmitting Antenna," *IEEE Trans. Antennas Propag*, vol. 46, no.12, December 1998 pp.1797-1801

[1.26] K. F. Casey, "Electromagnetic Shielding Behavior of Wire-Mesh – Screens," *IEEE Transactions on Electromagnetic Compatibility*, vol. 30, no. 3, August 1988 pp.298-306

[1.27] T. W. Ebbesen, H. J. Lezec, H. F. Ghaemi, T. Thio & P. A. Wolff, "Extraordinary optical transmission through sub-wavelength hole arrays," NATURE - *letters to nature* Vol. 391,12 February 1998, Macmillan Publishers Ltd., 1998

[1.28] Hen Wena, Bo Hou, Yang Leng, Weijia Wen, "Resonance-induced wave penetration through electromagnetic opaque object," OPTICS EXPRESS,

Vol. 13, No. 18 5 September 2005 pp.7005-7010

[1.29] Kraus, J. D., "Antenna Arrays with Closely Spaced Elements," *Proceeding of the IRE*, vol.28, Issue 2 Feb. 1940, p.76-84

[1.30] K. L. van der Molen, F. B. Segerink, and N. F. van Hulst and L. Kuipers, "Influence of hole size on the extraordinary transmission through subwavelength hole arrays," *Appl. Phys. Lett.*, Vol. 85, No. 19, 8 November 2004, pp.4316-4318

CHAPTER 2

THEORETICAL ANALYSIS

2.1 Introduction

The objective of this chapter is to review the fundamental concepts in the transmission of electromagnetic (EM) energy between reader and tag antennas. This is important because passive RFID systems unlike conventional wireless communication systems are powered at only one end of the communication link, and clearly have no leeway for inefficiency. Thus, a unique set of tag antenna design criteria needs to be satisfied [2.1].

The design goal is to achieve an antenna with improved performance at RFID frequencies specified by the electronic product code (EPC). The standard for a passive-backscatter interrogator-talks-first (ITF) transmission for radio-frequency identification (RFID) system operating in the 860 MHz - 960 MHz frequency range or at 2.45 GHz and 5.8 GHz frequencies is recommended in [2.2]. The frequency within the first band of 860 MHz - 960 MHz is usually specified by the national Government. For example, in the United Kingdom the operating frequency for this band is 869 MHz with a narrow operating bandwidth of 869.4 – 869.65 MHz. Despite different spectrum allocation constraints, tags are required to be recognized globally. The problem is to achieve a low cost antenna with sufficient antenna bandwidth to cover the range of frequencies in the different nations.

Printed antennas that are capable of exhibiting multifunctional operation, namely dual band and dual polarisation, are needed in RFID application. Their benefits will become apparent later on in Chapter 6 of this thesis where frequency diversity can be used for the standing wave problems. Dual band operation have been realised by: slot-coupled dipoles [2.3], and folded-slot monopole [2.4]. In reference [2.5], two bent dipoles and a modified T-matching network were configured to achieve a broadband tag antenna. Other broadband solutions for the application can be found in references [2.6] [2.7]. In both

cases, a single feed mechanism have been used which has advantages over the conventional method in [2.8]. David Pozar has carried out rigorous analyses of the different classes of antennas mentioned above [2.9], [2.10], [2.11].

The numeric methods used for analysing antennas vary from simple equivalent circuits [2.12], [2.13] to the more complex full wave techniques involving numeric techniques. The choice of solution depends on the structural geometry and also on the treatment of the electromagnetic parameters to be investigated. In the Method of Moments (MoM) the physical problem can be solved by a system of linear equations and has been extensively reported in [2.14]. The method of Finite Difference Time Domain (FDTD) analysis is useful for more complicated three-dimensional designs. It gives an efficient numeric algorithm in computational electromagnetics but is unable to generate the exact meshes for structures with curved boundaries [2.15]. The staircase approximation together with FDTD can generate fine mesh grids but leads to very small time steps.

In the CST Microwave software, which has been used in this work, the algorithm provides solutions for spatially discretized electromagnetic problems using the Finite Integral Technique (FIT) in conjunction with Perfect Boundary Approximation (PBA) methods [2.16]. It is therefore suitable for analysing both the irregular shaped antennas and the wire mesh roll cage that will be presented in the thesis.

This Chapter is divided into seven Sections. The fundamental principles of an antenna are outlined Section 2.2; Section 2.3 presents the conditions required for maximum power transfer between the antenna and chip circuitry while the fundamental operating principles of the system are presented in Section 2.4. The theories relating to the Read ranges are reviewed in Section 2.5. Sections 2.6 and 2.7 describe the simulation software and measurement systems in this work. Some conclusions about this chapter are drawn in section 2.8.

2.2 Some basic antenna theory

A proper understanding of the basic theory of antennas parameters is important for successful design and optimisation of antennas in RFID systems. As a foundation for this understanding an overview of the fundamental theorems upon which antenna characteristics are derived is recited.

Circuit models for a tag (antenna and chip) are provided, along with a set of experimental results and empirical equations for performance parameters of useful antennas.

2.2.1 The antenna impedance

Much of the work in chapters 3, 4 and 5 involves both in theory and in practice the S_{11} scattering parameter. Hence a brief revision will now be given of this topic. The Scattering Parameters (S-parameters) describe the scattering and reflection of a travelling wave when a network is inserted into a transmission line. Here this is applied to the antenna attached to the end of its feed line. Fig. 2.1 shows
a simplified equivalent circuit of an antenna model as a transmission line.

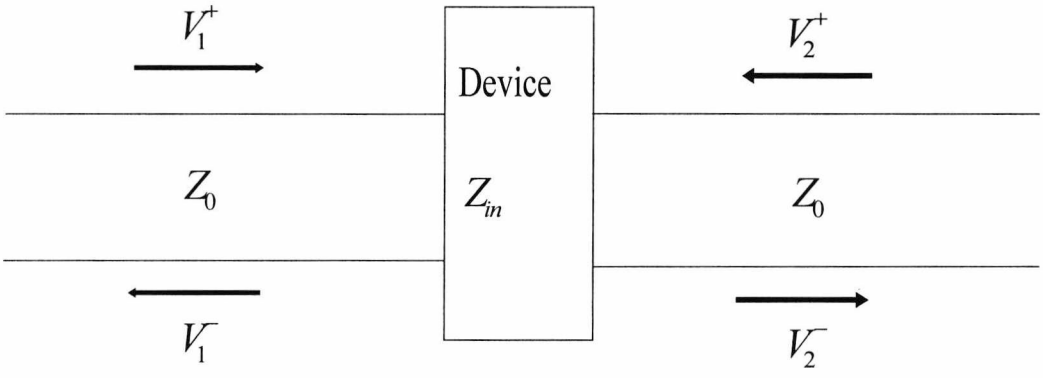

Fig 2.1: A simplified equivalent circuit of an antenna model as a transmission line

In this way, the ratio of a travelling incident voltage wave, V^+ to the scattered wave V^- can at each port be related. A set of relationships are defined in the matrix form [2.17]:

$$\begin{bmatrix} V_1^+ \\ V_2^+ \end{bmatrix} = \begin{bmatrix} S_{11} & S_{12} \\ S_{21} & S_{22} \end{bmatrix} \begin{bmatrix} V_1^- \\ V_2^- \end{bmatrix} \qquad 2.1$$

For a given element, e.g. S_{ij}, within the matrix in (2.1), the expression becomes:

$$S_{ij} = \frac{V_i^-}{V_j^+} \qquad 2.2$$

The antennas problems in this work are mainly of a single port, therefore only the S_{11} will be considered. Thus, from (2.2) the corresponding expression is given by:

$$S_{11} = \frac{V_1^-}{V_1^+} \qquad 2.3$$

where, S_{11} is the reflection coefficient of the input

Furthermore, within these specific elements of the S-parameter, the input impedance is related according to the following expression:

$$S_{11} = \frac{V_1^-}{V_1^+} = \frac{Z_{in} - Z_o}{Z_{in} + Z_o} \qquad 2.4$$

where, Z_{in} is the input impedance of the antenna and,

Z_o is the characteristic impedance of the feed system

From which

$$Z_{in} = \left(\frac{1 + S_{11}}{1 - S_{11}}\right) Z_o \qquad 2.4(b)$$

2.2.2 The antenna radiation pattern and directivity

Given that the antenna of the tag may be orientated in a variety of directions compared with the Reader that is interrogating it, it is necessary to describe how the power received and returned to the Reader depends on the particular angle of the tag with respect to the line of the interrogating signal.

The first step in doing this is to define the directivity of the antenna in an arbitrary direction given in spherical coordinates θ, ϕ.

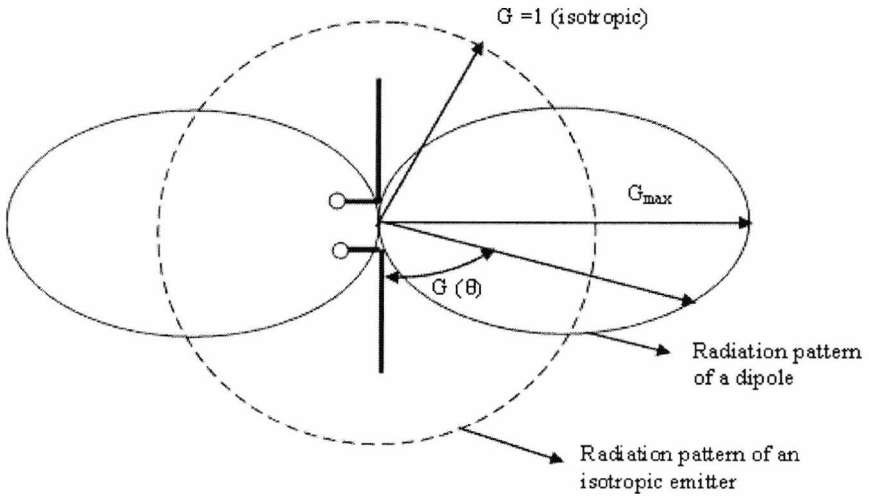

Fig 2.2: A comparison of the radiation patterns of an isotropic emitter and a dipole antenna

The directivity of an antenna represents the ratio of the radiation intensity in a given direction from the antenna to the radiation intensity averaged over all directions. The

average radiation intensity is equal to the total power radiated by the antenna divided by 4π [2.18].

$$D(\theta,\varphi) = 4\pi.\frac{power\ radiated\ per\ unit\ solid\ angle}{total\ radiated\ power} \qquad 2.5(a)$$

Assuming that the power radiated per unit solid angle is denoted by $S(\theta,\phi)$ and the total radiated power by P_{rad}, then the directivity denoted by $D(\theta,\varphi)$ can be expressed as:

$$D(\theta,\varphi) = \frac{4\pi.S(\theta,\varphi)}{P_{rad}} \qquad 2.5(b)$$

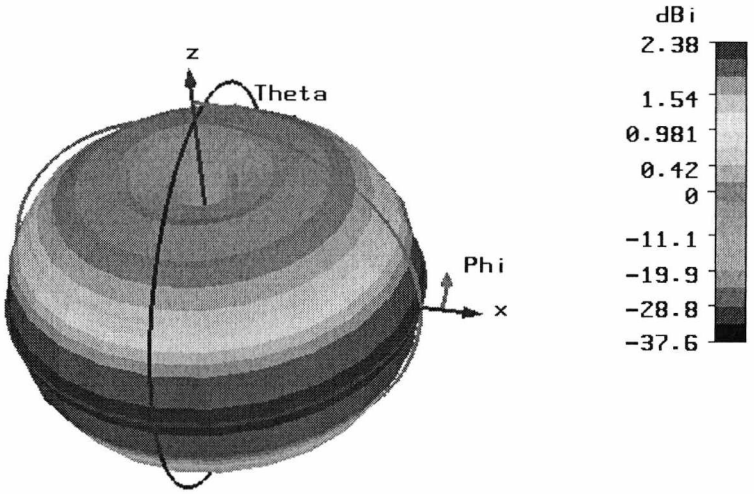

Fig. 2.3: A radiation pattern of a simple linear dipole using CST Microwave studio.

The antenna gain defined as in directivity but related to the input (or accepted) power, thus:

$$G(\theta,\varphi) = 4\pi.\frac{power\ radiated\ per\ unit\ solid\ angle}{input\ (accepted)\ power} \qquad 2.5(c)$$

The radiation efficiency is defined as the ratio of gain to directivity or the ratio between the radiated to input (accepted) power of the antenna.

$$G(\theta,\varphi) = e_{rad}\,.\,D(\theta,\varphi) \text{ or, } P_{rad} = e_{rad}\,.\,P_{in} \qquad 2.5(d)$$

The electromagnetic distance of a radiating wave can be classified into the near-field and the far field. The characteristics of a propagating EM field changes gradually with distance from the source. The near field consists of both the evanescent (reactive) and the radiating field. Although there are fluctuations in the localised field energy, the average field energy density here is relatively constant at different locations from the antenna. Here the electromagnetic energy decays rapidly with distance. The far field starts from the point where the distance r away from the antenna is approximately $r=2D^2/\lambda$, where D is the antenna diameter and λ is the radio frequency (RF) wavelength at the operating frequency [2.19]. The location of a tag is an important consideration in trying to understand the performance of an RFID system. Antenna characteristics at the far field regions are more relevant in this thesis. The underlining assumption in the above formulation is that the tag is located in the direction of strongest radiation from the interrogator antenna.

In the numerical software CST that will be used in this project, the far field is obtained through near field to far field transformation. The far field is represented by two components (E_θ, $E\varphi$) at spherical coordinates Theta and Phi in the azimuth plane. These components are derived from the calculated fields stored on the bounding box of the calculation domain. Since a tag can assume any orientation, the antennas studied in chapters 4 and 5 will be considered for the *x-y, y-z* and *x-z* planes.

2.3 Matching the antenna to the ASIC chip

An RFID tag consists of two major parts namely, the antenna and the RFID chip as illustrated in Fig 2.4.

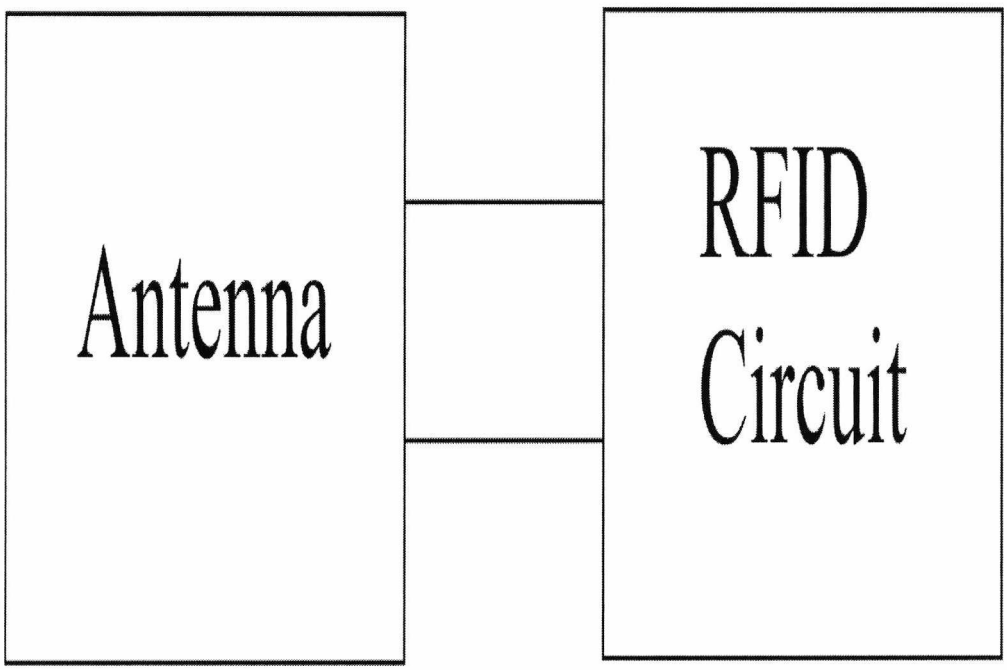

Fig. 2.4: A schematic diagram of RFID tag

Transponder chips have unique identification codes that can only realise the backscatter principle if the tag antenna attracts sufficient electromagnetic energy from the interrogating radio frequency (RF) of the Reader. As would be expected, the integrity of the power and data links can be quite severely degraded if the tag antenna is unable receive sufficient energy from the interrogating EM field to activate the transponder chip.

2.3.1 Equivalent circuit model of the available power at the tag

Assuming that the transmission line feed between the antenna and the chip is electrically short, Fig. 2.5 illustrates possible equivalent circuit for the antenna and the chip.

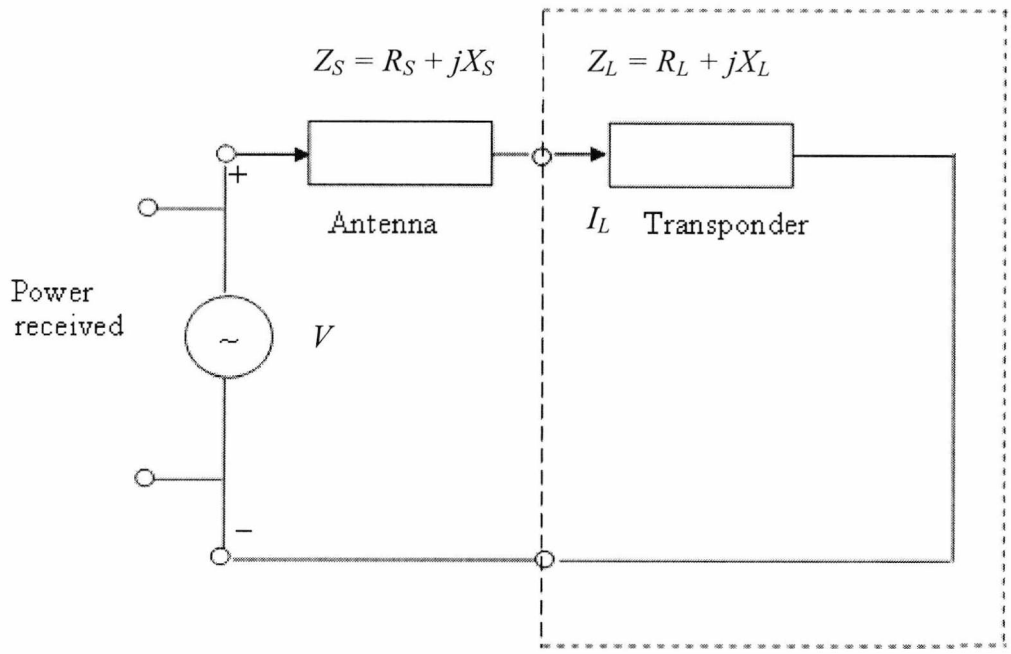

Fig. 2.5: The equivalent circuit showing the intercepted power

Assuming the power available as power collected by the antenna in receiving mode is (P_{rec}) [2.20], then in the above circuit, the power across the antenna terminals is given (where peak values of voltage and current are to be considered) by:

$$P_{rec} = \frac{1}{2}\left(V_A I^*\right) = \frac{1}{2} I^2 R \qquad 2.6$$

But, the current into the chip is given by:

$$I_{chip} = \frac{V}{Z_S + Z_{chip}} \qquad 2.7$$

The real part of the above expression yields:

$$p_{rec} = \frac{1}{2} I^2 R = \frac{1}{2}\left(\frac{|V_A|}{|Z_{chip} + Z_S|}\right)^2 \left(R_{chip} + R_S\right) \qquad 2.8$$

The power that goes into the chip because of the current and resistive part of the chip input impedance becomes:

$$P_{chip} = \frac{1}{2}(I)^2 R_{chip} \qquad 2.9$$

But, the current into the chip is given by:

$$I_{chip} = \frac{V}{Z_S + Z_{chip}} \qquad from\ equation\ (2.7) above$$

Therefore,

$$P_{chip} = \frac{1}{2}\left[\frac{V}{(Z_S + Z_{chip})}\right]\left[\frac{V}{Z_S + Z_{chip}}\right]^* R_{chip} = \frac{1}{2}\frac{|V|^2}{|Z_S + Z_{chip}|^2} R_{chip} \qquad 2.10$$

Conclusions to this section

Hence from 2.8 and 2.10, the ratio of power in the chip to the power received at the antenna is:

$$\frac{P_{chip}}{P_{rec}} = \left(\frac{R_{chip}}{R_{chip} + R_S}\right) \qquad 2.11$$

R_S is made up of radiation resistance(R_r) and loss resistance (R_L). The loss resistance is zero for a lossless antenna.

Furthermore, under conjugate matched condition $Z_S = Z^*_{chip}$, hence $jX_S = jX_{chip}$ and $R_S = R_{chip}$. Thus the *maximum power* that can be delivered to the tag becomes:

$$\frac{P_{chip,\max}}{P_{rec}} = \frac{1}{2} \qquad 2.12$$

2.3.2 Modifying the reactive component of the antenna in order to obtain the condition for maximum power transfer

The need to have a proper impedance matching between the antenna and the ASIC chip as assumed above required the conjugate matched condition $Z_S = Z^*_{chip}$.

Consideration will now be given how to tune out the reactive parts of the frequency-dependent complex impedances and achieve this maximum power transfer.

Possible options are to incorporate matching networks or design antenna whose impedance is a conjugate of the ASIC chips input impedance. A conventional matching network adds cost because of engineering complexities but, on the other hand, the cost of redesigning an ASIC chip by far outweighs that of an antenna redesign. A simple inductive loop constructed around the antenna feed point can solve the problem of matching by cancelling out the reactive effect of the capacitance of the chip. A full analysis of this loop method is presented in [2.21].

2.3.3 Considering the effect of mismatch in the real components of the antenna and chip impedances.

This will now be considered in terms of the equivalent circuit as shown in Fig 2.6.

Assume in the following that the antenna already has the reactive component of the antenna matched to that of the ASIC chip. That is:

$$X_L = - X_S \qquad 2.13$$

The fraction of the total power delivered to the transponder chip is given by $R_L / R_S + R_L$ while the fraction of the re-radiated power is given by $R_S / R_S + R_L$ (As R_S is the radiation resistance of the antenna).

Half of the total power drawn from the electromagnetic field is re-radiated (as represented by the power in R_S) whilst the other half is absorbed by the transponder IC [2.20].

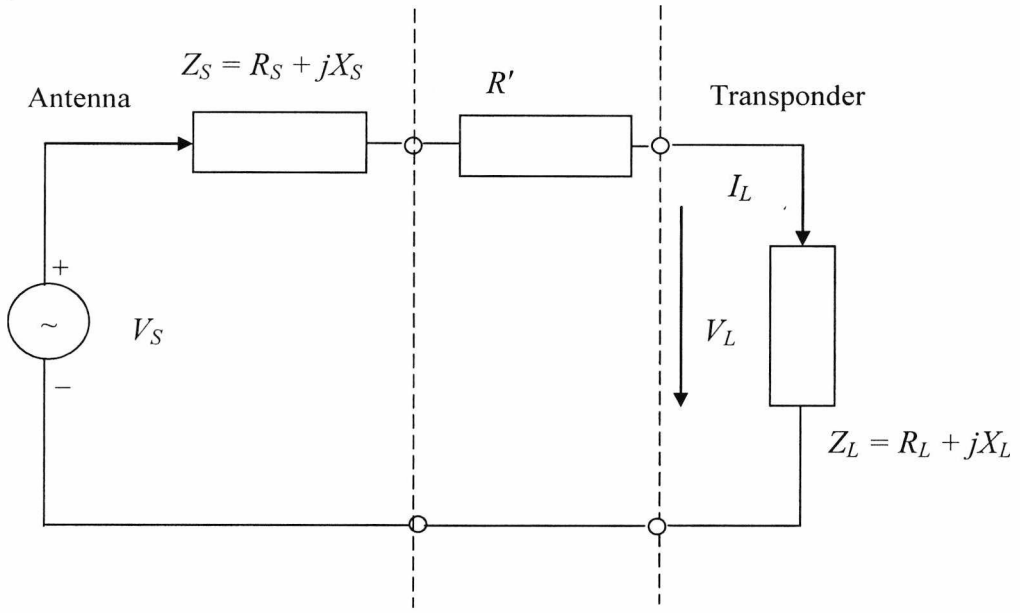

Fig 2.6: Equivalent circuit of a lossless tag antenna coupled to a transponder chip.

In practice the resistive part of the chip impedance will not equal that of the antenna radiation resistance. If this error in the impedance of the chip is represented by R', then this may be shown on the equivalent circuit as in the figure Fig 2.6 above.

If R' = 0, the circuit is considered matched and has a voltage reflection factor of 0. In other words, all of the maximum possible available power will be transferred to the chip. If R' is increased to R_L, the quality factor will be ½ of Q_L, where Q_L is the quality factor for only the load R_{chip}. If $R' = 2R_{chip}$ the quality factor will the become $^1/_3$ of Q_L. This indicates by how much the quality factor is reduced as the error in the chip input resistance increases. By increasing the value of R', the quality factor will reduce and therefore the bandwidth will increase. The compromise is that the efficiency will decrease however it may still be within the acceptable range while the bandwidth is usefully increased.

2.4 The analysis of the complete free-space there-and-back path between the Reader and the tag

This Section describes the basic relationship between tag and reader antennas (Fig. 2.7). The objective is to explore the mechanism by which energy is supplied to the tag which makes it possible for data to be transferred to the reader. The modulated backscatter method is preferred for transmissions in the microwave region for the reason that it offers the potential for a wider range [2.20]. Other transmission methods are inductive coupling at lower frequency regimes, typically 135 kHz or 13.45 MHz; the close coupling method which is used for high power consumption chip cards; electrical coupling which usually operates within a very high voltage condition.

Both the inductive coupling and EM backscatter methods employ the load modulation techniques for data transfer. This thesis emphasises the second method read range for the reason given above.

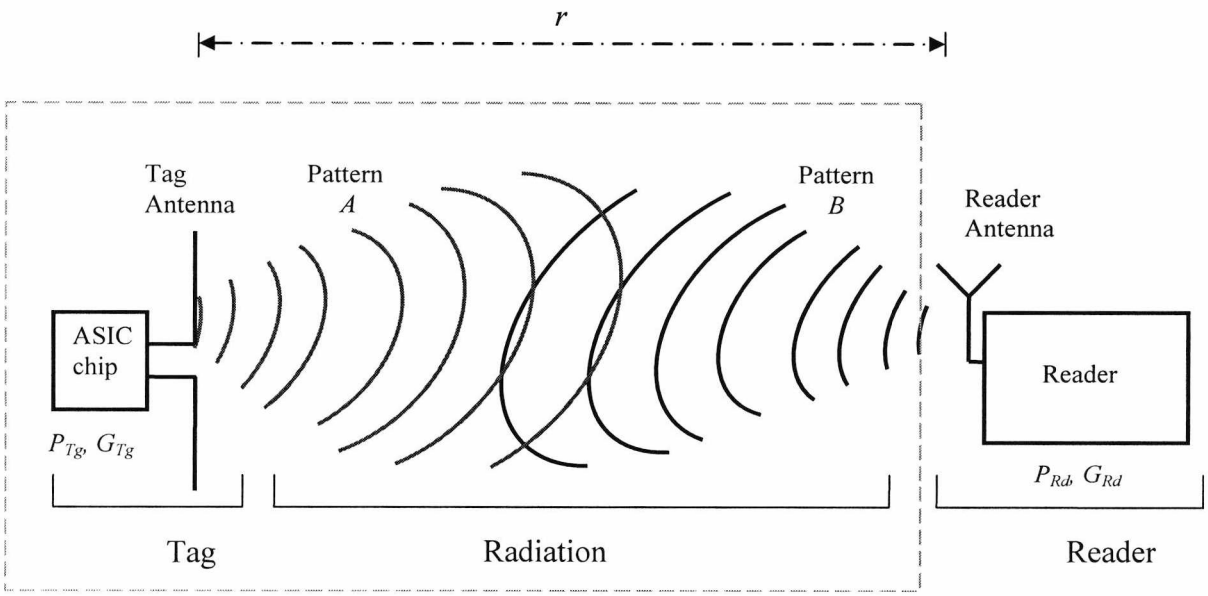

Fig: 2.7: Overall diagram of RFID system showing free space power transmission over a common link.

Definitions:-

G_{Rd} = the reader antenna gain on boresight

G_{Tg} = tag antenna gain on boresight

P_{Rd} = power transmitted from the reader (watts/m^2)

P_{Tg} = the power received by the tag in the forward link (watts)

2.5 Read range when both antennas are oriented for maximum gain.

The schematic diagram of Fig 2.7 depicts a reader antenna illuminating a tag antenna located a distance r in the direction of maximum gain. As earlier mentioned, a fraction of the wave incident on the tag will be reflected while the other fraction will be transferred to the transponder (under perfect matched condition). Assume also that the tag antenna is located for maximum transmitter gain in the direction of the Reader.

In reference [2.22], the budget link of an RFID system is analysed. It is shown in Fig. 2.8 that for a reader antenna transmitting with the power P_{Rd} and a gain G_{Rd}, the received power density at the location of the tag antenna, denoted by $\mathbf{P}_1$ is given by:

$$P_1 = \frac{P_{Rd}G_{Rd}}{4\pi r^2} \qquad 2.14$$

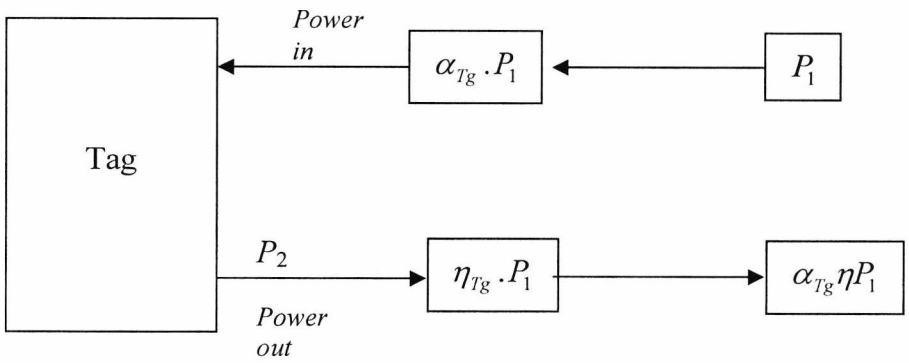

Fig. 2.8: Illustration of power in and out of a tag

Hence, due to the effective cross sectional area of the tag antenna, α_{Tg} and the transfer of power from the input to the output of the tag considered as an overall efficiency, η, power retransmitted out of the tag is:

$$P_2 = \alpha_{Tg}\eta \times P_1 = [\alpha_{Tg}\eta]\frac{P_{Rd}G_{Rd}}{4\pi r^2} \qquad 2.15$$

This generates a power density back at the Reader of P_3:

$$P_3 = \frac{P_2 G_{Tg}}{4\pi r^2} = \left[\alpha_{Tg}\eta \times P_1\right] . \frac{G_{Tg}}{4\pi r^2} \qquad 2.16$$

$$= \alpha_{Tg}\eta \frac{G_{Tg}G_{Rd}}{(4\pi r^2)^2} \times P_{Rd} \qquad 2.16(b)$$

where α represents the cross sectional area of the tag

η represents the efficiency of the tag

To finally obtain the total power received back at the reader, P_4 will take into account the cross sectional area of the reader antenna which is denoted by α_{Rd}.

Thus,

$$\text{Power at Reader, } P_4 = \alpha_{Tg}\,\alpha_{Rd}\,\eta \frac{G_{Tg}G_{Rd}}{(4\pi r^2)^2} \times P_{Rd} \qquad 2.17$$

If the *minimum detectable received power*, $P_{R\min}$ is the power that will satisfy RFID operations over a maximum distance, $r_{\max}$, these parameters may be substituted in the equation above:

$$P_{R\min} = \alpha_{Tg}\,\alpha_{Rd}\,\eta \frac{G_{Tg}G_{Rd}}{(4\pi r_{\max}^2)^2} \times P_{Rd} \qquad 2.18$$

where, $P_{R\min}$ = the minimum detectable received power.

P_1 = power density transmitted from the reader (watts/m^2)

P_2 = the power received by the tag in the forward link (watts)

P_3 = the power received by the reader (backscattered power) in the backward link (watts/m^2).

P_4 = the power back at the reader (watts)

Note 1.

$$\alpha = \frac{\lambda^2}{4\pi} G$$

Therefore,

$$\alpha_{Tg} = \frac{\lambda^2}{4\pi} G_{Tg} \quad and, \quad \alpha_{Rd} = \frac{\lambda^2}{4\pi} G_{Rd}$$

Hence,

$$P_4 = \frac{\lambda^4}{4\pi^4} \cdot \eta \frac{G_{Tg}{}^2 G_{Rd}{}^2}{(4\pi r^2)^2} \times P_{Rd} \qquad 2.19$$

From where the ratio between the power received back at the reader to that which was originally transmitted becomes:

$$\frac{P_4}{P_{Rd}} = \frac{\lambda^4}{4\pi^4} \cdot \eta \frac{G_{Tg}{}^2 G_{Rd}{}^2}{(4\pi r^2)^2} \qquad 2.19(b)$$

Note 2.

η is dimensionless and depends on:

a) proportion of incident power used in the re-transmitted information signal

b) the effect of modulation

2.5.1 Read range when the tag antenna is pointing off boresight by a direction θ, ϕ

As the tag antenna is turned away from the boresight direction of the Reader there will be two effects:

1. The amount of power from the Reader that is intercepted will be reduced
2. The radiation pattern from the tag antenna will give a reduced power in the direction back to the Reader.

2.5.2 Radar cross-section of a passive tag antenna.

The Radar Cross Section, RCS, denoted by σ, is the product of the antenna effective area and the intercepting power density. It is a measure of the power scattered in a particular direction when an antenna is illuminated by an incident electromagnetic wave. Thus, RCS gives knowledge of the degree of scattering inherent in an antenna. This concept, which will be explored in each of the antenna presented in the thesis, depends on the parameters of the incident wave such as polarization, angle of incidence, material composition and the operation frequency. It is also dependent on the antenna geometry as well as the material characteristics. A detailed analytic formulation for RCS can be found in [2.23].

The structural and antenna modes scattering associated with a radar cross section is discussed in detail in reference [2.24]. The structural mode RCS are due to the geometry and composition of an antenna while the antenna mode is related to the antenna design specification.

Four special considerations of possible tag antenna impedances and RCS can be made with reference to Fig. 2.6 and are given here in outline in order to further understand the level of modulated power transmitted by the tag.

1. The short circuit case (in which the returned power is not modulated), denoted by the subscript *s/c* representing when the backscattering is at its maximum. The reflection coefficient Γ_a = -1. In reference [2.23], the antenna scattering aperture under this condition has been found to be equivalent to four times its effective area. For this, only a small amount of energy per second is dissipated as heat in the internal resistance and the antenna is primarily regarded as a scatterer. The problem involved in a scattering mode antenna is to determine the scattered field; this will be treated further in chapters 3 – 5.

2. The open circuit case, denoted by the subscript *o/c* corresponds to the case when the backscattering is also at a maximum, the reflection coefficient is Γ_a = +1. The antenna RCS is zero since Z_T = 0, where Z_T is the combined impedances of the antenna Z_s and that of the ASIC chip Z_{chip} tends to infinite and also I = 0 (section 2.3).

3. The resistor loaded case denoted by the subscript R_x corresponds to when the tag is loaded with a resistive load. This usually happens under ideal situation in which the reactance of the antenna cancels that of the ASIC chip. Under this condition, the antenna scattering aperture is equivalent to its effective area.

4. In the ASIC case (usually for a very short duration) denoted by the subscript $_{ASIC}$, the reflection coefficient may vary between -1 through 0 to +1 or between the short circuit case and resistive load or open circuit in accordance with the chip design [2.24].

A tag antenna is considered as a scatterer when the transponder chip is in the short circuit position, but as an absorber when the switch is in the resistive load position. With regard to the second case, the magnitude of the scattered wave is reduced by virtue of the power used to activate the transponder.

2.6 Numeric and system modelling.

The objective of this Section is to briefly describe the basic operating principles of the software employed in this study. The CST Microwave Studio full-wave electromagnetic simulator has been used to analyse the characteristics of both the antenna and wire mesh roll cages that are studied in the thesis. It uses the Finite Integral Technique (FIT) to solve static or time-harmonic, low frequency and high frequency problems by discretizing Maxwell's integral equations [2.25]. Like the Finite Difference Time Domain (FDTD [2.26], the algorithm is suited for time domain analysis. Furthermore, it is imbued with additional capacity for frequency domain analysis.

In the discretization process, the FIT is applied to a conventional Cartesian grid, and then combined in time domain with the leapfrog time integral scheme. This results in a small memory requirement and an efficient explicit time stepping algorithm. A finite calculation domain, containing the application problem is defined which solves Maxwell's equations numerically. This domain is sub-divided into grid cells of numerous small cuboids as shown in Fig 2.9.

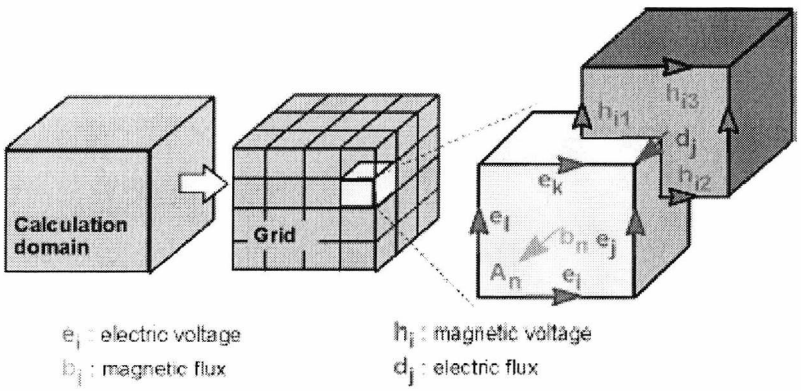

Fig: 2.9: Discretisation of problem space for implementation of Maxwell's equation as given by CST Microwave Studio.

This first or primary mesh can be visualized in the CST MICROWAVE STUDIO in the *Mesh View*, however, internally a second or dual mesh is set up orthogonally to the first

one. The spatial discretization of Maxwell's equations is finally performed on these two orthogonal grid systems, where the new degrees of freedom are introduced as integral values as well.

2.6.1 The CST advantage.

The standard FIT is constrained by the following:

1. The stair-case problem which results in poor modelling quality for irregular shaped geometric objects, if Cartesian grids are used.
2. The simulation of large structures with high quality factor leads to long transient and hence long simulation time.
3. The simulation of electrically large structures leads to large number of grid points for all volume-grid based methods including FDTD, FIT or the Finite Element Method (FEM). In addition, problems relating to numerical dispersion error of the above methods might arise in which small deviations in the phase of electromagnetic waves on the grid may accumulate and deteriorate the overall accuracy particularly if the structure is larger than 20 to 30 wavelengths. The Method of Moments (MoM) has an advantage over such methods and thus has been used for example in calculation of RCS for large aeroplanes [2.27].

As a solution, CST software combines FIT with a perfect Boundary Approximation and Thin Sheet Techniques.

2.6.2 Measurement of Systems.

This subsection presents general descriptions of the two measurement environments in which either the antenna frequency response is characterised or the tag read ranges tested. The measurement tools and procedure are also described.

Specifically, the Vector Network Analysers (VNA) was used to obtain the S_{11}; the anechoic chamber used for the far-field radiation pattern and the IPICO Reader system

for the tag read range. The read range was tested both in the open laboratory (free space) and inside the anechoic chamber. The following sub-sections detail the test procedures.

2.6.2.1 Open Laboratory Test for S_{11}.

The so-called open laboratory environment is distinct from the anechoic chamber environment in that the propagating electromagnetic waves were not restricted; however, care was used to keep scattering objects away from the vicinity of measurement. The tests undertaken here comprise the antenna S_{11} and the tag read range. The VNA has been used for characterising frequency responses (S_{11}). VNA calibration is relatively straightforward as has been extensively reported [2.28]. A standard two-port calibration procedure for error correcting all measurements has been followed.

The fundamental principle is that structural faults in the measurement system are characterised by first measuring a known standard. The characterized behaviours of the standards are then fed into the measurement to isolate their effects from those of the antenna under test, AUT.

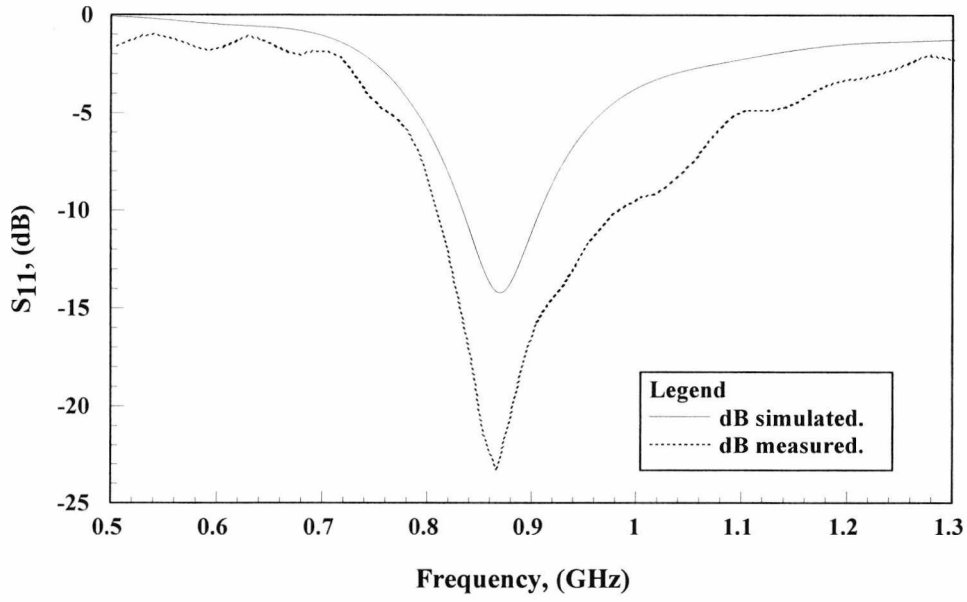

Fig. 2.10: Comparison of the simulated and measured S_{11} of a simple linear dipole at 869 MHz.

The viability of this method has been demonstrated by comparing results of the fabricated hardware prototypes with that of the numerical simulation using the full-wave software package CST Microwave Studio discussed in section 2.6 above. Shown in Fig. 2.10 above is an agreement between simulated and measured S_{11} of a simple linear dipole which will be presented later in Chapter 3 of this thesis.

2.6.2.2 Experimental investigation of Read Range of a Tag.

The next step involves testing the read range. The tag was supported with a foam substrate whose dielectric constant approximates that of free space. A tag constructed of the dipole mentioned above has been assessed for read range. For this case, a parametric study was carried out on the dipole which operated at 869 MHz. The dipole was fabricated from a thin copper layer printed on a paper substrate thus, allowing the dipole length to be trimmed successively from a full wavelength to an eighth of a wavelength by multiples of 2. The dipole was integrated with an EM4222 transponder chip. The design parameter used to study the tag performance was the resonant length of the dipole antenna.

A set of range values corresponding to tags of different dipole lengths (i.e. λ, $\lambda/2$, $\lambda/4$, $\lambda/8$ length) were tested. The schematic set-up for read range measurement has been described in Chapter 1 of this thesis and need not be repeated here. The enabling software was *Showtag* supplied by RF Tag Ltd. UK. The effect of the dipole antenna resonant length on the tag read range is shown in Fig. 2.11.

It can be seen from the above figure that the optimum range was obtained when the dipole length was 0.155 m. This corresponds to approximately half wavelength dipole at 869 MHz. In principle, a half wavelength dipole antenna should have a physical length 0.17 m at the operating frequency of 869 MHz (each arm of the dipole being 0.086 m). However, this adjustment was necessary as part of the antenna was printed on a circuit board, and the dielectric will have loaded the antenna causing it to be slightly larger than the free space half-wavelength.

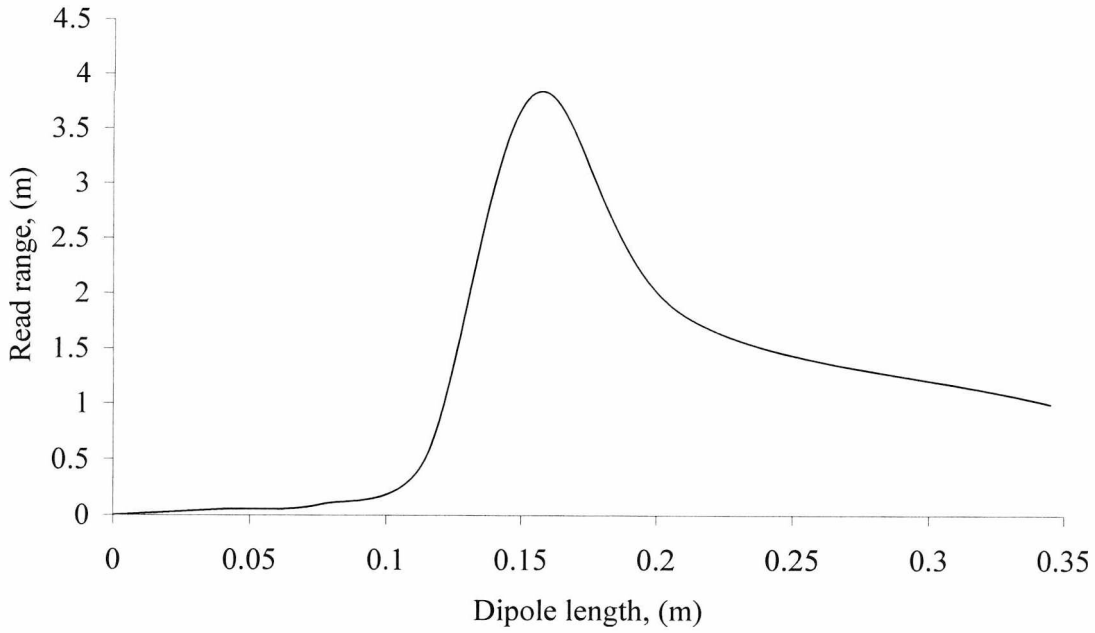

Fig. 2.11: Read range of a simple dipole as function its physical length.

2.6.2.3 Anechoic Chamber Measurements.

An anechoic chamber works by absorbing non-direct Radio Frequency (RF) signals. The walls of the anechoic chambers at the University of Kent are lined with a pyramidal microwave absorber composed of a foam sponge material impregnated with carbon graphite particles. Any extraneous energy coming into contact with this absorber material is changed into heat which is then dissipated along the absorber itself preventing it from reflecting back on to the test environment.

The anechoic chamber provided an environment of not only measuring the far field radiation pattern of the antenna, but also allowed the measurement of the tags read ranges. The radiation patterns of the antenna under test (AUT) were obtained in the azimuth plane. A laser pointer was used to align the AUT with the transmitting antenna. The internal view of the chamber along with an AUT is shown in Fig. 2.12.

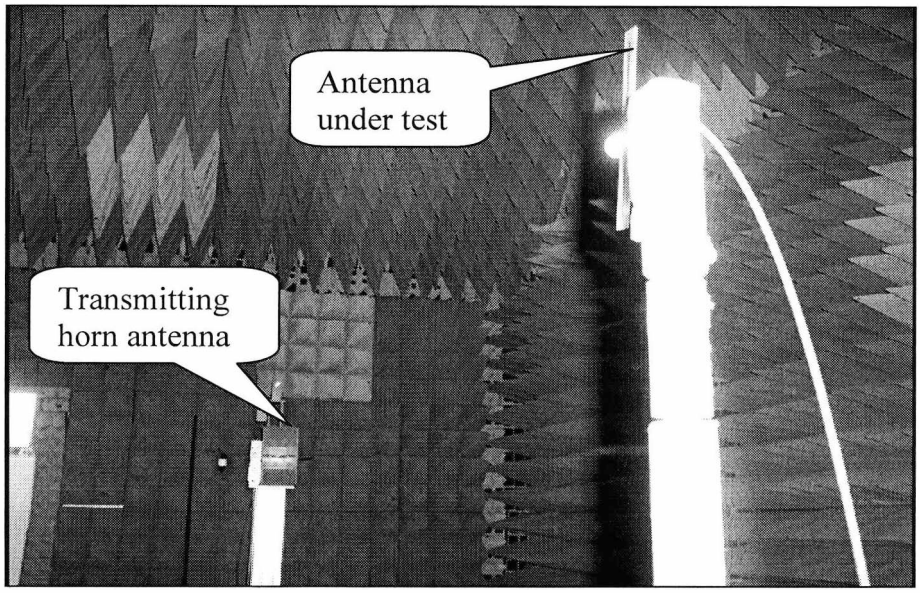

Fig. 2.12: Schematic layout for far field radiation measurement inside the anechoic chamber.

Further measurement using the anechoic chamber will be explored in the course of reading tags inside a wire mesh roll cage that will be presented later in chapter 6 of this thesis.

2.7 Conclusion

The basic theories of an antenna have been outlined, and the condition necessary for maximum power transfer between an antenna and its chip has been defined. A set of concepts suitable for describing the communication link between a tag and an interrogating Reader in an RFID system have been defined. Also, this chapter had identified some of the influences on the tag ability to receive power under various antenna load conditions. The theoretical read distances from which a tag can be detected have been shown to be predictable using the bi-directional radar equation. Tests results of a tag made of a simple dipole antenna demonstrate the variation of Read range as a function antenna length.

As a full wave electromagnetic simulator, the CST Microwave Studio is capable of discretizing problem space even for irregular shaped objects using the Perfect Boundary Approximation and Thin Sheet Techniques.

This chapter also presented overviews on the measurement and test systems, which will be used throughout this thesis. Network analyser was used to characterise the frequency response of the antennas. The antenna far field radiation patterns were measured inside the anechoic chamber and the IPICO Reader running on RF Tag *Showtag* Software was used for testing tag read performances both in the open laboratory and inside the anechoic chamber environments.

Chapter 3 supports this Chapter using further theoretical arguments and experimentation. The feasibility of complementarity options for tagging objects using linear dipoles will also be demonstrated. Chapter 4 extends the concept of comlementarity to an irregular shaped slot antenna.

2.8 References

[2.1] Stockman Harry, "Communication by Means of Reflected Power", Proceedings of the IRE, pp 1196-1204, October 1948.

[2.2] EPC global, "Specification for air interface: EPC Radio frequency identification protocols, Class-1 Gneration-2 UHF RFID, Protocol communications at 860 MHz – 960 MHz," Version 1.0.9, 2005

[2.3] S. Jeon, Y.Yu and J. Choi, "Dual-band slot-coupled dipole antenna for 900 MHz and 2.45 GHz tag application," *IET Electron. Letters*, Vol. 42 No.22, Oct. 2006

[2.4] M.T Zhang, Y.C Jiao and F.S. Zhang, "Dual-band CPW-fed folded-slot monopole antenna for RFID application," *IET, Electron. Letters*, Oct, 2006, Vol. 42 No.21

[2.5] Cho C, Choo H and Park I, "Broadband RFID tag antenna with quasi-

isotropic radiation pattern," Electronic Letters, Vol.41 No. 20, September 2005

[2.6] C.C Chang and Y.C Lo, "Broadband RFID tag antenna with capacitively coupled structure," *IET Electron. Letters*, Vol. 42 No.23, Nov. 2006

[2.7] D. Ma and W.X. Zhang, "Broadband CPW-fed RFID antenna at 5.8 GHz," *IET Electron. Letters*, Vol. 42 No.22, Oct. 2006

[2.8] Kin-Lu Wong and Tzung-Wern Chiou, "Broad-band dual polarised patch antenna fed by capacitiviely coupled feed and slot-coupled feed," IEEE Transaction on Ant. and Propagation Vol. 50 No. 3, March 2002

[2.9] D.M. Pozar, "A Reciprocity Method of Analysis for Printed Slot and Slot-Coupled Microstrip Antennas," *IEEE Transact. Ant. and Propagat.*, VOL. AP-34, NO. 12, DECEMBER 1986 1439 – current is analysed. Saved it slot folder

[2.10] D.M. Pozar, M. Kominami and D. H. Schaubert, "Dipole and Slot Elements and Arrays on Semi-Infinite Substrates," *IEEE Transact. Ant. and Propagat.*, VOL. *AP-33,* NO. *6,* JUNE 1985

[2.11] D.M. Pozar, and S.M. Voda, "A Rigorous Analysis of a Microstripline Fed Patch Antenna" *IEEE Transact. Ant. and Propagat.*, Vol. *AP-35,* No. 12, December 1987, p.1343 –

[2.12] G. Tzeremes, Tsai S. Liao, Paul K. L. Yu, and C. G. Christodoulou, "Computation of Equivalent Circuit Models of Optically Driven CPW-Fed Slot Antennas for Wireless Communications," IEEE ANTENNAS AND WIRELESS PROPAGATION LETTERS, VOL. 2, 2003

[2.13] Islam A. Eshrah et al, "Analysis of Waveguide Slot-Based Structures Using Wide-Band Equivalent-Circuit Model," *IEEE Trans. Microw. Theory Tech*, vol. 52, no. 12, December 2004, p.2691 –

[2.14] Sergey Makarov, "MoM Antenna Simulations with Matlab: RWG Basis Functions," *IEEE Transact. Ant. and Propagat*, Vol. 43, No. 5, October, 2001 p.100 - 107

[2.15] Yang Hao and Chris J. Railton, "analyzing electromagnetic structures with

curved boundaries on Cartesian FDTD meshes," *IEEE Trans. Microw. Theory Tech*, vol. 46. no. 1, Jan.1998

[2.16] Weiland T. "Discretization method for the solution of Maxwell's equation for six component field," *Electronics and Communication*, vol. 9, pp. 295-319, 1996

[2.17] K.C. Gupta, "Microwaves," Wiley Eastern Ltd., 1979, p.97

[2.18] Constantine A. Balanis, "Antenna theory: analysis and design," 2nd Ed. John Wiley and Sons Inc., p.39, 1997

[2.19] Dan Slatter, "Near-field Antenna Measurements," Arctech House, Inc, 1991 pp.7-10

[2.20] K. Finkenzeller, "RFID handbook: fundamental and application in contact smart cards and identification," John Wiley & Sons England, 2003, pp.111-145.

[2.21] Bruce G. Colpitts and Gilles Boiteau, "Harmonic Radar Transceiver Design: Miniature Tags for Insect Tracking," *IEEE Transact. Ant. and Propagat*, Vol. 52, No. 11, November, 2004 p.2825 - 2832

[2.22] J. D. Griffin, G.D Durgin, A. HAldi, B. Kippelen, "Radio link budget for 915 MHz RFID antenna placed on various objects," Georgia Institute of Technology, USA.

[2.23] E.F. Knott, J.F. Shaeffer and M.T. Tuley, "Radar cross section – its prediction, measurement and reduction", Artech House Inc., 1985, p.155

[2.24] K. Penttila, M. Keskilammi, L. Syd.anheimo and M. Kivikoski, "Radar cross-section analysis for passive RFID systems," *IEE Proc.-Microw Antenna Propag., Vol 153, No 1, February 2006.*

[2.25] R. Schuhmann and T. Wieland, "Recent Advances in Finite Integral Technique for High Frequency Applications," CST Workshop.

[2.26] M. Clemens, M. Wilke, T.Weiland: Rosenbrock, "Methods for Time Step Adaptive Transient Eddy Current Simulation without Nonlinear Iterations," CST Workshop

[2.27] A.A. Ergin, B.Shanker, E.Michielssen, "The plane-wave time domain

algorithm for the fast analysis of transient wave phenomena," *IEEE Ant. Propag. Magazine*, Vol. 41, No. 4, 1999, pp. 39-52

[2.28] Hewlett Packard, "User Guide to HP8722ES Network Analyser,"

CHAPTER 3

DIPOLE ANTENNAS FOR RFID TAGS

3.1 Introduction

The aim of this chapter is to consider at certain selected frequency bands, the strategy for tag antenna optimisation by considering the interaction of the choice of electric dipole or its complementary configuration magnetic dipole with the type of support materials. The study of the properties of antenna configuration has application in a variety of areas of RFID tag design. Of the various types of tag antennas, different configurations of dipoles have attracted the most attention. They are usually in the form electric or magnetic dipoles. Different electric dipoles have been proposed such as inductive linear [3.1], meander line folded [3.2], [3.3] configurations. They also take on shapes of the complements of the above configurations and are thus regarded as magnetic dipole or slots antennas [3.4]. Unfortunately, many of these applications have been chosen without due consideration to the platform upon which the tag is to be mounted mounted.

It has been the objective of this thesis to systematically select antennas whose electromagnetic properties are compatible with the mounting platforms. By adopting the concept of complementarity in the proposed antenna designs, the options for mounting tags on different object surfaces is increased. Complementarity requires the distribution of electric charges along an ideal strip antenna to be like the distribution of the complementary current along a slot antenna in an ideal ground plane screen [3.5]. The properties of either the electric or magnetic dipoles can be related to other antenna configurations in the subsequent chapters as they fit. Besides the complementarity option, this chapter also provides experimental support for some of the concepts introduced in the previous chapter.

The Chapter is organised into six sections. The strategy for creating a passive tag is discussed in Section 3.2. The analyses of the electric and magnetic dipoles are carried out in sections 3.3 and 3.4 respectively. The read range measurements are presented in section 3.5. The chapter concludes with section 3.6.

3.2 Strategy for Designing a Tag Antenna

Given that read range may be influenced by the platform upon which tags are mounted, the choice of a particular tag antenna geometry must be established early in the design stage. When applied to the RFID problem, mounting surfaces can be broadly sub-divided into two categories.

1. Objects whose outermost surfaces are made of lossy dielectric materials. The application for example of a paper based product proposed in [3.6] falls into this category. Other related application of this material include Teflon, Polytetrafluorethylene (PTFE), Polyimide, FR-4 fibreglass and Duroid type-materials with relative permittivity (ε_r) of 2.08, 2.55, 3.5, 4.9 and 12.8 respectively.
2. However, there are other materials whose outermost surfaces are lossy metals e.g. foil, metallic can, or metallised thin sheet. The affects of metals on the tag performance have been investigated e.g. in [3.7], [3.8].

This section will highlight the tools and criteria used for designing tag antennas. It will be followed by two examples applications using electric and magnetic dipoles.

3.2.2 Design Considerations

The EPC global specified operating frequencies for RFID systems are as given in Section 2.1 of the theoretical analysis. Within a chosen operating frequency, optimal performance can be achieved using different methods. The conventional method is to increase the antenna gain by increasing its size or aperture in the azimuth and elevation planes. An

optional method is to place a metallic reflective surface behind the antenna in order to direct energy towards a particular coverage area [3.9]. The alternative method reduces the antenna beamwidth by blocking energy from going backward thus increasing the front to back (F/B) ratio.

In order to decrease the beamwidth, the radiating elements can be piled on top of each other, which invariably increases the overall antenna size. Increasing the number of elements can bring about a corresponding increase in the effective aperture, and by virtue of Equation 3.1, the gain increases [3.10].

$$\text{Antenna Effective Aperture, } A_e = \lambda^2 Gain / 4\pi \qquad 3.1$$

However, the consequence of increasing the antenna gain in this way is that pattern nulls and side lobes also develop in the process and cause a decrease in the main lobe pattern beamwidth. This problem is similar to that which is likely to occur following the use of cross-layered, unbalanced feed structures such as microstrip antennas [3.11] for the application. For these types of antennas, not only does the vias or shorting pin across layers constitute the bulk of the problem, but also the mechanical IC integration can only be achieved with considerable difficulty.

One additional comment to emphasize is that increasing the number of radiation elements has the potential to weaken the tag's mechanical strength. Extra consideration is required in terms of mechanical robustness particularly for applications involving moving objects. A further consideration is the matching network between the antenna and transponder chip. The affect of an inductive loop, as a matching network, has been studied as part of optimisation process in [3.12], [3.13], [3.14].

Thus the CST simulation has been used to investigate the effect of the loop and it was found to reduce the input impedance considerably. In the case of a linear dipole it reduced the input impedance from 75.5 Ohms to 13 Ohms. The inductive loop acts like an impedance transformer.

To gain further insight into the nature of the loop, a transponder chip (BiStar 3981-3) with unknown impedance was integrated with a linear dipole antenna operating at 869 MHz. A set of range values was measured corresponding to different lengths of the dipole with and without the loop across the chip terminals. First, to enable easy trimming, the dipole arms were of copper foil (on paper) instead of on FR-4 substrate. Thus, the length of a full wavelength dipole $\ell = \lambda = 345$ mm was trimmed down to one tenth of its length ($\ell = 34.5$ mm) in discrete steps. In sub-section 3.5.1, the read range is investigated as a function of the dipole length with the short circuit loop and it can be seen that the optimal length was when $\ell = 142.2$ mm.

In all the cases studied, the current distribution plots were taken to detect peaks and nulls in the current along the wire antenna. The larger portion of each of the antenna determines the system resonance, while the resonance of the smaller loop is probably too high to be noticed by the tag system. However, care must be used to ensure that the smaller loop does not take on a harmonic or mixing product relationship to the larger system. Also, the designer would want to be certain that the bandwidth is adequate to trigger and sense the transponder, though this will be small in a low data rate system.

There is no doubt that with BiStar 3981-3 chip, the tag works best with a low impedance loop connected across the feed terminals. The best detection range was achieved for a dipole resonant at 869 MHz and 76.1 mm long. This improved the detection range slightly by 160 mm when compared to the magnetic dipole antenna. The feed loop (which acts like impedance transformers) lowers the antenna impedance to a few ohms to be concentrated around the loop with virtually no current on the antenna, and in general, it increases the reading ranges of the tags significantly. Although the current is small in the antenna its presence is important and should be tuned to 869 MHz. The length of the feed loop has been varied but it has little effect on the performance. The exact impedance value of the BiStar 3981-3 transponder remains unknown. However, there is a clear interaction between the chip, the antenna and the shorting loop.

In addition, consideration is to be given to the antenna size, frequency of operation and gain since any one of them can limit the maximum achievable range. When the beamwidth in a particular direction is decreased, the overall antenna gain is increased. In the light of this, the tag antenna behaviour will be significantly changed depending on the surface upon which it is mounted (e.g. cardboard boxes or metal cans). The nearness of other electromagnetically sensitive objects may also have an effect. Thus, tag antenna can be designed or tuned for optimum performance on a particular object or designed to be less sensitive to the content on which the tag is placed. As would normally be expected, the read range would also depend on the antenna orientation. Typically, some applications may require a tag to have a specific directional characteristic. A detailed design requirement can be found in the literature; for example in [3.14].

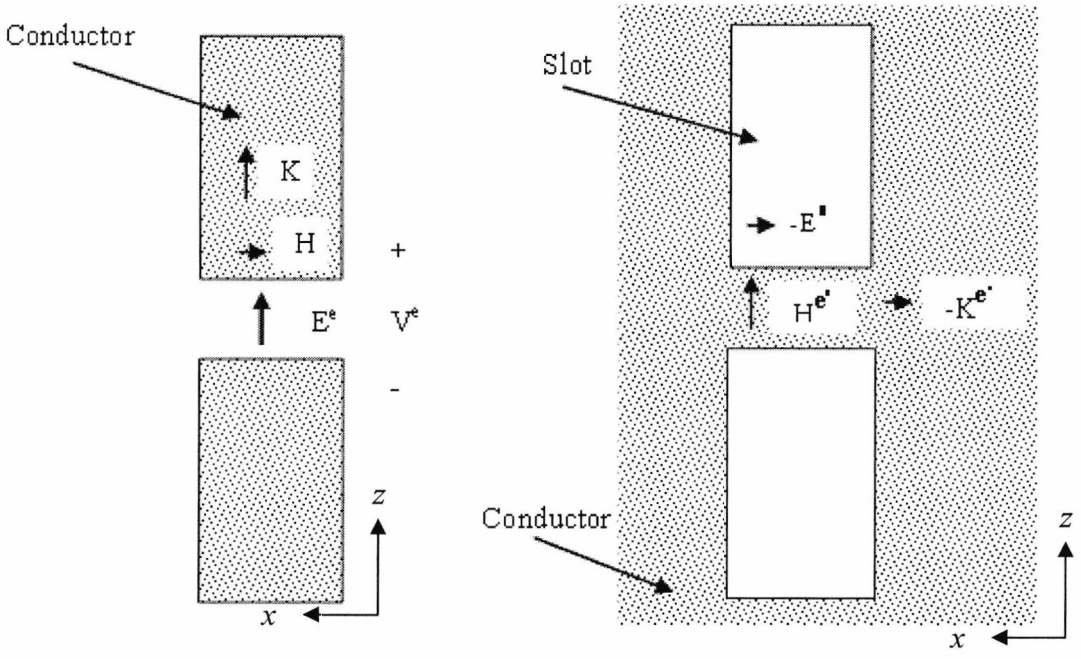

Fig. 3.1: (a) A half wavelength electric dipole antennas and (b) a half wavelength complement magnetic (slot) dipole.

Furthermore, conformation of an antenna structure with the attached object is important. Antennas whose shapes have complements have been proposed in this work as part of the process of increasing the choice of tag antennas. Depending on the complexity of application, a tag can incorporate two antennas that are complimentary to each other (positioned substantially parallel and close) thereby increasing the probability of detection. Complementarity in this case creates a choice for the use of cross polarised field pattern, wherein the electric dipole (or patch) E-field and H-field are substantially orthogonal to the magnetic dipole (or slot) E-field and H-field. This work addresses tags derived from either a patch or a slot antenna.

The basic principle of complementarity which is illustrated in the Fig. 3.1 is derived from Booker extension of Babinet's theorem. In optics, Babinet's principle states that the sum of the field behind a plane screen and the field behind the complimentary screen is equal to the field which would exist at the same point if there is no screen [3.15]. In [3.16], Booker considers polarisation effects and states that when an electric source **J** radiates into an unbounded medium with characteristic impedance $\eta = (\mu/\varepsilon)^{1/2}$ and produces at point P the fields $\mathbf{E}_o$, $\mathbf{H}_o$, the same field can be obtained (given the same medium) by combining the fields in the presence of:

1. A very thin, flat, infinite perfect electric conductor which produces at **P** the fields $\mathbf{E}_e$, $\mathbf{H}_e$ [Fig. 3.1 (a)]
2. A very thin, planar perfect magnetic conductor which produces at **P** the fields $\mathbf{E}_m$, $\mathbf{H}_m$ [Fig. 3.1 (b)]

That is,

$$\begin{aligned} \mathbf{E}_o &= \mathbf{E}_e + \mathbf{E}_m \\ \mathbf{H}_o &= \mathbf{H}_e + \mathbf{H}_m \end{aligned} \qquad 3.2$$

The electric dipole is a half-wavelength copper conductor. In accordance with the complementarity principle, the complementary antenna must consist of an infinitely thin perfect conductor located in all points where there is no conductor and no conductors

where the strip is located. The properties of the strip can be also be used to relate to those of a complementary slot which was cut in the same infinite perfectly conducting plane.

Physically, a fundamental condition for complete complementarity will be difficult to satisfy. However, reference [3.17] postulates an ideal condition that if the electromagnetic field is considered in two parts, the one generated by the electric and the other by the magnetic current and charges, complementarity principle requires that an interchange of the electric and magnetic sources requires the electromagnetic field to be related as follows:

$$E_x = -Z_0 H_x, \qquad H_z^{e'} = Z_0^{-1} E_z^e \qquad 3.3$$

Furthermore, Booker showed that in ideal condition when a screen and its complement are subjected to a medium with characteristic impedance η and have input terminal impedances of Z_S and Z_C, respectively, then the impedance are related by [3.18]:

$$Z_S = \frac{Z_0^2}{4Z_c} = \frac{35532}{Z_c} \qquad 3.4$$

wherein, $Z_0 = \sqrt{(\mu/\varepsilon)} = 2\sqrt{Z_S Z_C} = 377\ \Omega$ represents the free space characteristic impedance.

In practice this is not so due to the difference between the infinite and finite metallic plane of the simulated and measured magnetic dipole antennas.

3.2.3 A Simplified Design Process

In reference 3.13, the process for creating a simplified tag model was formulated and has been reproduced here in outline in Fig. 3.2. The design criteria will depend upon the selected application. The application in turn will determine the geometry for tag antenna

and its construction. Since this thesis is primarily concerned with tag antenna designs, a full wave simulation method is used to perform the antenna parametric study and optimization bearing in mind the various contributions of the antenna RCS and gain. Finally, the prototypes were constructed and their performance measured against the predicted results. It should be note for this work, that the transponder chip impedance was already specified by the manufacturers.

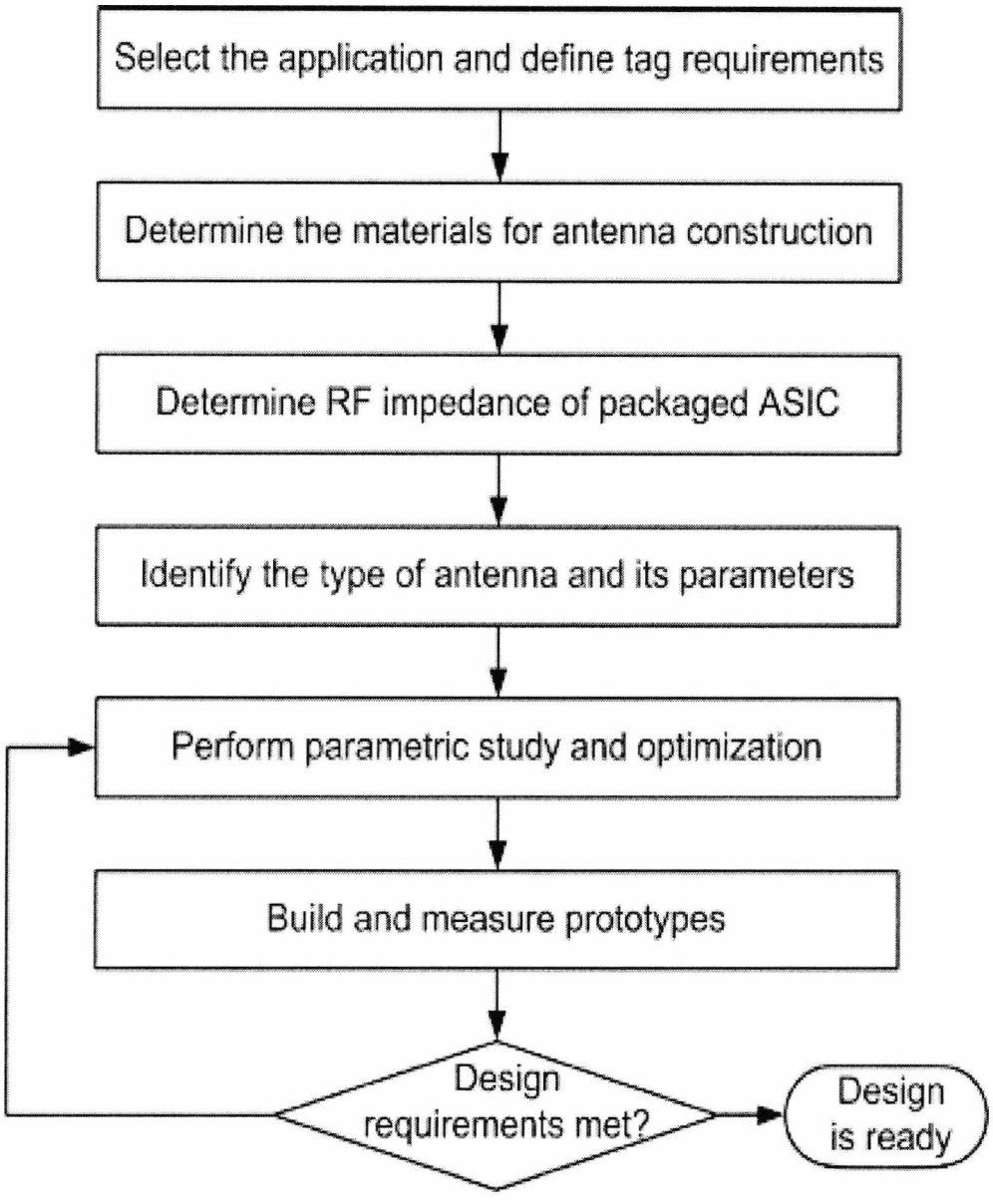

Fig 3.2: A typical RFID tag antenna design process

3.3 An Electric Dipole Antenna Applied To an RFID Tag

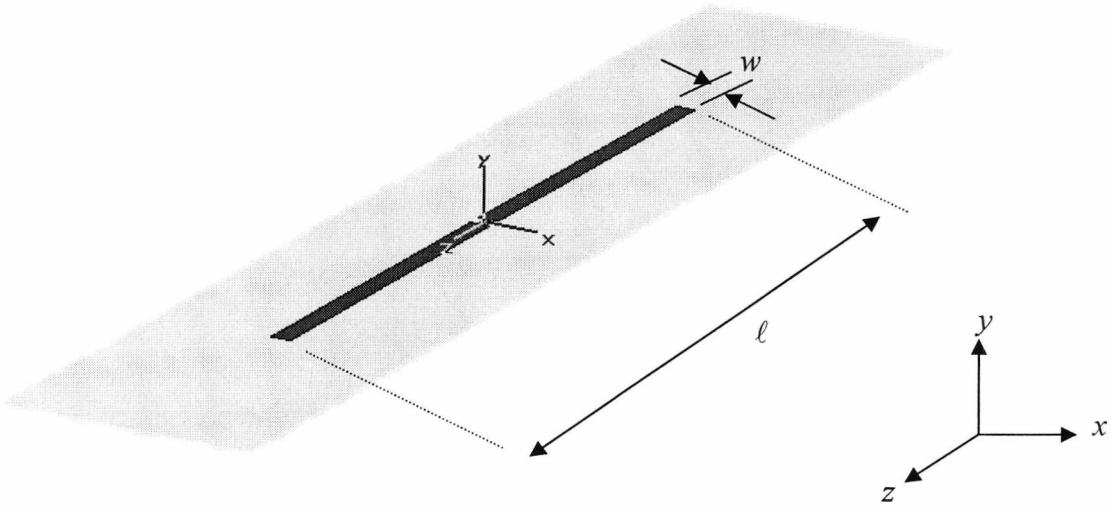

Fig. 3.3: A vertically polarized linear dipole antenna at 869 MHz for a passive RFID tag; $\ell \approx \lambda/2$ mm, $w=0.012\lambda$, $\varepsilon_r = 4.9$

A dipole antenna can be used to construct a tag. This configuration is shown in Fig. 3.3. The dipole is made up of a metallic strip with length $\lambda/4$ = 72.5 mm. The antenna was initially designed on a FR-4 substrate of relative permittivity, ε_r, = 4.9, *tan* δ = 0.025 and thickness 0.8 mm and after optimisation, fabricated on the same material. The measured and calculated results are plotted as thick and dashed lines, respectively. There is an agreement between the results of the simulated and measured S_{11}-parameter as shown in Fig. 3.4.

3.3.1 Input impedance

This antenna exhibits a measured 23.34 – dB return loss and a measured half power (S_{11} < - 10dB) bandwidth of 485 MHz which covers the UK RFID requirement. During measurement, a time delay of 623.85ps was applied to compensate for the length of the

50Ω coaxial feed cable with an electrical length of 12.44cm. A full-wave analysis with the CST was used to characterise dipole encountered in Fig. 3.3 above for the cases when the antenna is with and without an inductive loop across the input terminal.

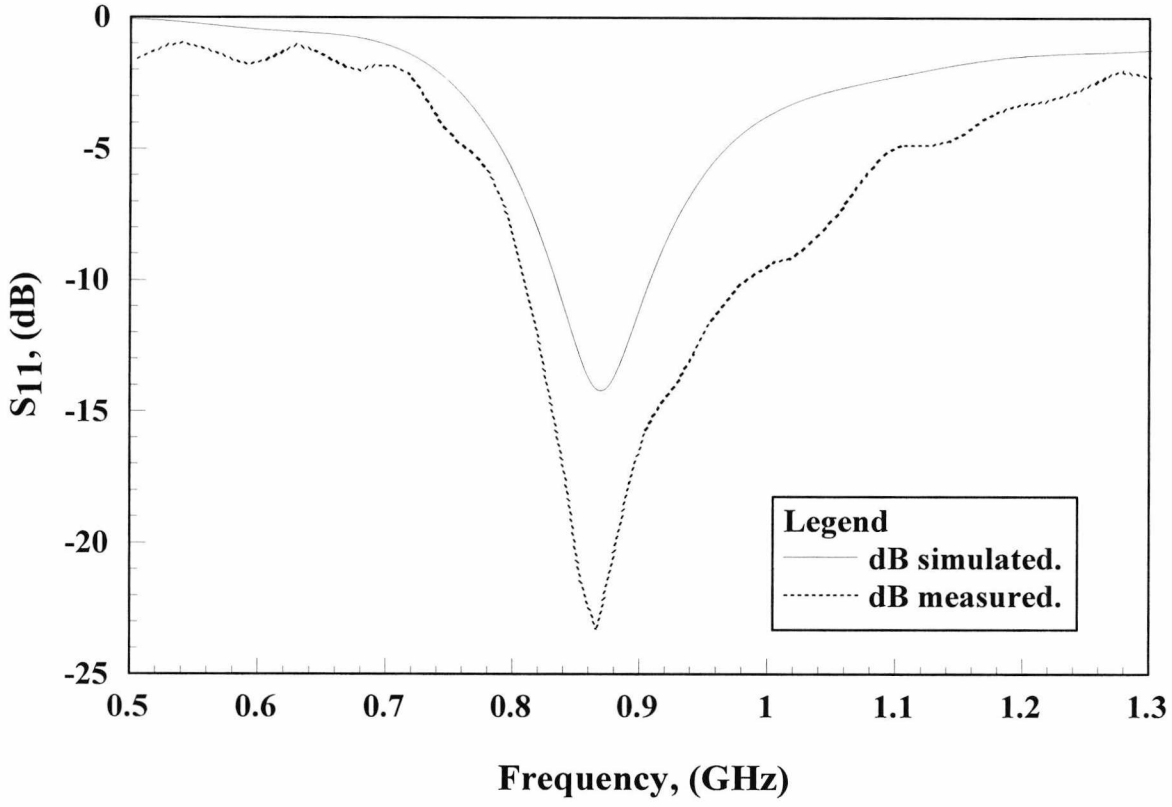

Fig. 3.4: Simulated and measured return loss for the linear dipole antenna $\ell \approx \lambda/2$ mm, $w=0.012\lambda$, $\varepsilon_r = 4.9$.

It was observed in Fig. 3.5 that the loop lowers the input impedance significantly. The essence of the loop will be explored for low impedance chip later in this chapter. It should be noted that high impedance chip do not need the inductive loops for improved read range.

There is relatively good correlation between the impedance value and what would be expected for the measured impedance of a linear dipole antenna. The correlation, however, can not be perfect due to the fact that the dipole structures are on substrates will alter the impedance values by virtue of their dielectric constants.

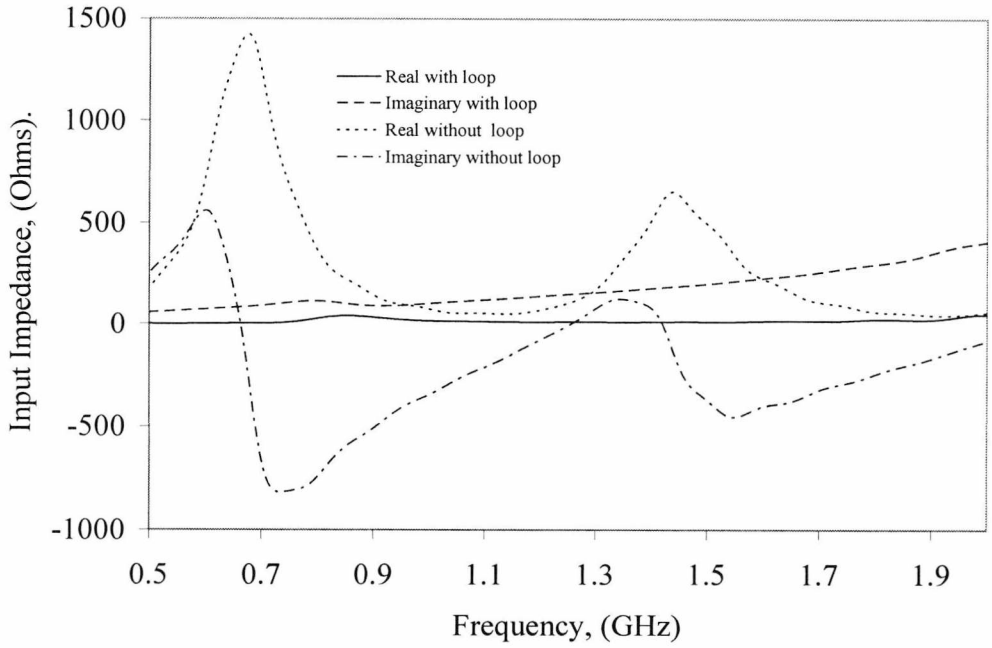

Fig: 3. 5: Simulated effect of the inductive loop on the input impedance of an electric dipole.

3.3.2 The Effect of Field Polarisation on Radar Cross Section

In this section is examined the ability of the tag to scatter energy. This is considered using the radar cross section (RCS) which gives an equivalent area that represents how much reflection is returned to the Reader. It does not correspond to physical size. The units of radar cross section are the equivalent area, expressed in square meters m^2. The RCS of the tag can be visualised as a comparison of strength of the reflected signal from a tag to the reflected signal from a perfectly smooth sphere of cross sectional area of 1 m^2. Given that the RCS is in units of area, dB can be related to a square meter (dBsm) by realising that when dBsm is considered, it is still referring to power, but the power aspect is hidden. The power that is now considered is the power received by the Reader. By holding constant all other terms in a received Reader power, the received power becomes directly proportional to the RCS. Hence the ratio of power received is the same as the ratio of the areas. Since a reference RCS of 1 m^2 has been chosen, the final expression is in decibels relative to a square meter, or dBsm.

The radar cross section (RCS) an antenna is not only dependent on the impedance characteristics of the antenna, but also on the polarisation of the incident electric field vectors with respect to the antenna orientation. Thus the effects of field polarisation on the RCS are investigated under four tag antenna load conditions namely: open-circuit, short-circuit, resistor loaded and transponder (IC) loaded. Additionally, the influences of the direction of arrival of the plane wave on the received power are presented.

Tables 3.1 - 3.3 show the results for the variation of the RCS for the electric dipole under different load conditions and for different polarisations. For each antenna load conditions different field polarisations for vertically polarised (VP), horizontally polarised (HP) and circularly polarised (CP) plane waves have been considered. The predicted results show that the received is at maximum when the antenna is short circuited.

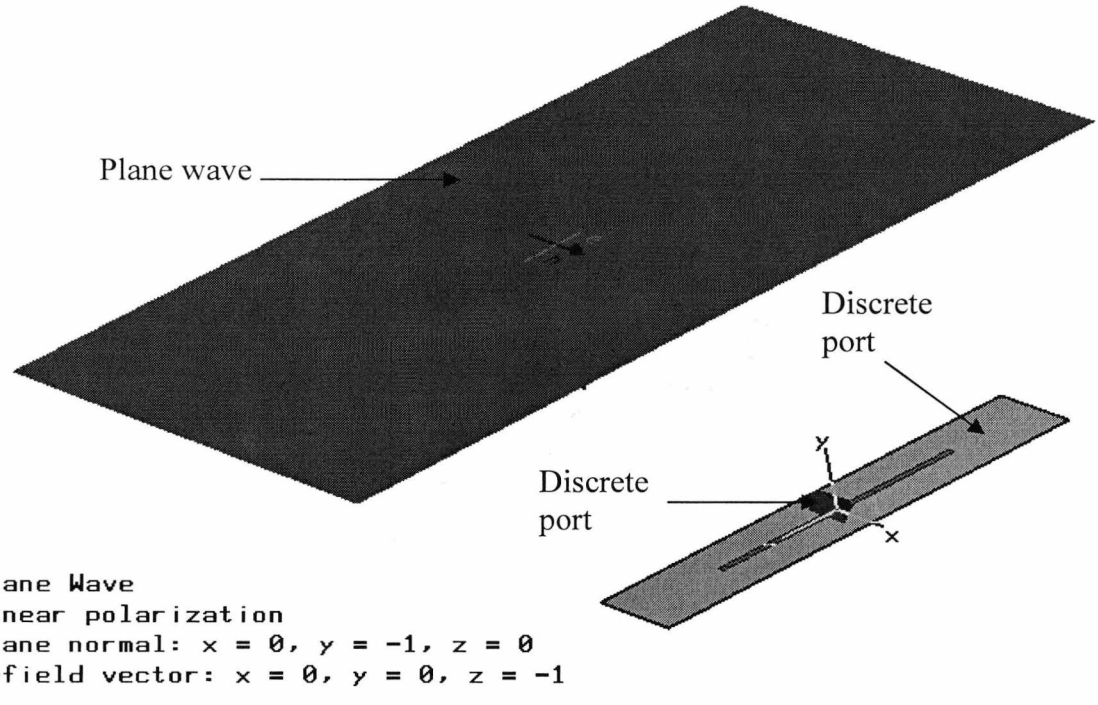

Fig. 3.6: A CST geometry file of an electric dipole illuminated by a plane wave.

The definition of the plane wave is visualized by a red plane as shown in Fig. 3.6. Coloured arrows indicate the electric and magnetic field vectors. Here the electric field vector of a plane wave is hitting the electric dipole. The plane wave is excited with an electric field vector in *z*-direction and a propagation normal (0,-1,0). The antenna is excited by a discrete port indicated in red colour along *z*-direction.

Antenna load	**Maximum RCS (dBsm) *y*-axis**		
	x-axis field vector	*z*-axis field vector	circularly polarised field
Open circuit	-15.29	-36.60	-18.40
Short circuit	-10.61	-42.32	-13.87
Resistor loaded	-14.96	-37.08	-17.66
Transponder loaded	-17.16	-37.08	-21.13

Table 3.1: Simulated maximum RCS for the electric dipole under different load conditions for the case when a plane wave is incidented from *y*-axis.

Antenna load	**Maximum RCS (dBsm) *x*-axis**		
	x-axis field vector	*z*-axis field vector	circularly polarised field
Open circuit	-15.51	-62.69	-18.64
Short circuit	-10.49	-68.82	-13.64
Resistor loaded	-14.38	-61.33	-17.54
Transponder loaded	-17.64	-61.33	-21.63

Table 3.2: Simulated maximum RCS for the electric dipole under different load conditions for the case when a plane wave is incidented from *x*-axis.

Antenna load	**Maximum RCS (dBsm) *z*-axis**		
	x-axis field vector	*z*-axis field vector	circularly polarised field
Open circuit	-47.59	-58.36	-51.41
Short circuit	-45.55	-67.88	-48.30
Resistor loaded	-46.57	-61.65	-50.28
Transponder loaded	-46.56	-61.66	-50.28

Table 3.3: Simulated maximum RCS for the electric dipole under different load conditions for the case when a plane wave is incidented from *z*-axis.

The RCS of the vertically polarised plane wave propagating along the ***x***-direction was larger than it was in the case of a circularly polarised plane wave; the horizontally polarised wave yielded the least received. Within the vertically polarised cases the open circuit, the resistor-load, and the transponder (IC) load conditions is smaller by 4.68 dB, 4.35 dB and 6.55 dB respectively compared with the short circuit case. In the case of a circularly polarised plane wave, the corresponding maximum received power was smaller by 4.53 dB, 3.79 dB and 7.26 dB respectively compared with the short circuit case. However, the received power in the short circuit load condition for a horizontally polarised wave is worst than were the cases for the open circuit, resistor loaded and transponder loaded conditions by -5.72 dB and -5.24 dB and -5.24 dB respectively.

The RCS for the case when the antenna is illuminated by a vertically, horizontally or circularly polarised plane wave propagating along the ***x***-axis are summarised in Table 3.2. As in the previous scenario where the plane wave was incidented parallel to the ***y***-axis, the received power for vertically polarised plane wave is larger than is the case with circularly polarised wave. Again, the horizontally polarised case resulted in the worst case. For the vertically and circularly polarised plane wave, the short circuit load condition surpasses those of the other load conditions. In the open-circuited, resistor loaded and transponder loaded cases, the short-circuited load condition is larger by 5.02 dB, 3.89 dB and 6.55 dB respectively. These correspond to 5 dB, 3.9 dB and 7.99 dB

respectively for the case when the plane wave is circularly polarised. However, the received power in the case of the horizontally polarised plane wave propagating in the *x*-direction is worst than were the cases in the open-circuited, resistor-loaded and transponder-loaded conditions by 6.13 dB and 7.49 dB and 7.49 dB respectively.

The result maximum RCS for the case when the antenna is illuminated by a *z*-directed plane wave that is either vertically polarised, horizontally polarised or circularly polarised are presented in Table 3.3. Although the largest amount of received power were recorded for the vertically and circularly polarised plane waves, in general however, these powers are less than were the cases for their equivalents for both the *y*- and *x*-directed plane waves. As can be seen from Table 3.3, the short-circuited case was larger than is in the open circuited, resistor-loaded and transponder-loaded conditions by 2.04 dB, 1.02 dB and 1.01 dB respectively for the vertically polarised plane wave. The short circuit is correspondingly larger by 3.11 dB, 1.98 dB and 1.98 dB for the case of circularly polarised plane wave. However, the short circuited case is smaller by 9.52 dB, 6.23 dB and 6.22 dB compared to the open-circuited, resistor-loaded and transponder loaded conditions.

It should be noted that these results were obtained within the limitations of matching uncertainties. The antenna is being matched to 50-Ohms coaxial feed and this indeed depends on internal matching uncertainties.

3.3.3 Radar Cross Section Analysis of the Tag Antenna

When a tag is illuminated by a plane wave, energy is spatially scattered in accordance with the size, shape and construction of the antenna and the frequency and nature of the incident wave. The scattering property of tag depends on the attitude at which it is intercepting the plane wave as well as the angle of interception. The contributions of some these parameters to the radar cross section (RCS) under the backscattering mode are presented in this section using CST. A detailed study on the RCS of antennas can be found in [3.19]. The RCS were studied at 90^{o} which represented the maximum amplitude.

The significance of RCS obtained can be explained in two ways. It allows the amount of radiated power to be calculated for a transmitting antenna, and also provide for a tag antenna a means of calculating the effective area of the antenna as earlier discussed in Chapter 2. In the light of the above explanations, the radiation resistance is a direct indication of the capacity of the antenna to collect electric field from an incident plane wave.

3.3.4 The effect of strip width on the RCS for the electric dipole antenna

The radar cross section analysis gives an intuitive knowledge of the degree of scattering inherent in the antenna. An increase in the patch width is synonymous with an increase in RCS due to the dependence of the RCS on the effective area of the antenna exposed to the power density. Thus, the variations due to the strip width on the scattered RCS for different values of dielectric constant are investigated. The result is shown in Fig. 3.7.

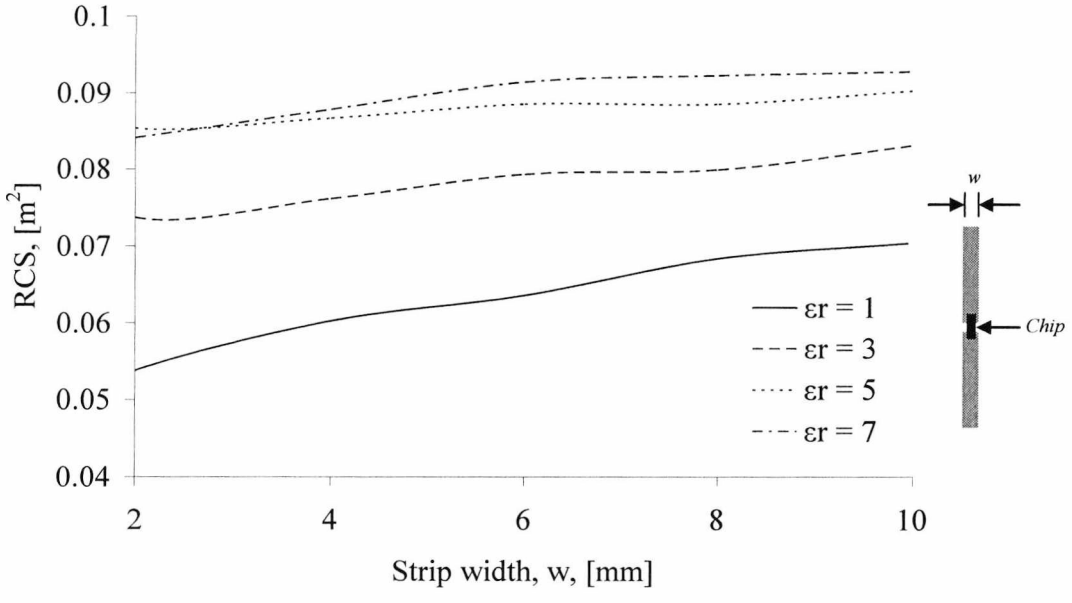

Fig. 3.7: Variation of the RCS for the halfwavelength electric dipole with conductor strip width

It can be seen that for a given dielectric constant, the RCS increases with increasing strip width. The percentage rise in RCS magnitude between when the strip has a width of 2 mm and when it has a width of 10mm for different substrate relative permittivities of 1, 3, 5 and 7 correspond to 31 %, 13 %, 5.8 % and 10.4 % respectively. The increase is slower for material having low dielectric constant. The work untaken by Penttila et al. [3.20] on the behaviour of RCS under different load conditions have been compared with the above results and the agreement is quite good.

3.3.5 The effect of substrate permittivity and height on the RCS for the electric dipole antenna

As well as varying with the strip width of the electric dipole, the scatter RCS is also expected to vary with substrate height and dielectric constants of the radiating elements. Figure 3.8 illustrates the relationship between RCS for five example of dielectric substrates whose relative permittivity are 1, 2.08, 3.55 and 4.9 which correspond to foam, PTFE, polyimide, and FR-4 fiber-glass materials respectively.

Apparently, the RCS curve in Fig 3.8 increases with increasing substrate permittivity for a given load condition. This increase is more noticeable for the short circuit case where an increase of 42 % is recorded for the range of relative permittivity under consideration. The increments for when the tag antenna is open circuit, short circuit, resistor loaded and IC loaded are 40 %, 42.3 %, 9 % and 9.5 % respectively.

Figure 3.9 shows the effect of substrate height on RCS for different values of substrate relative permittivity. It can be seen that except for the case of $\varepsilon_r = 1$ (foam), the RCS for all other cases tends to increase as substrate height increases. In the case when $\varepsilon_r = 1$, the RCS curve decrease sinusoidally by 37 % for substrate thickness ranging between 0.8mm and 4mm. On the other hand, the values for substrate thicknesses 2, 3, 4 and 5 increased by 37 %, 29.7 %, 116.7 % and 149.4 % respectively.

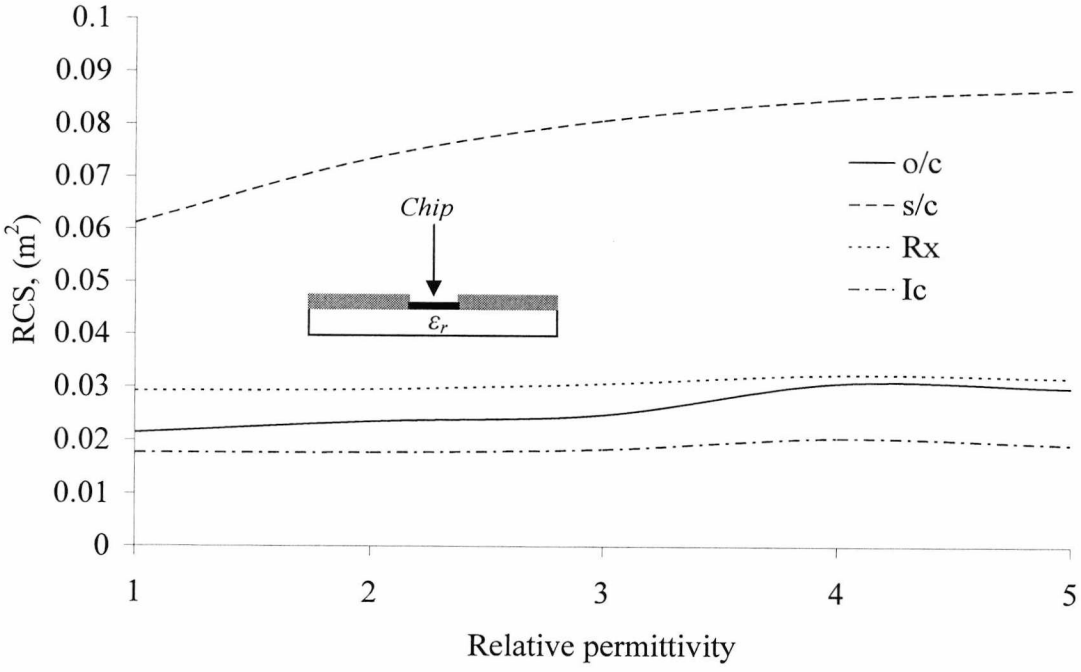

Fig. 3.8: Variation of the RCS for the halfwavelength electric dipole with substrate relative permittivity for different load conditions

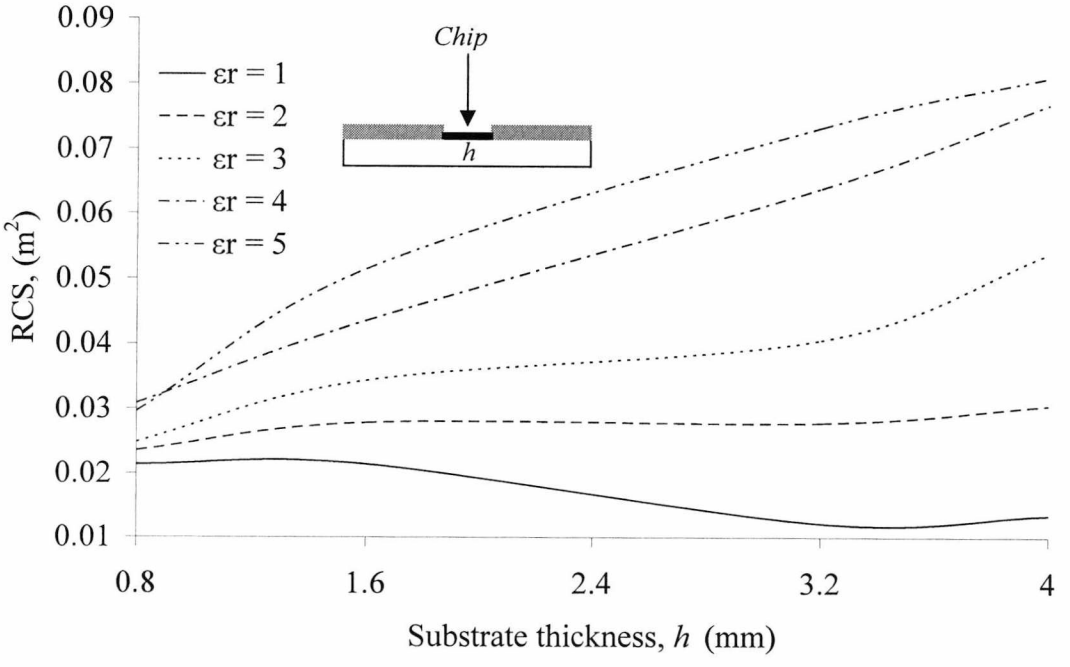

Fig. 3.9: Variation of the RCS for the halfwavelength electric dipole with substrate thickness for different substrate permittivity.

3.3.6 The Effect of Incident Angle on the RCS for the Electric Dipole Antenna

Figure 3.10 show the relationship between the RCS and angle of plane wave incidence under different tag antenna load conditions. Since the antenna is bidirectional and is symmetric with respect to the plane wave containing it, the RCS pattern in the lower half space are similar to those in the upper half space. Therefore only the pattern plots in the range of $0^{\circ} < \theta < 90^{\circ}$ are shown. It is observed that the antenna has similar RCS at the four load condition earlier mentioned and the shape of the pattern in this plane does not depend on the load condition. The magnitude of the RCS however varies with load having a highest value of 0.086942 m^2 obtained under the short circuit condition and lowest value at 0.019217 m^2 recorded under the IC load condition.

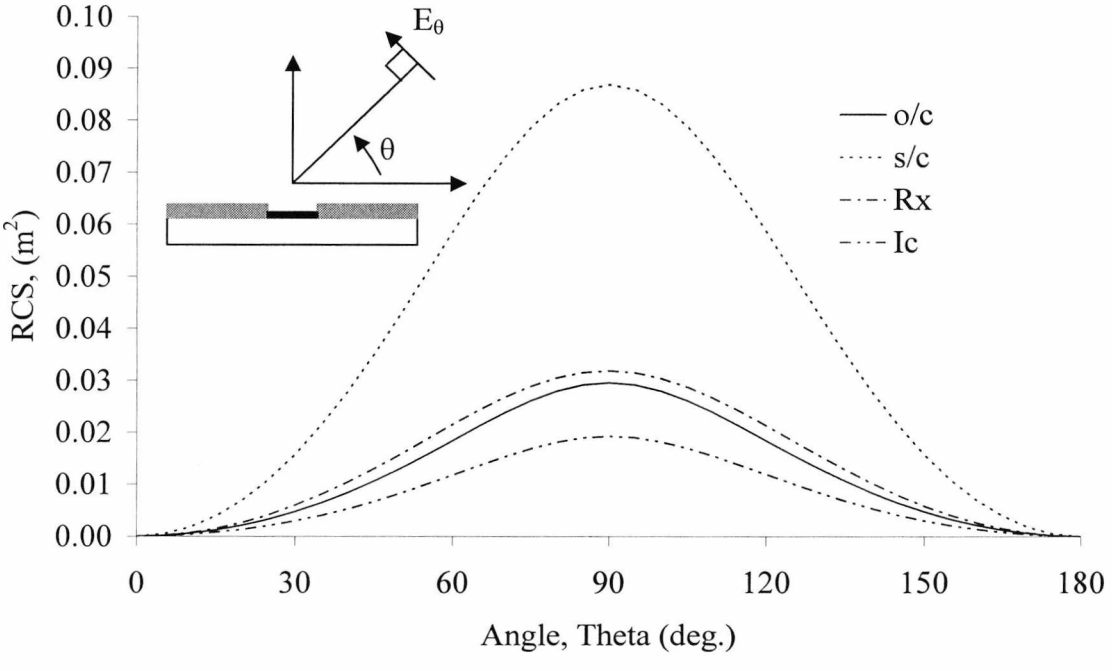

Fig. 3.10: Variation of the RCS for the halfwavelength electric dipole with angle for different load conditions using FR-4 with substrate relative permittivity, ε_r of 4.9 and thickness of 0.8mm.

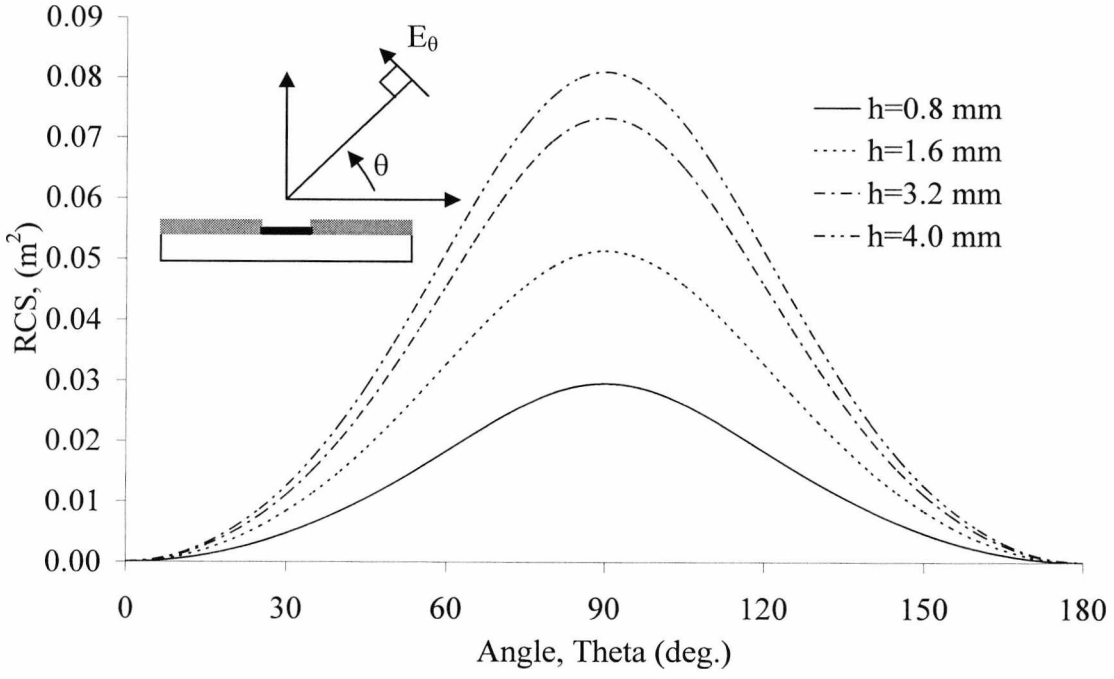

Fig. 3.11: Variation of the RCS for the halfwavelength electric dipole with angle for different thickness of dielectric substrate using FR-4 with substrate relative permittivity, ε_r of 4.9 and thickness of 0.8mm.

Similarly, the pattern of the RCS does not depend on the substrate thickness as is shown in Fig. 3.11. In the range of substrate thickness under consideration (staring from 0.8mm and at every 0.8 mm increments up to 6.4 mm) the RCS decreases as the substrate thickness increases; the highest RCS magnitude of 0.086942 m^2 was obtained for a substrate thickness of 0.8 mm while the lowest was at 0.0095193 m^2 for a substrate thickness of 6.4 mm. This effect is most clearly marked for the case of the plane wave incident normally on the tag antenna.

3.3.7 Sensitivity of the Electric Dipole to Potential Objects to be Tagged.

Given that the radiation patterns of a dipole are well known, this work only examines the effect different objects to be tagged have on tag radiation characteristics. These objects are represented by foam, dry wood, plastic, glass and metal with relative permittivity of

approximately 1, 1.4, 3.5, 4.8 and ∞ respectively. In order to do this, a full-wave simulation using CST Microwave Studio has been carried out on the dipole antenna shown in Fig. 3.3. Table 3.4 summarises the variation in the radiation parameters with respect to different platforms in terms of the gain, angular width (AW), main lobe direction (MLD) and side lobes (SL).

It was observed that the gain does not change significantly for materials whose relative permittivity lie between 1 and 4.8. However, for an infinite size metallic plane, the gain increases by 227 % when compared to an object whose outermost permittivity of approximately that free space. This is due to the fact that metallic surfaces block all back radiation thereby causing a narrower beamwidth to occur. It therefore follows that the resulting side lobes magnitude should be relatively large for a tag on an infinite size metallic object. The angular width does not change appreciably for materials whose relative permittivity lie between that of foam and glass. However, with metallic objects, the angular width (AW) reduces by 8 % compared with that of foam type of materials. The main lobe direction (MLD) is the same for all the above consideration.

Platforms	**Parameters**			
	Gain	AW (deg.)	MLD (deg.)	SL level (dB)
Foam	1.62	79.0	90	<(-30)
Wood	1.64	78.7	90	<(-30)
Plastic	1.64	78.7	90	<(-30)
PEC	5.28	73.4	90	-24.4

Table 3.4: Simulated data on radiation characteristics for the electric antenna when attached directly on different objects..

Definitions

AW represents angular width or 3dB beamwidth measured in degrees.

MLD represents the main lobe direction measured in degrees

SL represents the side lobe level in dB

3.3.8 The effect of ground plane on electric dipole

The effect of a placing the electric dipole immediately above a ground plane causes a decrease in the magnitude of the main beam. Additionally the boresight shifts from 0^{o} to 60^{o} as shown in Fig. 3.12. However, as the ground plane height increases (using foam spacer), the main beam magnitude increase relative to the free space radiation pattern.

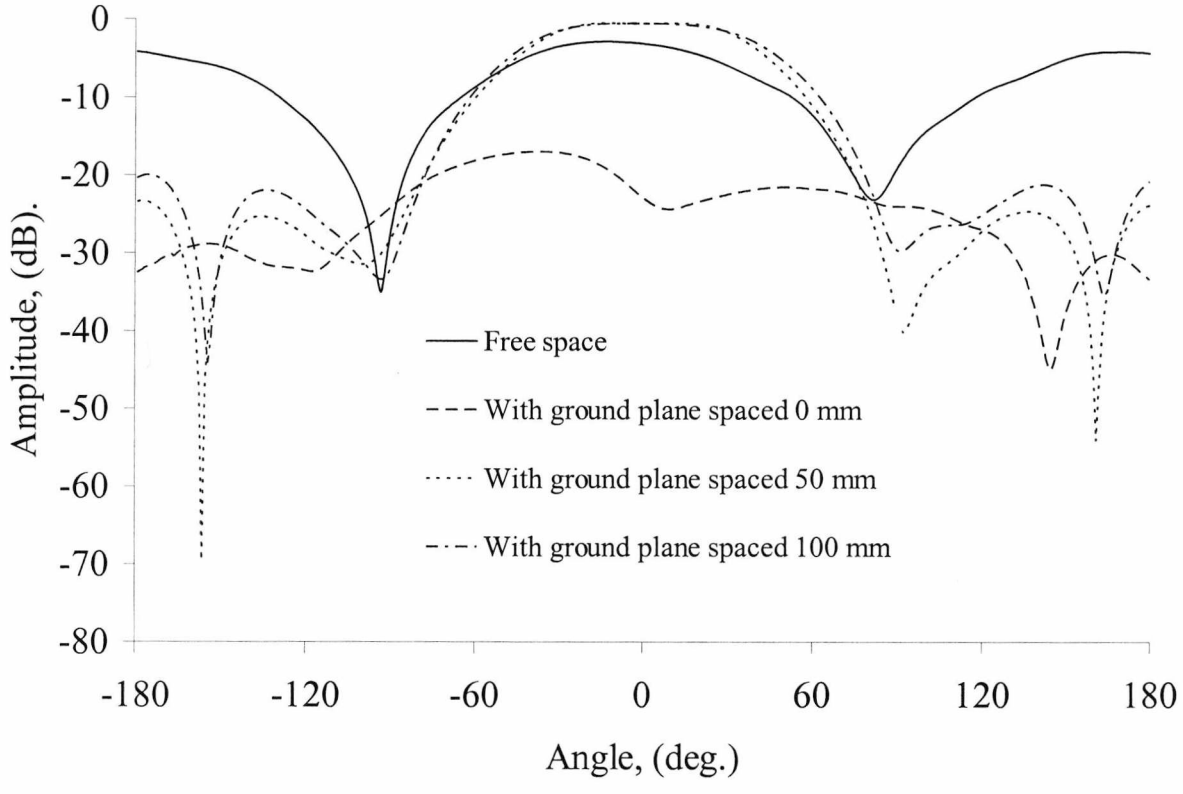

Fig. 3.11: Radiation pattern at 869 MHz for an electric dipole encountered in section 3.4: (1) in free space (2) with a ground plane and no spacer (3) with a ground plane and a 50 mm foam spacer and (4) with a ground plane and a 100 mm foam spacers.

The amplitude of the radiated energy is very low when the antenna is directly attached to the metallic object. Therefore, normal application of a tag made of this antenna to metallic objects requires that a foam space having a minimum height of 50 mm be used to separate the tag from the object to be tagged.

3.4 A Magnetic Dipole Antenna Applied to a passive RFID Tag

The characteristics of an electric dipole have been presented in the previous section. In this section, the principle of complementarity has been applied to the electric dipole in order to obtain the so-called magnetic dipole which is illustrated Fig. 3.13.

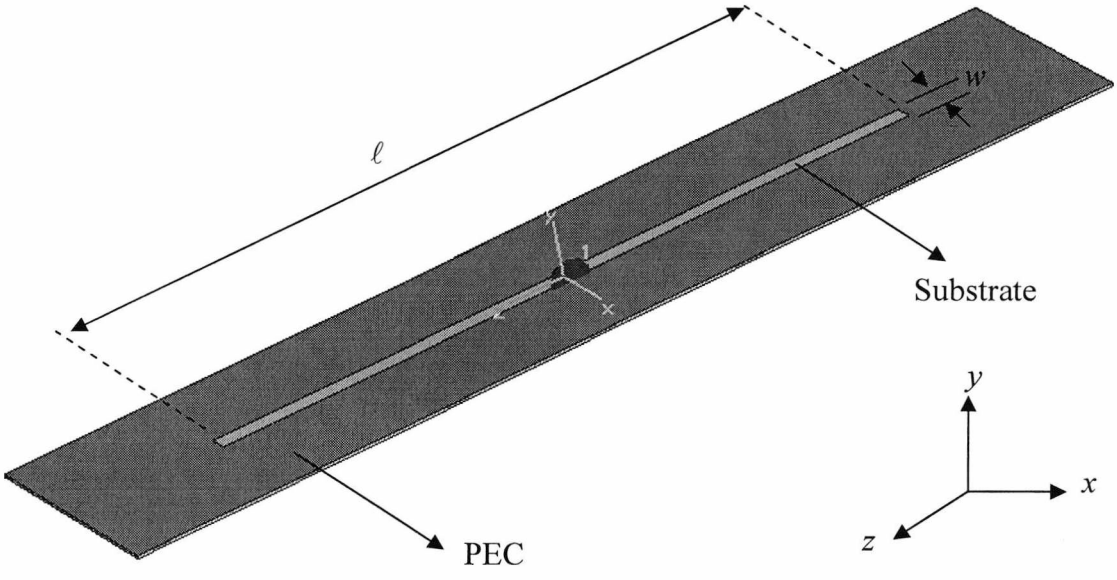

Fig.3.13: A vertically polarized magnetic dipole antenna at 869 MHz for a passive RFID tag; $\ell \approx \lambda/2$ mm, $w=0.012\lambda$, $\varepsilon_r = 4.9$

It can be seen from the above figure that the regions of perfect electric conductor (PEC) and free space in the electric dipole are now interchanged with dielectric substrate aperture and semi-infinite metal plane space. The direction of the **E-** and **H-** fields are also transposed accordingly. Note that when added together the electric and magnetic dipoles form a complete infinite metal screen. After confirming the optimum parameters of the antenna under investigation, prototype hardware was fabricated on planar FR-4 dielectric substrate having a relative permittivity of 4.9 and height 0.8 mm. Fig. 3.14 show a comparison of the simulated results using CST Microwave Studio and the

measured S_{11} for the antenna. Good agreement can be noticed. The slight discrepancies observed in the centre frequencies, may have resulted from either fabrication process (for example, during the photo-etching process) or due to uncertainties in the real permittivity of the FR-4 substrate.

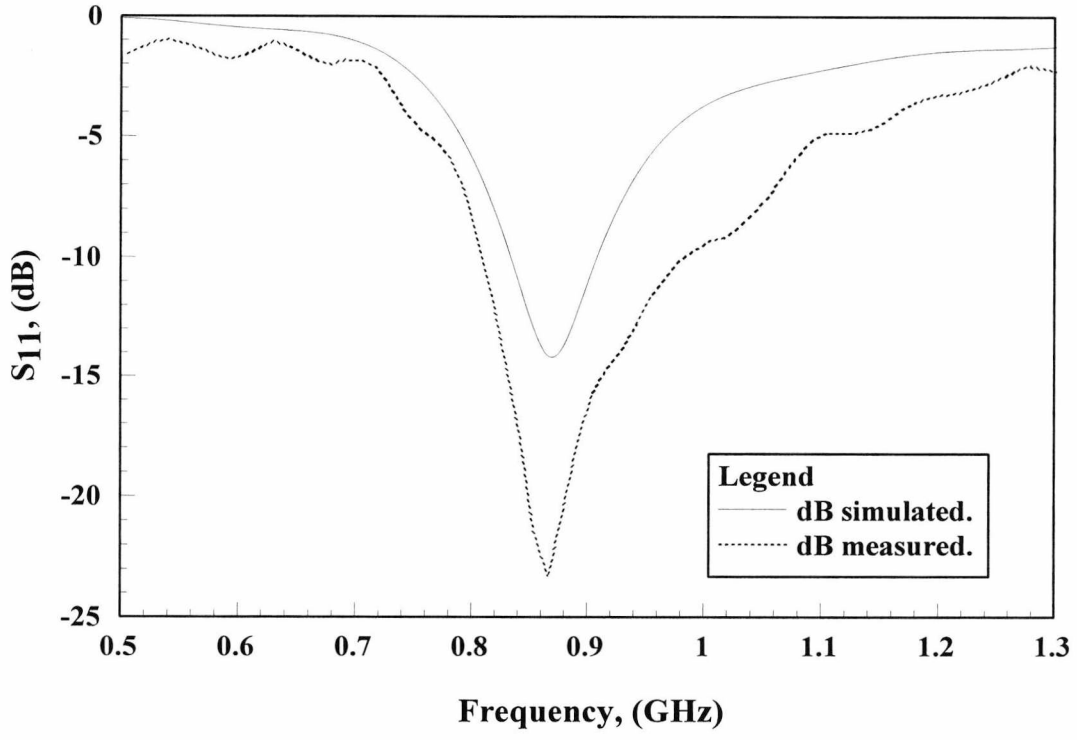

Fig. 3.14: calculated and measured return loss for the magnetic dipole $l/2 = 78$ mm, $w = 4$, $\varepsilon_r = 4.9$.

3.4.1 Effect of ground plane height on the radiation characteristics

Figure 3.15 shows the measured radiation patterns of the magnetic dipole in free space is compared with those when the antenna is mounted over different height of an infinite ground. As can be seen, the bi-direction pattern in free space becomes uni-direction when the ground plane was increased to 50 mm and 100 mm. The directivity increases as the ground plane height increases. Compared to the rest, the directivity is at maximised at the height of 100 mm and minimised when the antenna is at immediate proximity to the

ground plane. Another important consequence noticed during experimentation is that placing above ground plane at the distance of 50 mm and 100 mm causes the main beam to steer away from the boresight direction by 15°.

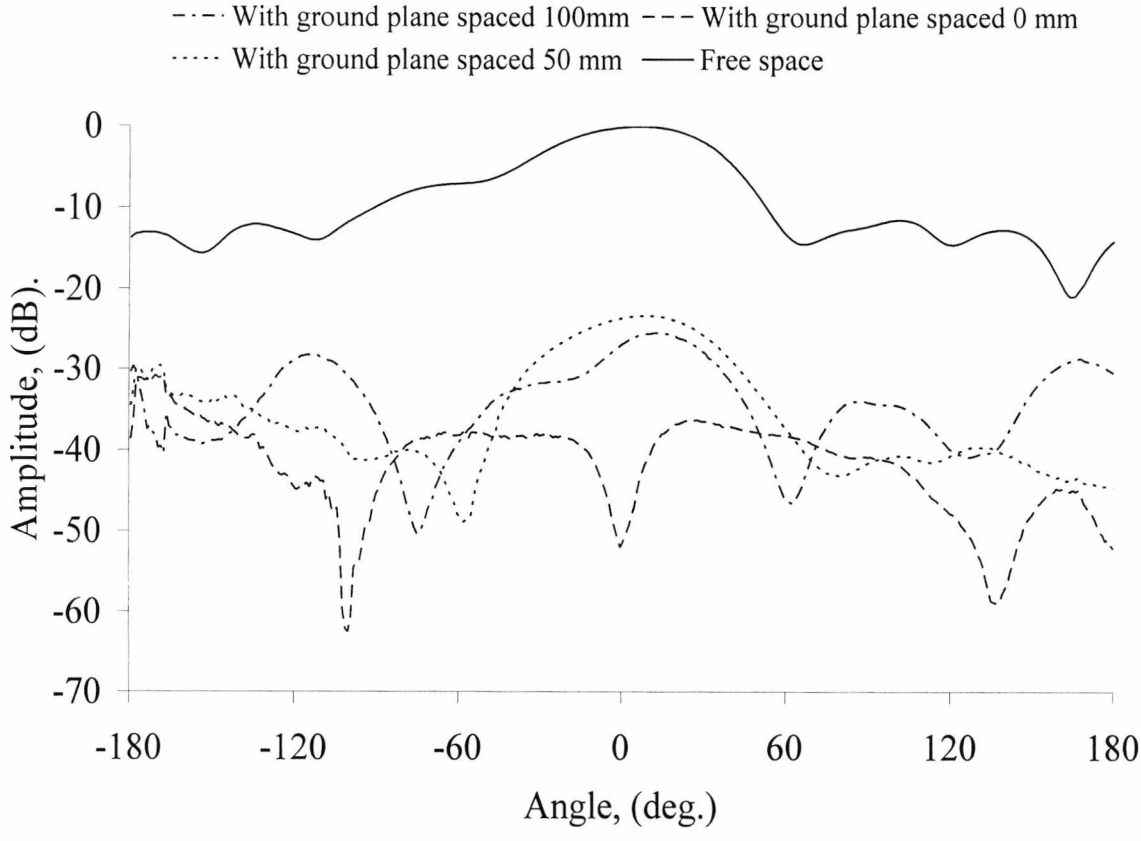

Fig. 3.15: Radiation pattern at 869 MHz for the magnetic dipole encountered in section 3.4: (1) in free space (2) with a ground plane and no spacer (3) with a ground plane and a 50 mm foam spacer and (4) with a ground plane and a 100 mm foam spacers.

3.4.2 The Effect of Polarisation on the Radar Cross Section

In this section, the effects on the radar cross section (RCS) are examined under four antenna load conditions: short circuit, open circuit, transistor loaded, and IC loaded using CST simulation. The variation of the RCS with electromagnetic field polarisation is further examined within each load condition. As expected, the short circuited case

exhibits the largest RCS depending on the field polarisation. Short circuit can be realised in practice when the tag shorts off the transponder chip. Under this condition, it is assumed that all energy is scattered.

On the other hand, a low RCS which in this case was observed under the resistor loaded case indicates a situation when the antenna is collecting all the interrogating electromagnetic waves, or when the antenna is open circuited.

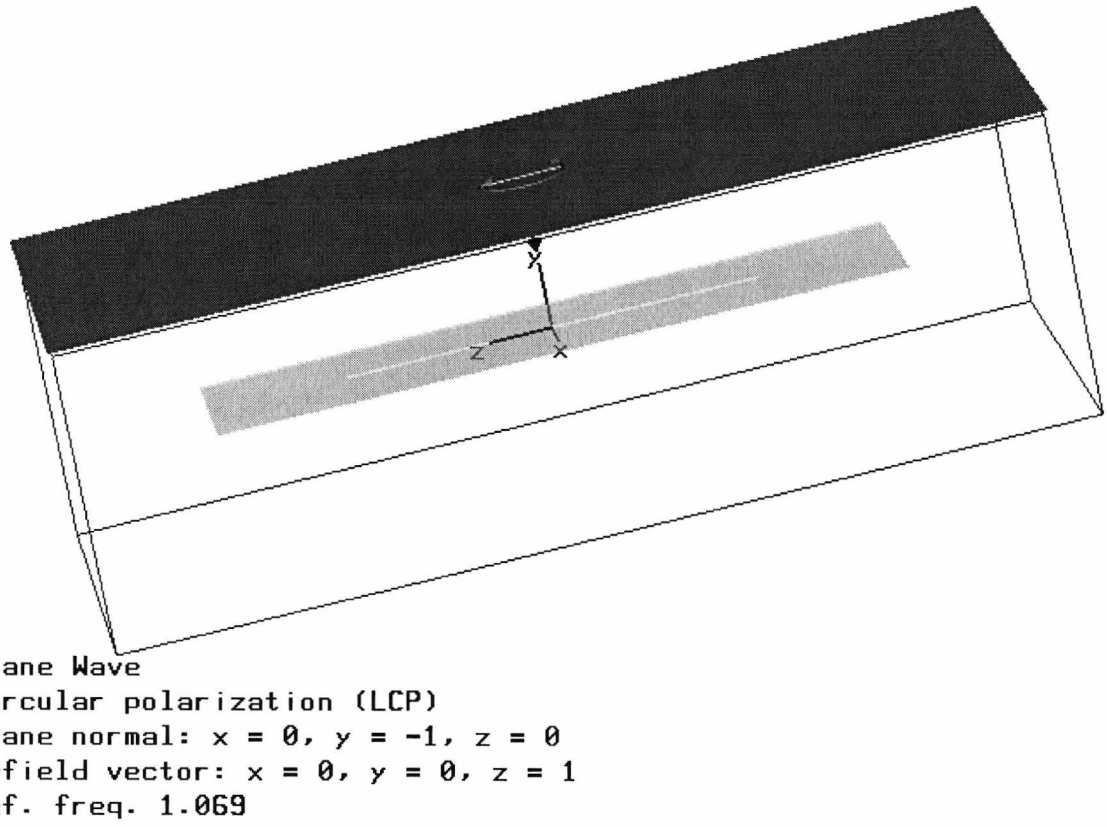

Fig. 3.16: A CST geometry file of a magnetic dipole illuminated by a plane wave.

As in the electric dipole, the definition of the plane wave is visualized by a red plane a shown in Fig. 3.16. Coloured arrows indicate the propagation direction as well as the electric and magnetic field vectors. Here the electric field vector of a plane wave is hitting the magnetic dipole. The plane wave is excited with an electric field vector in z-direction and a propagation normal (0,-1,0).

Antenna load	**Maximum RCS (dBsm) *y*-axis**		
	x-axis field vector	*z*-axis field vector	circularly polarised field
Open circuit	-7.818	-24.35	-10.54
Short circuit	-7.551	-6.988	-7.168
Resistor loaded	-7.824	-23.07	-10.56
Transponder loaded	-7.824	-21.45	-10.25

Table 3.5: Simulated maximum radar cross section (RCS) results for the magnetic dipole shown in Fig.3.13 under different load conditions for the case when a plane wave propagating normal to *y*-axis (0,1,0).

Antenna load	**Maximum RCS [dBsm] *x*-axis**		
y-axis field vector	*z*-axis field vector	circularly polarised field	
Open circuit	-10.79	-62.69	-13.71
Short circuit	-10.76	-58.98	-13.64
Resistor loaded	-10.82	-62.45	-13.60
Transponder loaded	-10.79	-61.90	-13.62

Table 3.6: Simulated maximum radar cross section (RCS) results for the magnetic dipole shown in Fig.3.13 under different load conditions for the case when a plane wave propagating normal to *x*-axis (1,0,0).

Antenna load	**Maximum RSC [dBsm] *z*-axis**		
	x-axis field vector	*y*-axis field vector	circularly polarised field
Open circuit	-21.46	-56.00	-24.77
Short circuit	-19.23	-55.68	-22.12
Resistor loaded	-25.35	-55.99	-30.06
Transponder loaded	-21.07	-55.79	-24.75

Table 3.7: Simulated maximum RCS results for the magnetic dipole shown in Fig.3.13 under different load conditions for the case when a plane wave propagating normal to *z*-axis (0,0,1).

3.4.3 The effect of slot width on the RCS for the magnetic dipole antenna

This section examines the effect of slot width on the scatter RCS. Fig 3.17 shows the effect varying the width of the slot produce on the radar cross section (RCS) for fixed values of substrate relative permittivity. As is observed from the figure, the RCS decreases with increasing slot width. This effect however is more slowly varying for substrate permittivity of 5. In this case, the decrease becomes more significant when the slot width reaches 8 mm. It should be noted that the percentage drop in RCS magnitude between when the slot has a width of 2 mm and when it has a width of 10 mm for different substrate relative permittivities of 1, 3, 5 and 7 correspond to 0.65 % 1.3 %, 1.5 % and 1 % respectively.

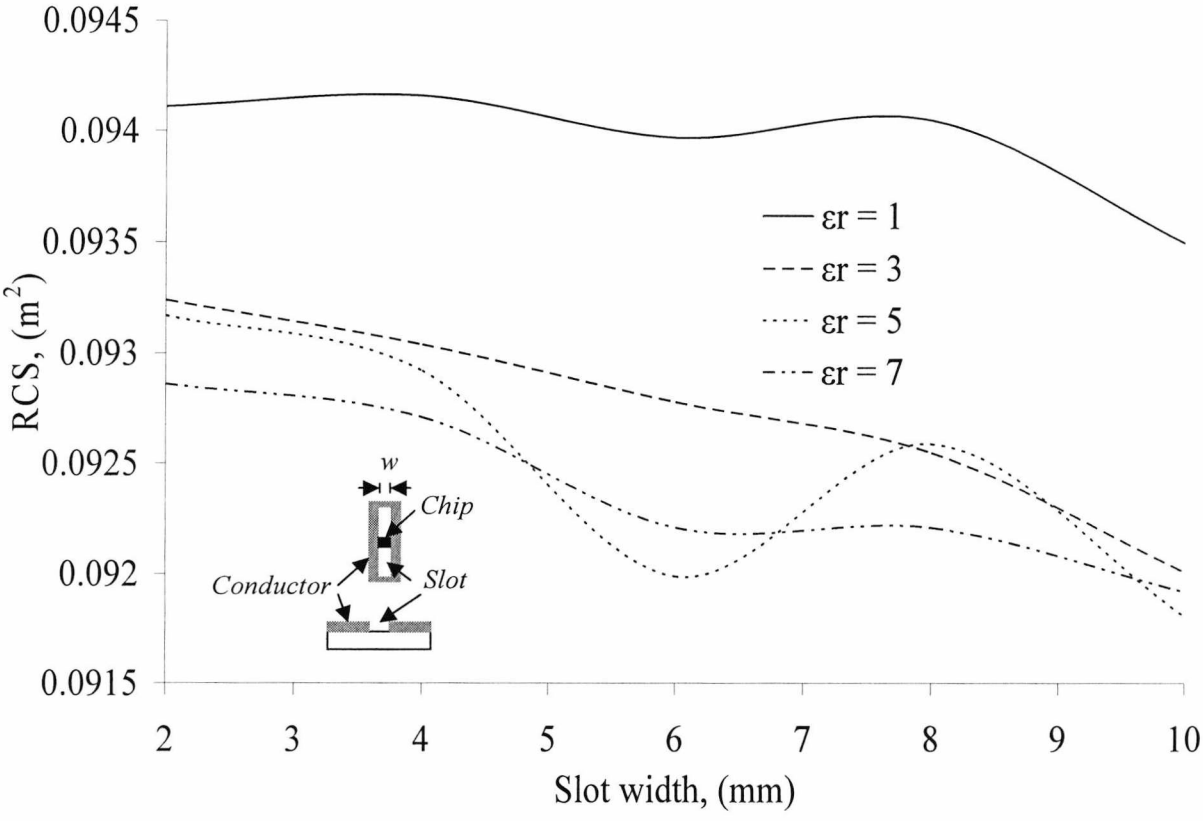

Fig. 3.17: The Effect of Slot width on RCS.

3.4.4 The effect of substrate permittivity and height on the RCS for the magnetic dipole antenna

The effect of substrate relative permittivity on RCS is shown in Fig. 3.18. There is a similarity in the variation in RCS magnitude for the various loaded conditions: open circuit (oc), short circuit (s/c), resistor loaded (Rx), and loaded by the lumped element equivalent input impedance of IC type EM4222 transponder [3.21]. Under open circuit and resistor load conditions, the RCS magnitude is expected to decrease rapidly for a substrate relative permittivity greater than 2. It however reaches its trough when the substrate relative permittivity reaches 4 and then shows a gradual increase.

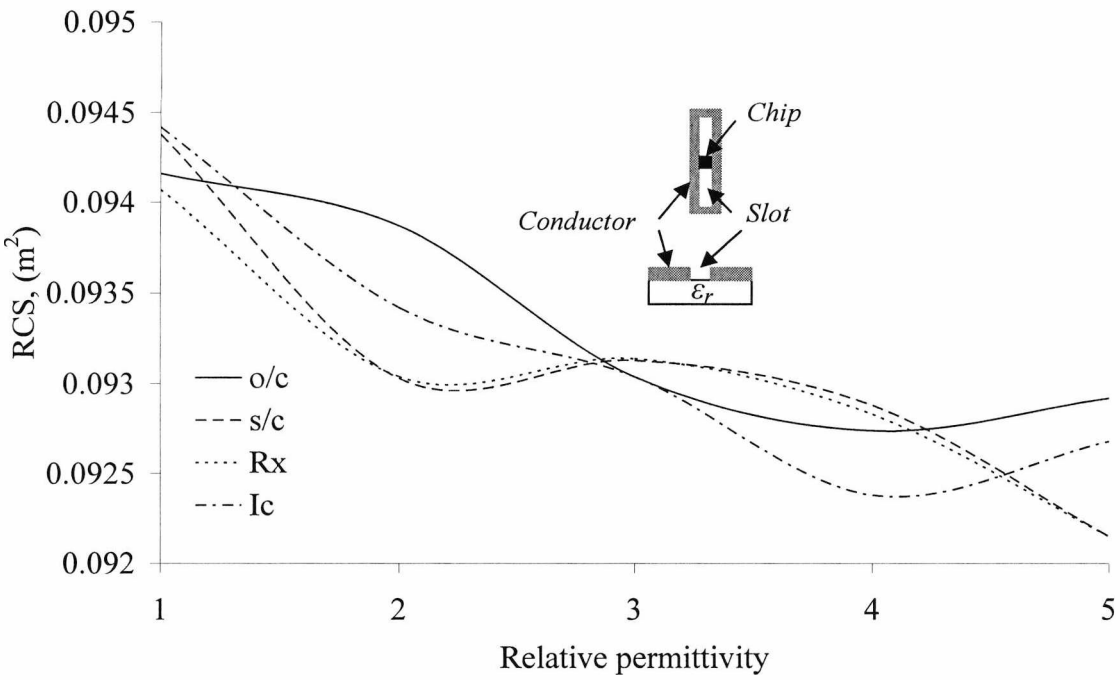

Fig. 3.18: Variation of the RCS for the halfwavelength magnetic dipole with substrate relative permittivity for different load conditions for substrate thickness 0.8 mm and 72 x 240 mm^2 metallic portion.

The case for the IC load condition shows that the RCS magnitude varies sinusoidally reaching its peak and trough at substrate relative permittivity of 1 and 4 respectively. The short circuit case shows a general decrease, except for the slope noticed when the relative permittivity is 3.

The effect of substrate thickness on RCS is shown Fig. 3.19 which shows the RCS decreasing steadily with increasing substrate thickness for fixed substrate relative permittivities of 1 and 5.

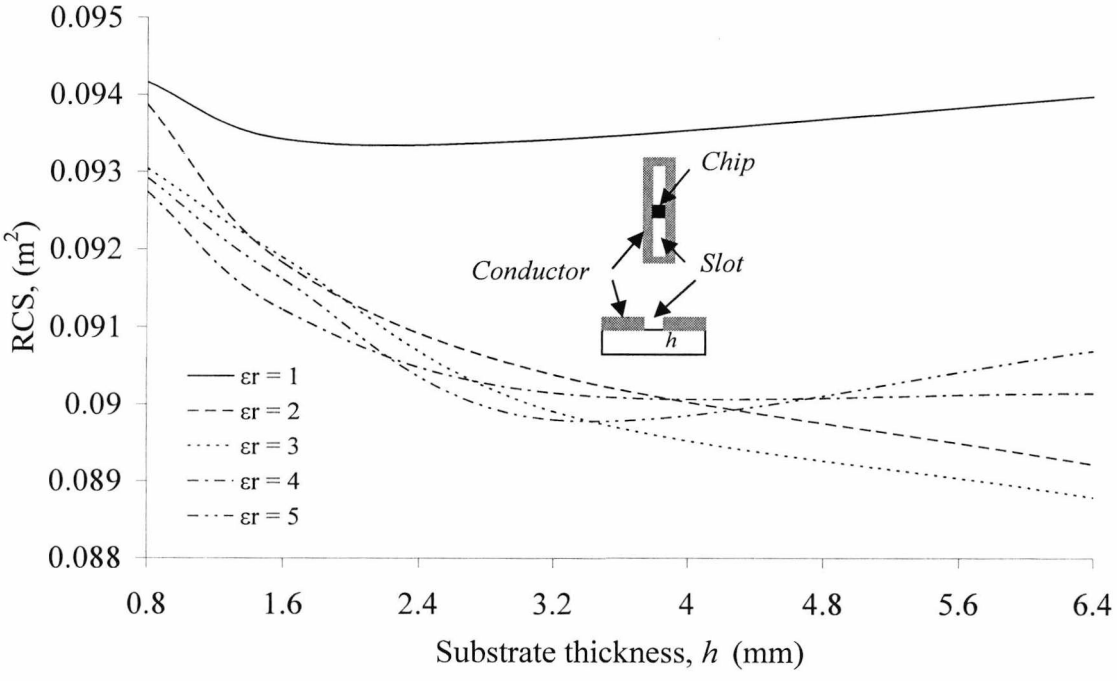

Fig. 3.19: Effect of substrate dielectric substrate thickness on RCS for different substrate relative permittivity using open circuit load condition for the magnetic dipole.

The corresponding curves for substrate relative permittivities of 2 and 3 exhibit a U curve in which the peak and trough are obtained at substrate thicknesses of 1.4 mm and at about 3.2 mm respectively. For the range of substrate thicknesses between 0.8 mm and 4 mm, the decay in the RCS magnitude for substrate relative permittivity of 2, 3, 4 and 5 are of

the order of 3.7 %, 3.38 %, 3.92 % and 4 % respectively. However, the case when the substrate relative permittivity is 1 show somewhat a peculiar characteristic of a U-shaped curved with an increase of 0.3 % for the range of substrate thicknesses under consideration.

3.4.5 The Effect of Incident Angle on the RCS for the Magnetic Dipole Antenna

The simulated RCS pattern of the magnetic dipole versus angle of plane wave incidence under various load conditions is shown in Fig. 3.20. It can be seen that, as in the case of the electric dipole, a similar shape of RCS magnitude is observed as the tag rotates through 180°. Here the lowest RCS is for normal plane wave incidence under open circuit load condition, while the highest magnitude was obtained under the resistor load condition.

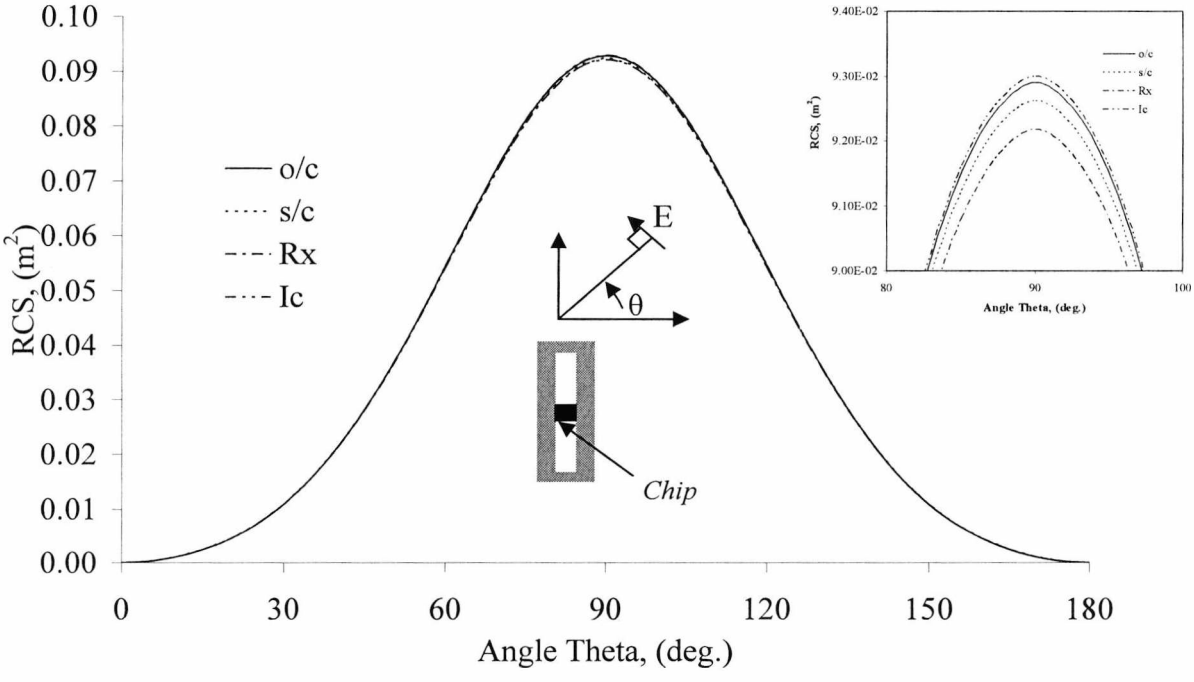

Fig. 3.20: Effect of angle on RCS for different load conditions for a magnetic dipole Inset graph show the RCS values at high resolution.

The effect of incidence angle on RCS for different substrate heights is presented in Fig. 3.21. The shape of the RCS pattern is similar to that obtained for the equivalent electric dipole. This figure shows a decrease in the RCS value with increasing substrate thickness for a fixed substrate permittivity. It should be noted that the difference in the RCS magnitude becomes greater when the plane wave is at normal incidence to the tag antenna.

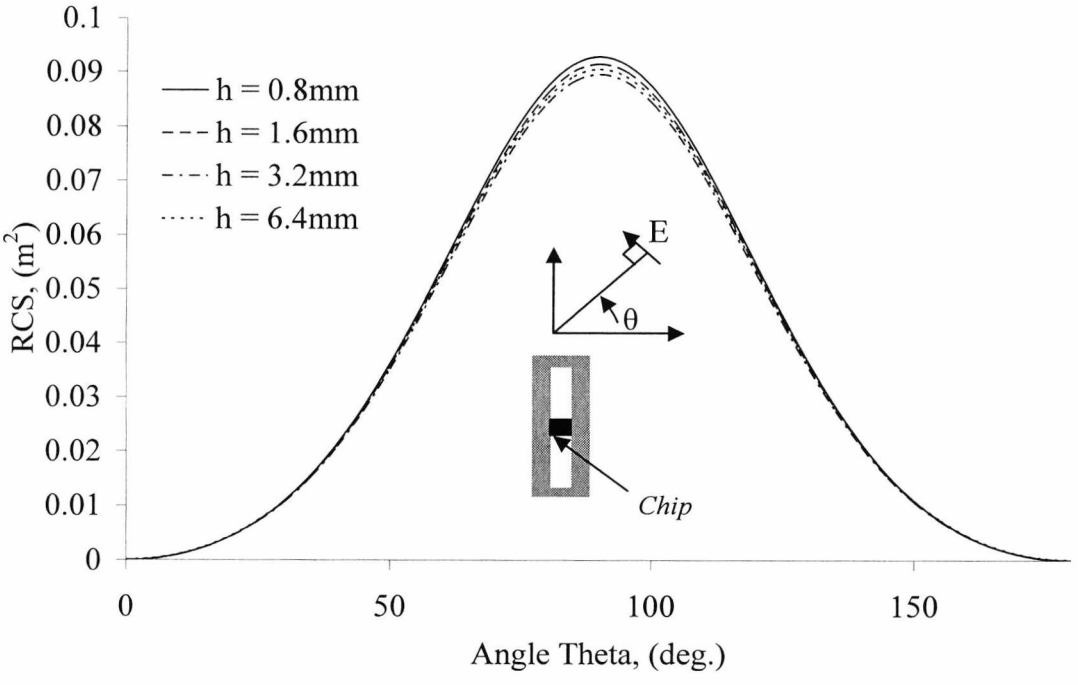

Fig: 3.21: The effect of angle on RCS for different dielectric substrate thickness

3.4.6 Sensitivity on the Magnetic Dipole Tag Antenna to Potential Objects to be Tagged.

Like in the case of the electric dipole, the magnetic dipole encountered in section 3.3 was analysed for sensitivity to potential mounting surfaces using numeric simulation. These materials were represented by foam, dry wood, plastic, glass and metal corresponding to substrate permittivity of approximately 1, 1.4, 3.5, 4.8 and ∞. Table 3.8 summarises the

variation in the radiation parameters with respect to the above material in the context of the gain, angular width (AW), main lobe direction (MLD) and side lobes (SL).

It was observed that the gain does not change significantly across the range of objects under consideration. However, for an infinite size metallic plane, the gain increases by 16 % when compared to an object whose outmost surface is say plastic. This is due to the fact that metallic surfaces block all back radiation thereby causing a narrower angular width (beamwidth) to occur. It therefore follows that the resulting side lobes magnitude should be relatively large for a tag on an infinite size metallic object. The angular width does not change appreciably for materials whose relative permittivity lie between that of foam and glass. When the antenna was simulated on metallic objects, the reduction in the angular width was less significant for this antenna than in the case the electric dipole studied in section 3.3, however, the main lobe direction was tilted by 15 %.

Platforms	**Parameters**			
	Gain	AW (deg.)	MLD (deg.)	SL level (dB)
Foam	3.6	65.3	90	<(-45)
Wood	3.62	65.5	90	<(-45)
Plastic	3.64	66.3	90	<(-45)
PEC	4.17	65.0	65	-10.1

Table 3.8: Simulated data on radiation characteristics for the magnetic antenna when attached directly on different objects.

Definitions

AW represents angular width or 3dB beamwidth measured in degrees.

MLD represents the main lobe direction measured in degrees

SL represents the side lobe level in dB

3.5 Measurement of the Tag Read Range

Apart from the considerations given to the return losses, impedances characteristics and radiation patterns and the RCS in the preceding subsection, another test parameter is the read range. Read ranges were both reviewed according to theory and measured practically where the read range is defined as the maximum distance from which a tag can be detected. The theoretical maximum read range obeys Friis law subject to the power reflection coefficient [3.22].

3.5.1 Test set up

The read range tests procedure described here equally apply to the ones to be presented later in chapter 4 and 5 involving the slot patch and complementary patch antennas respectively. In order to interrogate the tags, a circularly polarised IPICO Reader was used to transmit a 500 mW continuous wave (CW) signal at 869 MHz as already described in Chapter 1. A few key points are described in the following paragraphs.

1. To accurately evaluate the performance of a tag in the light of the range definition given above, it is essential that the tag is stock on a low dielectric constant carriage, which should be long enough to offset the effects of human body.

2. To avoid interactions with sensitive objects, materials surrounding the tag under test need to be minimised, or made of low relative permittivity. Tags that are meant for metallic object should normally be installed above a tolerance height over the metallic plane.

3. Of great interest is the assessment of tag performance within a potential supply chain environment such as roll cages. This will be presented in Chapter 6 of this thesis.

A simplified diagram of a typical measurement set has been described in Chapter 1. The measurement is based on detection of backscattered modulated signals from tags. By

sequentially detecting the modulated signals it is possible to identify a tag in real time. The Reader is connected to a host computer for data management. Thus the main sub-systems in the measurement are the tag, the Reader and the host computer including the enabling software. *Showtag* software supplied by RF Tag Ltd, UK has been used for the tests.

3.5.2 Test materials

The EM4222 and BiStar 3891-3 transponder chips were respectively integrated with the antennas for these tests. The ranges were tested with the tag attached to six materials. These were foam ((40×40×10)mm, cardboard paper(33×28×5) mm, dry wood(38×35×2.5)mm, plastic(40×40×2.8)mm, glass (50×36×3)mm and metal(42×42×4) mm. The choices of these were made to reflect a variety of complex permittivities and conductivities; besides, they are potential candidates for tag attachments. The estimated loss tangent for these materials were similar to one gives in CST software.

The clamp fixture used to attach the tag to the objects was an ordinary masking tape of 0.11 mm thickness which ensured that the antenna performance was not degraded. The object together with the tag was suspended on PVC and tested for different orientation. The results are summarised in Table 3.9

3.5.3 Test results

Firstly, in order to establish the optimal dipole length at 869 MHz, a set of range values corresponding to tags of different dipole structures: λ, $\lambda/2$, $\lambda/4$, $\lambda/8$ length were tested. It can be seen in Fig. 3.22 that a half wavelength dipole gives a greater range when compared to a full wavelength, quarter wavelength or an eighth of a wavelength. It also exhibits a greater read range compared to its complementary slot antenna. According to simple theory, the maximum read range for a half wavelength dipole antenna of physical length

λ, operating at 869 MHz is when the length of each arm of the dipole $\lambda/2$ is 0.086 m. However measured results show maximum read range was recorded when $\lambda/2$ is 0.076 m. This adjustment is necessary as part of the antenna was printed on a circuit board, and the dielectric will have loaded the antenna causing it to be slightly larger than the free space half-wavelength. Also dipoles routinely require trimming to compensate a capacitive end effect.

It was observed that improved read range can be achieved for the cases of when the length of the dipole's arm is between 0.076 m and 0.086 m depending on the tag orientation and height with reference to the floor.

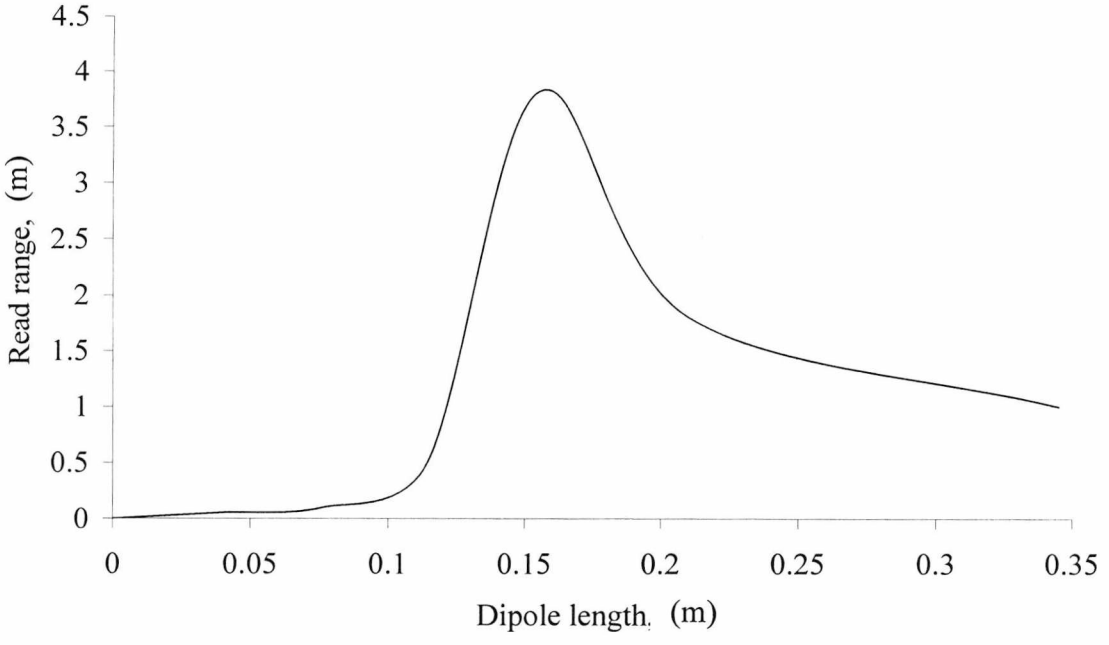

Fig. 3.22: Range variation with dipole length with short circuit loop

Further tests were carried out under a variety of conditions listed in the Table 3.9 below. The average read range was obtained by averaging, in a set of random measurements, the maximum distance at which the antenna could backscatter. The tag range measured on foam is identical to free space measurement and was optimum at 3.82 when placed horizontally. Paper and dry wood showed a slightly reduced range than in the foam material. This decrease is attributed to losses in the wood and paper.

Category	Reading conditions	Electric dipole Range	Magnetic dipole range
Reader RF Interferences	-	Transmitting at 869 MHz with 0.5W EIRP	Transmitting at 869 MHz with 0.5W EIRP
Reading range for different tag orientations with reference to the reader antenna	Horizontal (0°); x-axis	3.82 m	2.8m
	Vertical (90°); y-axis	2.83 m	1.5m
	Horizontal (90°); z-axis	1.5 m	1.2m
Mounting platforms maximum read orientation (y-axiz)	Foam	3.82m	2.8m
	Paper mounted	3.61m	2.70m
	Dry wood	3.52m	2.98m
	Plastic	3.45m	2.77m
	Glass	3.40m	2.50m
	Metal	0m	0m

Table 3.9: Comparison of tag performance using electric and magnetic dipoles antennas using *IPICO* reader; one tag read under static condition at a time.

The range for ceramics and glass showed further reduction due to detuning. Furthermore, since the impedance of the tag is very low when on metal, this range in this case was zero.

3.5.4 The Effect of the Inductive Loop on the Read Range

Furthermore, the read range for the electric dipole has been investigated for the effect of connecting a match loop across the antenna terminals. The effect of this loop on the input impedance of the antenna has been analysed in sub-section 3.3.1 of this chapter.
For this investigation, a 3891-3 transponder chip was integrated to the antenna terminal (parallel to the loop) for different dipole structures as in the previous case.

The chip was considered to be a few hundred ohms. Therefore, in theory, the best reading range should be detected when a low impedance antenna is connected across the chip terminals. As expected, the maximum read range here was achieved when a matching loop was connected across the antenna terminal and was comparable to the one obtained in Fig. 3.22 above (using the EM4222 transponder chip). Again, the best range was realised when the dipole was 76 mm. On removing the loop the range was plotted in Fig. 3.23 as a function of length. These show a much reduced range but an otherwise similar result – again the best range is obtained at a dipole length of 76 mm. However, in the case of the EM4222 chip, this highest read range was obtained without the matching loop.

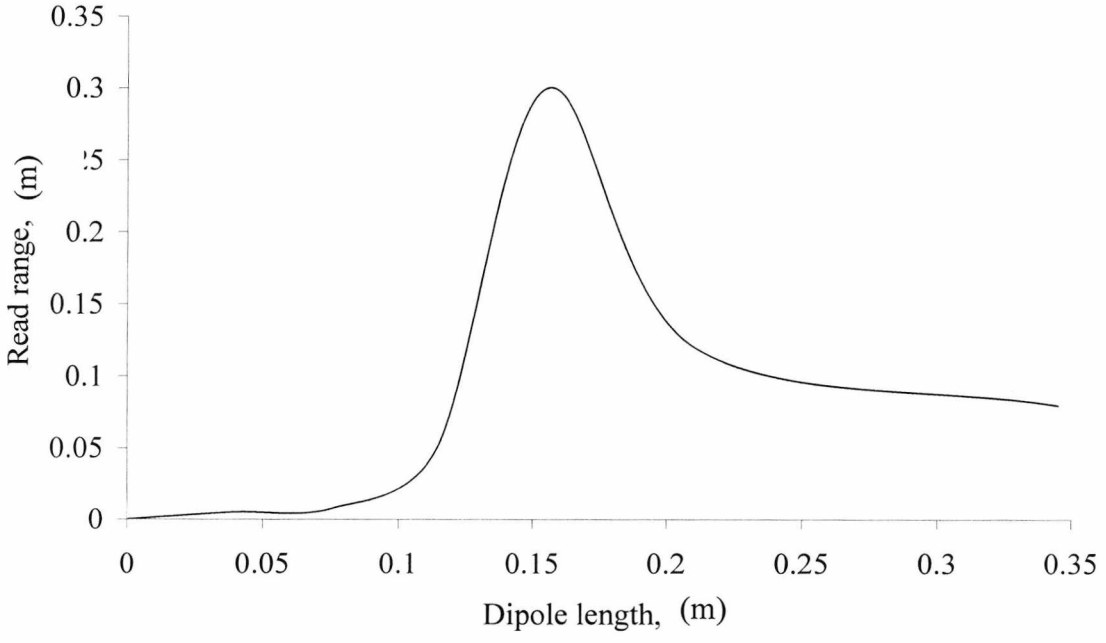

Fig 3.23: Range variation versus dipole length without a matching loop across chip terminals.

Read range measurements demonstrate that the loop around the so-called feed loop produces a substantial improvement in detection range. The antenna impedances are very low when the loop was present as it essentially short circuited the feed point (see section

3.3.1). Hence, the impedance results for the antenna with and without the chip connected are consistent and allow a clear conclusion to be draw that the chip has a much lower impedance value hence a longer read was achieved.

3.6 Conclusion

The aim in this chapter was to investigate the practicability of using an electric dipole or a complementary magnetic dipole to tag objects at 869 MHz. It was shown that both antenna configurations can be used for the application depending on the design criteria. Simulated results show that the variation in the gain is less severe in the case a magnetic dipole than it was for an electric dipole. Although measurement results show that variation in ground planes heights produce similar effects on the radiation patterns for both antenna configurations, the magnetic dipole was more.

The sensitivity of the dipoles when attached to different objects has been used as a figure of merit which combines the effects of antenna gain and decreasing beam width into a single consideration. The variation in the sensitivity has been used to predict the effects of increasing antenna gain or decreasing beamwidth of the tag antenna on the overall RF tag performance. The knowledge of these variations in sensitivities will be useful, when as a future work the free space RF tag sensitivity can be adjusted to its actual value when attached to objects by substituting the gain penalty into the bi-directional radar equation of chapter 2 on the power received by the tag.

On the hand, the variations on the RCS for both antennas were dissimilar. Simulations results show that increasing the strip width (in the electric dipole) tend to increase the RCS value whereas the effect was opposite in the case when the slot width (of the magnetic dipole) was increased. Both antennas exhibit maximum RCS value at 90^{o}, which correspond to when the antenna is in a straight line with direction of plane wave propagation (for a horizontally polarised electric field).

The results of experimental measurement of the read range indicate the following:

1. Complete detection and location in all cases of tags within an average distance of 0.12 meters from a circularly polarised reader antenna irrespective of antenna polarisation or tag orientation.

However, the results presented here lie within the further constraints that:-

1. Only the free space conditions of the operational environment were simulated with CST microwave studio. In practical tests, challenges are to be expected from propagation variables such as obstructions, refractions and reflections.
2. The actual impedance values of the transponder chips, 3981-3 remain unknown. Nevertheless, optimal performance of a tag requires that the antenna impedance matches the chip impedance.

The read range measurements conclude that the electric dipole gives a superior performance as compared to the complementary magnetic dipole.

3.7 Reference

[3.1] J. Siden, H. Nilsson, A. Koptyug and T, Olsson,"A distanced RFID dipole for metallic supply chain label," in *Proc., IEEE AP-S Int. Symp.* and USNC/URSI National Science Meeting, July 2006, pp. 3229-3232.

[3.2] N. Kim, H. Kwon, J. Lee and B. Lee, "Performance analysis of RFID tag antenna at UHF (911 MHz) Band," in *Proc., IEEE AP-S Int. Symp.* and USNC/URSI National Science Meeting, July 2006, pp. 3275-3278

[3.3] Gaetano Marroco, "Gain-Optimisation Self-Resonant Meander line Antennas for RFID Application," *IEEE Trans. Antennas and Wireless Propag. Lett.,* vol. 2, 2003, pp.302-305

[3.4] L. Ukkonen, M. Schaffrath, L. Sydänheimo and M. Kivikoski, "Analysis of Integrated Slot-Type Tag Antennas for Passive UHF RFID," in *Proc., IEEE AP-S Int. Symp. and USNC/URSI National Science Meeting*, July 2006 pp. 1343 - 1346

[3.5] Ronold W. P. Kings and Charles W. Harrison, "Antennas and Waves: A

Modern Approach," M.I.T. Press, p.677

[3.6] L. Ukkonen, M. Schaffrath, L. Sydänheimo and M. Kivikoski, "Modelling the Effects of Stacked Paper on the Radiation Pattern of Bow-Tie RFID Tag," in *Proc., IEEE AP-S Int. Symp. and USNC/URSI National Science Meeting*, July 2006, pp. 3225-3228

[3.7] J.T. Prothro, G.D Durgin and J.D. Griffins, "The effect of a metal ground plane on RFID tag antenna," in *Proc., IEEE AP-S Int. Symp. and USNC/URSI National Science Meeting*, July 2006, pp. 3241-3244

[3.8] B. Yu, S. Kim, B. Jung, F. Harackiewicz, M. Park and B. Lee, "Balanced RFID tag antenna mounted on metallic plates," in *Proc., IEEE AP-S Int. Symp. and USNC/URSI National Science Meeting*, July 2006, pp. 3237-3240

[3.9] Blakes, L.V., (1966) "Antennas," Artech House, p.133

[3.10] Green, D.C., "Radio Systems for Technician," Longman Group Ltd., 1995, p.102

[3.11] R. Lelarante and R. J. Langley, "Dual –band patch antenna for mobile satellite systems," *IEE Proc.-Microw. Antennas Propag.,* vol 147, No 6, Dec 2000

[3.12] Bruce G. Colpitts and Giles Boiteau, "Harmonic radar transceiver design: miniature tags fore insect tracking," *IEEE Trans. Antennas Propag.*, vol.52, no.11, pp 2825-2832

[3.13] Chihyun Cho, "Novel RFID Tag antenna for metallic object" in *Proc., IEEE AP-S Int. Symp. and USNC/URSI National Science Meeting*, July 2006, pp. 3245-3248

[3.14] Rao, K.V.S., Nikitin, P.V., Lam, S.F., "Antenna design for UHF RFID tags: a review and a practical application", *IEEE Trans. Antennas Propag* vol. 53, issue 12, Dec. 2005 Page(s):3870 - 3876

[3.15] Edward A. Wolff, "Antenna Analysis," Artech House, Inc., 1988, p.143

[3.16] Constantine A. Balanis, "Antenna Theory: analysis and design," John Wiley & Sons, Inc., 1997, pp.616-617

[3.17] E.C, Jordan and K.G. Balman, "Electromagnetic wave and radiating systems," Prentice-Hall Inc, 2nd ed. 968, Chapter 13, pp.513-516

[3.18] H.G. Booker, "Slot aerials and their relation to complementary wire aerials," JIEE (London), 93, pt. IIIA, No. 4 1946

[3.19] E.F. Knott, J.F. Shaeffer and MT Tuley, "Radar cross section – its prediction, measurement and reduction", Artech House Inc., 1985, p.155]

[3.20] K. Penttila, M. Keskilammi, L. Sydanheimo and M. Kivikoski, "Radar cross-section analysis for passive RFID systems," *IEE Proc.-Microw Antenna Propag., Vol 153, No 1, February 2006.*

[3.21] EM Microelectronics: EM4222 data sheet, 2004

[3.22] Nikitin, P.V.; Rao, K.V.S.; Lam, S.F.; Pillai, V.; Martinez, R.; Heinrich, H., "Power reflection coefficient analysis for complex impedances in RFID tag design," Microwave Theory and Techniques, IEEE Transactions on, Volume 53, Issue 9, Sept. 2005 Page(s):2721 - 2725

CHAPTER 4

SLOT PATCH ANTENNA FOR PASSIVE RFID TAGS

4.1 Introduction

This chapter presents the design and development of a dual band Slot Patch Antenna (SPA) for passive RFID tags. The antenna system employs various resonant slots to perturb the field distributions along a conventional slotline and thereby excite frequencies above its fundamental mode. Thus, without increasing the antenna size, dual resonance operations are achieved. The excited frequencies at 869 MHz and 2.45 GHz are compatible with the European ISO 1800 - 6 specified operating frequencies for RFID systems [4.1]. A narrow operating band within the general band of 869.4 – 869.65 MHz is needed in order to minimise interference from adjacent frequencies in this more crowded band, for example from mobile phones. The antenna is tuneable to accommodate other frequencies specified by Electronic Product Code Global (EPCglobal) for RFID tag operation.

The dual band SPA evolved from a conventional Patch Antenna (PA) and covers two UHF frequencies. Although the antenna is uniplanar, its topology is asymmetrical and arises out of the need to manipulate the current distribution within the patch structure in order to achieve the dual resonant modes at the RFID operating frequencies. The proposed SPA antenna is scalable and thus is useful for operation at higher RFID frequencies such 2.45 GHz and 5.8 GHz. Each of the SPA antenna exhibit quasi-isotropic radiation characteristics. They have two planes of polarisation (vertical and horizontal) which improves tag detection.

Other techniques can be used to achieve dual band operation and include the use of slots to load a rectangular patch in such a way as to create additional resonant modes [4.2]. These slots can also be arranged to yield wide band behaviours. For example, in [4.3], a

modified U-slot rectangular patch is reported in which the current along the edges of the slot is capable of introducing supplementary resonances which when added to the resonance of the main patch produces wide-band operation. By using space-filling slots, Ghali and Moselhy were able to create a broad band antenna that has an impedance bandwidth of 86.6% (voltage standing wave ratio, VSWR < 2) [4.4].

The SPA combines the advantages of low profile, lightweight, conformation to mounting surfaces and ease of fabrication. Furthermore, ASIC integration can be carried out with relatively great design freedom. The drawbacks however include their narrow bandwidth and low power capacity due to the resonant nature of the patch [4.5], [4.6]. A full-wave method using CST Microwave Studio enables optimization of the antenna. The viability of this simulator has been demonstrated by comparing the results obtained from fabricated prototypes with numerical simulation. The simulated results agree well with the experimental results.

4.2 The basic antenna geometries

In order to proceed with the choice of an antenna for the application, three different patch antenna configurations are illustrated in Fig. 4.1 and their performances compared. The patch antenna (PA) illustrated in a) consists of a supporting dielectric substrate of thickness h and relative permittivity ε_r sandwiched between an infinitely thin perfectly conducting patch with dimension $a \times b$ and an infinite-size ground plane. The slot patch antenna (SPA) shown in b) consists of a narrow slot embedded in one of the radiating edges of an infinitely thin perfectly conducting patch which in turn is on a supporting dielectric substrate. Fig 4.1 (c) is defined as in (b) but differs by the inclusion of a perturbation stub. There are no ground plane in (b) and (c).

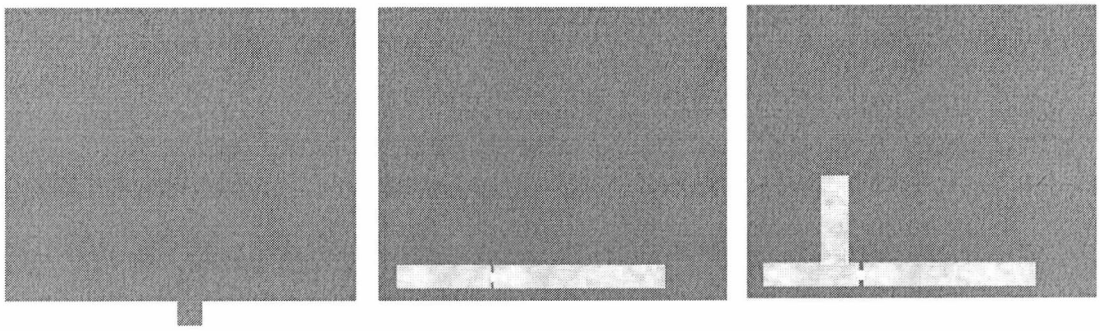

Design 1	Design 2	Design 3
Patch antenna (PA)	Slot patch antenna SPA1	Slot patch antenna SPA2
(a)	(b)	(c)

Fig 4.1: Schematic diagrams of the (a) linearly polarised patch antenna; (b) linearly polarised slot patch antenna without perturbation; (c) dual linearly polarised slot patch antenna with a single perturbation (70 × 70) mm.

In simulations, the patch antenna was fed by a stripline which was modelled as a discrete port with a characteristic input impedance of 50 Ω. The feed were modelled as discrete ports of characteristic input impedance of 50 Ω. The behaviour of the slot L1 is akin to that of a magnetic dipole at its first resonant frequency (Chapter 3, Section 3.4). Its length is $\lambda_g/2$, where λ_g the guided wavelength in the slot [4.8]. The antenna parameters are identified in Fig. 4.2 and defined in Table 4.1.

The resonance of a slot antenna (Fig. 4.2) can be influenced by the feed location (d_S) and the vertical position of the slot (d_L). Table 4.2 shows the effect of moving the feed locations along the slotline of L_1 (horizontal or x-axis). It can be seen that by increasing the distance d_s, the first frequency decreases while the second frequency increases. There is no discernable increase in resonant frequency by varying the dimension d_L.

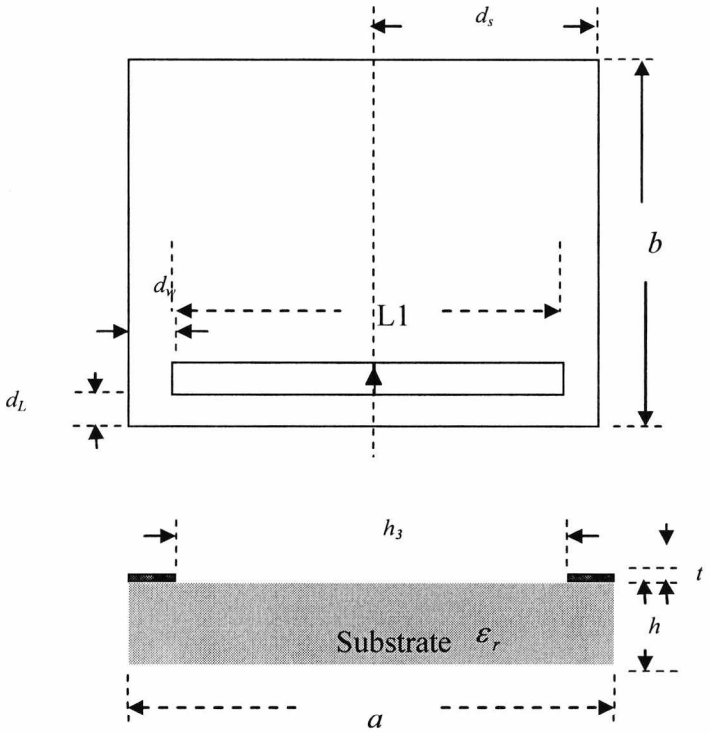

Fig 4.2: Schematic diagram of the linearly polarised slot patch antenna showing the elevation and side views.

Parameter	Description		Parameter	Description
a	Length of the patch		t	Thickness of the patch
b	Width of the patch		d_L	Distance slot away from edge to antenna length
$L_1....L_n$	Slots 1 to n		d_w	Distance slot away from edge to antenna width
$l_1....l_n$	Length of the slot 1 to n		ε_r	Relative permittivity
$w_1....w_2$	Width of the slot 1 to n		$tan\delta$	Loss tangent
d_s	Distance of the fed from edge		h	Thickness of the substrate
l	Length of slot		w	Width of slot

Table 4.1: Physical parameters of the antennas.

Distance d_s (mm)	Fc1(MHz)	Fc2 (MHz)	$^{Fc1}/_{Fc2}$ (MHz)
5 mm	1.31	1.31	1
25 mm	1.2621	1.618	1.28
45 mm	1.2298	1.95	1.59

Table 4.2: Frequency characteristics of the reference planar RFID tag antenna (SPA1); l_1 =63 mm and w_1 =52 mm. Fc1 represent the lower resonant frequency, Fc2 represent the intermediate resonant frequency and Fc3 represent the upper resonant frequency.

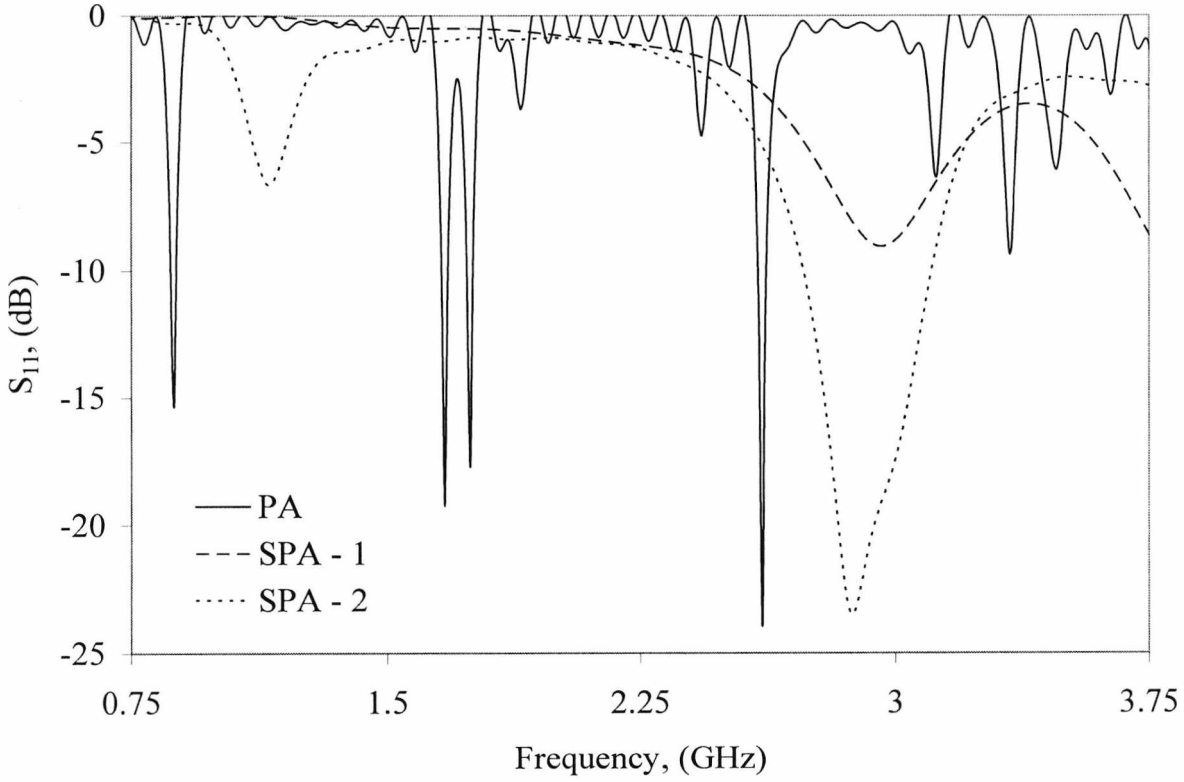

Fig. 4.3: Simulated return loss of antenna patch antenna, slot patch antenna SPA1 and SPA2 for which dimensions are given in Table 4.1

Investigations have been carried out on the return losses for the antenna shown in Fig. 4.2: (a) microstrip patch (PA), (b) slot patch with one slot perturbation (SPA1) and (c) slot patch without double slot perturbation (SPA2). It was found in Fig. 4.3 that the MPA exhibits a narrower bandwidth compared to any of the SPA; and within the SPAs, it was further observed that by adding an orthogonal slot to L1, other modes outlined in the short broken line of Fig. 4.3 can be excited.

The difference in bandwidth between the slotted patch and the microstrip patch is mostly due to the absence of ground plane. The main advantage of the slot patch antenna for this application consists in the realisation of dual band operation without necessarily having a dual feed. In this case, the slots are orthogonal to each other. The likelihood of using additional slots to realise both compact and dual polarised uniplanar slot antenna makes the SPA a more suitable candidate for RFID application. Furthermore, integration of ASIC with patch configuration is easier with the SPA; hence is easier to physically construct the connection between the planar antenna and surface mount transponder than, say, in microstrip patch antennas [4.8]. Thus, the SPA has been chosen and will be investigated further; a parametric study will be carried out to establish the optimal design dimensions.

4.3 Slot patch antenna and optimisation

This section focuses on examining the influence of further perturbations on a SPA using more coupled slots of different dimensions. Additionally, the combined effects of slot width and dielectric constants are presented. Fig. 4.4 distinguishes each tuning slot elements in a normal design that is presented here.

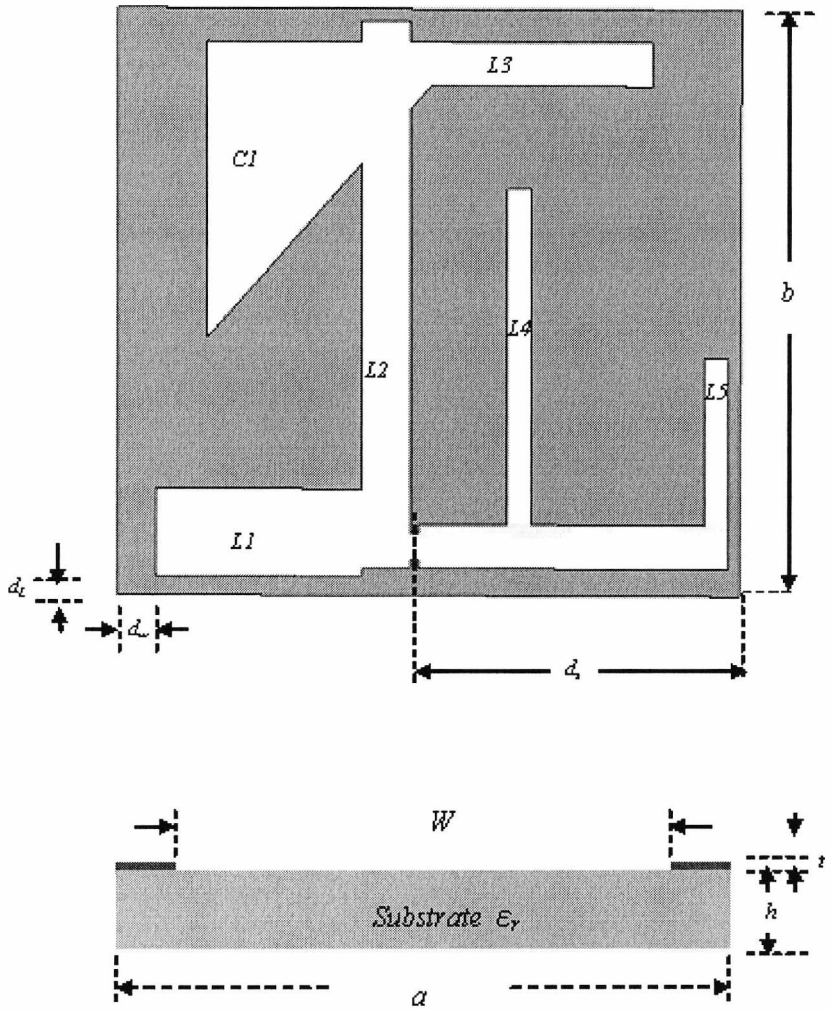

Fig. 4.4: Schematic of the dual polarised slot patch antenna with dimensions enlisted in Table 4.1 fabricated on an FR-4 substrate with relative permittivity, ε_r = 4.6 and height = 0.8 mm, copper conductor height = 0.007 mm, Length (L) = Width (W) = 70 mm.

To evaluate the extent to which these parameters affect the frequency response, a stepwise numerical simulation was carried out to analyse each stage of the evolution from the addition of one stub to four. The SPA1 which incorporates a simple slotted stub (earlier introduced in Fig 4.1 (b)) has been chosen as the reference case. Slot elements L2, L3, L4 and L5 were introduced to antenna resulting in designs 2, 3, 4, 5 and 6, respectively, as shown in Fig. 4.5.

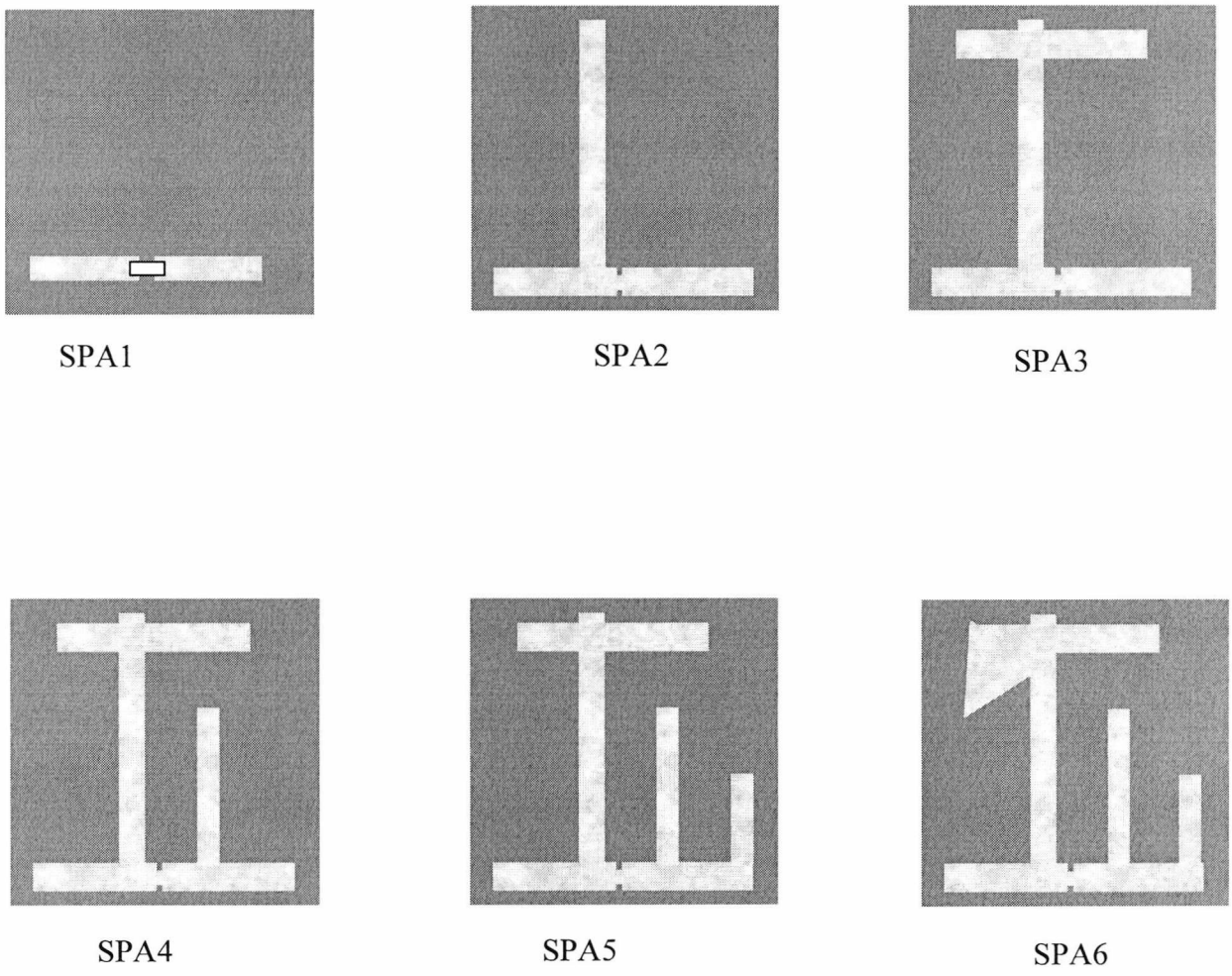

Fig. 4.5: Slot patch antenna with increasing number of perturbation elements.

The slot L2 extends from an off-center position along the baseline slot, (L1), towards the radiating top edge of the antenna (SPA2). Additional perturbations occur in SPA3, SPA4, SPA5 and SPA6 which are comprised of narrower and shorter slotlines labelled L3, L4 and L5 respectively all of which are also orthogonal to the baseline slot. L4 and L5 are of equal width but different lengths. Through selective excitation of modes, C1 has the potential to enhance the sensitivity of field polarisation beyond the limit set by the design in SPA5. The corresponding improvement in the tag detectability is demonstrated using read range measurement of sub-section 4.5. Each of the SPAs was excited by an off-center gap-feed which was modelled as a discrete port with characteristic impedance of

50 Ω. For a practical realisation of a tag, the transponder ASIC will be used to replace the feed. The simulation was carried out with CST Microwave Studio.

4.3.1 A theoretical investigation of the surface current distribution around the SPA antenna

The enclosing length of an antenna has series of resonance effects. There also will be resonances relating to the length of each radiating elements when embedded in such antenna. Correspondingly there is a surface current going around the antenna perimeter. Part of the radiation that goes into space depends on the surface current distribution on the antenna. The surface current magnitudes around the perimeter of the SPA antenna at the lower and upper resonant frequencies are shown in Figs. 4.6 and Fig. 4.7 respectively. The perimeter refers to the entire antenna distance (moving anti-clockwise) A-B-C-D-A as shown in the right hand corner of the figures.

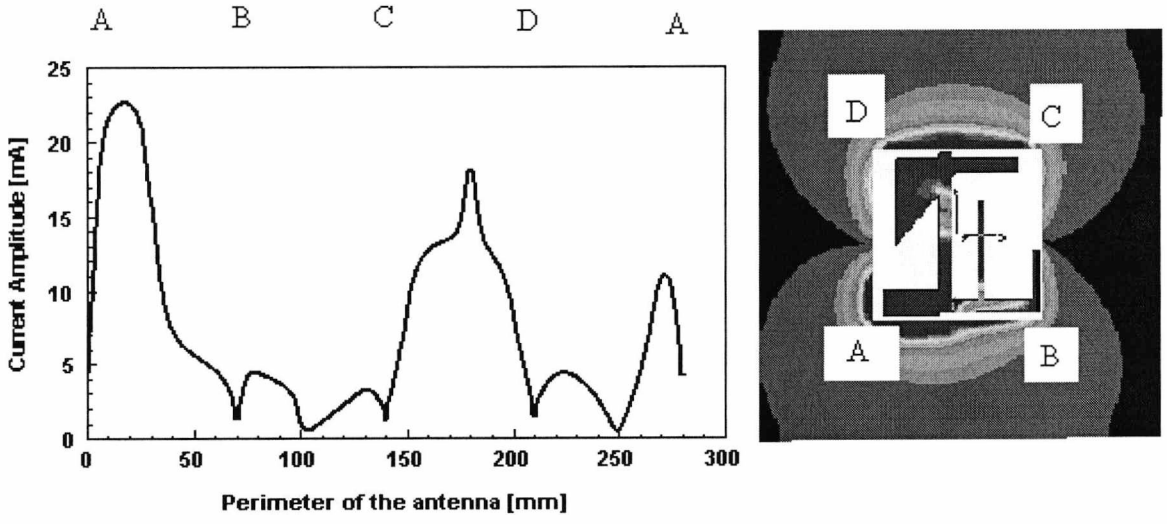

Fig. 4.6: Graph of surface current distribution at 869 MHz along the lengths of all the slot patch antenna sides. The current distribution is visualised in CST as shown on the right hand side.

In Fig. 4.7, the current amplitudes exhibit a sinusoidal variation with zero currents at the end of the each curve. The peak of the current amplitude was located at an approximate distance of 17.25 mm followed at 179.4 mm. The lowest current amplitude was located at a distance approximately 131 mm from point A (moving anti-clockwise). The largest current amplitudes, with one-half period each correspond to the bottom (labelled A – B) and top (C – D), that is, y = z = 0, x = 0 to 70 and x = 0 to 70, y = 70, z = 0. On the other hand, those at the side walls of antenna at the left and right sides at x = y = 0, y = 0 -70 and x = 70, y = 0 to 70, z = 0, have two half-cycles each with relatively low field amplitudes.

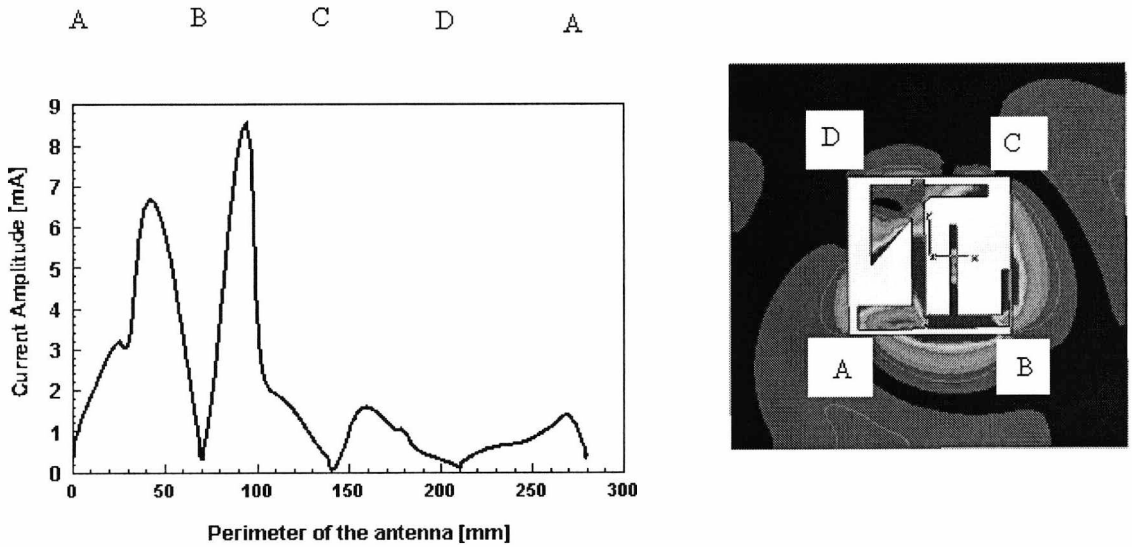

FIG. 4.7: Graph of surface current distribution at 2.45 GHz along the lengths of all the slot patch antenna sides. The current distribution is visualised in CST as shown on the right hand side.

The surface current distribution for the upper band (2.45 GHz) is shown in Fig. 4.7. Clearly, the peak current amplitude occurs at approximate distance of 96 mm followed at 41.4 mm while the lowest was at 255 mm. Although the field distribution at each of the four sides is one-half waveform, the largest current amplitudes occurs at the bottom (labelled A – B) and right side (B – C) corresponding to x = 70, y = 0 to 70, z = 0 and y =

$z = 0$, $x = 0$ to 70. The least current amplitude is observed at the top and the left side corresponding to $x = 0 - 70$, $y = 70$, $z = 0$ and $x = z = 0$, $y = 0$ -70.
From the comparison between Fig. 4.6 and Fig. 4.7, all of the simulated current values were consistently higher in the lower resonant frequency that those obtained at the upper resonant frequency.

The specific distribution of this current is of great importance in determining the location of the ASIC chip. In order to enable an ASIC chip absorb sufficient energy from its antenna to backscatter, the chip should be located near enough to a point of high current amplitude at the frequency of operation. In this particular case the chip was located at a point along the side labelled A-B in Fig 4.6. It should be noted that any conclusion drawn do not rely on any absolute values that were obtained, only on trends within the data.

4.3.2 Dual band SPA tuning: parametric study

The SPA consists of the main slotline L1 and four tuning elements L2, L3, L4 and L5 as shown in Fig 4.5. The stubs are resonate slots and mutual coupling exists between them. This results in the current distribution of one cavity influencing that of the adjacent stub. To elucidate this phenomenon, numeric simulations were performed in which the S_{11}-parameter was analysed as a function of the length of the individual elements. Fig. 4.8 compares the S_{11}-parameters and shows a progressive and systematic variation in the parameters being studied. Thus, the behaviour of each resonant mode can easily be associated with a particular element.

The effect of each tuning cavity on mode frequencies is identified (Fig 4.6 a – e) in the S_{11}-parameter curve in accordance with frequency response to the element tuning dimension. In Fig 4.8 (a), a variation of the L2 length, denoted by l_2, beyond 6 cm produced a second mode at 1.2 GHz; the lowest S_{11} was realised when l_2 became 60 mm long.
The length of L3 in design 4 can be used to vary the first resonant mode. A decrease from 1.12 GHz to 833 MHz is observed as the separation distance between L3 and the base

line slot L1, denoted by $\delta L3$, increases from 56 mm to 60 mm. The optimal height of 56 mm was however chosen in order to make allowance for the inclusion of an additional polarisation enhancement cavity denoted by C_1 in Fig. 4.4. The influence of L3 can further be demonstrated in terms of its length, L3 as shown in Fig. 4.8 (*c*). Here the best match at 820 MHz was realised when L3 is 50 mm wide. Thus L3 of 50 mm was chosen which was at a height of 56.6 mm above L1.

The introduction of L4 in SPA4 causes a third mode as shown in S_{11} Fig. 4.8 (d) to occur which is located between the lower and upper band to appear. Its impact is also felt in the upper mode where the existing mode at 3.12 GHz is divided into two modes at 3.12 GHz and 3.56 GHz. The optimal dimensions were obtained when L4 was 17.5 mm long.
It is observed in Fig. 4.8(e) that the return loss curve vary substantially at the upper bands when the length of L5 (introduced in design 6) is increased between 9 mm and 37.5 mm which corresponds to frequency drop from 3.12 GHz to 1.58 GHz. However, the above variation produced no discernible effect on the resonant frequency for the lower band. Table 4.3 summaries the initial parameter values for the antenna parameters where two resonant modes at 869 MHz and 2.45 GHz were achieved.

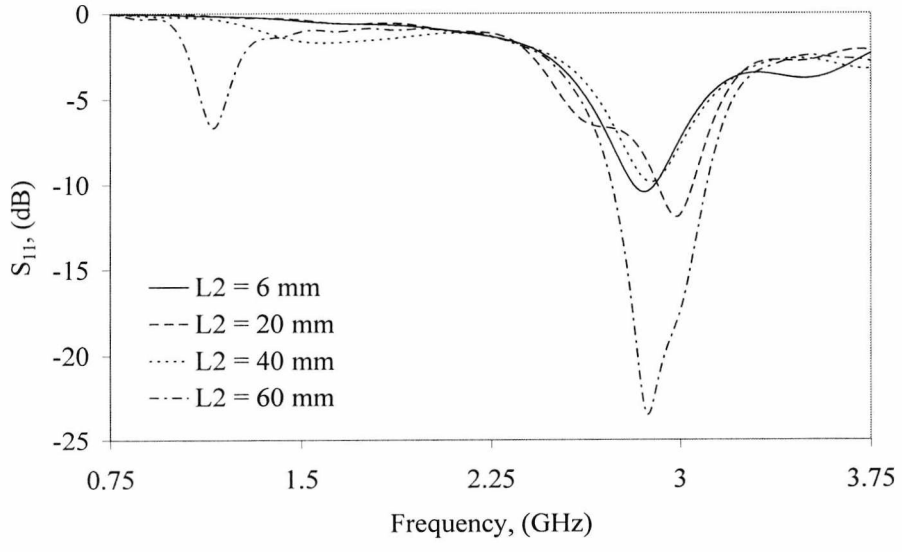

Fig 4.8 (a): The effect on S_{11} due to L2 for the design 3 of Fig. 4.5

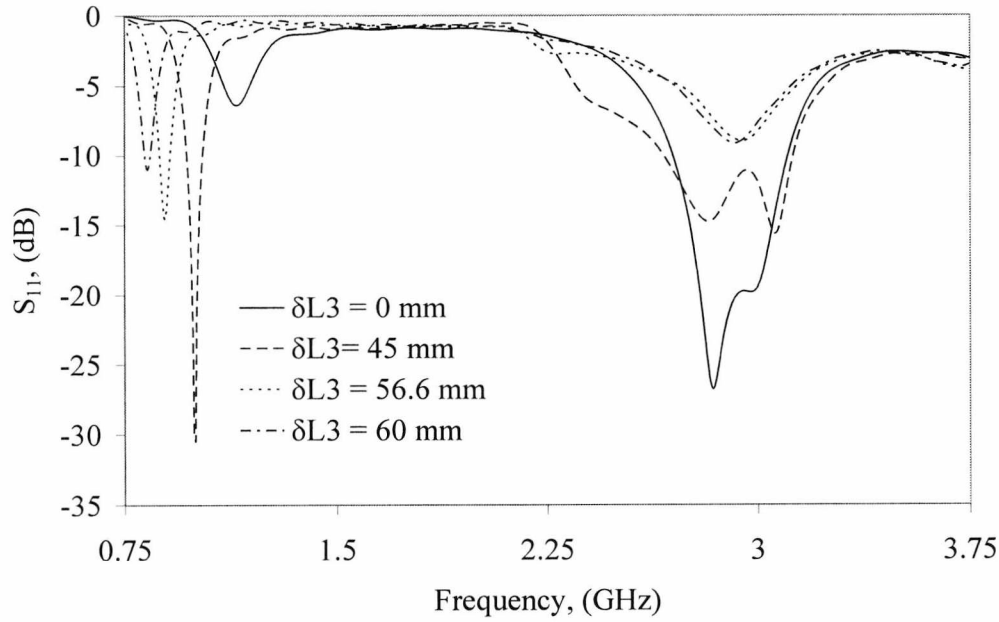

Fig 4.8 (b): The effect on S_{11} due the length of L3 for the design 4 of Fig. 4.5 , where *δL3* represents the separation distance between L3 and the base line slot L1.

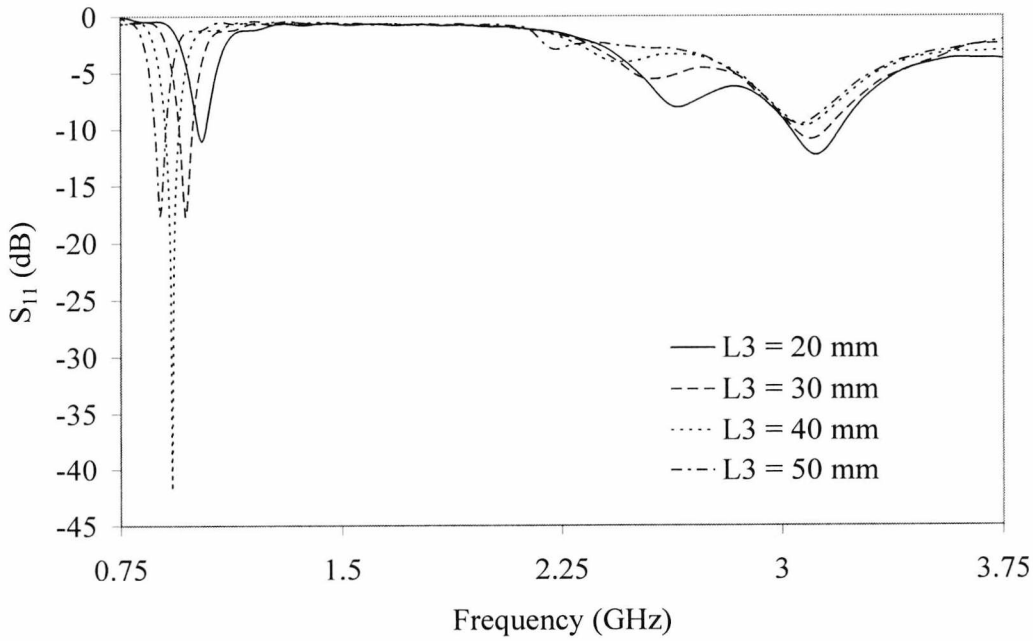

Fig 4.8 (c): The effect on S_{11} due to the width of L3 for the design 4 of Fig. 4.5.

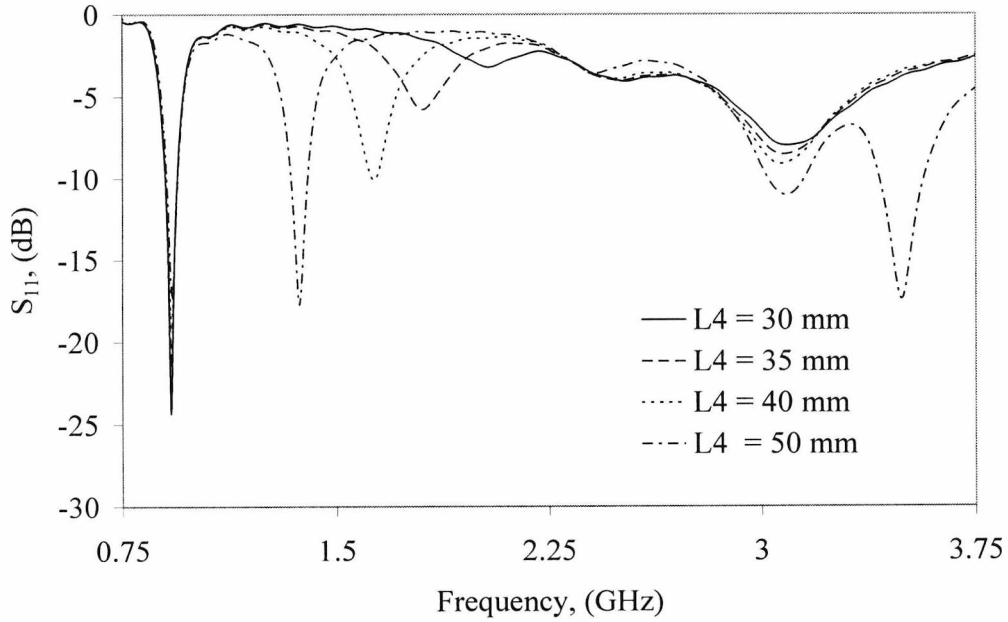

Fig 4.8 (d): The effect on S_{11} due L4 for the SPA4 of Fig. 4.5.

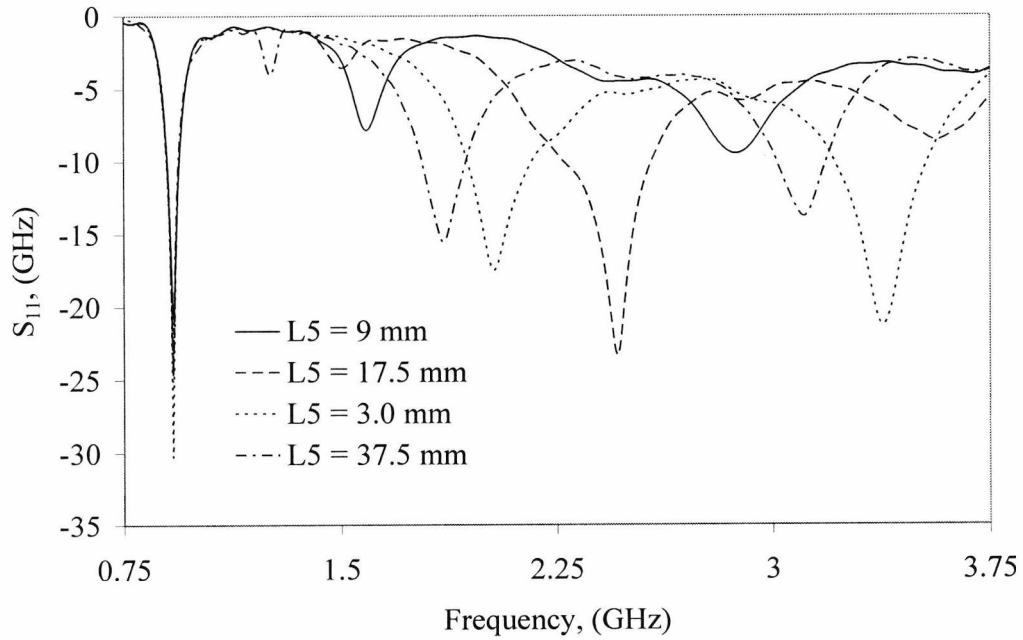

Fig 4.8 (e): The effect on S_{11} due to L5 changing for the SPA5 of Fig. 4.5.

Parameter	Definition	Value	Parameter	Definition	Value
a	Length of patch	70 mm	b	Width of patch	70 mm
ℓ_1, (w_1)	Length and width of the element, L1	64.4, (5.2) (10.4)	t	PEC thickness	0.007
ℓ_2, (w_2)	Length and width of the element L2	60, (5.4)	h	substrate thickness	0.8 mm
ℓ_3, (w_3)	Length and width of the element L3	50, (5.2)	S	Feed gap	2 mm
ℓ_4, (w_4)	Length and width Vertical element L4	40, (2.7)	ε_r	Relative permittivity	4.9
ℓ_5, (w_5)	Length and width Vertical element L5	20, (2.7)	$tan\ \delta$	Loss tangent	0.025

Table 4. 3: Initial design parameters values for the SPA based on the parametric study of the tuning elements.

After embedding the entire slot in the patch, it became apparent that keeping the length of the left arm of L1 constant, a tuneable frequency range between 860 MHz and 1.1 GHz (representing an increase by 26 %) for the first band can be achieved by decreasing the length of right arm of L1 from 58 mm to near the fed point (23 mm). The decrease results in an increase in the patch size to maintain the same centre frequency. However, when the L1 is increased beyond 58 mm, the centre frequency of the lower band drop by approximately 1 %; when L1 becomes 62 mm the steady state energy criterion of the time domain simulator becomes difficult to achieve causing a sharp frequency drop to 477 MHz.

The tuneable capacity of the first band is necessary to offset possible variations when an ASIC transponder is eventually integrated. It can equally offset variations that might arise due to the effect of a particular mounting surface. This type of variation in antenna self-

resonance and tag resonance is common in RFID and has been extensively covered in [4.10]. The upper band remains predominantly the same irrespective of the variations in the dimensions of L1 but it covers a relatively large bandwidth of about 470.78 MHz.

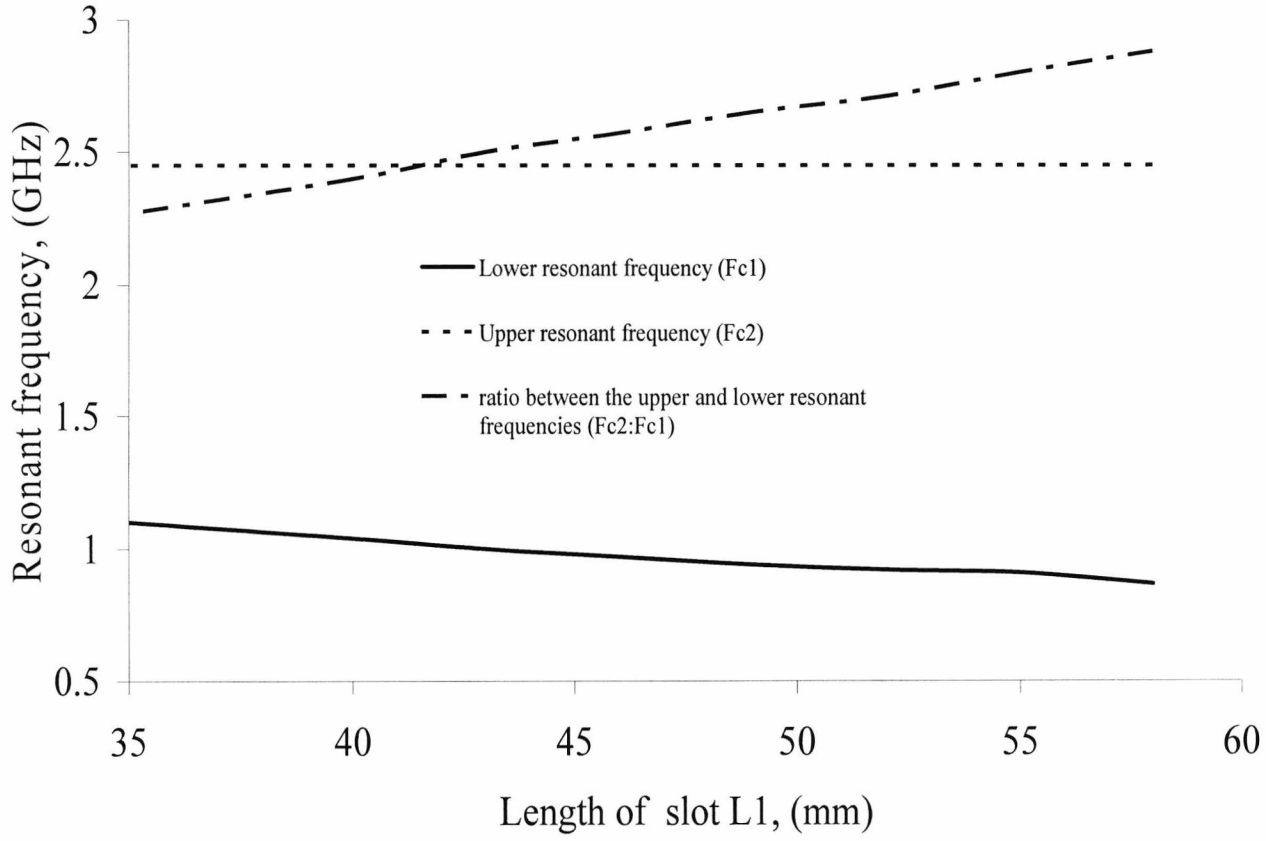

Fig. 4.9: Simulated results showing the characteristics of the lower and upper resonant frequencies as a function of L1 of the dual-band slot patch antenna encountered in Fig. 4.4.

Fig. 4.9 shows how the simulated frequency ratios of the upper and lower bands of the slot antenna vary with the length of L1 the cavity. It can be seen that by decreasing the length of L1 from 35 mm to 6o mm, the ratio of the upper resonant frequency to the lower (represented as Fc1.Fc2) also decreases from 2.88 to 2.27. The frequency ratio can thus be tuned continuously by this variation.

4.3.3 The effect of frequency scaling of the SPA

To design tags at higher frequencies a scaling of the metal pattern was implemented on the same substrate as the original designs. This technique also increases the option of applying the SPA design to different sized objects to be tagged.

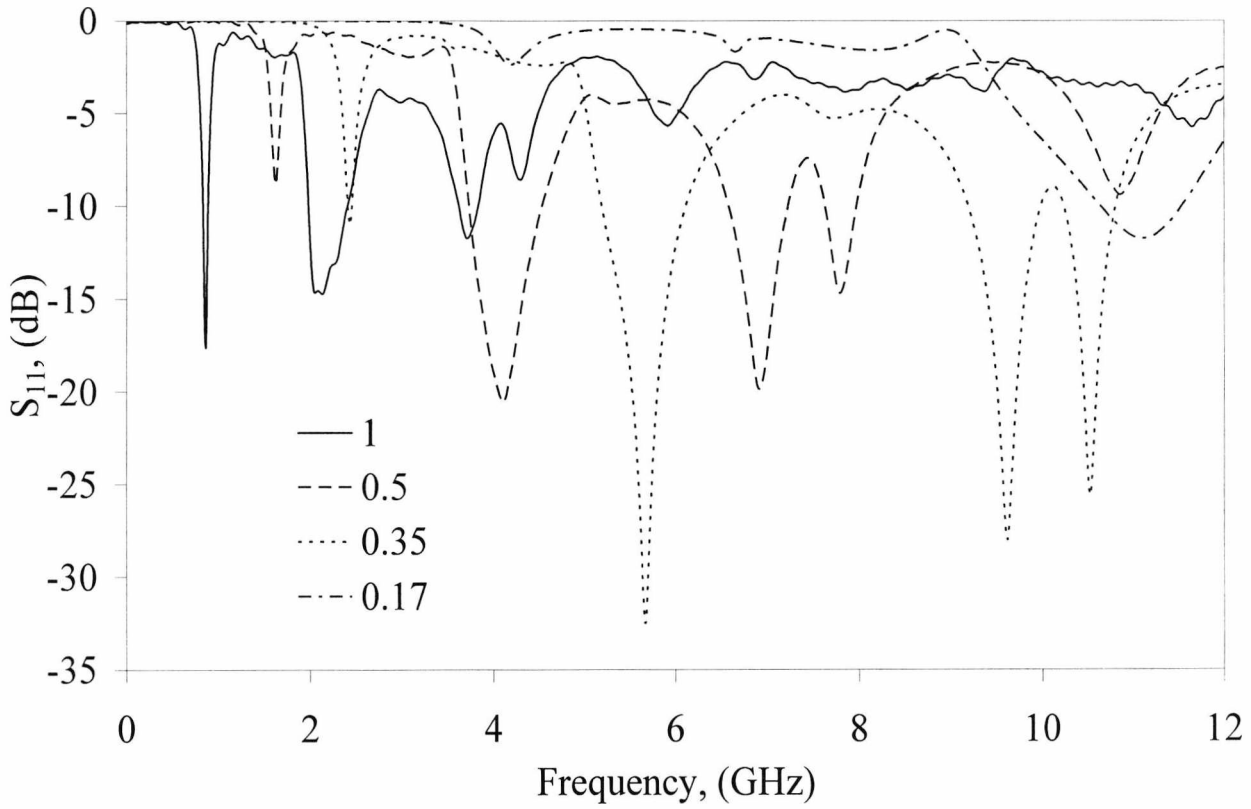

Fig 4.10 – Simulated return losses for different frequency-scaled versions of the SPA; full scale is represented by 1 with dimensioned 70 mm × 70 mm; 0.5 dimensions 35 mm× 35 mm; 0.35 dimensioned 24 mm × 24 mm and 0.17 dimensioned 12 mm × 1.2 mm.

Fig 4.10 compares the return losses for various sizes of the miniaturised versions. The result adequately represents what should be expected when the length of an antenna is reduced since the resonant frequency is proportional to the reciprocal of the antenna

length (i.e. *resonant frequency* $\propto L^{-1}$) [4.7], [4.11]. It can be seen that only the one scaled down by a factor of 0.35 shows significant potential for application at the proposed RFID frequencies of 2.45 GHz and 5.8 GHz. This particular size 24 mm × 24 mm has therefore been chosen for fabrication alongside the full-scaled size 70 mm × 70 mm.

Fig. 4.11 shows the relationship between the bandwidth and the miniature SPAs. A common trend can be seen in the frequency behaviours at the two excited frequencies as the antenna scales down. In fact the frequency gap between the two excited modes remains predominantly the same across the different scales. It should be noted that the slots close at small scale (i.e. becomes narrow) which leads to low impedance.

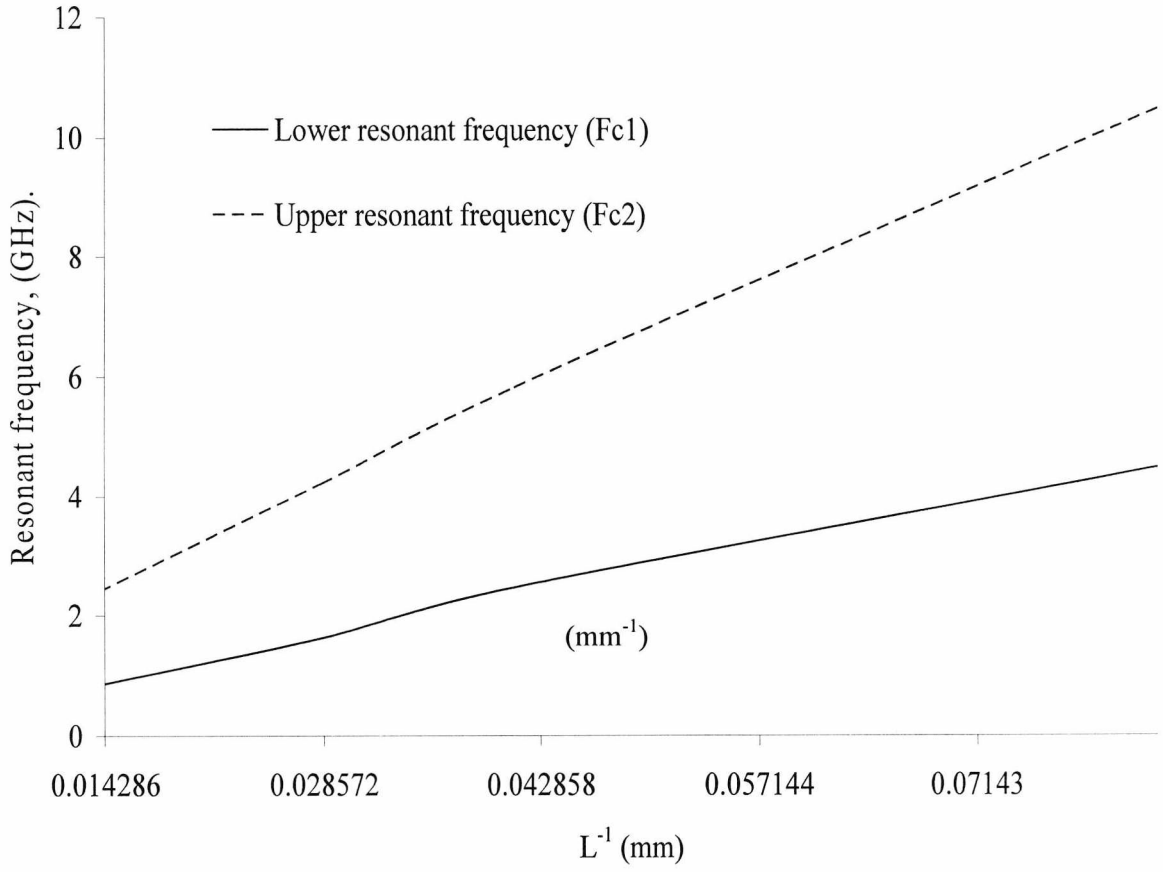

Fig. 4.11: Variation of centre frequencies as a function of the reciprocal of the length of different scaled down slotted patch antenna shown in Fig. 4.4; Fc1 and Fc2 are the centre frequencies for the lower and upper frequency bands.

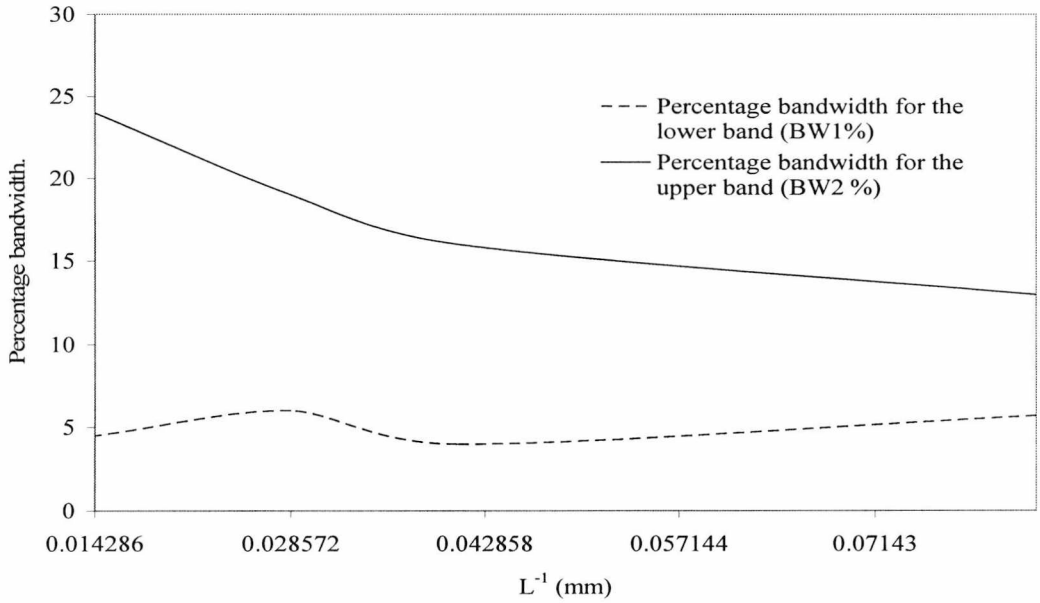

Fig 4.12. The variation of bandwidth as a fun (mm^{-1}) e reciprocal of the length of different scaled down slotted patch antenna shown in Fig. 4.4.

In Fig 4.12 the variation of bandwidths as a function of the various scaled down sizes is shown. The first and second bandwidth are designated in percentages as BW1 (%) and BW2 (%) respectively. From the results above, it is safe to conclude that while the bandwidth of the first band is slightly increasing with decreasing scale factors, the second is decreasing faster with the same decreasing scale factor. In effect the gap between the bands decreases in direct proportion to the antenna scale factor.

4.3.4 Summary of tuning element optimisation and frequency scaling of the novel SPA.

It can be concluded from the above analysis that dual band tuning was realisable with the contributions of every slot but L1. Introducing an orthogonal slot to an existing horizontal one can cause a frequency drop in the lower band. This is because slot L2 which is larger than the straight one L1 has been created. Besides, exciting higher order modes, the use of multiple slots allows the tuning of frequency ratios and at the same time significantly reduces the antenna size by 60 % compared to the magnetic dipole size in Chapter 3.

The possibility of applying the antenna design to other RFID frequencies has also been investigated. It was found that by reducing the size of the SPA by a factor of 0.35, dual frequency operation can be achieved at 2.45 GHz and 5.8 GHz.

4.3.5 The effect of substrate on the antenna performance

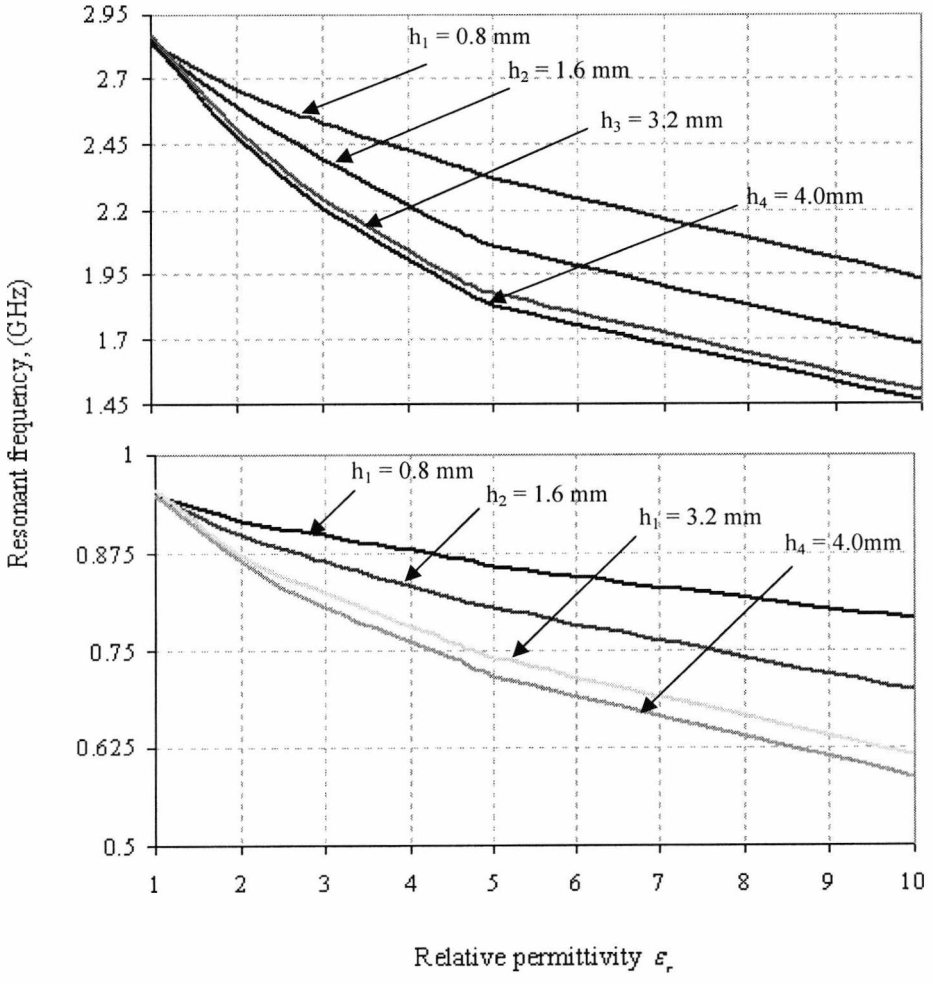

Fig 4.13: The Effect of substrate permittivity and on the frequency behaviour of the SPA with dimension $a = b = 70$ mm, $h = 0.8$ mm *and* $\varepsilon_r = 4.6$ for different slot widths.

This section is concerned with the effect of dielectric substrate on the frequency characteristics of the SPA. Fig 4.13 shows the numerically investigated results. As expected, the resonant frequency decreases with increasing value of the relative permittivity and, it decreases even faster for a thicker substrate. It is apparent that increasing substrate thickness tends to excite other surface wave modes thereby creating additional resonances. For example, a third resonance appeared when the substrate height was increased to 3.2 mm and even becomes very prominent when the dielectric constant, ε_r was 5.

4.3.6 The effect of slot width

In order to achieve a comprehensive study of the effects of substrates on the frequency characteristics, the SPA was modelled with different slot widths ranging from 3.2 mm cm to 10.2 mm and on two different dielectric substrates with a constant thickness (0.8 mm). The dielectric constant, ε_r of one substrate (designated Substrate 1) was 4.6 while the other, designated Substrate 2 has dielectric constant, ε_r of 10.6. A reference frequency of 869 MHz was used which corresponds to one the EPC global approved RFID frequencies in Europe.

Fig. 4.14 shows that the antenna size decreases faster for increasing slot width in the case of a lower permittivity substrate than a higher one. It is observed that for a given the frequency of the antenna designed on substrate 1 changes faster than that designed on substrate 2 using the SPA antenna size of in Table 4.2.

This implies that the second substrate is varying more slowly. Quantitatively, the SPA designed on substrate 1 has an overall percentage variation of 29 % whereas that for substrate 2 is 13 %. For the cases when both antennas had the same slot widths of 3.2 mm, 6.3 mm and 10.6 mm, the permittivity ratio were 1.7, 1.5 and 1.4 respectively. The comparison shows that the ratio decreases with increasing permittivity. In terms of the antenna size, it can be assumed that for a slot width of 3.2 mm, the antenna size, if

constructed on substrate 2 (ε_r = 10.6) is 36 % smaller than if constructed on dielectric substrate 1 (ε_r = 4.6).

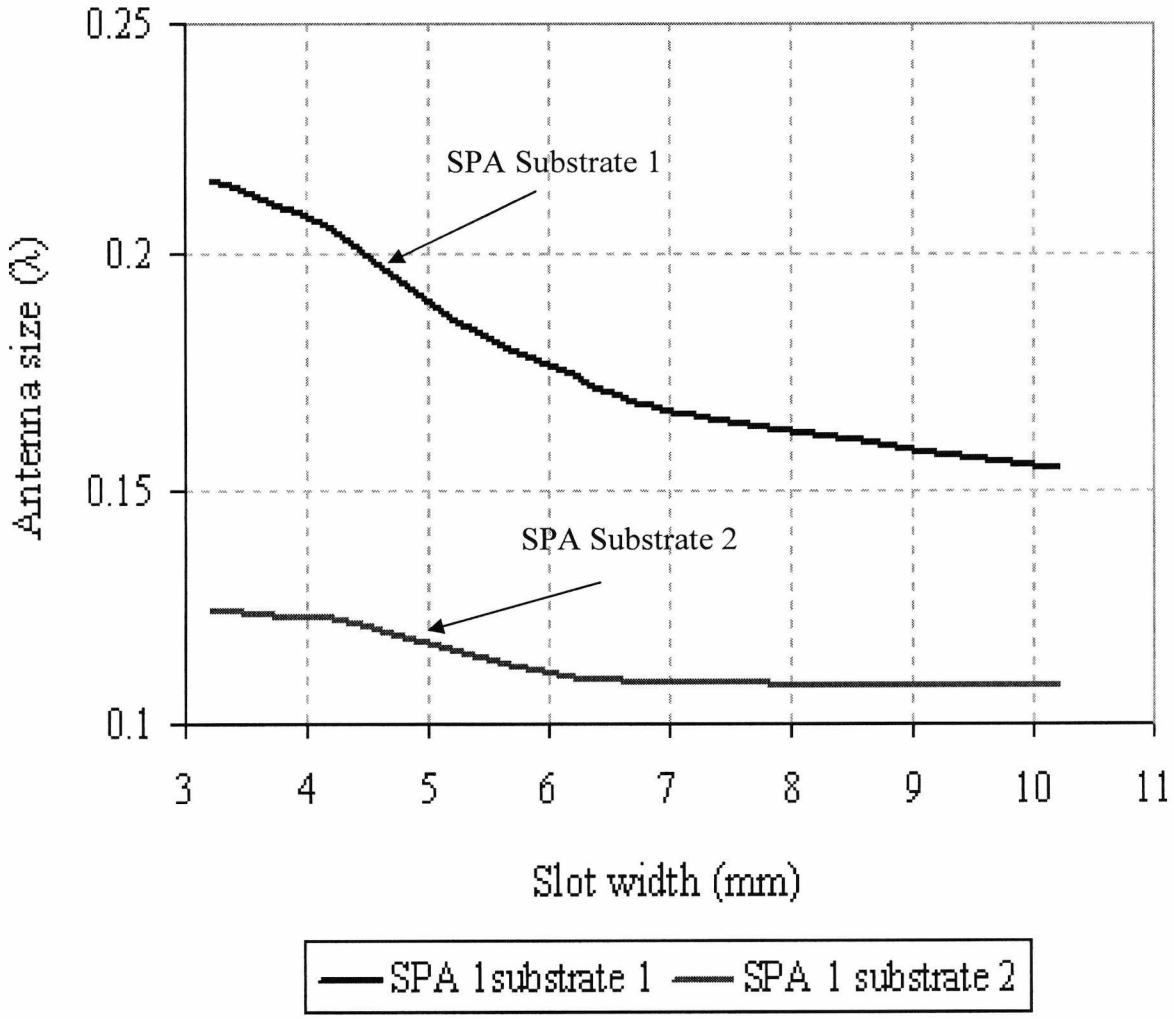

Fig. 4.14: Comparison of the electrical antenna sizes versus the slot width of the unperturbed slot patch antenna (SPA 1).

When the slot width was 5.2 mm, the size of the antenna fabricated on dielectric 1 was 62 % bigger than that which was fabricated on dielectric substrate 2. Furthermore, consider the case when the slot width is 10.2 mm, the antenna fabricated on dielectric substrate 1

is 59 % larger than that fabricated on dielectric substrate 2. This implies that given the same slot width, the difference in size becomes smaller as the slot width increases.

4.3.7 Summary of the effects of dielectric substrate and slot width

In the above parametric study, two SPAs modelled on two different dielectric substrates have been analysed in terms of size, and dielectric substrate height. The width of the slot, L1 has been varied from 2. 5 mm to 41.6 mm and the substrate thickness varied from 0.8 mm to 4 mm. The antenna size depended on the dielectric constant, the baseline slot width and the height. A broader slot width or a lower substrate permittivity decreases the antenna size.

It should be noted that an increase in the antenna size also increases the radiation surface (and hence bandwidth) of the antenna which decreases the antenna quality factor [4.12]. This results in larger impedance bandwidth and lower losses. For this reason, a smaller antenna will have a performance worse than a large antenna in terms of read range. In comparison with a thinner substrate, thicker substrates operating frequency decreases faster. For a given substrate relative permittivity, high value of substrate thickness implies low frequency.

4.4 Experimental validation of the theory

The parametric studies of the preceding sections elucidated the general characteristics of different perturbed slot patch antennas (SPA). The influence of dielectric substrate on antenna form factor and performance has also been examined. In this section, the S_{11}-parameter results of a hardware prototype of the full scale SPAs are presented and compared with the numeric results as shown in Fig. 4.15. It can be seen that the lower frequency band exhibits an inherently narrow bandwidth of 13.56 MHz.

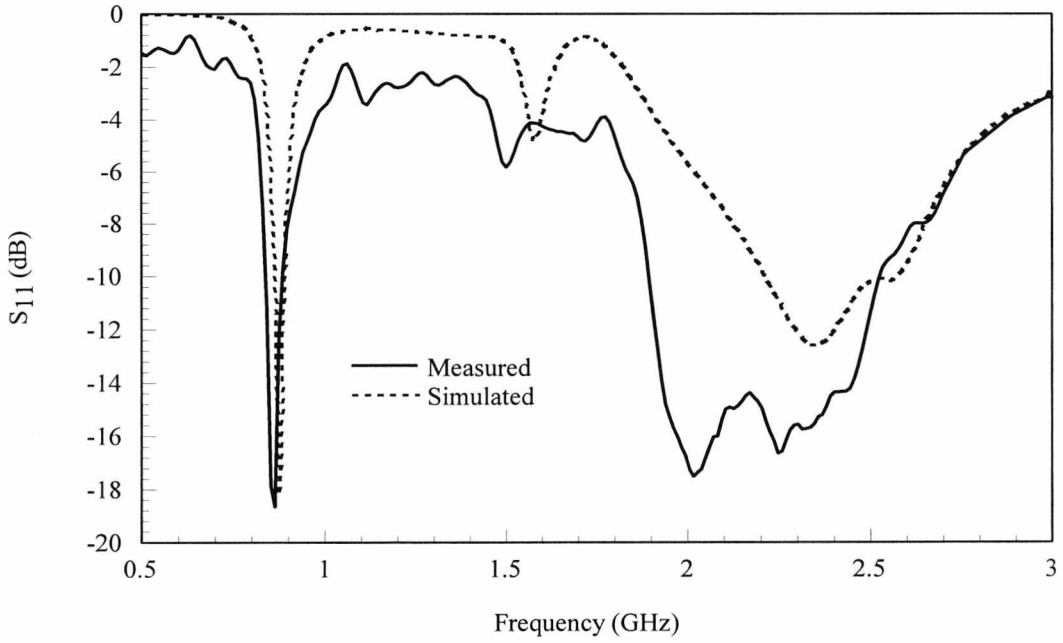

Fig. 4.15 Simulated and measured return loss for the slot patch antenna in Fig. 4.5 after optimisation; $a = b = 70$ mm $\varepsilon_r = 4.6$, $h = 0.8$ mm.

The lower band is narrow because it is determined by the longest current path across the structure. Additionally, at low frequencies the structure is mainly capacitive (low inductance) so the bandwidth is low. It is important to note that the relatively large bandwidth at the upper frequency makes this antenna a good candidate for use in conjunction with other ISM applications. There is a close agreement between the simulated and measured results especially in the first band. However, the small difference between simulation and measured responses was probably because substrate losses were not included in simulation. It might as well have resulted from fabrication process (for example, during the photo-etching process).

The return loss for the 0.35 scale SPA is shown in Fig. 4.16. The antenna exhibit dual band characteristics at the centre frequencies of 2.45 GHz and 5.8 GHz respectively making it useful for the 2.45 GHz and 5.8 GHz RFID tags. The most likely reasons for

the discrepancies in the simulation and measured responses have been outlined for the case of full scale SPA.

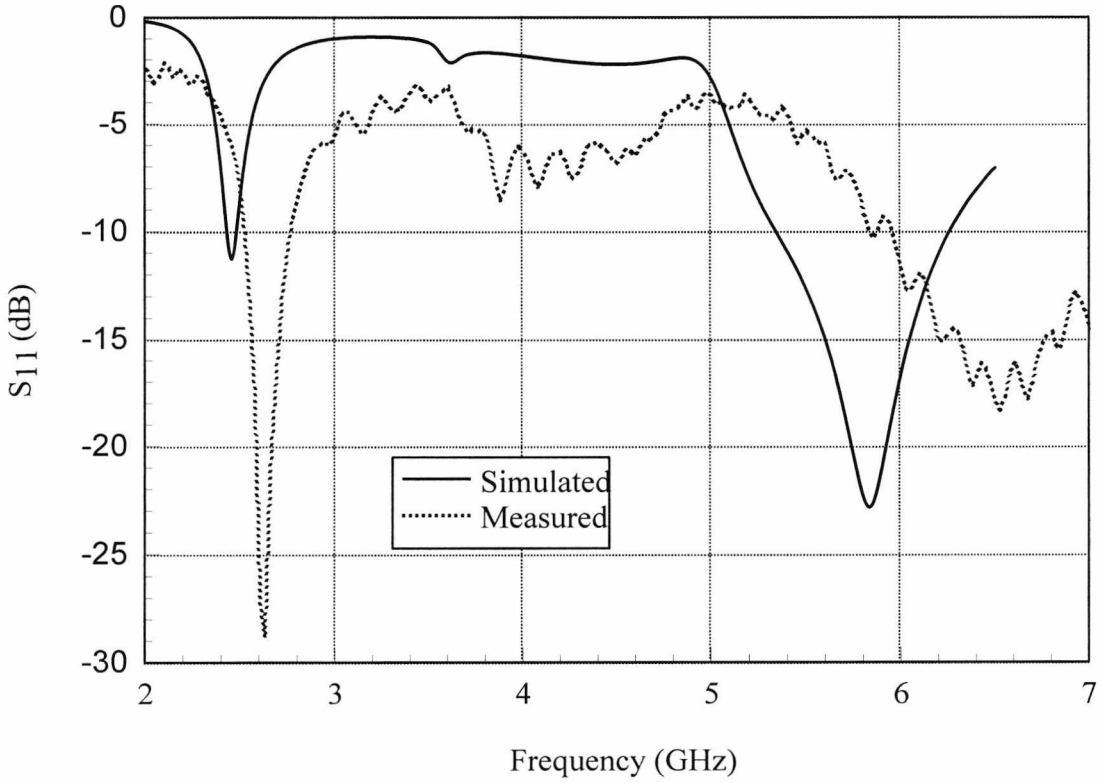

Fig. 4.16 Simulated and measured return loss for the slot patch antenna; slot antenna scaled down by a factor of 0.35; $a = b = 24.5$ mm, FR-4 substrate $\varepsilon_r = 4.6$, $h = 0.8$ mm.

4.4.1 The experimental radiation characteristics

Firstly, in order to visualise the radiation pattern, the geometry and coordinates of the antenna are shown in Fig. 4.17. The SPA radiates in both direction – above and below the substrate – and therefore two main beams are observed. The mainbeam directions for all the resonant frequencies are shown in Fig. 4.18 for all the resonant frequencies of 869 MHz, 1.43 GHz and 2.45 GHz and also for the different planes. As would normally be expected, the two mainbeams are different owing to the truncation of the otherwise infinite perfect electric conductor in antenna measurement.

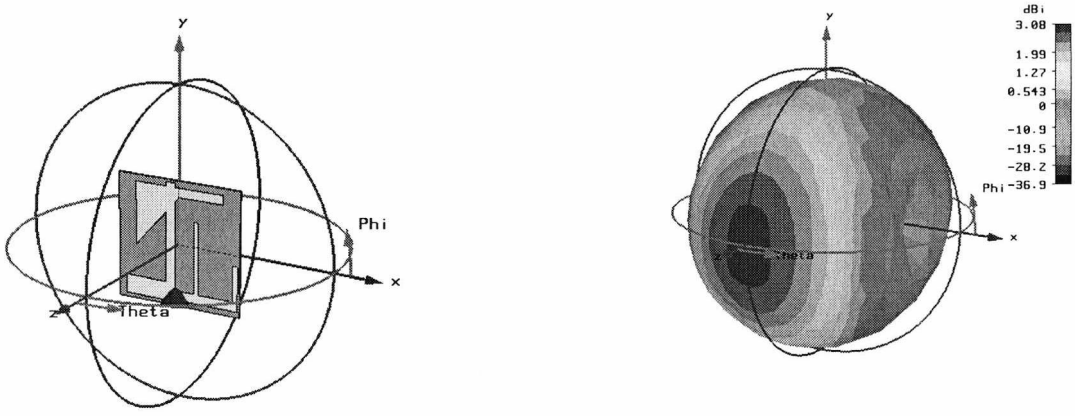

Fig 4.17: Geometry and coordinates for the measurement of the SPA radiation pattern.

It can be seen that in all the planes, there are nulls, which are associated with out of phase radiation from the edge of the slots elements. The antenna has the advantage of exhibiting very high cross-polarization characteristics. There is a deeper null at the upper resonant frequency in the $x - y$ plane at + 90° due to the oppositely directed magnetic current in one section of the slot. It can be seen that the modes have a similar broadside radiation pattern and polarisation plane. A cross polarisation level less than -15dB is also obtained. A gain of 3 dB was achieved.

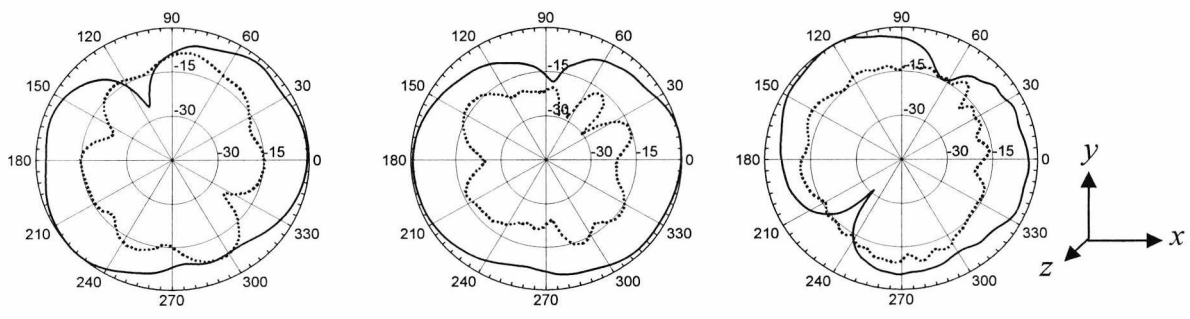

xy-plane 869 MHz *xy*-plane at 1430 MHz *xy*-plane 2450 MHz

(a)

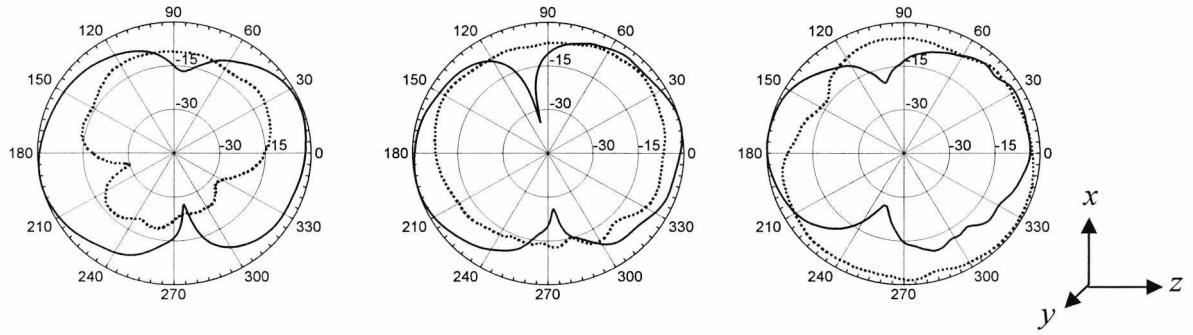

xz-plane at 869MHz *xz*-plane at 1430 MHz *xz*-plane at 2450 MHz

(b)

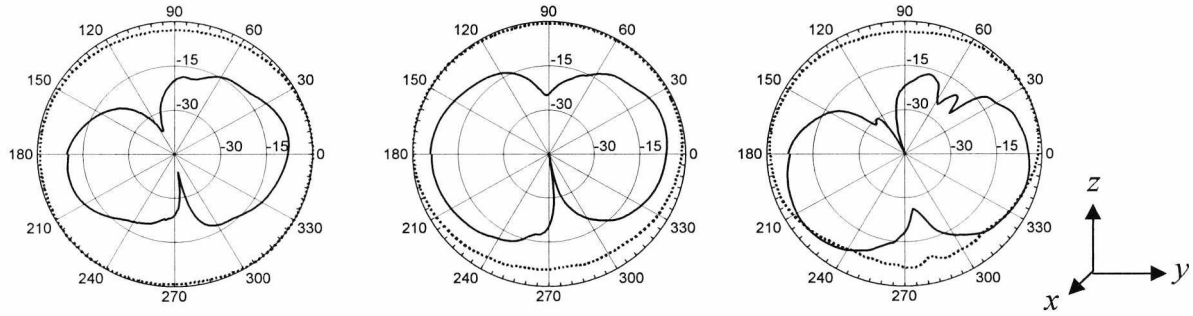

yz-plane at 869 MHz *yz*-plane at 1430 MHz *yz*-plane at 2450 MHz

Fig 4. 18: Measured radiation patterns for the SPA antenna with L1 = 56.6 mm.

4.4.2 The Effect of Field Polarisation on Received Power for the SPA

The polarisation of a tag antenna with respect to the reader antenna determines the amount of energy it receives. Simulation data on the effect of antenna orientations, under different load conditions, on the received power have been investigated. These were for the cases when the SPA antenna is illuminated by a plane wave whose E-field vectors were either polarised along the *x*-, *y*- or z– axis depending on the direction of propagation as exemplified in Fig. 4.19.

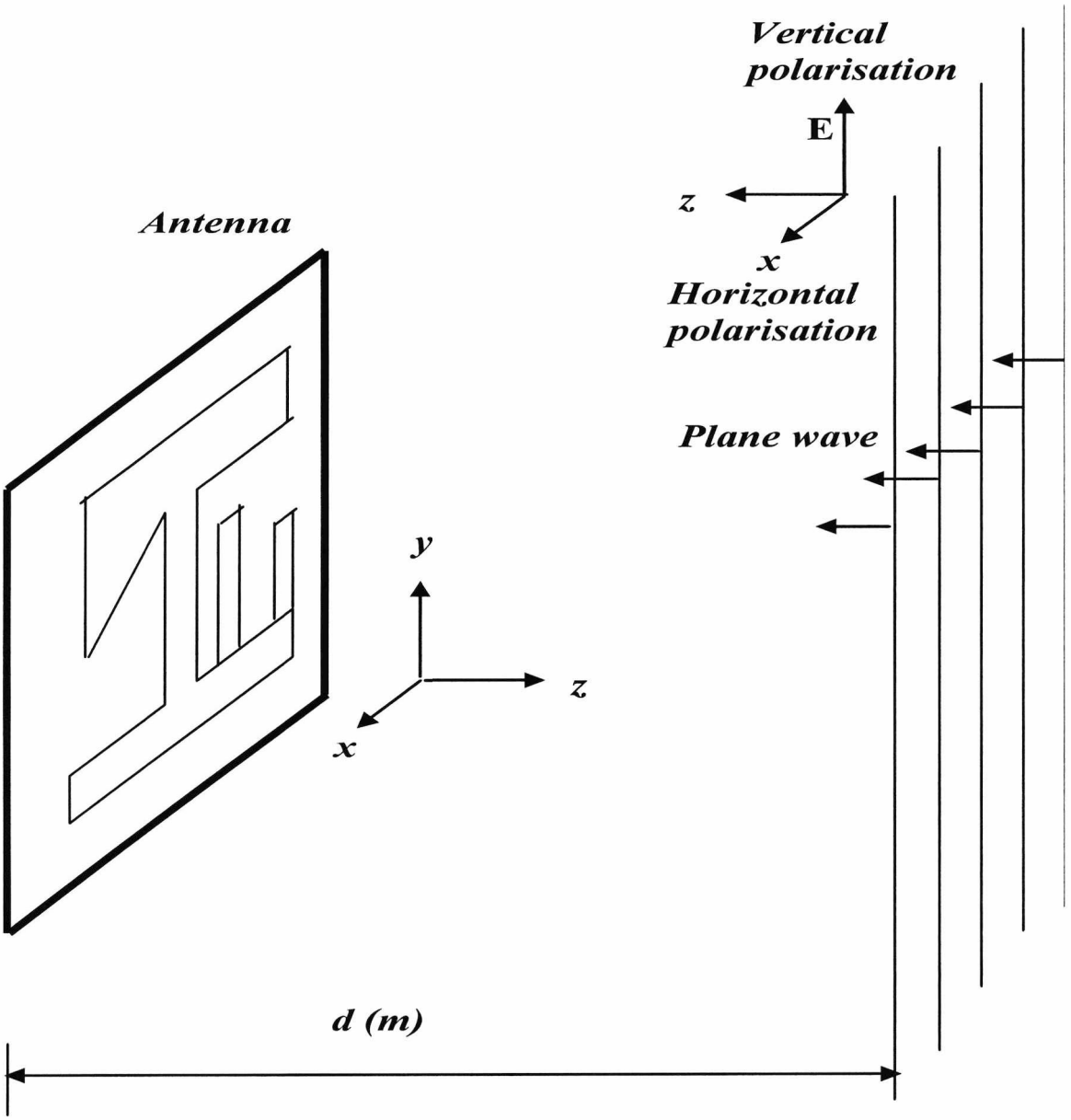

Fig. 4.19: Vertical polarised slot patch antenna encountered in Fig. 4.5.

A CST geometry file for a left hand circularly polarised plane wave hitting the antenna is shown in Fig. 4.20. The definition of the plane wave is visualized by a red plane. Coloured arrows indicate the propagation direction as well as the electric and magnetic field vectors. The electric field vector of a left hand circularly polarised plane wave is hitting the SPA antenna with a plane wave excited with an electric field vector in *z*-direction and a propagation normal (0,-1,0) at the frequency of 869 MHz.

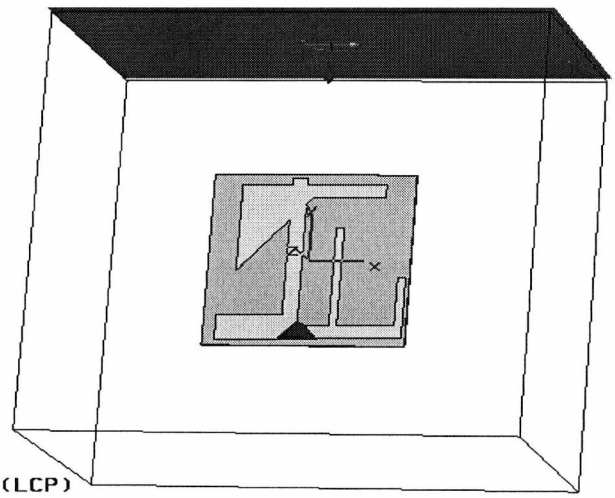

Fig. 4.20: A CST geometry file of the SPA antenna illuminated by a left hand circularly polarised plane wave.

The simulation RCS values obtained here are similar to the ones obtained for both the electric and magnetic dipoles in Chapter 3. The relationship between Decibels and square meter (dBsm) had been covered under the electric dipole case. The RCS value a circularly polarised wave is also studied. Results are summarised in the tables below. Table 4.4 shows that for a plane wave propagating along the z-axis (see Figs. 4.19 and 4.20). The RCS for the case when the electric field vectors are oriented along the x-axis is about 5.71 dB higher than the case when the electric field vectors are oriented along the y-axis for the open circuit load condition. For the short circuit, resistor load and IC-load cases, the RCS when the electric field vectors are oriented along the x-axis is larger than when it is oriented along the y-axis by 15.99 dB, 2 dB and 1.91 dB respectively.

Table 4.5 shows overall reduction in the RCS when the plane wave is propagating along to the x-axis and with the electric field vectors aligned parallel to the y-axis (i.e. cross-polarised) compared to the previous summarised result in Table 4.4. Table 4.6 is for the maximum RCS when the plane wave is propagating along the y-direction. In both Tables 4.5 and 4.6 the electric field vectors were cross-polarised hence the RCS are smaller than in the co-polarised state corresponding to plane wave propagating normal to z-direction.

Antenna load	**Maximum RCS (dBsm) along the z – direction**		
	x-axis field vector	y-axis field vector	circularly polarised field
Open circuit	-25.01	-30.72	-27.08
Short circuit	-9.33	-25.32	-12.45
Resistor loaded	-23.22	-25.22	-24.69
Transponder loaded	-24.9	-26.81	-25.98

Table 4.4: Simulated maximum RCS value for the SPA antenna shown in Fig .4.4 under different load conditions for the case when a plane wave is propagating normal to z-axis.

Antenna load	**Maximum RCS (dBsm) along the x – direction**		
	y-axis field vector	z-axis field vector	circularly polarised field
Open circuit	-26.36	-66.25	-29.34
Short circuit	-26.13	-66.39	-29.36
Resistor loaded	-26.39	-66.28	-29.18
Transponder loaded	-26.18	-66.15	-29.36

Table 4.5: Simulated maximum RCS value for the SPA antenna shown in Fig .4.4 under different load conditions for the case when a plane wave is propagating normal to x-axis.

Antenna load	**Maximum RCS [dBsm] along the y - direction**		
	x-axis field vector	z-axis field vector	circularly polarised field
Open circuit	-30.48	-64.14	-33.91
Short circuit	-12.04	-63.61	-15.44
Resistor loaded	-25.12	-63.87	-28.11
Transponder loaded	-27.83	-64.02	-31.11

Table 4.6: Simulated maximum RCS value for the SPA antenna shown in Fig .4.4 under different load conditions for the case when a plane wave is propagating normal to y-axis.

Compared with the maximum RCS value when the plane wave is linearly polarised (either vertical or horizontal) the tables shows that a circularly polarised wave is intermediate between the vertical and horizontal polarised results.

4.4.3 RCS Analysis of the SPA

The radar cross section (RCS) analysis is presented for different load conditions and gives knowledge of the degree of scattering inherent in the CPA antenna. The considered cases were for the open circuit, closed circuit, resistor load and IC load. The effects on the RCS magnitude of the substrate thickness and permittivity were also examined. Given that RFID tags receives EM energy to activate, it was considered more useful to carry out the RCS analysis under antenna receiving modes, hence a plane wave was used to illuminate the antenna.

Figure 4.21 (a) and (b) show the variation of the RCS for the slot patch antenna with substrate relative permittivity for different load conditions using ε_r = 4.9 and 0.8mm substrate thickness. In (a), for a given load, except for the resistive load, the RCS magnitude increases slowly as the substrate thickness increases. In the case of the open circuit load, the RCS decreases with increasing substrate thickness. The open circuit effect becomes less remarkable as the frequency increases to 2.45 GHz in (b). The magnitude of RCS under IC load tends to slightly decrease at 2.45 GHz. All other load conditions show a small increase with increasing substrate thickness.

Varying the substrate thickness alone changes the aggregate observed tag RCS at 2.45 GHz, relative to 869 MHz; for example, the open circuit and short circuit cases show a rise in the RCS beyond substrate thickness of 4 mm (Fig. 4.20). On the other hand, increasing the substrate relative permittivity beyond 3.2 mm will result in an aggregate RCS reduction of 49 % and 23 % for the resistor load and IC load conditions.

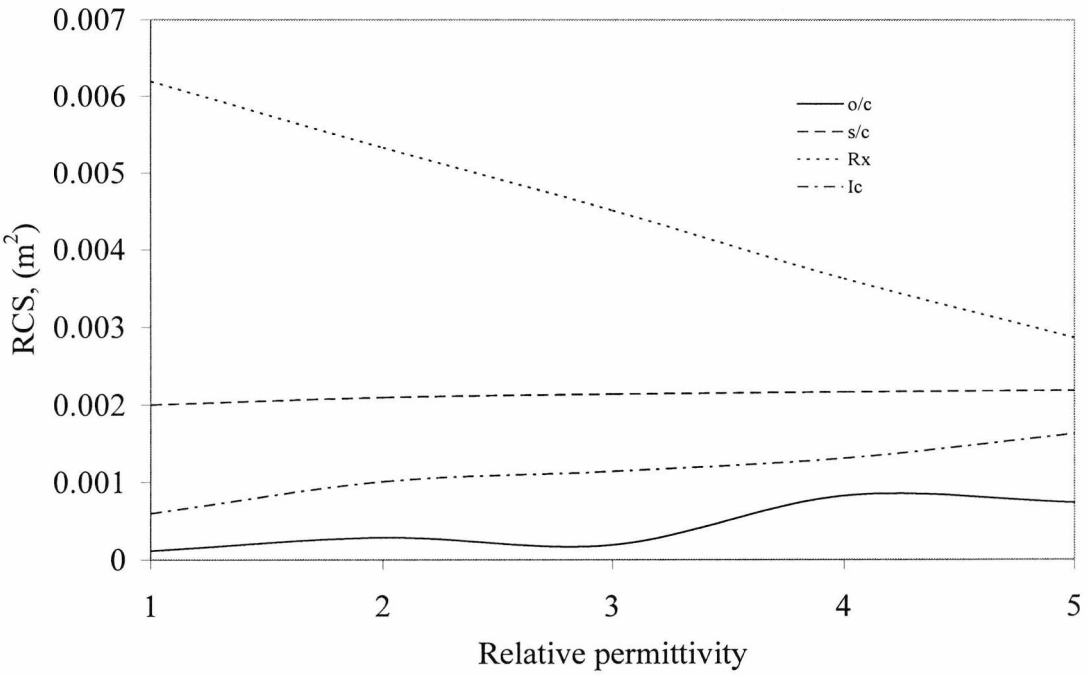

(a)

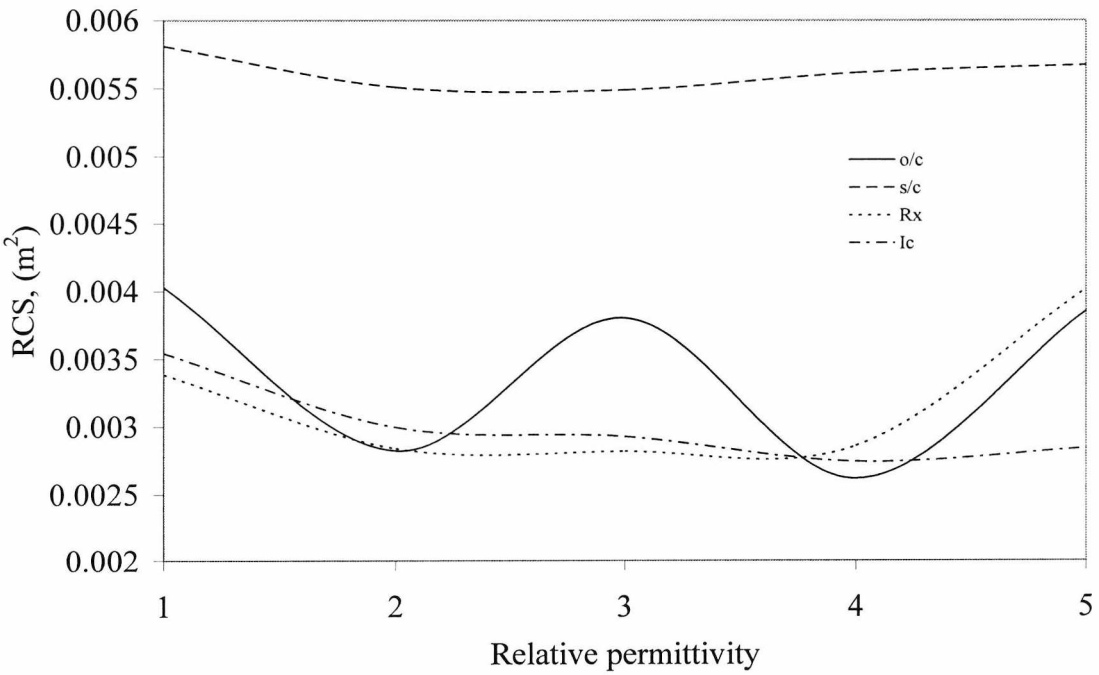

(b)

Fig. 4.21: Variation of the RCS for the slot patch antenna with substrate relative permittivity for different load conditions (a) 869 GHz and (b) 2.45 GHz.

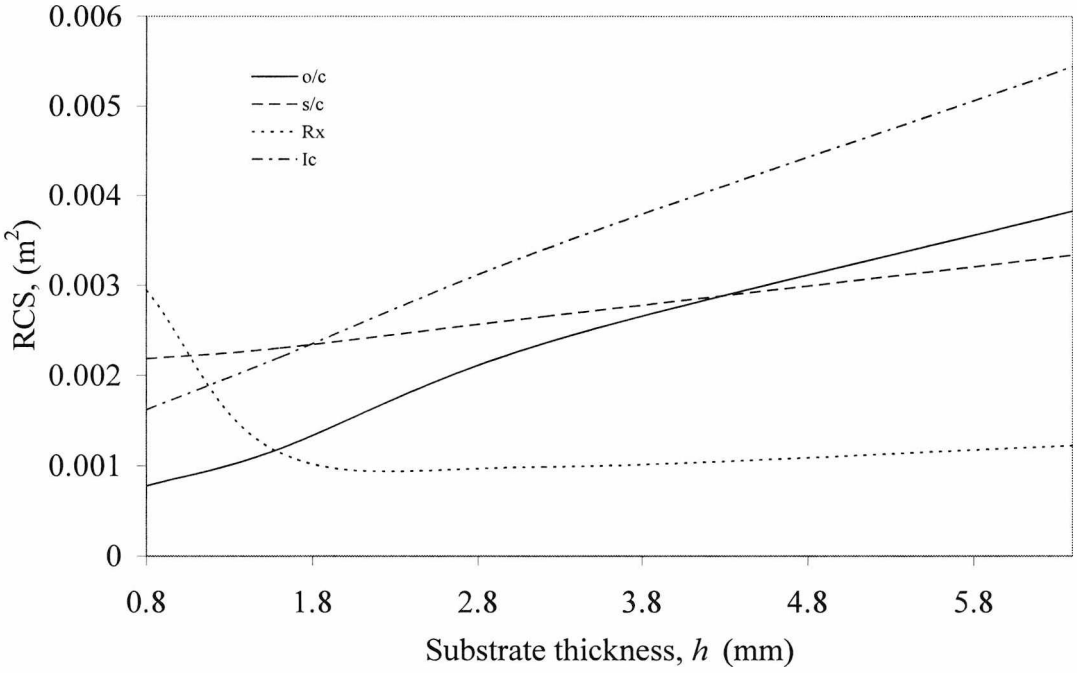

(a)

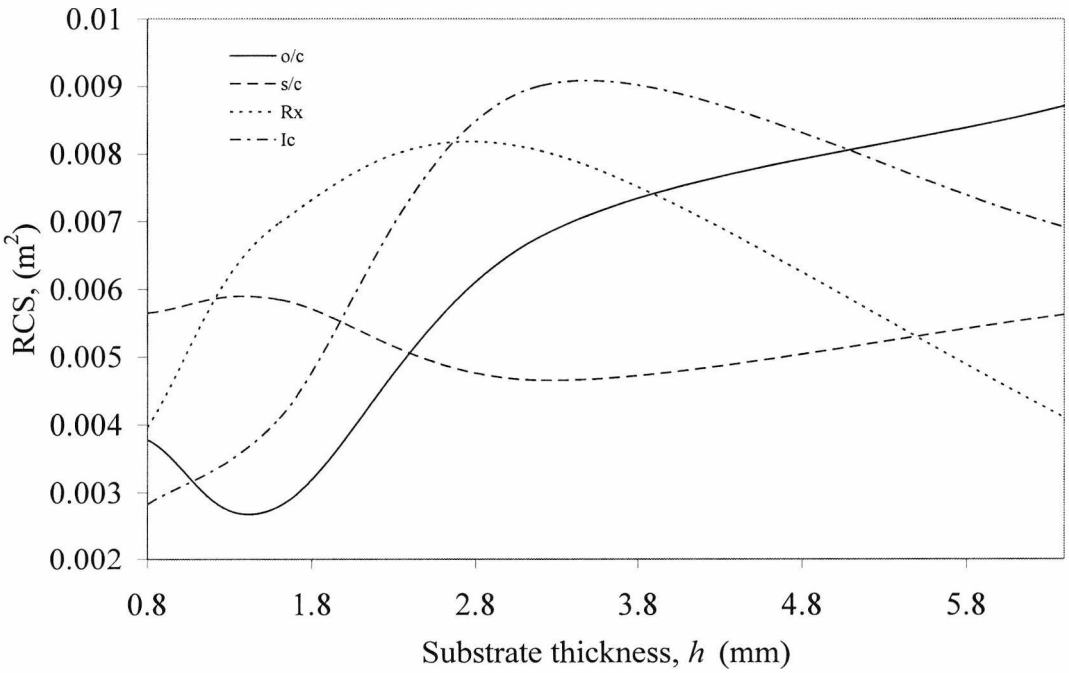

(b)

Fig. 4.22: Variation of the RCS for the slot patch antenna with substrate thickness for different load conditions at (a) 869 MHz and (b) 2.45 GHz

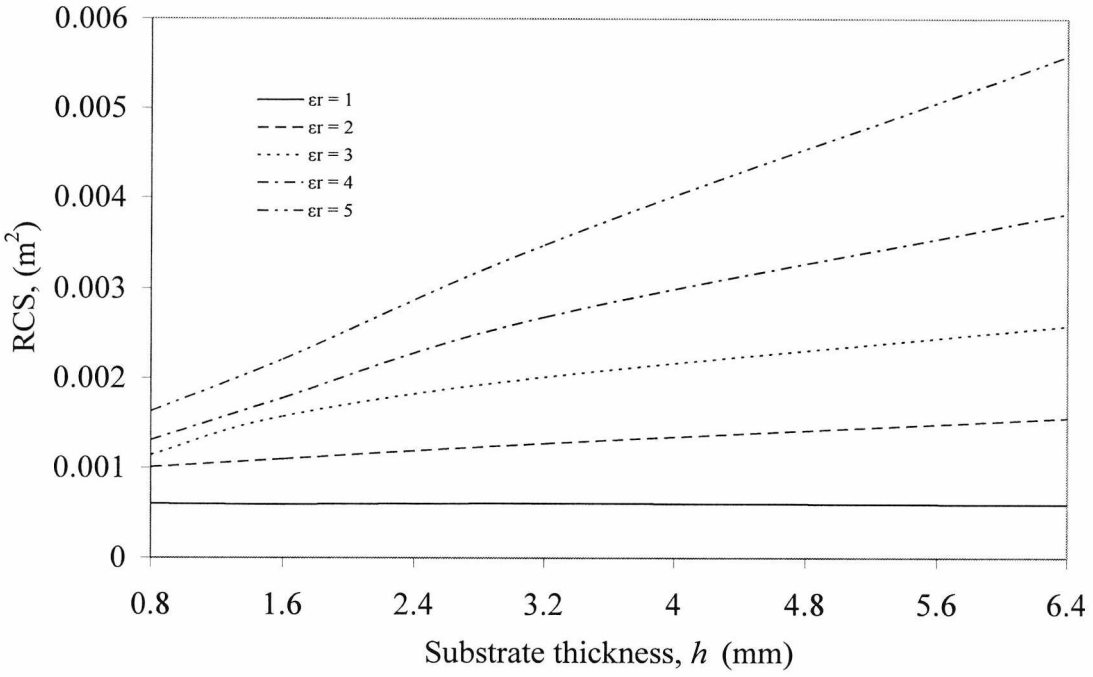

(a)

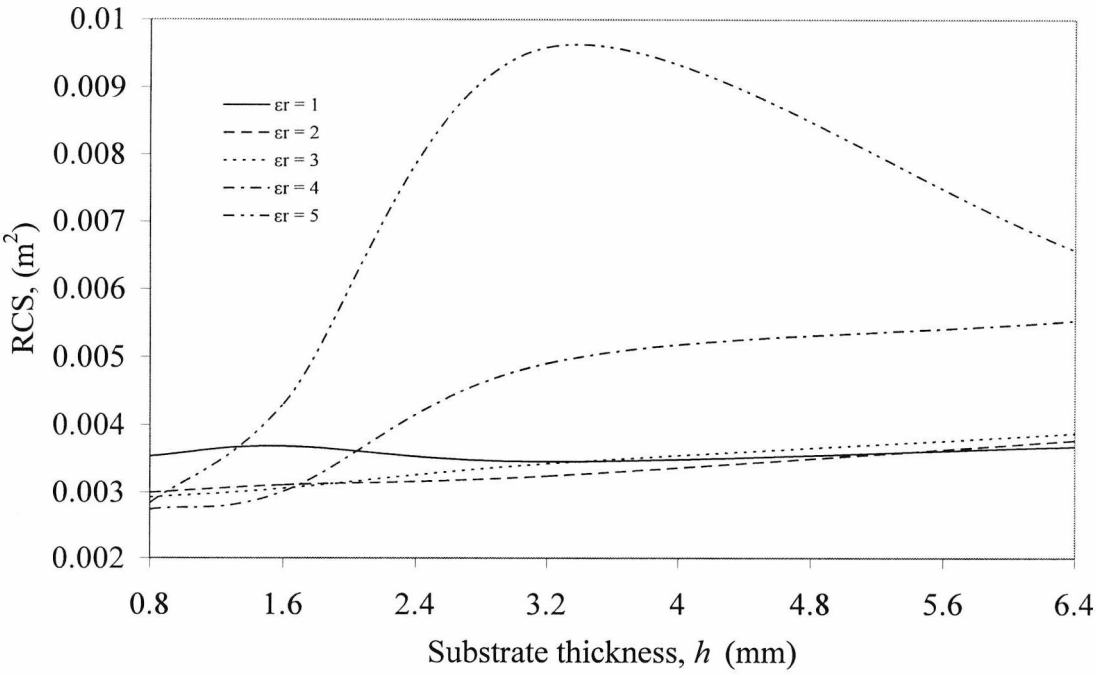

(b)

Fig. 4.23: Variation of the RCS for the slot patch antenna with substrate thickness for different substrate permittivity at (a) 869MHz and (b) 2.45 GHz under IC load condition.

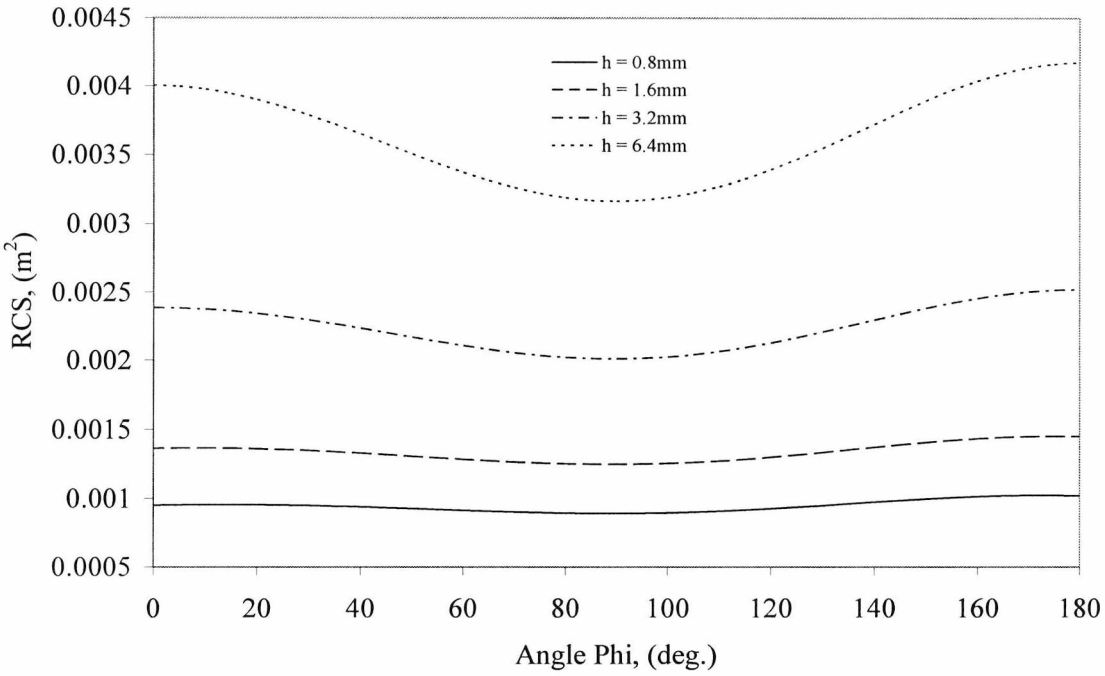

(a)

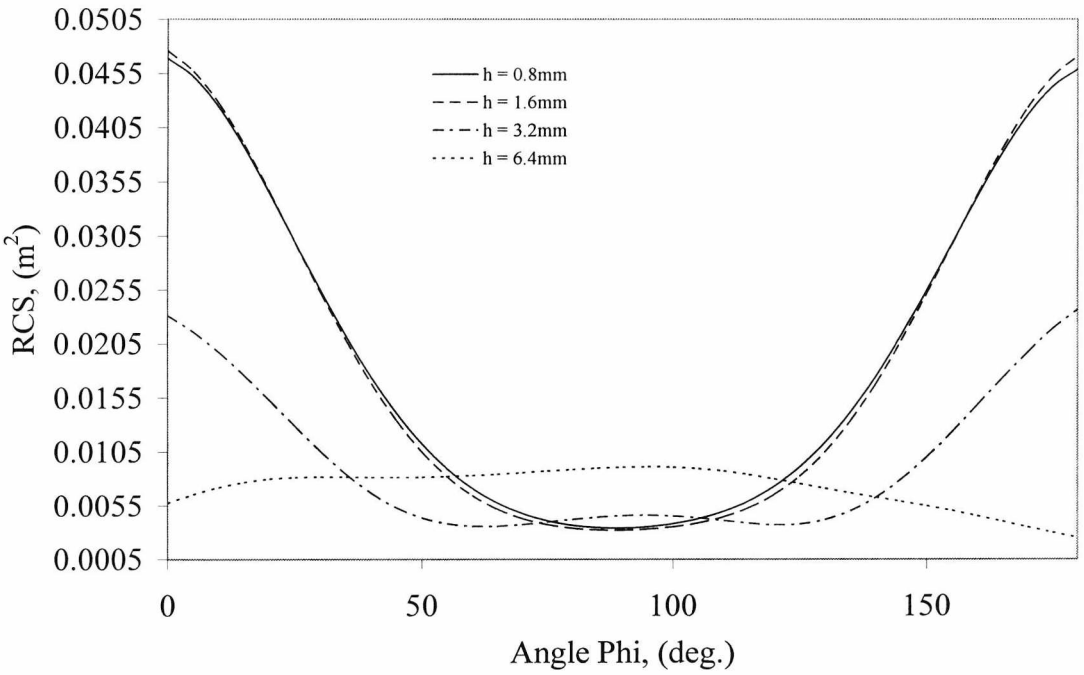

(b)

Fig: 4.24: The effect of angle on RCS for different substrate thicknesses at (a) 869 MHz and (b) 2.45 GHz.

Figures 4.22 (a) and (b) show increases in the RCS as the substrate thickness increases for the two operation frequencies. In normal use with IC, (b) shows no further advantage is obtained by increasing substrate thickness beyond 3.5.

Fig 4.23 (a) and (b) show that for more dielectric substrate results in shorter wavelength which appears to make the antenna look larger. The peak in (b) at $\varepsilon_r = 5$ indicate that the dielectric substrate has a larger effect on the system at the operating frequency.

The effect of varying the plane wave incident angle, φ on the RCS for different the substrate thicknesses and relative permittivities are shown in Fig. 4.24; (a) is for the 869 MHz while (b) is for the upper frequency at 2.45 GHz. Low RCS are observed in both figures at 90°, which may have resulted from interferences of the slots although, negligible since the largest distance between elements is of the order of one-sixth at the first operating frequency.

4.5 Read range measurement

The SPA antenna was integrated with EM422 ASIC chip and attached to various materials such as foam, paper ream, dry wood, plastic, glass, and metal) whose electromagnetic properties vary. These materials were selected based on the assumption that they were potential candidates for tag attachment, and offered a variety of complex conductivities and permittivities.

The test procedure outlined in Section 3.5 (chapter 3) had been followed. The measurements were conducted in an open laboratory and every effort was made to ensure that the tag was not in close proximity with reflective surfaces in order to keep the effect of scattering to minimum. In all the measurements, a circularly polarised *Ipico* Reader was used.

The clamp fixture used to attach the tag to the objects was an ordinary masking tape of 0.11 mm thickness which ensured that the antenna performance was not degraded. The

object together with the tag was suspended on PVC and tested for different orientation. The results are summarised in Table 4.7.

Category	**Reading conditions**	**Read Range**
Reader RF Interferences	–	Transmitting at 869 MHz with 0.5W EIRP
Reading range for different tag orientations with reference to the reader antenna	$x - y$ plane vertical (0°); wave incident along z- axis	2.8 metre
	$x - z$ plane horizontal (90°); wave incident along z- axis	2.65 metre (2.1 metre without C1)
	$x - z$ plane vertical; wave incident along y- axis	0.4 metre
	$y - z$ plane vertical; wave incident along x- axis	0.7 metre
Read ranges on platforms at maximum orientation x–y plane; plane wave incident along z-direction	Foam Paper ream Dry wood Ceramic Glass Metal	2.8 metre 2.5 metre 2.65 metre 1.25 metre 2.35 metre 0 metre

Table 4.7: A summary of the read range measurements using iPico reader having a circularly polarised antenna; one tag read under static condition at a time.

The average read range was obtained by averaging, in a set of random measurements, the maximum distance at which the antenna could backscatter. The tag range measured on foam is identical to free space measurement and was optimum at 2.8 m. Paper and dry wood showed a slightly reduced range than in the foam material. This decrease is attributed to losses in the wood and paper. The range for ceramics and glass showed further reduction due to detuning. However, since the impedance of the tag is very low when on metal, this range in this case is zero.

4.6 Conclusion

This chapter has developed a Slot Patch Antenna (SPA) using various optimization technique to achieve dual-band, dual polarisation behaviour. In particular, the excited frequencies are 869 MHz and 2.45 GHz, which are specific to RFID UHF and microwave operations. The usefulness of coupling slots of various sizes to a conventional slotline in order to excite the different bands has been established. Wide band can be achieved if the dimensions of the slots are close to each other. It has also been shown that the slot width and the substrate thickness and relative permittivity are additional parameters that determine the performance of the antenna. In order to achieve higher RFID operating frequencies, the SPA antenna was scaled in terms of frequency. An important outcome was that reducing the size of the antenna by half excited a couple of higher RFID frequencies namely 2.45 GHz and 5.8 GHz, which are also needed in this application.

The power that the antenna receive under different antenna load conditions was predicted to be largest when the incident plane wave field vectors were oriented along the x-direction irrespective of the direction of incidence. For a given substrate thickness, the Radar Cross Section, RCS was shown to increase with increasing substrate relative permittivity.

Measurement results show that the antenna performance is optimum when attached to a foam-like object and worsen as the relative permittivity of the attached object increases. As would be expected, no range was obtained when the antenna was close proximity with metallic surface.

4.7 References

[4.1] EPC global, "Specification for air interface: EPC Radio frequency identification protocols, Class-1 Gneration-2 UHF RFID, Protocol communications at 860 MHz – 960 MHz," Version 1.0.9, 2005

[4.2] Maci, S, Biffi Gentili, G., Piazzesi, P and Salvdor, C.: 'Dual-band slot-loaded patch antenna', *IEE Proc., Microw. Antenna Propag. 1995, 142, pp.225-232*

[4.3] Kin-Lu Wong and Jia Yi Sze: 'Dual-frequency slotted rectangular microstrip antenna', *Electronics Letters* 1998, Vol. 34, No. 14

[4.4] Hani A. Ghali and Tarek A. Moselhy, "Broad-band and circularly polarized space-filling-based slot antennas," *IEEE Trans. Microw. Theory Tech.*, vol. 53, no. 6, June 2005, pp.1946 - 1950

[4.5] J. R. James and P. S. Halls, "Handbook of Microstrip Antenna," London: Peter Peregrinus Ltd, 1989, vol 1, Chapter 1

[4.6] S. Maci and G. Biff Gentili, "Dual-frequency patch antenna," *IEEE Antennas. Propag. Mag.* Vol. 39, No. 6 December 1997, pp.13-20

[4.7] Ki Fong Lee and Wei Chen, "Advances in microstrip and printed antenna," Wiley-Interscience publications, p.143

[4.8] Kamal Sarabandi, "Design of an efficient miniaturised UHF planar antenna," *IEEE Trans Antennas Propag.* Vol. 51, No 6 June 2003

[4.9] D.C. Ranasinghe, D.M. Hall, P.H. Cole, D.W. Engels, "A small label antenna for embedding in metallic objects," Auto-id centre, Massachusetts Institute of Technology -

[4.10] Rao, K.V.S.; Nikitin, P.V.; Lam, S.F.; 'Antenna design for UHF RFID tags: a review and a practical application', *Antennas and Propagation*, IEEE Transactions on Volume 53, no. 12, Dec. 2005 pp. 3870 - 3876

[4.11] Constantine A. Balanis, "Antenna Theory: Analysis and Design," John Wiley and Sons Inc. 1982, Chapter 14, p.729

[4.12] Arto Hujanen, Jan Holmberg, and Johan Carl-Erik Sten, "Bandwidth Limitations of Impedance Matched Ideal Dipoles," *IEEE Trans Antennas Propag.*, Vol. 53, No. 10, October 2005

CHAPTER 5

COMPLEMENTARY PATCH ANTENNA FOR PASSIVE RFID TAGS

5.1 Introduction

This chapter continues the exploitation of closed spaced radiating elements, used in the previous chapter, and involves patch elements. In particular, the theory of complementarity has been used to obtain a complementary shape of the slot patch antenna simply by interchanging the regions of slot and PEC spaces, Fig.5.1. Both the slot patch antenna and the complementary patch antenna (CPA) are truncated of the otherwise infinite perfect electric conductor and dielectric substrate respectively.

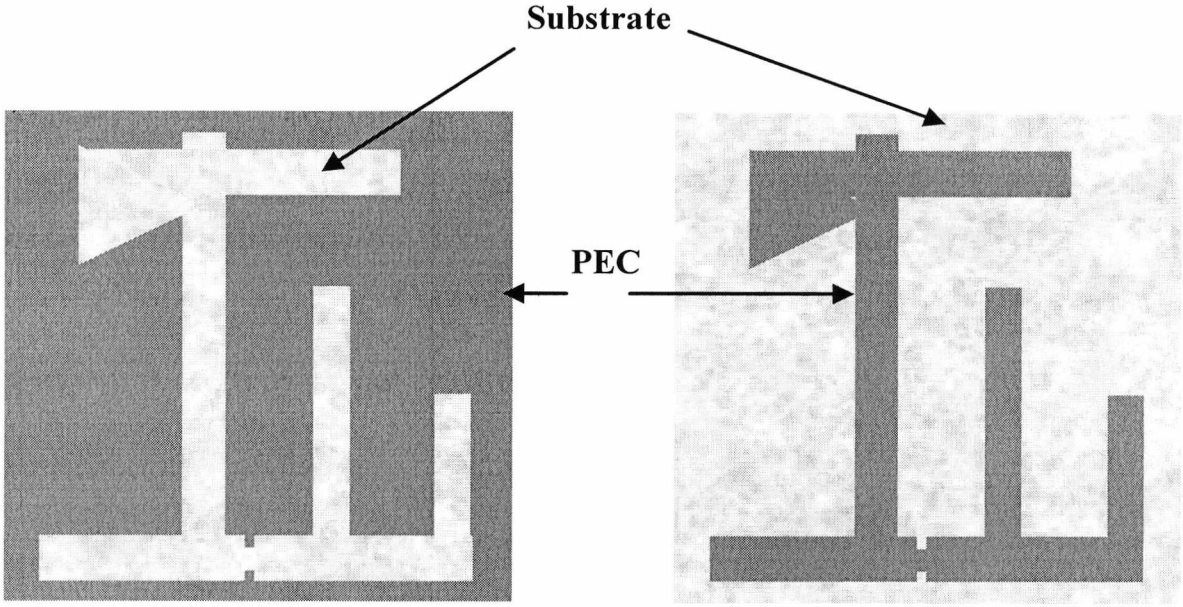

(a) Slot Patch Antenna (b) Complementary Patch Antenna

Fig. 5.1: Topologies of the (a) Slot Patch Antenna, SPA and (b) complementary patch antenna, CPA.

An important requirement in RFID is to match the passive tag chip input impedance to that of the tag antenna. The optimisation can be achieved by using a slot antenna such as the Slot Patch Antenna (SPA) introduced earlier in Chapter 4 of this thesis. The slots, mainly capacitive, in the SPA are needed in order to cancel the effect of the inductive reactance of the ASIC chip. On the other hand, when the capacitive reactance of tag chip is to be cancelled, then a patch antenna (mainly inductive) will be a preferred candidate. An option for designing patch antennas is provided in this chapter. Clearly, the choice of either a slot or patch is dependent on the ASIC design. The nature of the platform upon which a tag is attached is also a determinant for the choice of antenna architecture.

The advantage of using this method is to improve design flexibility and also to increase the options for mounting tags on different objects which exhibits different electromagnetic properties. In effect, the solution offers a compromise between structural complexities and electromagnetic compatibility of tags on different mounting platforms. The complementary patch antenna offers the same features as the slot patch antenna including low-profile, light-weight, ease of integration with ASIC chip and the inconvenience of narrow bandwidth due to the resonant nature of the patch [5.1]. In order to increase the bandwidth, wide band antennas have been proposed that include: simple printed patch structure [5.2], a long rectangular patch incorporating a single feed system [5.3], dual-patch triangular patch [5.4]. In reference [5.5] a broad band operation was achieved by reactively loading an aperture-fed patch antenna. The large bandwidth in [5.5] was possible due to the combined reactive loading and aperture feeding techniques.

Other tag optimisation strategy requires enhancing the agility of the tag antenna polarisation. In reference [5.6], a reconfigurable microstrip circularly polarised antenna was developed for short range communication systems which is adaptable to RFID application. The antenna excites both right-hand and left-hand circularly polarised wave. The application of cross-layered, unbalanced feed structures such as PIFA/microstrip [5.7], [5.8] to obtain increased gain in a particular direction has been proposed. The inclusion of ground planes is minimising the antenna back radiation particularly if the tag

is meant for wearable application. However, a major drawback for IC integration is that the parasitics of the interconnection become significant and degrade antenna performance [5.9]. The vias or shorting pin across layers constitutes the bulk of the problem. A uniplanar antenna offers both the advantage of achieving multifunctional behaviour and integration with IC's on the same surface. Hence they are more economical.

The antennas presented in this chapter each has orthogonal patches of various dimensions, which results in increased bandwidth and two planes of polarisation. While its polarisation offers improved detection range over a standard dipole, the broadband match increases the capacity to accommodate variations in resonant frequency which might arise from the effect of mounting platforms. In addition, the amount of power the antenna receives will be used in section 5.3 to establish that at any random angle of polarisation, a tag antenna is expected to maintain reasonable cross-polarised radiation patterns over the operating frequency range. This capability is demonstrated in section 5.5 using the tag maximum read range). Ideally, circularly polarised RFID reader antennas should be used because they overcome the problems associated with tag orientation. However, there are also dual polarized reader antennas [5.10]; this requires that in order to achieve improved tag detection, tag antenna designs should be of dual linear polarisation.

This chapter consists of six sections. Section 5.2 introduces the antenna structure and its behaviour is investigated. In section 5.3, the effect of field polarisation is examined. Section 5.4 analyses the radar cross sections (RCS) of the antenna. The maximum read range is used in section 5.5 to evaluate the antenna performance when used as a tag. Section 5.6 concludes the chapter.

5.2 The Topology of the Complementary Patch Antenna

The square-shaped (70 × 70) mm^2 dielectric substrate defined on the $x-y$ plane supports a PEC layer, t = 0.007 mm thick, which is the exact complementary shape for the slot

patch antenna studied in Chapter 4. The complementary patch antenna is illustrated in Fig. 5.2.

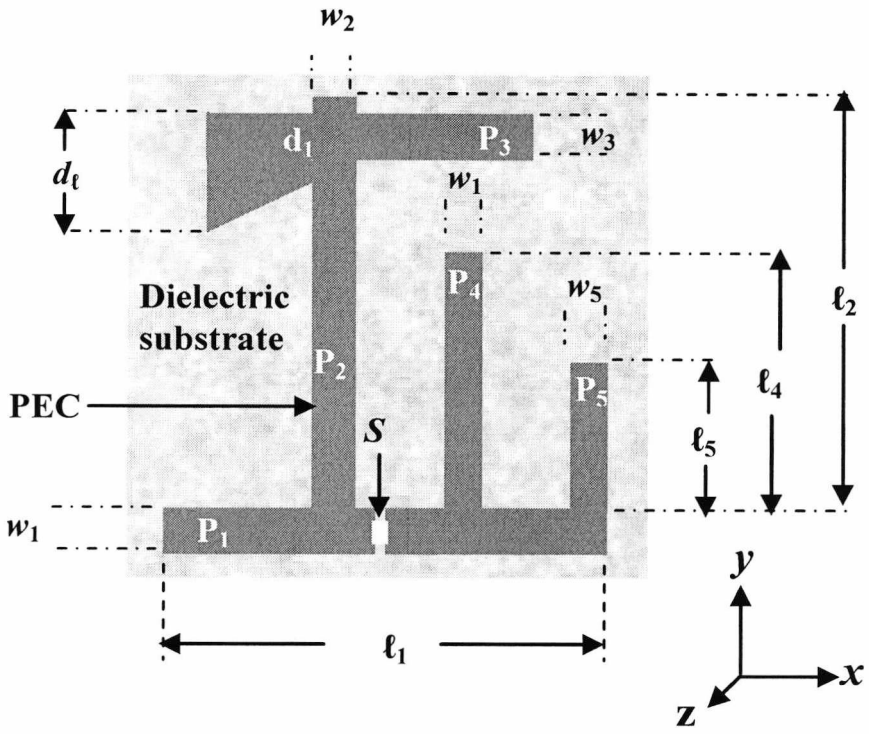

Fig. 5.2: Geometry of the complementary patch antenna.

Only the side with the complementary patch shape is metallised and consists of patches P_1, P_2, P_3, P_4 and P_5 whose respective lengths and widths are denoted by ℓ_i and w_i; where, i correspond to an individual patch; S is the feed gap. In the upper region P_2 crosses a modified horizontal strip P_3. Patches P_4 and P_5 are orthogonal to P_1. The antenna was designed and fabricated on FR-4, with $\varepsilon_r = 4.9$, $tan\ \delta = 0.025$. The lossy FR-4 was chosen to demonstrate that cheap substrate can be used without suffering from substantial losses. The antenna is excited by an off-centred discrete port modelled with characteristic impedance of 50 Ω and located at the position labelled S in Fig. 5.2. The antenna physical parameters are summarised in Table 5.1. The substrate size is 70×70 mm^2 and conducting plane size of 64×64 mm^2.

Parameter	Definition	Dimension	Parameter	Definition	Dimension
ℓ_1, w_1	Length and width of the lower horizontal strip, P_1	58, 5.2 (10.4)	a	Length of antenna	65.3 mm
ℓ_2, w_2	Length and width of the first vertical patch, P_2	50, 5.2	b	Width of antenna	58 mm
ℓ_3, w_3	Length and width of the upper horizontal patch, P_3	65.2, 5.4	h	Thickness of substrate	0.8 mm
ℓ_4, w_4	Vertical patch P_4	40, 2.7	t	Thickness of conductor	0.007
ℓ_5, w_5	Vertical patch P_5	20, 2.7	S	Feed gap	2 mm

Table 5.1: The physical parameters with dimensions for the complementary patch antenna shown in Fig. 5.2.

5.2.1 The input impedance characteristics

The antenna exhibits multiple resonances at 869 MHz, 1.430 GHz and 2.8 GHz with corresponding measured return loss of -12dB, -13.7dB and -11.2 dB. The antenna has been fabricated on an FR-4 substrate; Fig. 5.3 compares the simulated and measured return loss for the optimised case.

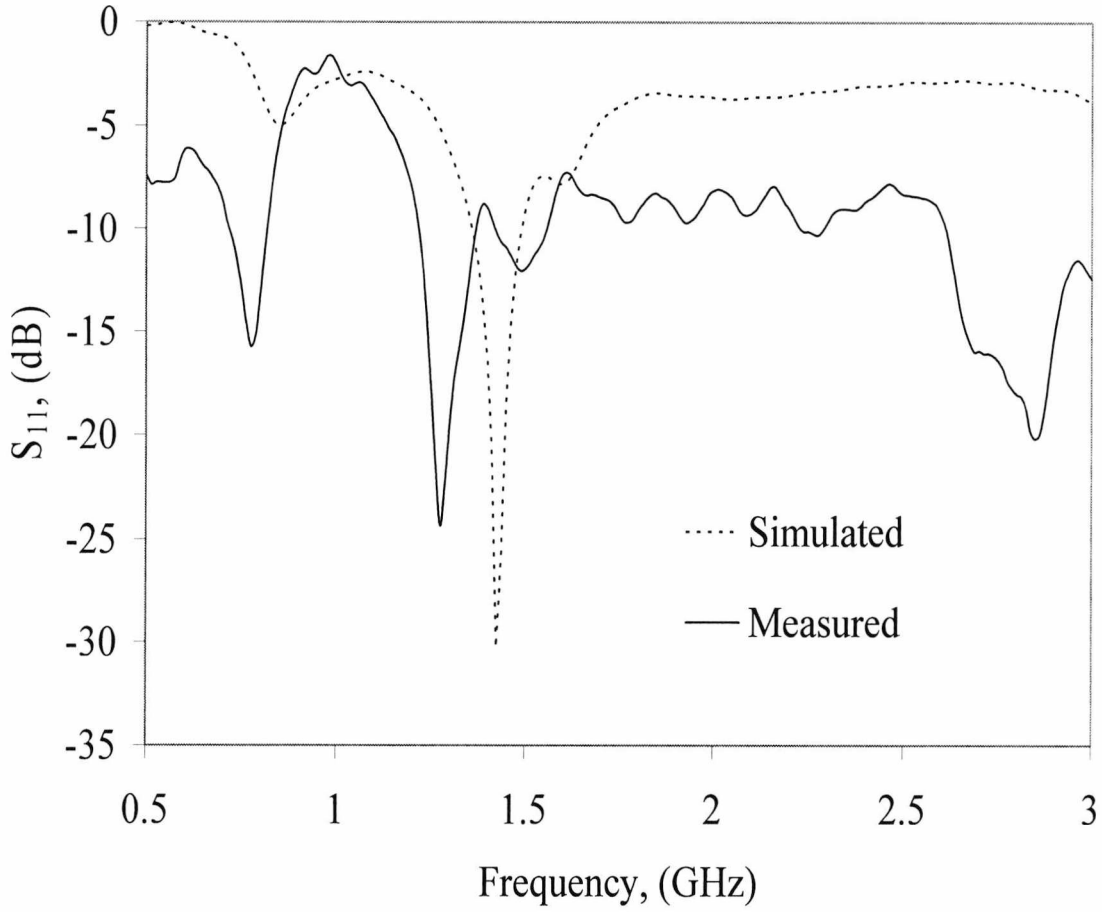

Fig. 5.3: Simulated and measured return loss for the CPA complementary patch antenna shown in Fig. 5.2.

The dashed and solid lines denote the simulated and measured return loss in agreement. A small discrepancy is observed between the simulated and measured centre frequencies. This may have resulted from either fabrication process (for example, during the photo-

etching process) or from the fact that substrate losses were not included in the simulation. It may have also resulted from parasitic coupling between the terminals of the antenna in the case of measurement (i.e. the terminals of the coaxial cables were at close proximity to each other) or from soldering defects. The corresponding measured -8 dB bandwidths are 77 MHz and 197 MHz which is larger than that of an equivalent single strip operating at the same frequency.

5.2.2 Parametric study

The dimension of some of the physical parameter defined in Table 5.1 were varied, while keeping the others constant, in order to understand their individual contributions to the antenna behaviour. The study is carried out using simulation in CST Microwave Studio. The surface current distribution has been used to predict the contribution of each patch on resonant frequencies. The surface current distribution on the CPA antenna is illustrated in Fig. 5.4. It can be seen (from the high current density) that the lower frequency is predominantly controlled by P_2. It can also be deduced that the intermediate frequency (1.43 MHz) is controlled predominantly by P_4. P_4 and P_5 are predominant in tuning the upper frequency.

The graph in Fig. 5.5 shows the effect varying the width (w_1) of patch P_1, has on bandwidth. As expected, the bandwidth increases as the patch width increases; this effect is more noticeable in the upper band. The percentage increase in bandwidth between when the patch has a width of 3.2-mm and when it has a width of 10.4-mm for substrate relative permittivity 4.9 correspond to 12 % and 77 % for the lower and the upper bands respectively. The effect of varying the length of patch P_1 (i.e. ℓ_1) on resonant frequency is plotted in Fig. 5.6. It can be seen that the upper frequency increases by 481 MHz when ℓ_1 is decreased from 64.4-mm by 23-mm to the point where P_2 intercepts P_1 (ℓ_1 = 41.4-mm). The middle frequency decreases by merely 36 MHz while no remarkable variation is noticed in the lower frequency.

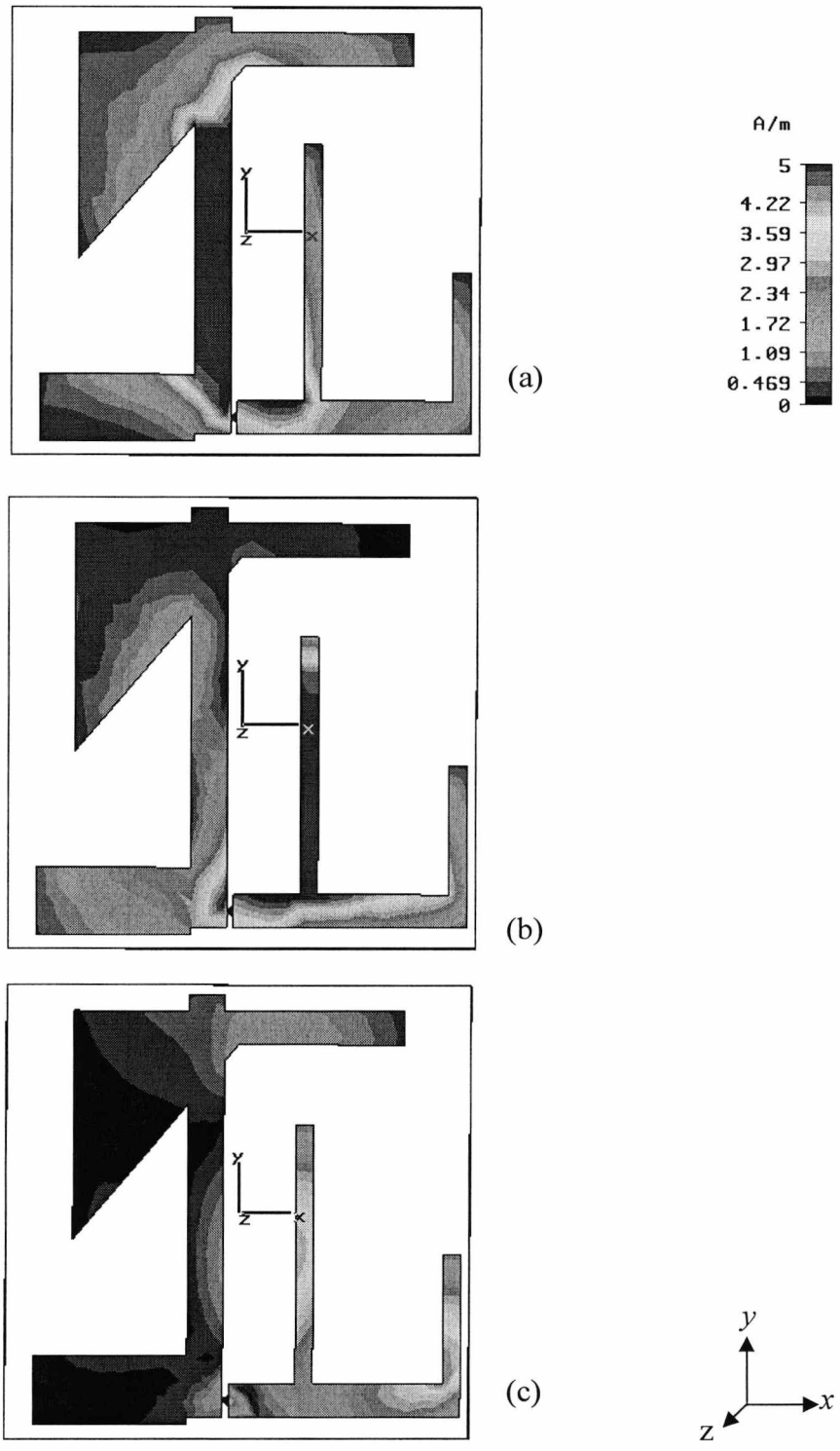

Fig. 5.4: Surface current distribution for the CPA antenna shown in Fig. 5.2 at the operating frequencies of (a) 869 MHz (b) 1.43 GHz and (c) 2.8 GHz and at 0^{o} phase.

Figures 5.7 and 5.8 correspond to the effects of patches P_4 and P_5 on the resonant frequencies. Decreasing the length of patch P_4 (i.e. ℓ_4) from 40-mm to 0-mm, causes the upper frequency to drop by 1.7 GHz. For the same range, the middle and the lower frequencies decrease by 113 MHz and 35 MHz respectively. In the case of P_5, a decrease in its length, ℓ_5 results in a decrease for the upper resonant frequency by 583 MHz while no discernible effect is produced in the middle and lower frequencies. The parametric study shows the possibility of tuning the antenna to cover 2.45 GHz.

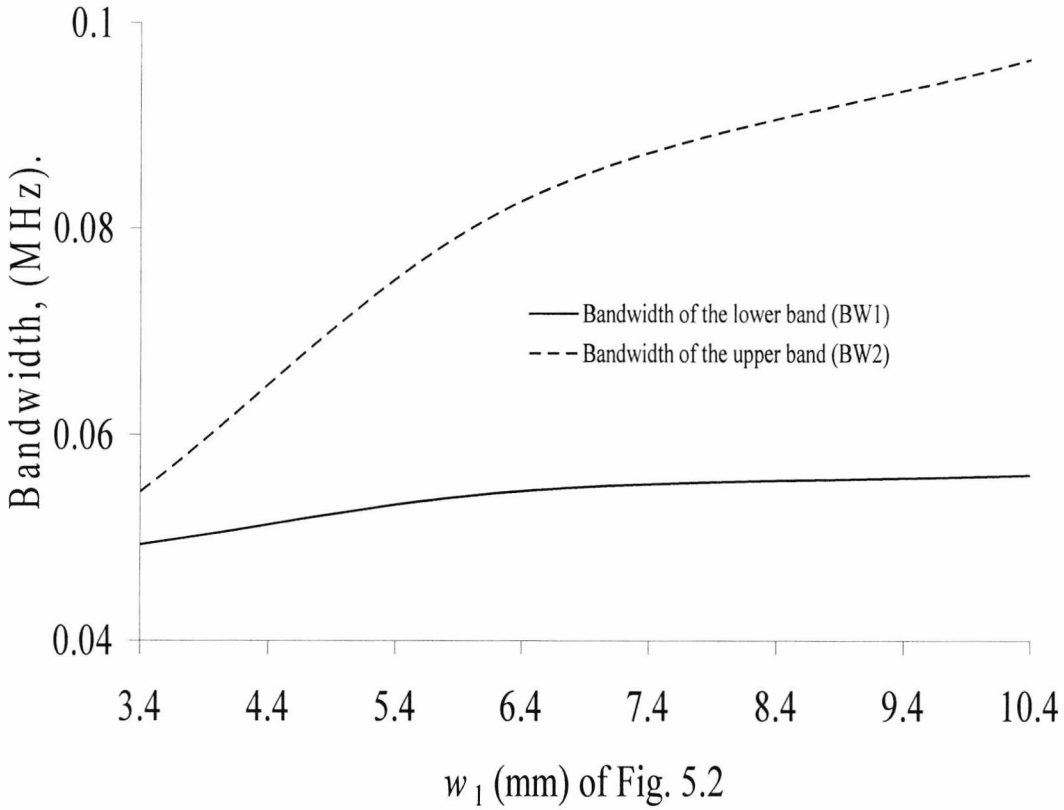

Fig 5.5: The effect of increasing the width of P_1 as shown in Fig. 5.2 on the CPA antenna bandwidth.

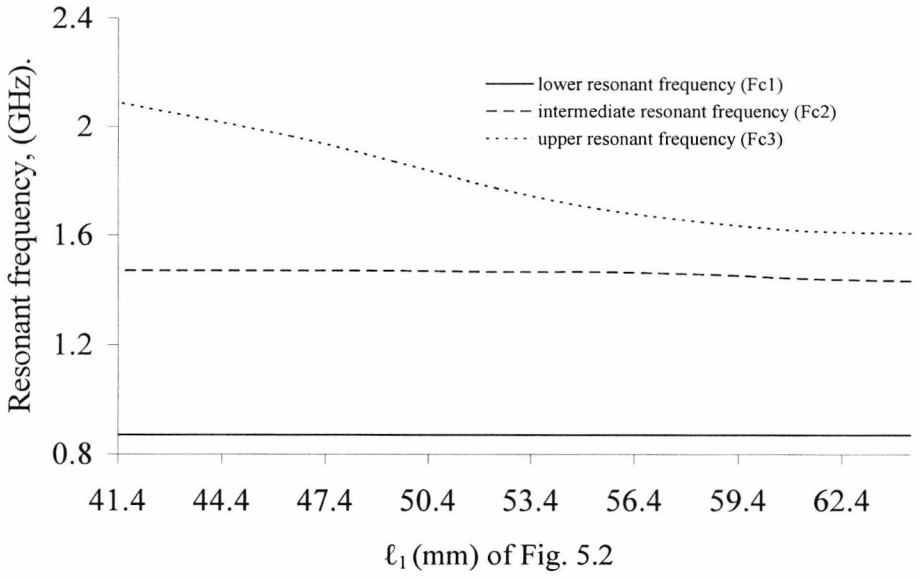

Fig.5.6: The effect on resonant frequency of varying ℓ_1 of Fig. 5.2 on resonant frequency of the CPA antenna.

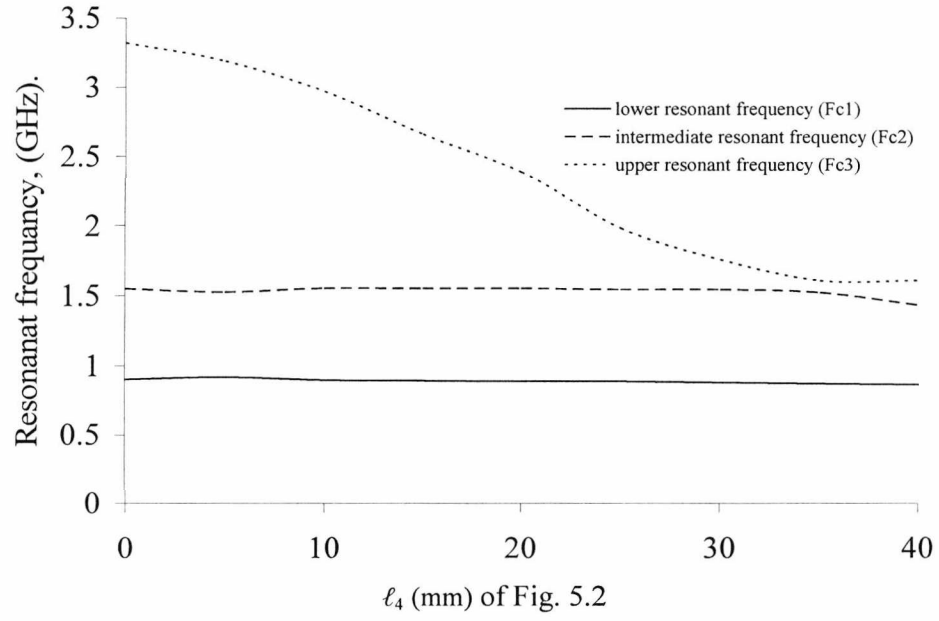

Fig 5.7: The effect on resonant frequency of the CPA antenna by varying ℓ_4 of Fig.5 .2 from 40 mm down to 0 mm.

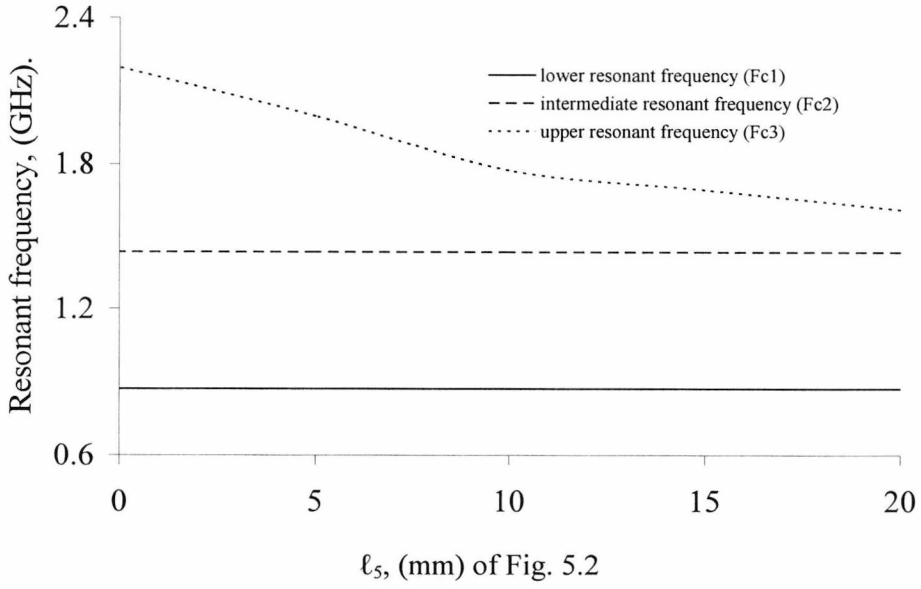

Fig 5.8: The effect on resonant frequency of the CPA antenna by varying ℓ_5 of P_5 from 20 mm down to 0 mm.

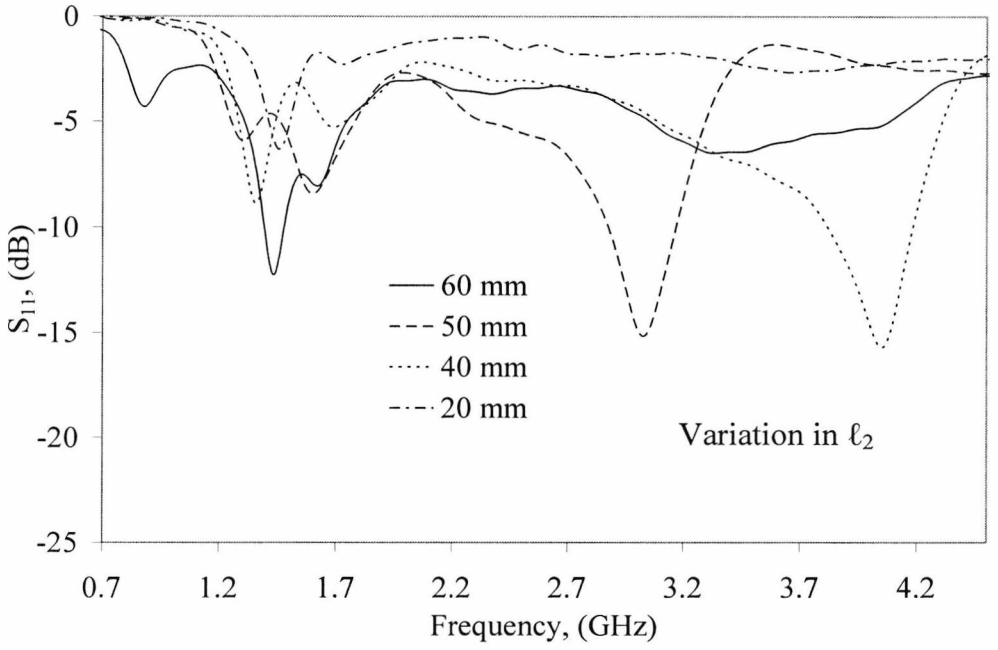

Fig. 5.9: The effect on resonant frequency of the CPA antenna by varying ℓ_2 of Fig 5.2 from 60 mm down to 20 mm.

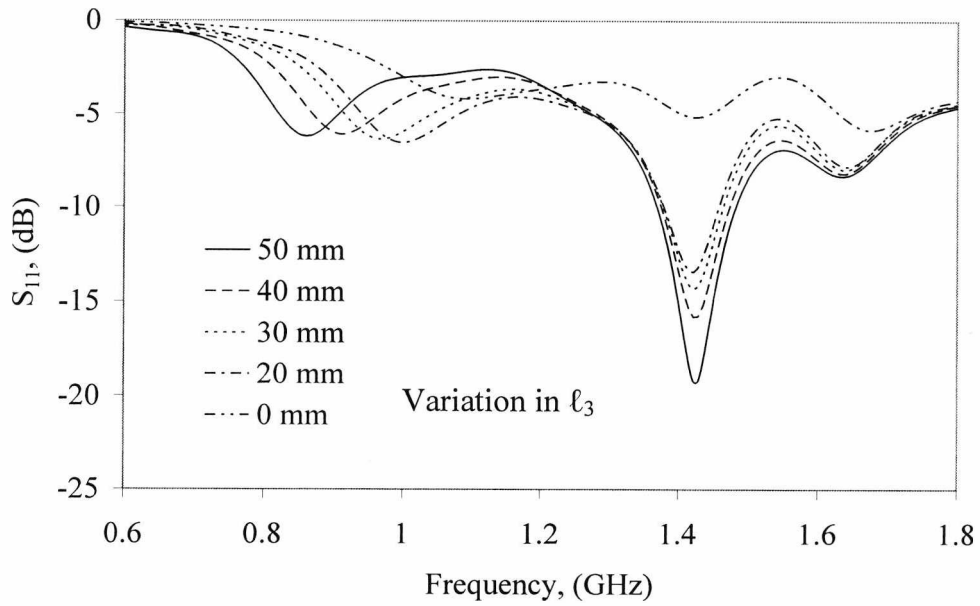

Fig. 5.10: The effect on resonant frequency of the CPA antenna by varying ℓ_3 of Fig. 5.2 from 50 mm down to 0 mm.

From the above analysis, the dominance of each tuning element over the operating frequencies has been established and summarised in Table 5.2.

Frequency	Lower	Intermediate	Upper
Dominant tuning elements	P_1, P_2 and P_3	P_2 and P_3	P_1, P_4 and P_5

Table 5.2: the dominance of tuning element on resonant frequencies

5.2.3 The effect of frequency scaling on the CPA

So far, consideration has been given to the full scale CPA antenna shown in Fig. 5.2 (i.e. 64.4 × 64.4 mm). However, when tags are required to operate at higher frequencies, it might become necessary to carry out a frequency scaling operation. Table 5.2 is used to demonstrate the ability of the CPA to scale-up to higher RFID frequencies. For the

frequency sweep across 0 to 7 GHz, the 35.4 × 35.4 mm^2 size CPA (i.e. $^1/_\ell$ = 0.028249 mm^{-1}) exhibits resonances at 1.45 MHz, 2.45 and 2.7834 GHz of which only the intermediate frequency is relevant to RFID system. In the case of the 13-mm × 13-mm size CPA (i.e. $^1/_\ell$ = 0.076923 mm^{-1}, where, is the ℓ antenna length), the lower, intermediate and upper resonances correspond to 3.69 GHz, 5.8 GHz and 6.58 GHz; only the 5.8 GHz is relevant to the application.

The frequency gap between resonances is comparable to that of the SPA studied in Chapter 4 for the equivalent frequency scaling factor. The simulated -10dB bandwidths of the CPA are relatively larger than that of its slot patch antenna (Chapter 4) and up to 362 MHz and 2.07 GHz respective bandwidth were achieved.

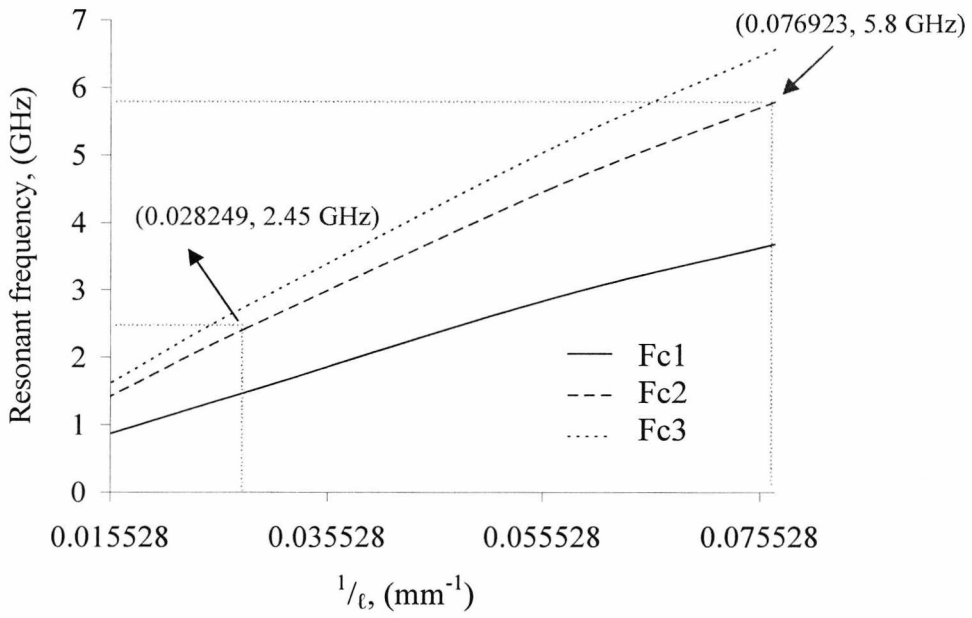

Fig. 5.11: Simulated frequency characteristics of the frequency-scaled complementary patch antennas shown in Fig. 5.2 at the first three resonant frequencies. fc1

Comparing these antennas with those of their SPA counterpart (in Chapter 4) shows that frequency scaling down by a fraction of half, or a quarter, produces useful operation at 2.45 GHz and 5.8 GHz. As might be expected, Fig. 5.11 shows how the resonant

frequency increases as the antenna size decreases. During all the frequency scaling process no additional tuning effort was required to achieve a good match at the resonance frequency.

5.2.4 Measured far field radiation pattern of the CPA

The radiation patterns of the patch antenna have been measured for the co- and cross-polarisation. As was the case for the SPA, the CPA antenna radiation is bidirectional but asymmetric with respect to the plane in which it is contained. The fields in the lower half-space are different to those in the upper half-space. Therefore, a complete pattern plots in the 0^{o} – 360^{o} range are shown. The co- and cross polarized radiation patterns were measured for the three resonant frequencies: 869 MHz, 1430 GHz and 2.45 GHz. Fig. 5.12 shows the measured co- and cross-polarized radiation patterns of the antenna in $x-y$, $y-z$ and $x-z$-planes for the lower and upper bands respectively.

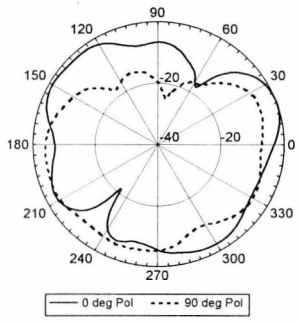

x–y plane co- and cross polarisation at 869 MHz

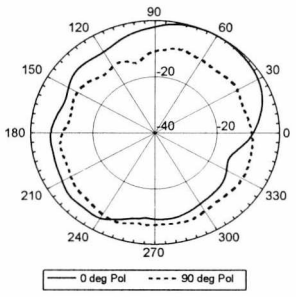

x–y plane radiation patterns at 1430 MHz

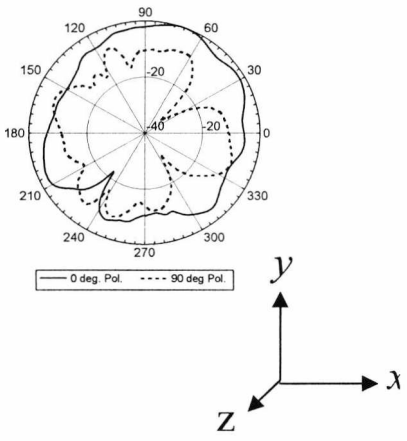

x–y plane radiation patterns at 2450 MHz

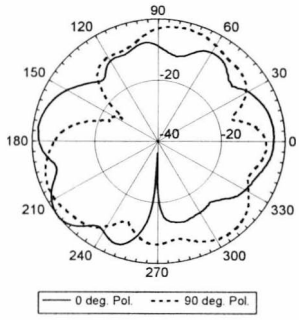

$y-z$ plane radiation patterns at 869 MHz

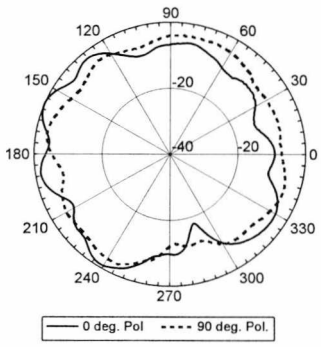

$y-z$ plane radiation patterns at 1430 MHz

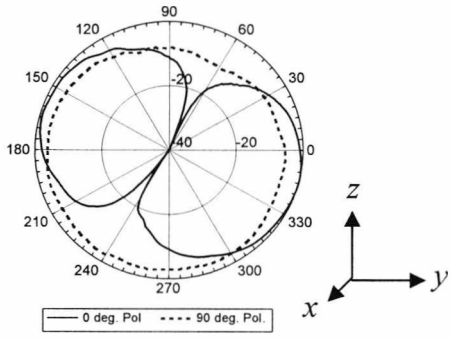

$y-z$ plane radiation patterns at 2450 MHz

(b)

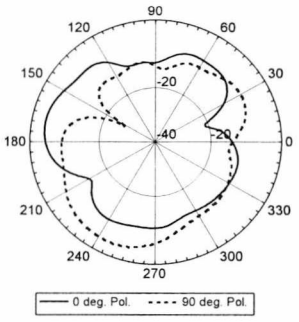

$x-z$ plane radiation patterns at 869 MHz

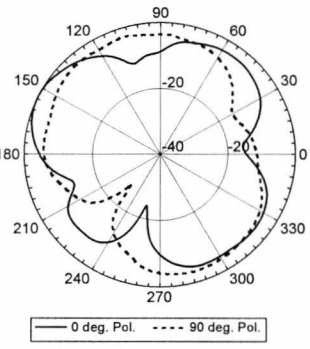

$x-z$ plane radiation patterns at 1430 MHz

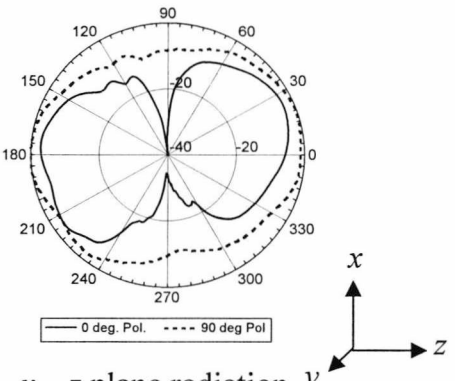

$x-z$ plane radiation patterns at 2450 MHz

(c)

Fig. 5.12: Radiation patterns of the antenna studied in Fig. 5.2 at the resonant frequencies of 869 MHz, 1.43 GHz and 2.45 GHz for 0^{o} and 90^{o} polarisations (a) x-y plane, (b) y-z plane and (c) x-z plane.

The co- and cross polarisation levels across the operating frequencies indicate the improved ability of a tag constructed with this antenna to be detected in any orientation.

5.2.5 The effect on the radiation patterns of mounting CPA at different heights above a metal plane

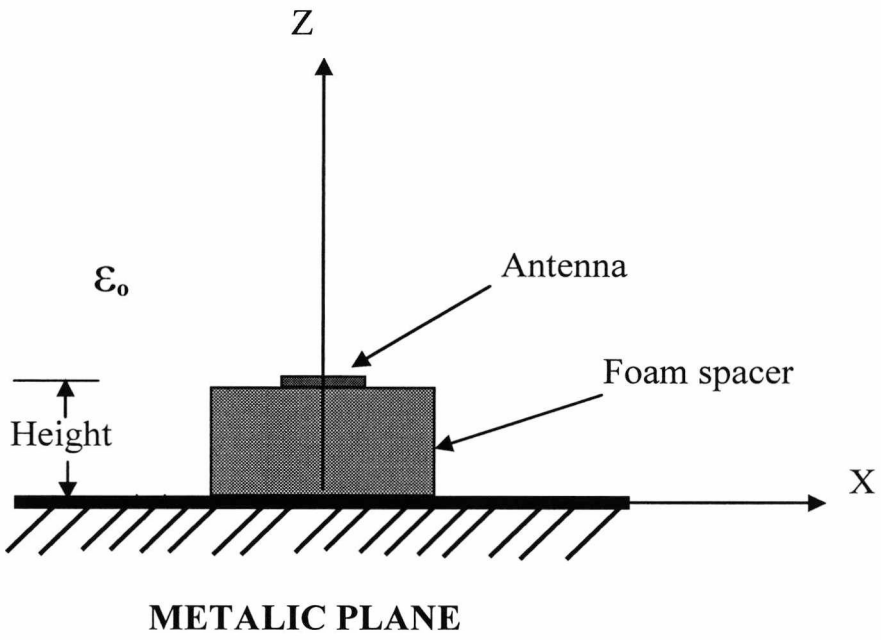

Fig. 5.13: Schematic diagram of the complementary patch antenna (CPA) mounted over a metallic plane.

It will be demonstrated in section 5.5 that reading tags over metallic platforms is problematic. The reason for this is that closely placed metals surfaces reduce efficiency by phase reversal at reflection. If the ground plane is placed further from the antenna resonant modes are established that couple energy from the antenna and can detune it. A reduction in the overall antenna gain in the boresight direction is observed when an electrically close metal plane is added. The development of sidelobes also degrades antenna performance. The effects of increasing the metallic plane heights as illustrated in Fig. 5.13 have been measured inside the anechoic chamber. The free space radiation pattern was used as a reference. Fig. 5.14 gives the measured relative radiation patterns

amplitudes of the complementary patch antenna for the case when the antenna was directly attached to a metallic plane (with dimension 1200×1200) mm^2 and, when the metallic plane height is increased to 50 mm ($\approx \lambda/7$) and 100 mm ($\approx 2\lambda/7$) respectively.

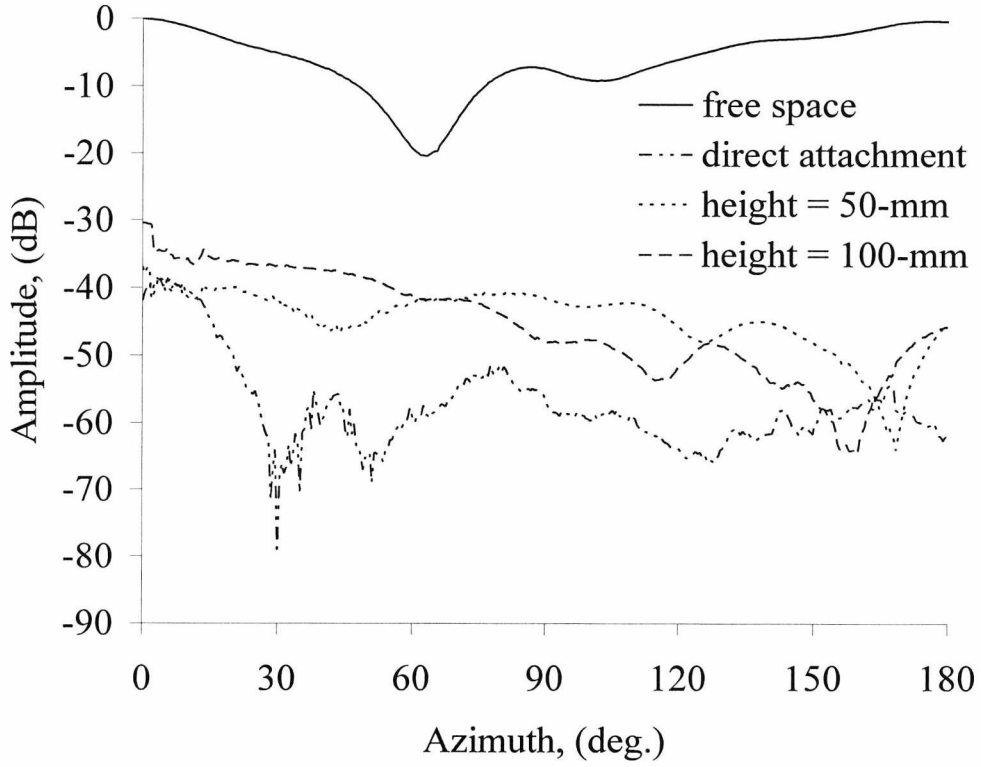

Fig. 5.14: Measured effects of metallic plane height on the radiation patterns at 869MHz of the complementary patch antenna studied in Fig. 5.2.

The unbroken line represents the free space radiation pattern, which shows a null at 60°. The dashed lines are for the cases when the antenna was at close proximity to the metallic platform (i.e. 50 mm and 100 mm). It is obvious from Fig 5.14 that the side lobes which are very prominent when the antenna is directly attached to the metallic surface persist (with relatively smaller magnitudes of side lobes) even when the metallic plane height has been increased to 50 mm. However, when the metal plane height is 100 mm, the number of side lobes reduces and their magnitude decreases.

5.3 The Effect of Field Polarisation on the Radar Cross Section

The polarisation of a tag antenna with respect to the reader antenna determines the amount of energy it receives. Simulation data on the effect of antenna orientations, under different load conditions, on the received power have been investigated. These were for the cases when the CPA antenna is illuminated by a plane wave whose E-field vectors were either polarised along the *x*-, *y*- or z– axis depending on the direction of propagation as exemplified in Fig. 4.19 of sub-section 4.4.2 in Chapter 4. Fig. 5.15 shows a plane wave visualized by a red plane. The coloured arrows indicate the propagation direction as well as the electric and magnetic field vectors. The electric field vector of a plane wave is hitting the CPA antenna. The plane wave is excited with an electric field vector in *x*-direction and a propagation normal (0,1,0).

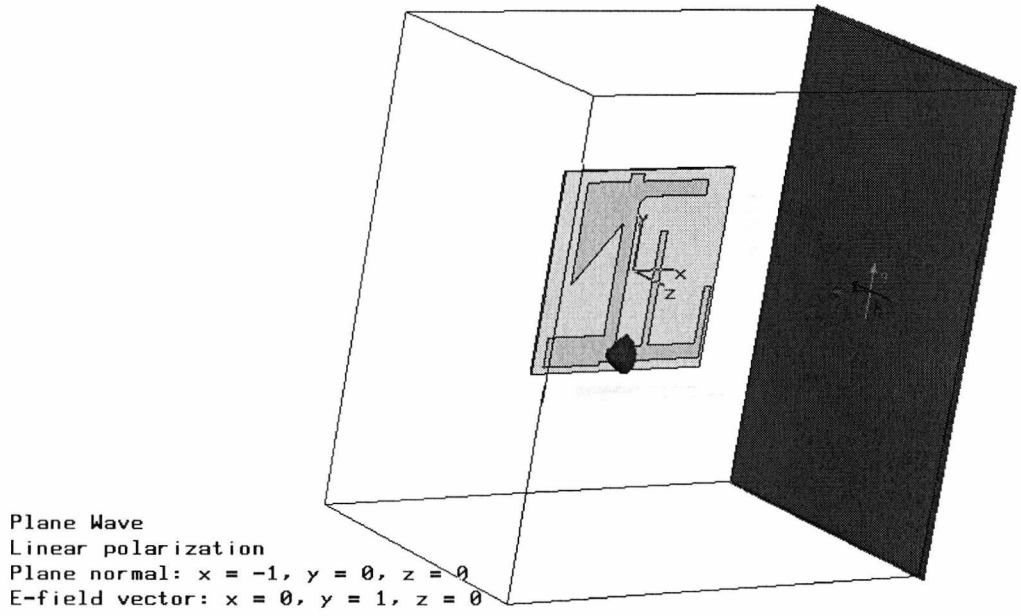

Fig. 5.15: A CST geometry file of the CPA antenna illuminated by a linearly polarised plane wave.

The RCS under a circularly polarised wave is also studied. Results are summarised in the tables below. Table 5.3 shows that for a plane wave propagating along the *z*-axis (see Fig.

5.2). The RCS for the case when the electric field vectors are oriented along the *x*-axis is about 9.56 dB higher than the case when the electric field vectors are oriented along the y-axis for the open circuit load condition. For the short circuit, resistor load and IC-load cases, the RCS when the electric field vectors are oriented along the x-axis is larger than when it is oriented along the y-axis by 2.86 dB, 6.08 dB and 9.84 dB respectively.

Table 5.4 shows that when the plane wave is propagating along to the *x-axis*, and with the electric field vectors aligned parallel to the *y*-axis (i.e. cross-polarised), power level decreases substantially compared to the previously summarised case in Table 5.3. Table 5.5 gives the maximum RCS when the plane wave is propagating along the *y*-axis. As in the preceding cases, when the electric field vector cross-polarised, the received power is smaller than in the case for a vertically polarised wave.

Antenna load	**Maximum RCS (dBsm) along the *z* – direction**		
	x-axis field vector	*y*-axis field vector	circularly polarised field
Open circuit	-24.19	-33.75	-26.69
Short circuit	-20.81	-23.75	-22.34
Resistor loaded	-24.34	-30.42	-27.90
Transponder loaded	-23.87	-33.71	-26.46

Table 5.3: Simulated maximum RCS value for the CPA antenna shown in Fig. 5.2 under different load conditions for the case when a plane wave is propagating normal to *z*-axis.

Antenna load	**Maximum RCS (dBsm) along the *x* – direction**		
	y-axis field vector	*z*-axis field vector	circularly polarised field
Open circuit	-23.95	-68.38	-27.40
Short circuit	-20.43	-66.49	-23.20
Resistor loaded	-24.78	-67.36	-27.87
Transponder loaded	-23.53	-67.58	-27.03

Table 5.4: Simulated maximum RCS value for the CPA antenna shown in Fig. 5.2 under different load conditions for the case when a plane wave is propagating normal to *x*-axis.

Antenna load	**Maximum RCS (dBsm) along the y - direction**		
	x-axis field vector	z-axis field vector	circularly polarised field
Open circuit	-35.32	-67.13	-37.78
Short circuit	-23.66	-67.19	-25.74
Resistor loaded	-29.85	-67.21	-32.85
Transponder loaded	-35.06	-67.03	-38.23

Table 5.5: Simulated maximum RCS value for the CPA antenna shown in Fig. 5.2 under different load conditions for the case when a plane wave is propagating normal to y-axis.

As in the case of the slot patch antenna studied in chapter 4, compared with the maximum RCS when the plane wave is linearly polarised (either vertical or horizontal) the tables below shows that a circularly polarised wave is intermediate between the vertical and horizontal polarised results. These results are in agreement with that obtained for the case of the slot patch antenna studied in Chapter 4.

5.4 RCS Analysis of the CPA Antenna

The radar cross section (RCS) analysis gives knowledge of the degree of scattering inherent in the CPA antenna. Given that RFID tags receives EM energy to activate, is was considered more useful to carry out the RCS analysis under antenna receiving modes. A plane wave was used to illuminate the antenna.

Figure 5.16 presents the effect on the antenna RCS of different load conditions: open circuit, closed circuit, resistor loaded and IC loaded. It can be seen that under any load condition, the RCS magnitude increases as the substrate thickness increases. Thus, thicker dielectric substrate shortens resonant wavelength thereby making the antenna appear larger. It is for the above reason that higher substrate relative permittivity also causes an increase in the RCS magnitude, Fig. 5.17. In comparison to Fig. 5.16, this effect is less remarkable in the case when the substrate relative permittivity is increased. Figure 5.17 further shows that there is no further advantage by increasing the substrate

relative permittivity beyond 2.5. The effect of increasing the substrate thickness for different values of substrate relative permittivity is shown in Fig.5.18. For this case, the combined effort of increasing both the substrate thickness and relative permittivity produces a sharp increase in the RCS magnitude.

The effect of varying the plane wave incident angle, φ on the RCS for different substrate thicknesses and relative permittivities are shown in Fig. 5.19. The effect for when the θ is varied is shown in Fig. 5.20. From these figures are observed low RCS at 90^{o} which may have resulted from interferences of the patches albeit negligible since the largest distance between elements is of the order of one-sixth at the first operating frequency.

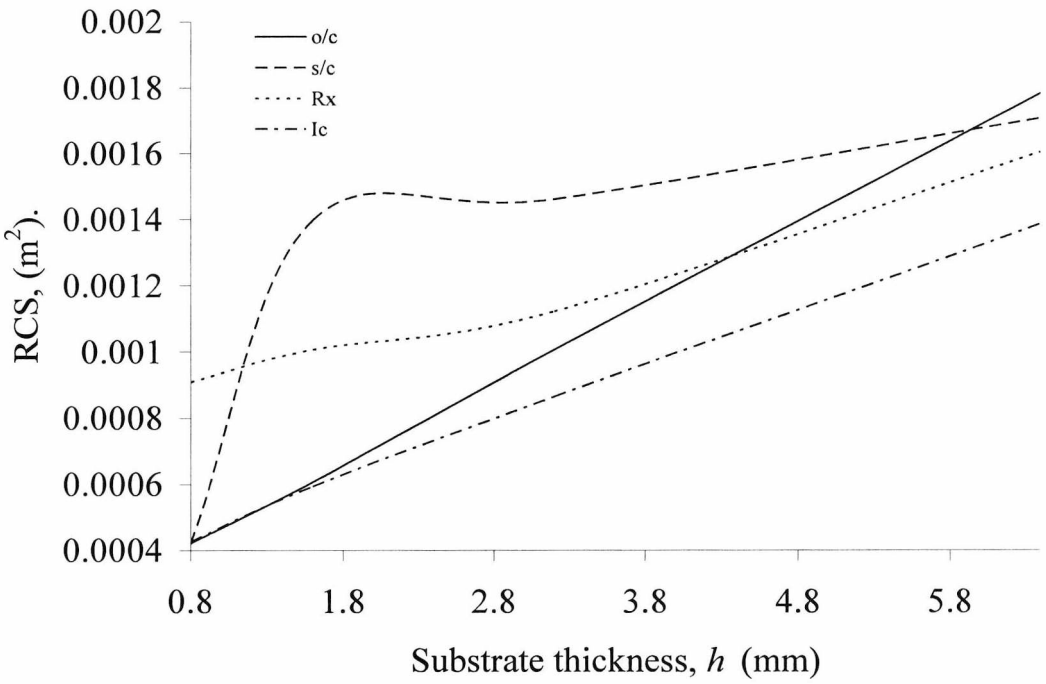

Fig. 5.16: The effect of dielectric substrate thickness on RCS for the CPA antenna with parameters $\varepsilon_r = 4.9$ and at maximum RCS angle of 180^{o}.

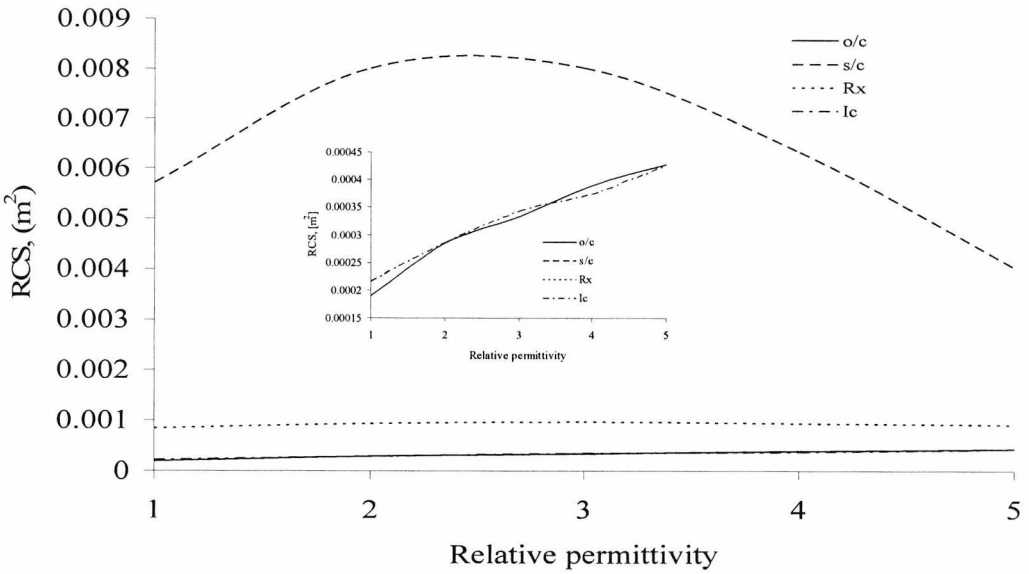

Fig. 5.17: The effect of dielectric substrate relative permittivity on RCS for the CPA antenna with parameters $\varepsilon_r = 4.9$ and at maximum RCS angle of 180°. Inset graph shows low RCS values at high resolution.

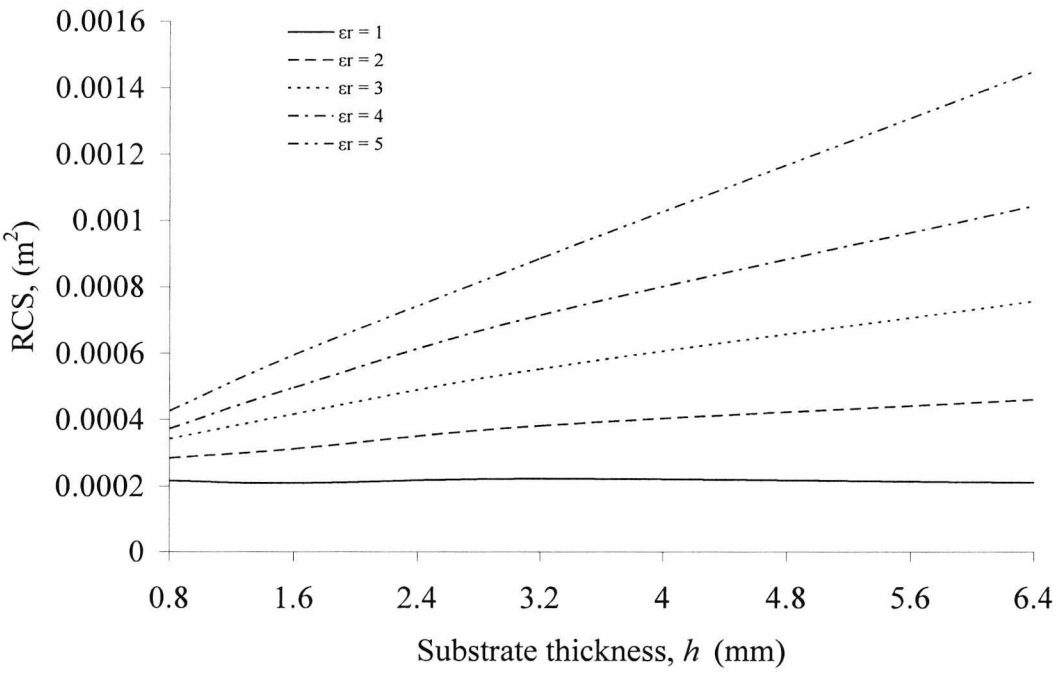

Fig. 5.18: Variation of the RCS for the complementary patch antenna with substrate thickness for different substrate permittivity at 869MHz under IC-load condition.

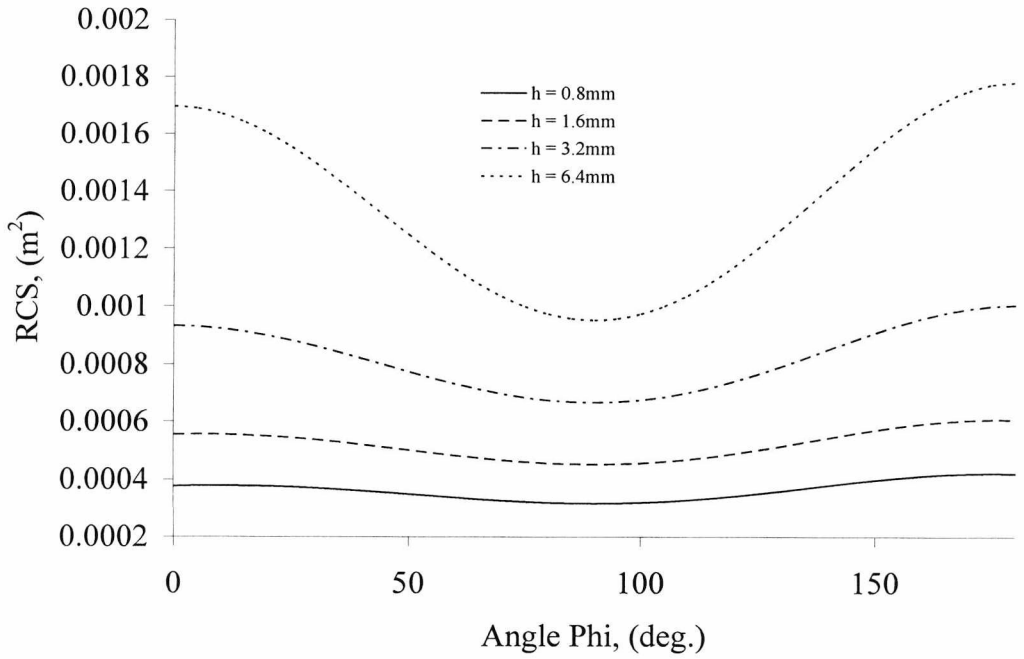

Fig: 5.19: The effect of angle on RCS for different substrate thicknesses 0.8mm and o/c load condition.

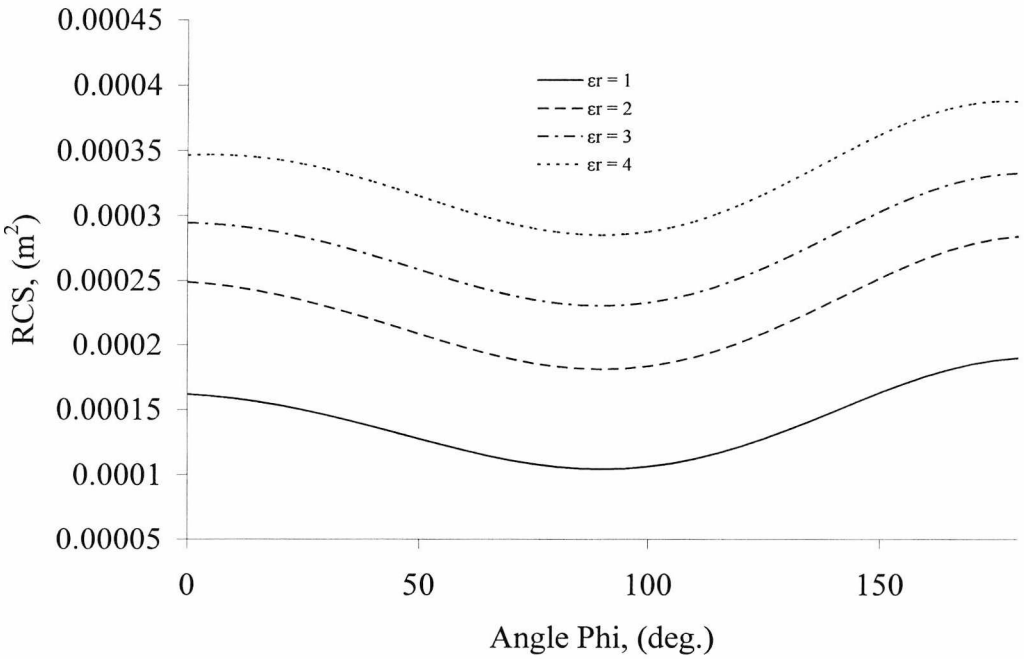

Fig: 5.20: The effect of angle on RCS for different substrate permittivities at 0.8mm and o/c load condition.

These results underscore the need to select tag antenna composition (Fig. 5.16 and 5.18) with additional measure such as inclining tags (Fig. 5.19 and 5.20) at different angles to achieve true RCS maximisation.

In the former case, figures 5.16 and 5.18 show that thicker substrate with higher permittivity offers predictably a higher RCS than its counterpart with a thinner substrate and lower permittivity. RCS values were higher in case for the SPA antenna (Chapter 4) than in the corresponding CPA antenna. At the frequency of 869 MHz and under open circuit condition, the RCS of an SPA antenna having a substrate relative permittivity of 1 and thickness of 0.8 mm is 2.77 times higher than its CPA counterpart. When the substrate thickness is increased to 6.4 mm the SPA becomes 2.79 times higher than its CPA counterpart. Under the same operating condition but substrate relative permittivity of 5, the SPA RCS values are greater than its CPA counterpart by 3.82 times and 3.84 times for substrate thickness of 0.8 mm and 6.4 mm respectively. Clearly a relationship has been established between the two antenna types in terms of their RCS values.

While all radar signals attenuate with distance, an equally important factor in reducing observed RCS has to do with the orientation (azimuth and elevation) of the Reader relative to the tag. A goal of traditional RCS maximization schemes is to manoeuvre the tag in a manner that changes the radar azimuth and elevation such that "peaks" in the tag are presented to the Reader. Figures 5.19 and 5.20 show deeps at angle 90^{o} probably resulting from interferences between closely spaced radiating elements. The graphs suggest that by installing the tag to align to particular direction occasionally causes the tag to present a larger observed RCS.

Tags should be carefully designed to minimize the number of radiating elements that are likely to interfere with each other. The more deeply the tag modulates its radar cross-section, the longer the tag-to-reader link range will be. This study will help route planning scheme which significantly relies on RCS values to align tags to the line of sight with the Reader. The simple route planning scheme will ensure interrogation points were selected minimise the distance to the nearest Reader.

5.5 Read range measurement of the CPA

To obtain a general knowledge of the read ranges, the CPA antenna was integrated with EM422 ASIC chip and attached to various materials (namely: foam, paper ream, dry wood, plastic, glass, and metal) whose electromagnetic properties vary. These materials were selected based on the assumption that they were potential candidates for tag attachment, and offered a variety of complex conductivities and permittivities.

The measurements were conducted in an open laboratory and every effort was made to ensure that the tag was not in close proximity with reflective surfaces in order to keep the effect of scattering to minimum. In all the measurements, a circularly polarised *Ipico* Reader emitting 500 mW was oriented for polarisation match with the tag. The clamp fixture used to attach the tag to the objects was an ordinary masking tape of 0.11 mm thickness which ensured that the antenna performance was not degraded. The tag was oriented along the y-axis and together with the object suspended on PVC.

For each measured range (except for the case of metal), the maximum read range was in excess of 3.0 meters. The average read range was obtained by averaging, in a set of random measurements, the maximum distance at which the antenna could backscatter. The range data achieved is summarised in Table 5.6. The tag range measured on foam is identical to free space measurement. Paper and dry wood showed a slightly reduced range than in the foam material. This decrease is attributed to losses in the wood and paper. The range for ceramics and glass showed further reduction due to detuning. However, since the impedance of the tag is very low when on metal, this range in this case is zero.

The CPA tag performance was specifically tested on wire grid surfaces such as in roll cage that will be encountered in chapter 6 and also on flat sheet of metal. A read range of up 2.5 metre was achieved when the tag was attached directly to a roll cage. However, the range decreases to 0.05 metre when placed directly on flat sheet of metal. By putting a 5mm foam spacer in-between the tag and flat the sheet of metal, a range of 0.2 metre was achieved.

Category	Reading conditions	Read Range
Reader RF Interferences	–	Transmitting at 869 MHz with 0.5W EIRP
Reading range for different tag orientations with reference to the reader antenna	$x - y$ plane vertical (0°); wave incident along z- axis	3.8 metre
	$x - z$ plane horizontal (90°); wave incident along z- axis	3.52 metre
	$x - z$ plane vertical; wave incident along y- axis	0.5 metre
	$y - z$ plane vertical; wave incident along x- axis	1.0 metre
Read ranges on platforms at maximum orientation x–y plane; plane wave incident along z-direction	Foam Paper ream Dry wood Ceramic Glass Wire grid surfaces Close proximity to flat metal sheet Separated with a 5mm foam spacer from metal sheet	3.8 metre 3.41 metre 3.42 metre 3.25 metre 3.20 metre 2.5 metre 0.05 metre 0.2 metre

Table 5.6: A summary of the read range measurements using *iPico* reader having a circularly polarised antenna; one tag read under static condition at a time.

In general, the CPA achieved better read range than its slot patch counterpart (studied in the previous chapter) because matching was influential.

5.6 Conclusion

One of the primary objectives of tag design is to select its antenna configuration based on known electromagnetic properties of the attached objects. To increase the choice of antenna configurations, a patch antenna has been considered, which is of exact complementary shape for the slot antenna studied in Chapter 4. Different frequency-

scaled CPA antennas were examined; it was found that scaling down to (35.4 x 35.4 mm) and (13 x 13 mm) yielded resonant frequencies at 2.45 GHz and 5.8 GHz respectively and can be useful for higher RFID frequencies. The read range of a tag fabricated using the CPA were also investigated and showed variations with attached objects. The CPA tag was read at close proximity to both wire grid surface such as roll cages (roll cage is presented in the next chapter) and flat sheet of metal. This shows potential of using the tag on metallic objects. The CPA achieved a longer read range compared to slot patch due to better matching with the ASIC chip.

The next chapter will investigate the application of tags to a specific profile that is metallic roll cage with periodic surfaces.

5.7 References

[5.1] S. Maci and G. Biff Gentili, "Dual-frequency patch antenna," *IEEE Antennas. Propag. Mag.* Vol. 39, No. 6 December 1997, pp.13-20

[5.2] S. Gao and A. Sambell, "A simple printed antenna," *Progress in Electromagnetics Research*, PIER 60, 119-130, 2006

[5.3] Bhattacharyya A. K., "Long rectangular patch antenna with a single feed," *IEEE Trans. Antennas. Propag.* Vol. 38, No. 7, July 1990, pp.987-993

[5.4] S. H. Al-Charchafchi, W. K. Wan Ali, M. R. Ibrahim and S. R. Baines, "Design of a dual patch triangular microstrip antenna," Applied Microwave & Wireless, March 1998, pp.60-67, p.182-185

[5.5] Greg McFeetors, Michael A. J. Weldon and Michal Okoniewski, "Apreture-fed patch antenna with planar reactive load," *IEEE Antennas and Wireless Progat, Letter,* Vol. 3 2004

[5.6] Hakim Aïssat, Laurent Cirio, Marjorie Grzeskowiak, Jean-Marc Laheurte, and Odile Picon, "Reconfigurable Circularly Polarized Antenna for Short-Range Communication Systems," *IEEE Trans. Microw. Theory. Tech.,* Vol. 54, No. 6, June 2006

[5.7] W. Choi *et al*, "An RFID tag using a planar inverted-F antenna capable of being stuck to metallic objects.

[5.8] Hirvonen, M.; Pursula, P.; Jaakkola, K.; Laukkanen, K., "Planar inverted-F antenna for radio frequency identification", IET Electronics Letters, Volume 40, Issue 14, 8 July 2004 Page(s): 848 – 850

[5.9] Dilbagh Singh, "Small H-shaped antenna for MMIC application," *IEEE Trans. Antennas. Propag*. Vol. 48, No. 7, July 2000.

[5.10] S.K. Padhi, N.C. Karmakar, C.L. Law, "An EM-coupled dual-polarized microstrip patch antenna for RFID applications," *IEEE Microwave and Optical Technology Letters*, Vol. 39 No. 5, December 2003, Page(s): 354 - 360

CHAPTER 6

AN APPLICATION TO WIRE MESH SURFACES

6.1 Introduction

This chapter investigates the feasibility of reading tags through wire meshes such as those on a roll cage. Roll cages are used in distributing goods as they offer adequate security, visual access and ventilation, Fig. 6.1. Wire meshes are preferred in constructing roll cages because they offer a reduction in metal surface area compared to a whole sheet of metal. In addition, their analysis saves on computational time. Roll cages are described later in the chapter. To read all goods simultaneously, it is essential that the read field does not fall below the tag threshold at any location within the roll cage. Thus, the composition of roll cages will be investigated in the context of the behaviour of a tag inside the enclosing volume.

Unfortunately, the detection of RF signals through such reflective screens is difficult due to fundamental physical limitations [6.1]. In particular, the reflections off other surfaces of the cage interfere with the direct signal and therefore develop standing waves with associated nulls. Additionally, the mesh apertures act as efficient frequency dependent surfaces and can become causes of reduction of the EM wave for both transmission and reception. Thus, it is desirable to be able to predict the effect of roll cages on tag performance.

Generally, the aperture in the walls of the enclosure can serve to exchange electromagnetic energy by selecting energy bands [6.2]. The local resonances induced by the sub-wavelength periodic structures can be exploited to enhance electromagnetic wave transmissions [6.3] - [6.5]. Efficient use of bandwidth can be achieved by controlling the transparency of such roll cages at the frequencies of operation. In addition, the link

between a Reader and a tag can be strengthened while reducing unwanted sources of interference [6.6].

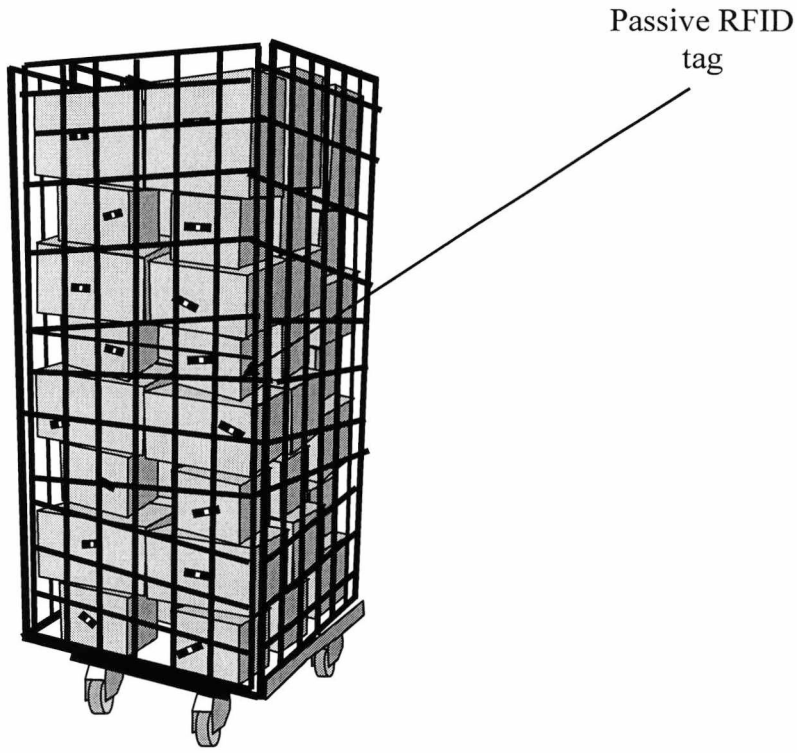

Fig. 6.1: Loaded roll cage containing tagged cartons

Kraus applied the analysis of closely spaced elements to the application of frequency selective surfaces [6.7]. Following this publication and work by other including Parker [6.8], the capability of a surface to discriminate certain frequencies was firmly established.

In reference [6.9], the electromagnetic wave penetrating through apertures in conducting surfaces was investigated. Bunting and Yu used statistical models to study the field penetration in a rectangular box [6.10] and showed the transmission of the external field into the enclosure depends to a large extent on the mesh sizes. This chapter will focus on investigating this effect in the particular application of an RFID system. Since the operational constraints within an enclosed surface have not been completely studied, this

extends the previous work that has already been done on transponder antennas in free space (see Chapter 3 – 5). If the influence of the reflective side of such roll cages can be characterized, then a more robust communication system can be designed.

In Section 6.2, the roll cage model is illustrated; the transmission responses for various wire-mesh size cages are explored in Section 6.3. In Section 6.4, the standing wave is analysed for various mesh size roll cages. Section 6.5 presents the read field of roll cages for the cases when empty and loaded. The Chapter concludes in section 6.6.

6.2 Roll Cage Models

Roll cages consist of various mesh sizes and shapes of meshes of wire and as example is illustrated in Fig. 6.2. The figure shows a perfectly conducting mesh enclosing a volume within which electromagnetic (EM) fields propagate. There is no single standard for roll cage design and some have up to two sides removable. The cages all have a metal trolley base and between 2 and 4 sides as shown in Fig. 6.1. The exact dimensions vary between designs, but typical values are given in Table 6.1.

CST Microwave studio was used to calculate results that simulate the field distribution within a cage, using the cage bar separations given in Table 6.1 which were measured from a real roll cage. The electrical spacing of the bars at 869 MHz and 2.45 GHz was considered. There are roll cage designs with wider mesh sizes, but these dimensions give insight into the extreme case of the situation where standing waves may be induced across the width of the enclosure.

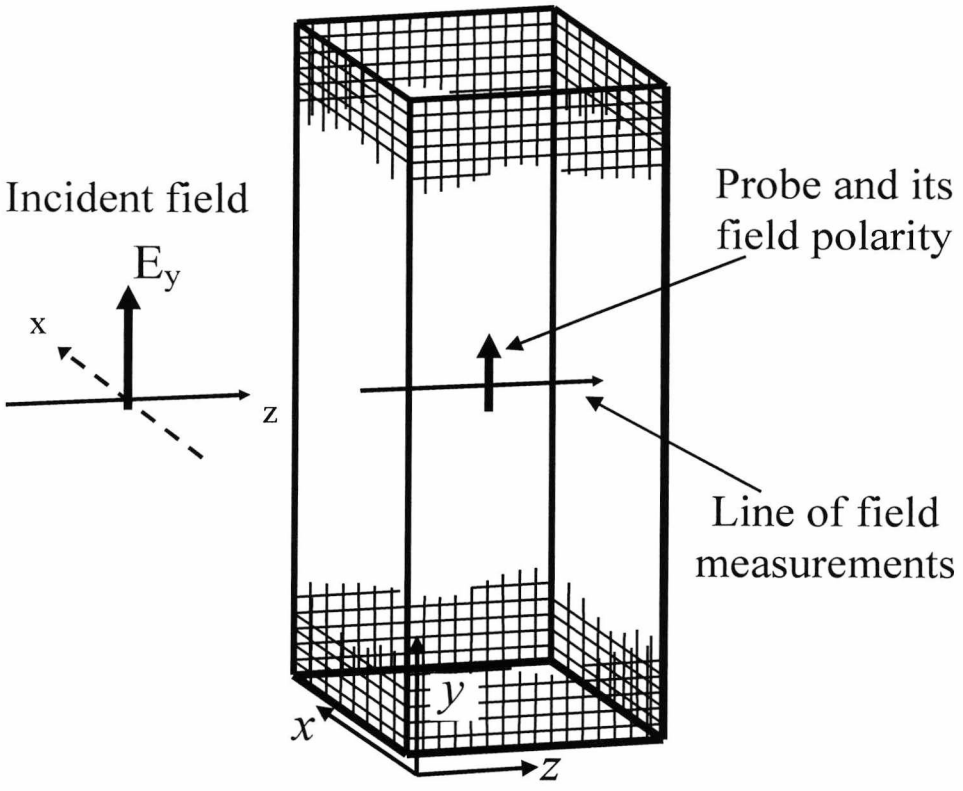

Fig.6.2. Simulated roll cage line of field variation

Cage dimensions	Square mesh horizontal and vertical mesh sizes equal
x: 650 mm *z*: 700 mm *y*: 1200 mm	50 mm; 0.14λ × 0.14λ at 869MHz and 0.41λ × 0.41λ at 2.45 GHz
	75 mm; 0.2λ at 869MHz and 0.6λ at 2.45GHz
	100 mm; 0.28λ at 869MHz and 0.8λ at 2.45GHz

Table 6.1: Dimension of a typical roll cage

6.3 The effect of mesh sizes on the transmission response of roll cages

In this section, the transmission response for EM radiation through an electrically large metal grid roll cage, measuring $650 \times 1200 \times 700$ mm, is numerically predicted using the CST Microwave simulator. In the simulation, the front surface is evenly illuminated by a plane wave incident in the direction of the z-axis (refer to Fig. 6.2). The wave is linearly polarized with the E-field in the direction of y-axis. The resultant fields were investigated for both the single probe and multiple probes responses. The finite conductivity of the walls gives rise to power loss and an effective resistance [6.11].

6.3.1 Transmission responses due to mesh sizes

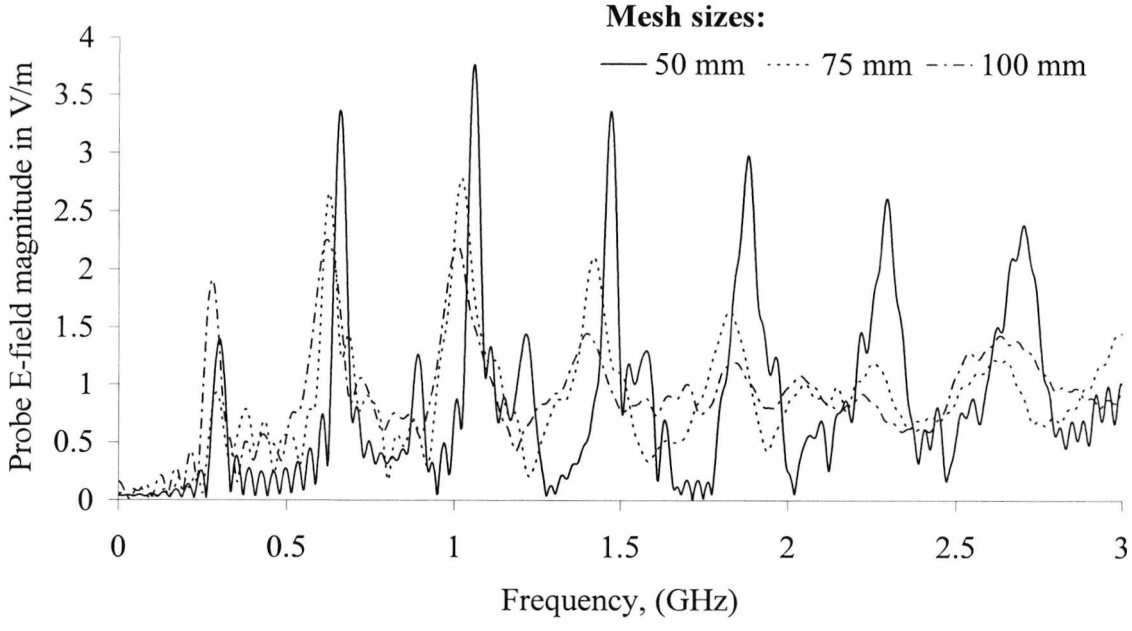

Fig. 6.3: A comparison of the transmission response for different mesh sizes showing the y-component of the electric field for the frequency variation from 0 to 3 GHz.

Typical transmission response for a probe located at x = 325 mm, y = 600 mm, z = 350 mm and oriented in the y-direction inside empty cages having mesh sizes of 50 mm, 75

mm and 100 mm are shown in Fig. 6.3. In the Time domain analysis, all field values are normalised to the peak power of the simulated reference signal, which in the case of plane wave here is defined as 1 V/m.

The simulated frequency ranges from 0 to 3 GHz. The results show the dependence of transimissivity on the mesh sizes of the roll cage. A common trend is observed in the curves having frequency spacing (looking at the peak waveforms) of approximately 380 MHz. The spacing slightly increases as the frequency increases and this is due to the nature of the reflective surface. The implication of the spacing will be explored under subsection 6.4.2. The peak amplitudes are seen to decrease slightly with increasing mesh sizes. A decrease in the frequencies at which these peaks occur is observed as mesh sizes increases, which accounts for further deviation in the transmission responses.

The resonances are caused by cavity standing wave which will now be considered in relation to frequency peaks discussed in Fig. 6.3. Let the frequency be denoted by f_n, and n, the numbers of standing half waves inside the cage of length L, (n is 4 and L is 0.7 m according to Fig. 6.6 (a)) from which follows:

$$n\left(\frac{\lambda_n}{2}\right) = \left(\frac{\upsilon}{2f_n}\right)n = L \qquad \frac{\upsilon n}{2L} = f_n \quad (n=1 \ \textit{for} \ \textit{fundamental}) \tag{4.1}$$

As the frequency is increased, the next resonance is at $f_{(n+1)}$:-

$$\left(\frac{\upsilon}{2f_{(n+1)}}\right)(n+1) = L \qquad \frac{\upsilon(n+1)}{2L} = f_{(n+1)} \quad (\textit{harmonics}) \tag{4.2}$$

Hence the frequency spacing, which is the difference between equations 4.1 and 4.2 becomes:

$$f_{(n+1)} - f_n = \frac{\upsilon}{2L}[n+1-n] = \frac{\upsilon}{2L} = 380 \ MHz \tag{4.3}$$

where,

$\upsilon = 3.8 \times 10^8$, the velocity of light

$L = 0.7$ *metres* , the length of cage in z direction.

The frequency spacing is not exact across the frequency under consideration due to imperfection in the metallic mesh cavity. Lima and Parker carried out a detailed research on the design of double layer FSS using Fabry-Perot approach [6.12]. Their work gives a framework for interpretation of the transmission and reflection characteristics of multilayer FSS which leads to a systematic procedure that overcomes much of the trial and error involved in the design of these structures.

In the following section, the insertion loss due to planar grid surfaces will be investigated.

6.3.2 Insertion loss due to mesh sizes

Figure 6.4 (a) illustrates a wire mesh structure with mesh sizes of 50 × 50 mm typically used in constructing roll cages. Roll cages grids are frequency selective surface (FSS) screens with filtering characteristics. Properly designed FSS would pass field at tag frequency and stop standing wave in the roll cage. Using equivalent-circuit model, Zhi Liang Wang *et al.* designed and tested frequency-selective surfaces (FSS's) with gridded- and double-square elements useful for suppressing the harmonics radiation in microwave power transmission system [6.13].

Multiple reflections between internal surfaces create nulls or regions of low field which give poor reception and low sensitivity areas for the tag. This will be demonstrated later in the chapter by determining field levels that range over a series of positions through the system. The generation of this field includes electromagnetic energy passing through the roll cage apertures that is expected to be scattered by the wire grids [6.14].

The insertion loss (often referred to as attenuation) caused by a single side of the cage was obtained by simulating the electric field magnitude 200 mm behind an infinite grid of mesh sizes 50 × 50 mm [Fig. 6.4 (b)] and then repeating the process without the wire mesh surface present. For maximum power transfer the insertion loss should be as small

as possible. That is, the ratio of received power to the transmitted power should be as close to unity or as close to 0dB as possible. The losses due to the various mesh sizes are presented in Table 6.2 below.

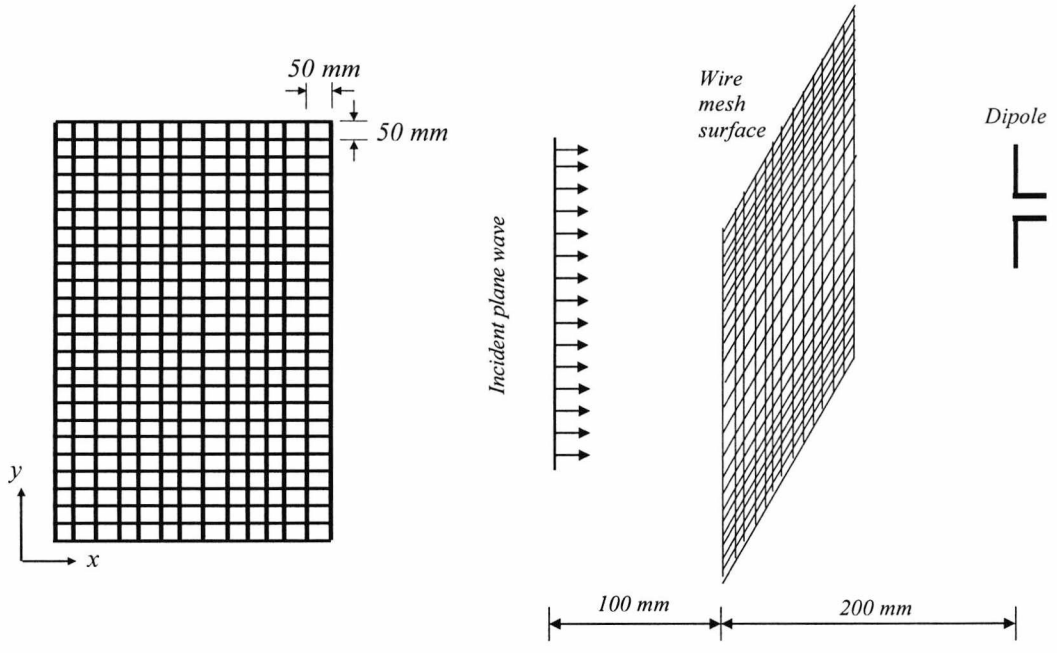

(a) (b)

Fig. 6.4: Wire mesh structure with mesh sizes of *50* × *50* mm typically used in constructing roll cages (a) planar mesh surface (b) schematic for predicting insertion loss due to (a).

Mesh sizes (mm^2)	**Insertion loss (dB)**	
	869 MHz	**2.45 GHz**
50 × 50	- 8.05dB	-3.07dB
75 × 75	-3.31	-2.02
100 × 100	-1.18	-1.64

Table 6.2: The insertion loss due meshes sizes of the roll cage

In so far as these losses represent the waves reflected back from the surface of the cage, it is an important parameter in determining the size of the standing wave ratio and hence the likely depth of nulls within the cage.

6.4 Standing wave inside roll cages

The insertion losses of a planar wire mesh due to the mesh sizes has been analysed in subsection 6.3.2 above which shows that the loss decrease with increasing mesh sizes. Next, consideration is given here on the situations which exist when there are interfaces forcing two waves to travel in opposite directions (such as in the positive and negative z-direction of the roll cage illustrated in Fig. 6.2). The overall reflections off the second interface combine with further incident waves to build up standing waves.

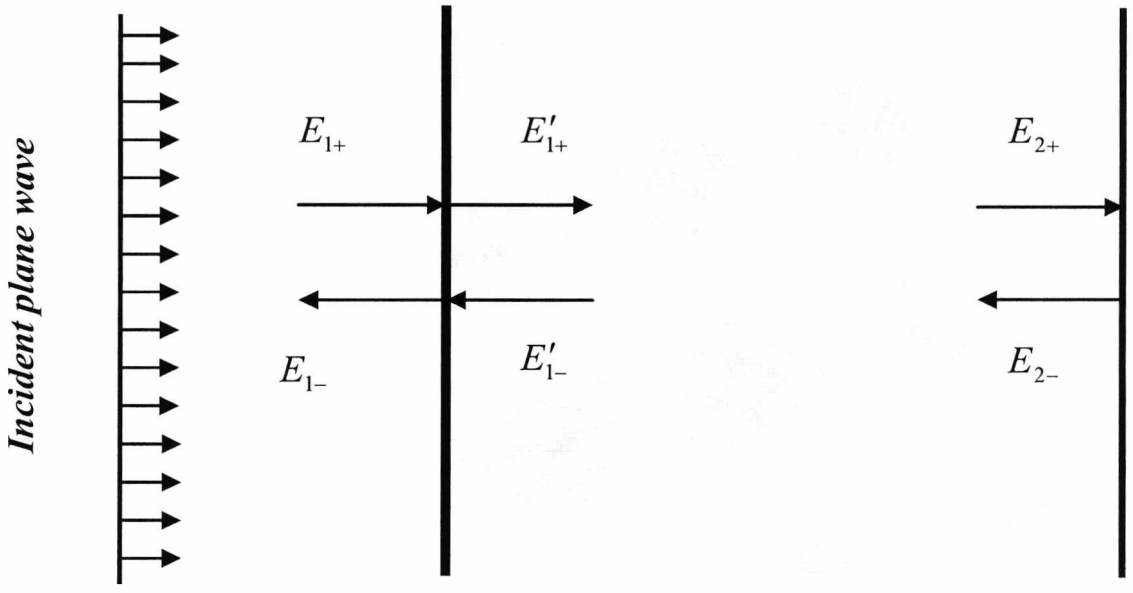

Fig. 6.5: Two roll cage interface

A detailed analysis of the standing wave ratio (VWSR) can be obtained in reference [6.15], [6.16]. With reference to Fig. 6.5:

$$\mathbf{VSWR} = \frac{E_{\max}}{E_{\min}} = \frac{E'_{1+} + E_{2+}}{E'_{1} - E_{2+}} \qquad 6.1$$

where,

E'_{1+} = amplitude of the incident wave and E_{2+} = the amplitude of the reflected wave.

$(E'_{1+} + E_{2+})$ = the maximum value of a standing wave envelope given by the sum of the amplitudes of the incident and reflected waves.

$(E'_{1+} - E_{2+})$ = the minimum value of a standing wave envelope given by the difference in the amplitudes of the incident and reflected waves.

The transmission through the roll cage enables a numerical estimate to be made in terms of the standing waves inside the cavity which develop because the reflections off the second cage surface trap energy. However, the magnitude or ratios of the resultant standing wave in relation to the specific range structure (in particular mesh size) must be considered to achieve numerically accurate. Thus, in this section, the dependence of the standing wave on the mesh sizes will be critically examined.

6.4.2 Standing wave along the *z*-direction

The variations of the electric fields inside the 50 mm mesh sized cage due to standing waves at 869 MHz and 2.45 MHz in the *z*-direction are shown in Fig. 6.6 for the coordinate: $x = 325$ mm, z ranging from 0 to 700 mm and for different planes of y. Figure 6.6 (*a*) and (*c*) indicate minima occurring adjacent to the both sides of the cage and at intervals of 0.5λ at the operating frequency. The corresponding field contours are shown in Fig. 6.6 (*b*) and (*d*). Obviously, the field contours vary as for (*a*) and (*b*) respectively.

Figure 6.7 (*a*) and (*c*) shows the simulated standing wave obtained from a roll cage with mesh size of 75 mm for the two frequencies. The electric fields were evaluated along a line curve passing through the coordinates $x = 325$ mm, $y = 170$, 300 and 600 mm, and $z = 0$ - 700 mm at the RFID frequencies of 869 MHz and 2.45 GHz respectively. Figure 6.7

(b) and (d) show the contour maps at the two frequencies which varies in accordance with the plots in (a) and (c). The corresponding standing wave for the 100 mm mesh sized cage is shown in Fig. 6.8. Fig. 6.8 (*a*) and (*c*) are for the standing waves plot in the z-direction at 869 MHz and 2.45 GHz while Fig. 6.8 (*b*) and (*d*) illustrate their contour maps at the respective frequencies.

The standing wave for the case of the 75 mm cage is similar to that for the 50 mm mesh size cage with peaks and nulls located at every half wavelength interval. The first peak occurs at quarter wavelength from the surface. The most obvious and significant variation in the standing wave form is that the nulls increasingly becomes shallower as the mesh size increases. For example, the field magnitude at the first trough corresponding to a half wavelengths from the surface increases from 0.25 Vm^{-1} (for the 50 mm cage) to 0.3 Vm^{-1} and 0.55 Vm^{-1} for the 75 mm and 100 mm mesh size cages. On the other hand, the first peak magnitude for the standing waves, corresponding a quarter wavelength from the surface, decreased from 2.4 Vm^{-1} (for the 50 mm mesh size cage) to 1.64 Vm^{-1} and 1.35 Vm^{-1} for the 75 mm and 100 mm mesh size cages.

Compared with the fields for the 50 mm cage, the peak amplitude decreased while the minimum amplitude increased. In the 50 mm cage, the peak amplitude was 3 Vm^{-1} at 113.75 mm while the minimum was 0.28 Vm^{-1} at 600 mm for 869MHz; at 2.54 GHz the corresponding amplitudes are 2.5 Vm^{-1} and 0.015 Vm^{-1}. While the peak amplitude for both frequencies decreased to 2.75 Vm^{-1} and 1.4 Vm^{-1} respectively, the minimum amplitude increased to 0.75 Vm^{-1} and 0.48 Vm^{-1} respectively (the nulls are now less severe as the mesh size increased). This trend continued for all the fields considered in the two planes: x – y and y – z plane.

The contour maps of the field inside the various mesh sized cages were also shown for the operating frequencies, which replicate the corresponding standing wave pattern. Hence, the position of the peak field corresponds to $\lambda/4$ which is at z = 86.25 mm and

repeats at every halfwavelength interval. Conversely, the receptivity is low at $\lambda/2$ which corresponds to $z = 172.5$ and repeats at every halfwavelength interval.

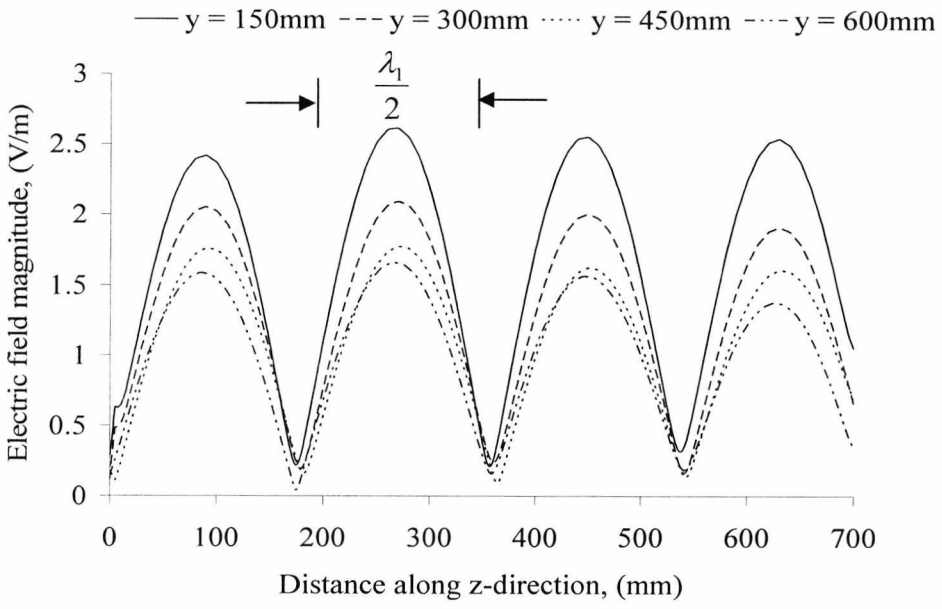

(a)

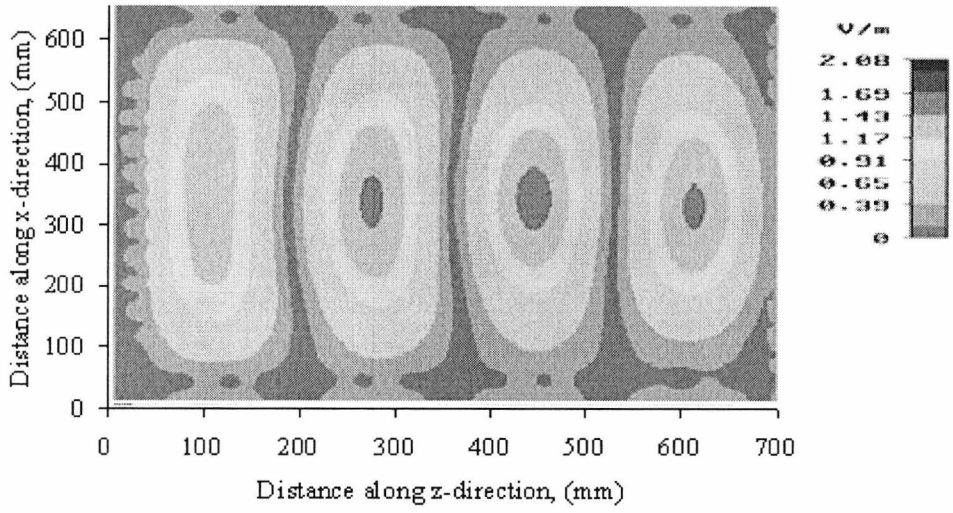

(b)

Fig 6.6 (a) and (b): Comparison of the variation of field in the z- direction for the roll cage encountered in Section 6.2 with mesh size of 50 mm through the coordinates

x = 325 mm, y = 600 mm and z = 0 to *700* mm at 869 MHz (a) standing wave (b) contour maps of the field at y = 600

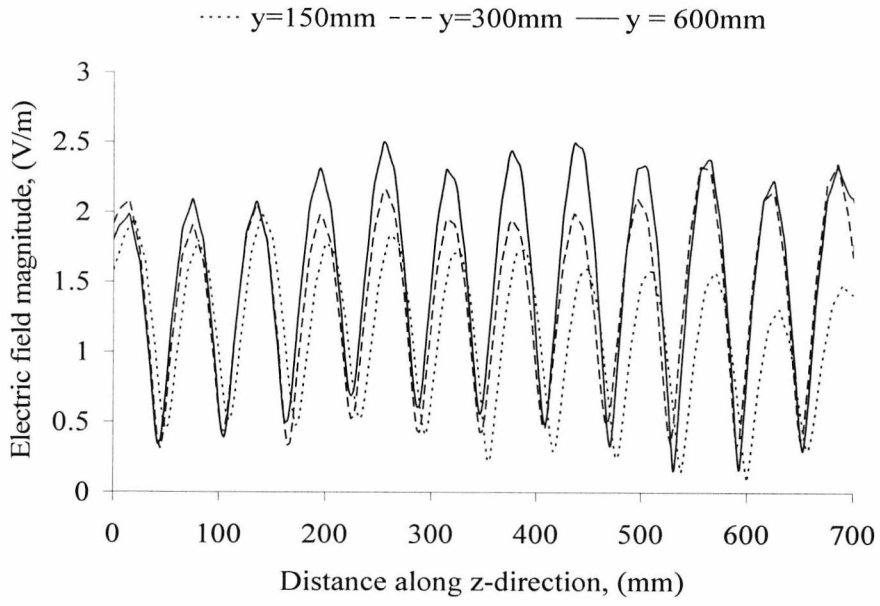

(c)

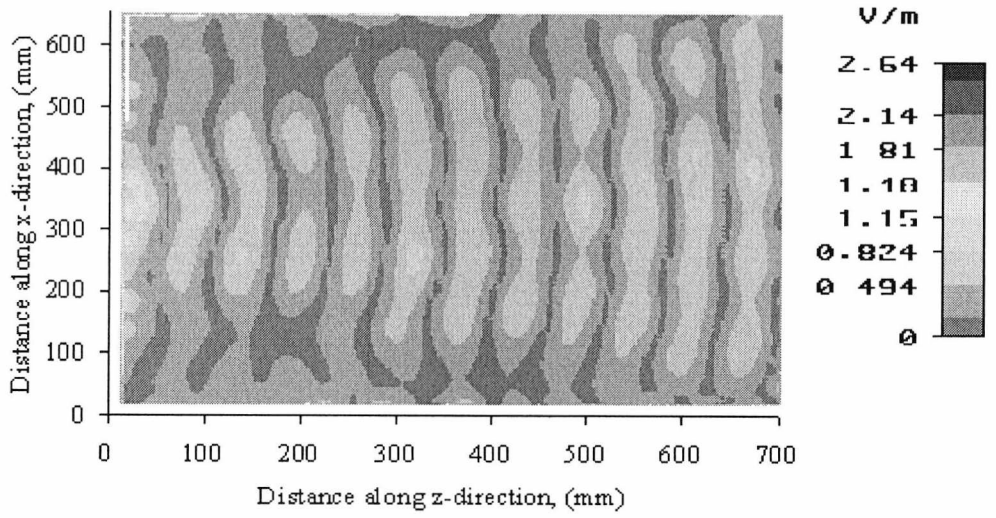

(d)

Fig 6.6 (c) and (d): As for (a) and (b), but (c) standing wave at 2.45 GHz (d) contour maps of the field at y = 600 at 2.45 GHz.

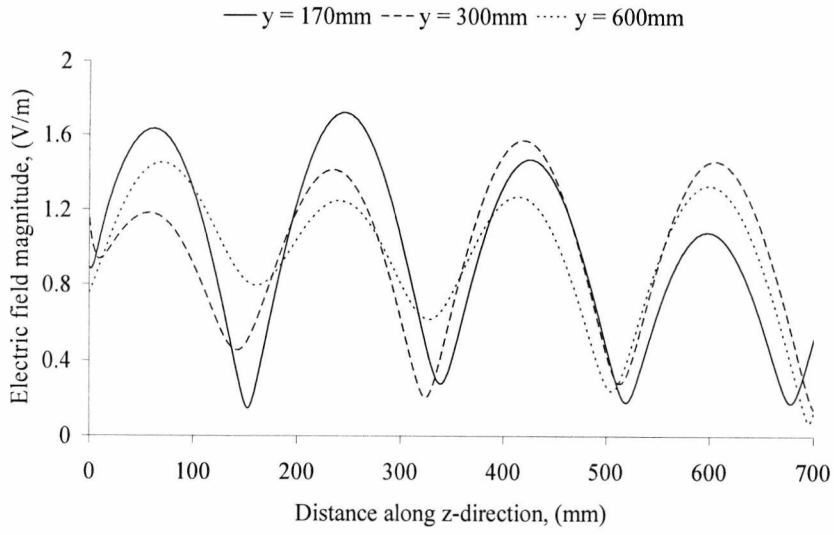

(a)

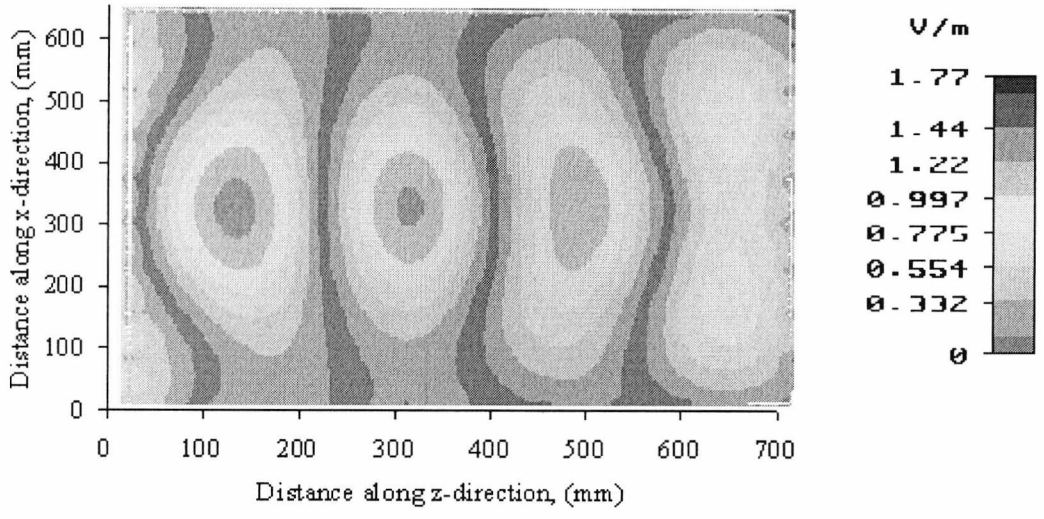

(b)

Fig. 6.7 (a) and (b): Comparison of the variation of the field in the *z*-direction for different planes at y for the roll cage encountered in section 6.2 with mesh size of 75 mm at the coordinate: x = 325 mm, y = 170 mm, 280 mm and 600 mm and for z ranging from 0 to 700 mm for the frequencies of 869 MHz (a) standing wave (b) contour maps of the field at y = 600.

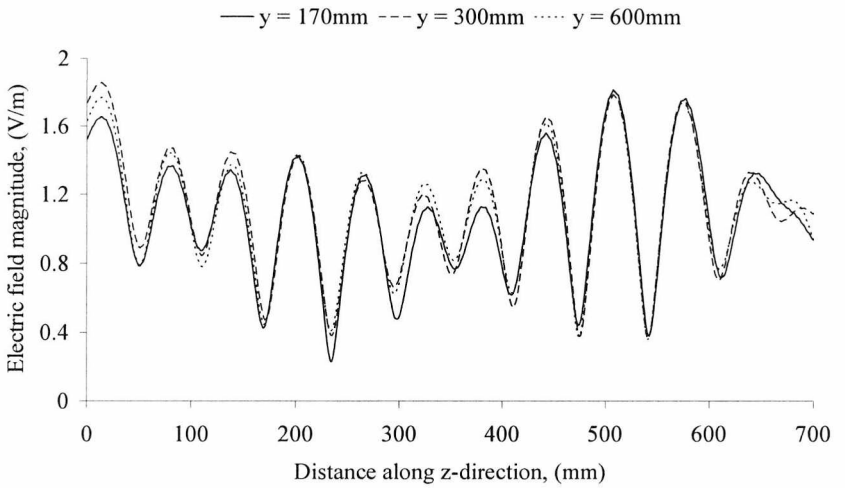

(c)

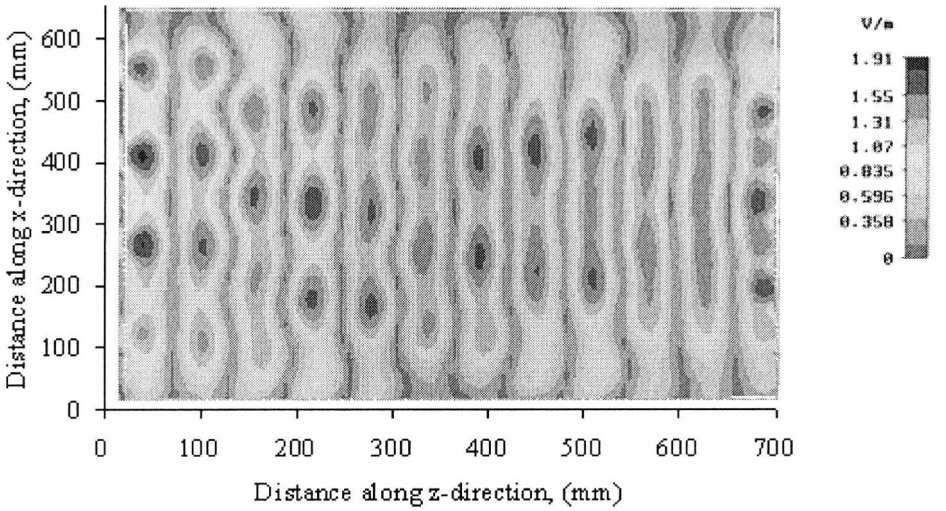

(d)

Fig. 6.7: As for (a) and (b), but (c) standing wave at 2.45 GHz (d) contour maps of the field at $y = 600$ at 2.45 GHz.

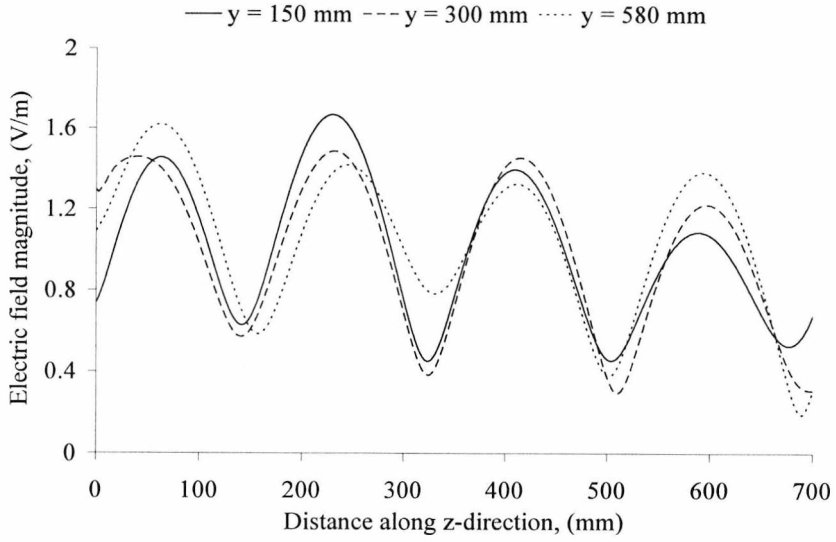

(a)

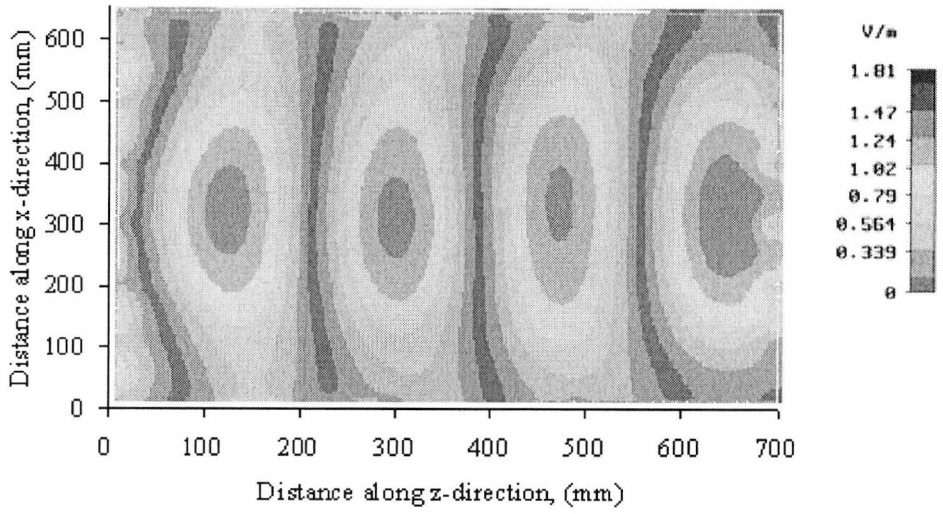

(b)

Fig 6.8: Comparison of the variation of the field in the z-direction for different planes at y for the roll cage encountered in section 6.2 with mesh size of 100 mm at the coordinate: x = 325 mm, y = 170 mm, 280 mm and 600 mm and for z ranging from 0 to 700 mm for the frequencies of 869 MHz (a) standing wave (b) contour maps of the field at y = 600

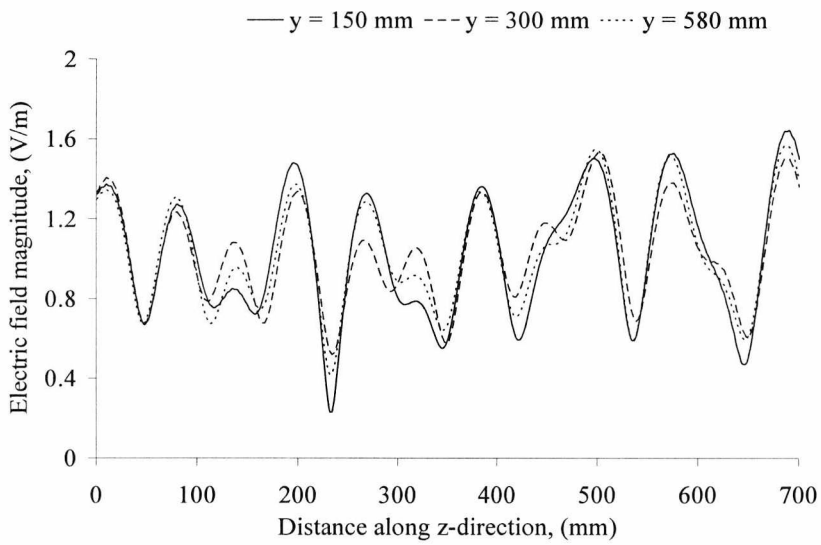

(b)

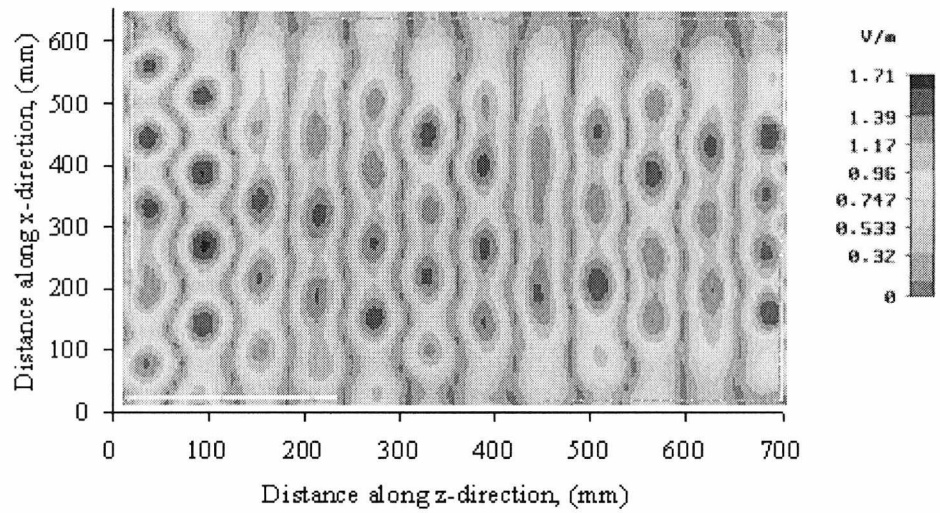

(c)

Fig 6.8: As for (a) and (b), but (c) standing wave at 2.45 GHz (d) contour maps of the field at $y = 600$ at 2.45 GHz.

Fig. 6.6 (*b*) and (*c*) show that for both frequencies, the levels of peaks are very close to each other across the z-direction however, it decreases from the centre (i.e. x = 325 mm) spreading out in the positive and negative x-direction which are associated with the reflection coefficient of the cage. The peaks levels become increasingly distorted as the mesh sizes increases; this effect is more noticeable as the frequency of operation increases and as mentioned earlier is attributed to resonance or diffraction effects. Another interesting phenomenon here is that coupling between the field and the mesh surfaces induce more energy near x = 0 and 650 mm. This coupling enhances the detection of tag inside the enclosure as will be presented later in this chapter. At the boundaries of the cages, the magnitude of the reflected and diffracted wave re-enforce each other and vice versa depending on the location along the z-direction.

A comparison between the different mesh sized cages studied above shows that in the case of a 50 mm mesh, a clear standing wave due to the compact nature of the wire meshes is shown to have, at most -10dB deep nulls occurring at z = 172.5 mm or 345 mm. Larger mesh size cages of 100 mm tend to allow more travelling wave to pass through the surfaces which leads to more energy being lost to the system. Consequently, the resulting standing wave is imperfect with shallower nulls. In this case, the null was at most -1.67dB. The null for the 75 mm mesh sizes cage is intermediary between the above two cases and at most -4.8dB. At the frequency of 2.45 GHz, the depth of the nulls for the 50 mm, 75 mm and 100 mm sized cages correspond to -5.4dB, -4.75dB and -1dB. All results were obtained for the case of a line taken through the coordinate x = 325mm, y = 600 for z ranging between 0 and 700mm.

Comparing Fig. 6.6 (*c*) with Fig. 6.7 (*c*) and Fig. 6.8(*c*) shows increasing distortion as the mesh spacing increases from 0.4λ to 0.6 λ and 0.8 λ respectively. This can be attributed to resonance or diffraction effects which occur as the mesh sizes approach the operational wavelength.

It is expected that a tag capable of operating at both frequencies (such as the novel Slot Patch Antenna, SPA proposed in Chapter 4) will benefit from frequency diversity for all but two nulls situated at z equal to 178 mm and 538 mm respectively.

6.4.3 Standing wave along the *y*-direction

In the vertical direction (i.e. y-direction), the field varies as shown in Fig. 6.9 (*a*) and (*b*) for the absolute value of the electric field lying along a line at the coordinates: x = 325 mm, z = 355 mm and y = 0 to 1200 mm at the operating frequencies of 869 MHz and 2.45 GHz respectively. Although the field strength falls to its minimum at the mid-height of the cage, there are no severe nulls in the vertical direction which correspond to the peaks at z = 86.25 mm and 623.75 mm for both frequencies under consideration. Nevertheless, nulls occur when the vertical line corresponds to the nulls along the z axis: for example at z = 172.25 mm and 345 mm for both frequencies. In general, the field variations here are associated with the direct reflections between the top and bottom wire meshes of the roll cage.

In Fig. 6.10 (*a*) and (*b*), the variations of the field in the y-direction of the roll cage with mesh sizes of 75 mm for the lower and upper frequencies are shown. The electric field was evaluated along a line passing through the coordinates x = 325 mm, and z = 65 mm for the two RFID frequencies under consideration. The corresponding fields for the 100 mm mesh size cage are shown in Fig. 6.11 (*a*) and (*b*).

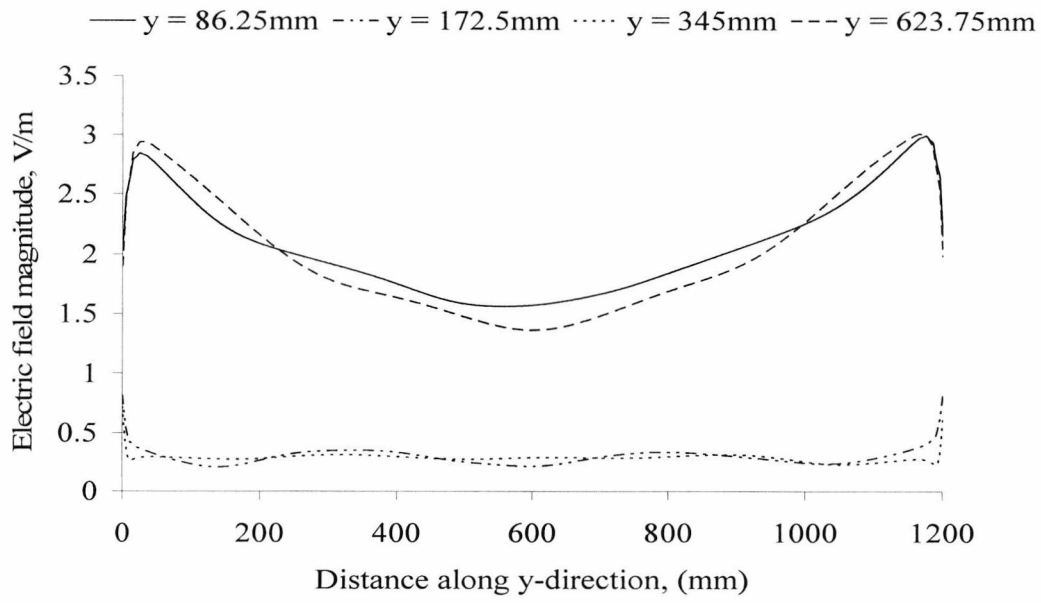

(a)

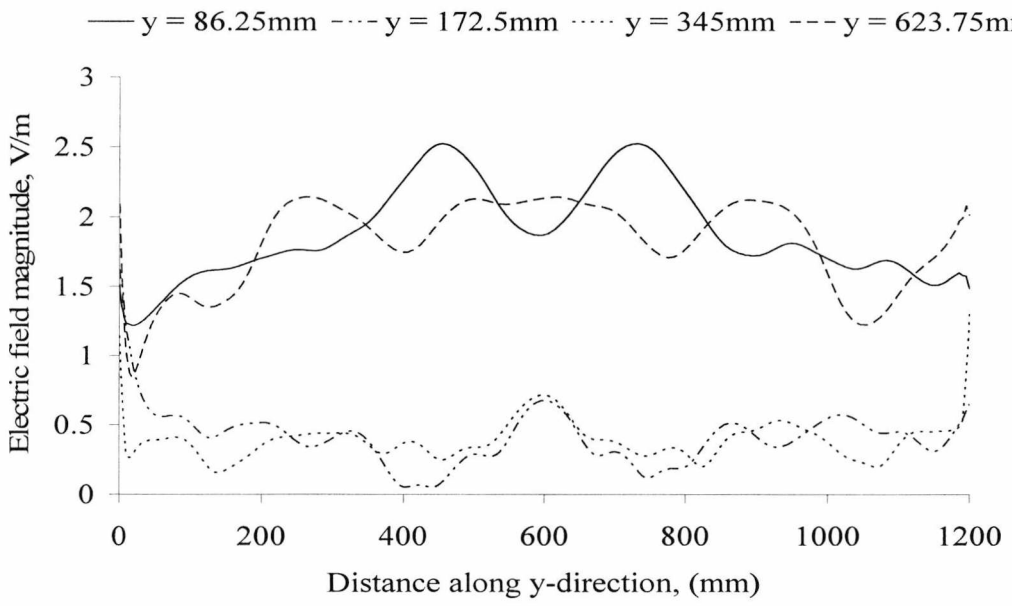

(b)

Figure 6.9: The variation of the field in the y-direction in roll cage with bar to mesh sizes of 50 mm at the coordinates x=355 mm, y = 0 to 1200 mm, z = 355 mm for the frequencies of 868MHz and 2450MHz for a cage with mesh size of 50 mm, (*a*) At 869 MHz (*b*) 2.45GHz.

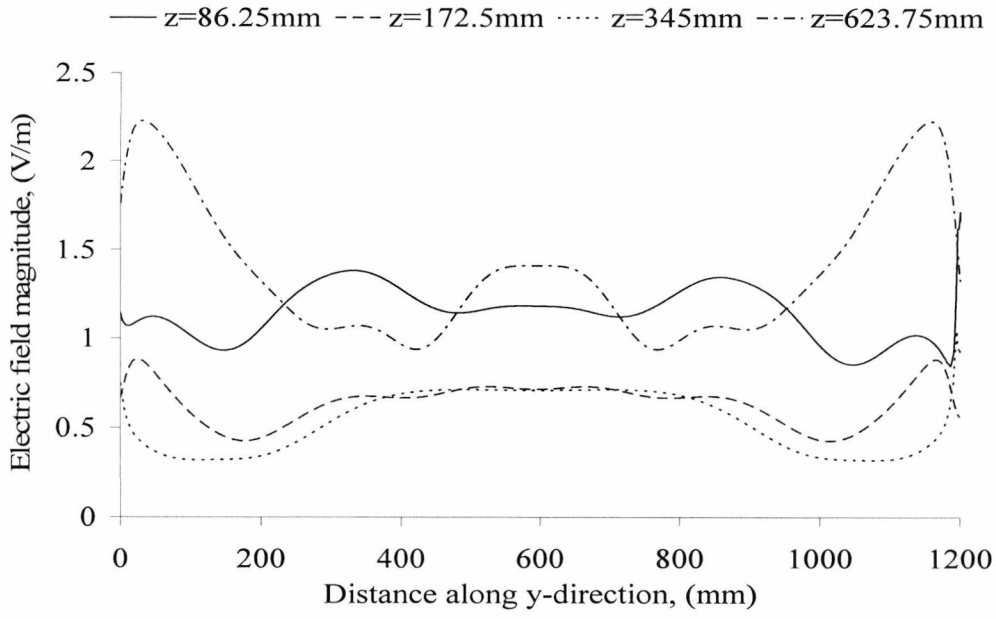

(a)

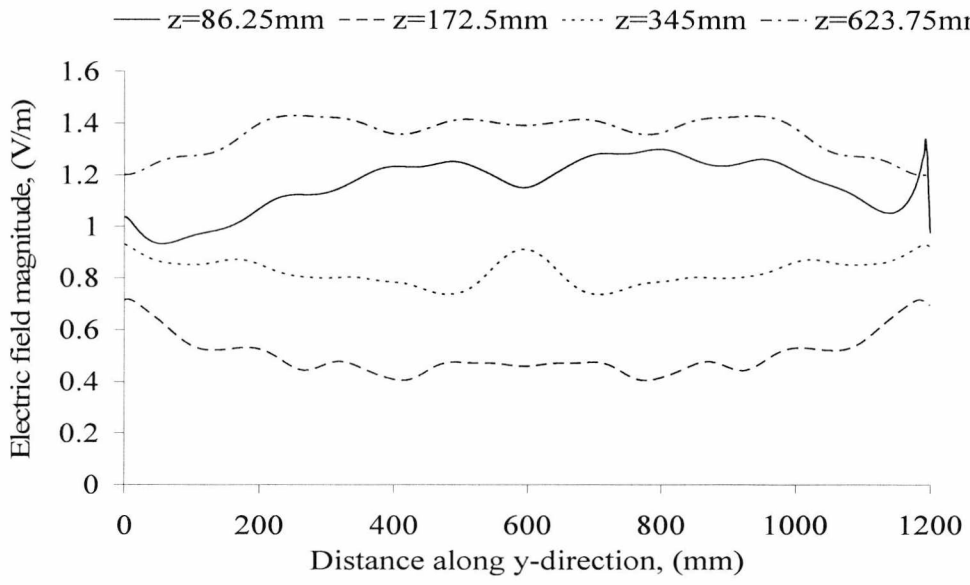

(b)

Figure 6.10: Comparison of the variation of the field in the y-direction for different planes at z for the roll cage encountered in section 6.2 with mesh size of 75 mm at the coordinate: x = 325, z = 86.25 mm, 172.5 mm, 355 mm and 623.75 mm and y = 0 – 1200 mm for the frequencies of (***a***) 868MHz and (***b***) 2450MHz.

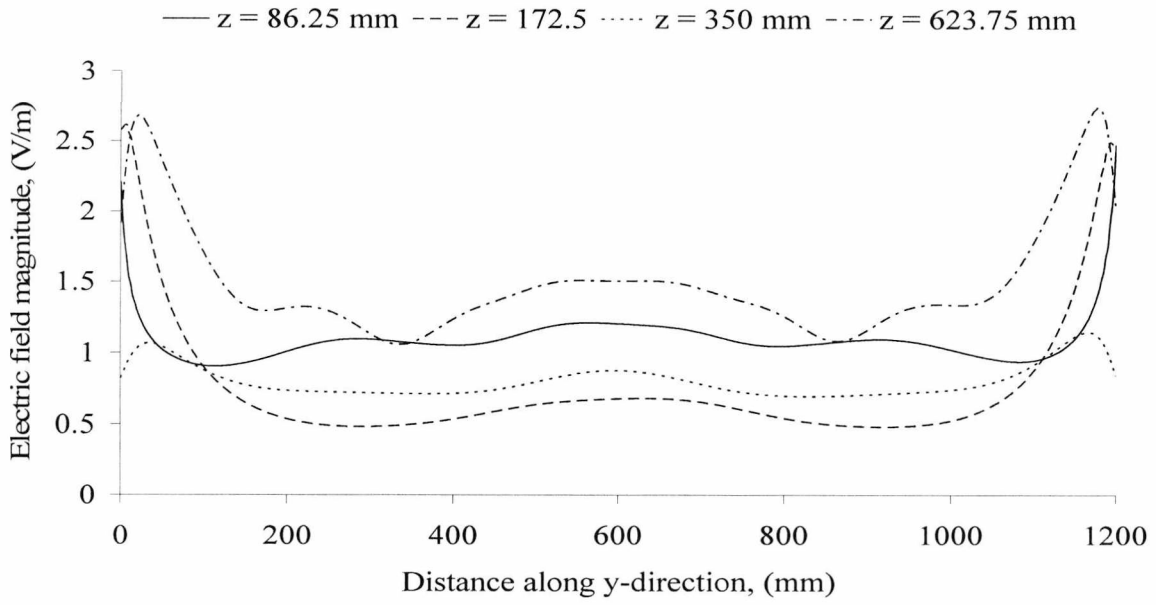

(a)

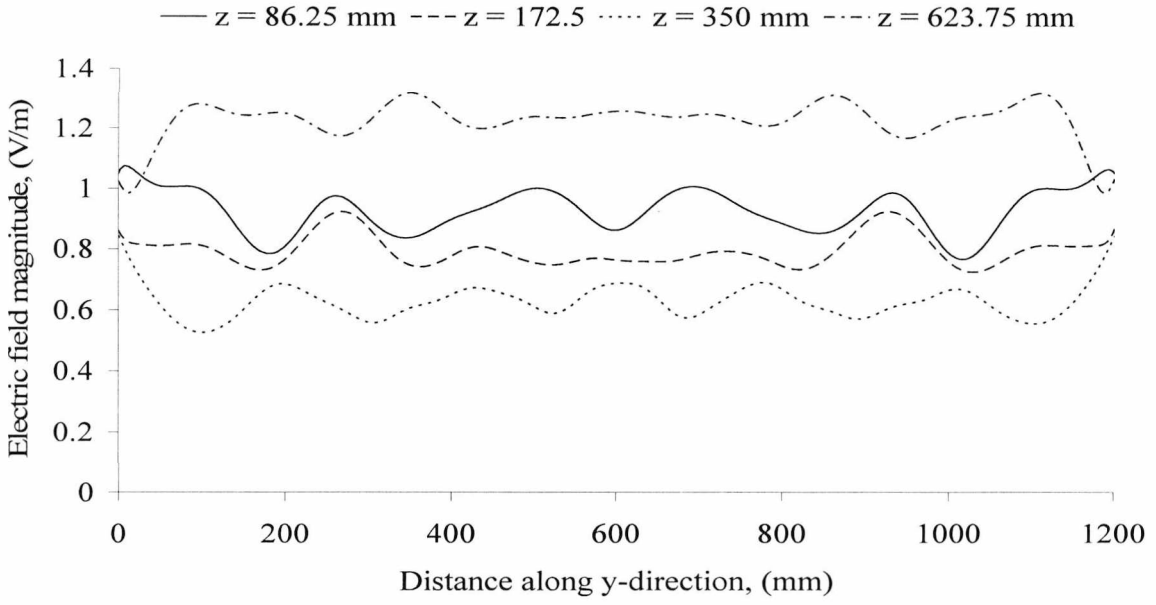

(b)

Fig. 6.11: The variation of the field in the y-direction in the roll cage encountered in section 6.2 with mesh size of 100 mm through the coordinates x = 325 mm, and z =650 mm for the frequencies of (*a*) 869 MHz and (*b*) 2450 MHz.

6.4.4 Standing wave along the *x*-direction

In the ***x***-direction, the field variation has been evaluated along the coordinates: $y = 600$, ***x*** ranging from 0 to 650 mm and for different planes at $z = 86.25$ mm, 345 mm and 623.75 mm (corresponding to 0.25λ, λ and 1.8λ). A comparison of the curves for a cage with mesh size 50×50 mm is shown in Fig 6.12 for the two RFID frequencies under consideration. Fig. 6.13 shows the corresponding field distributions for a cage with mesh size 75×75 mm while Fig. 6.14 corresponds to 100×100 mm mesh size cage. In general, there are no severe nulls in the vertical direction, though at 869 MHz, the field strength falls to its minimum in the mid-height of the cage.

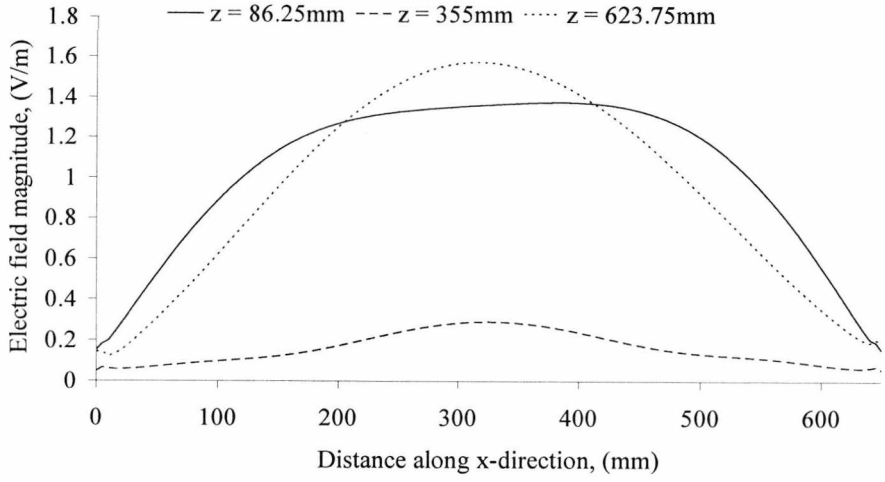

(a)

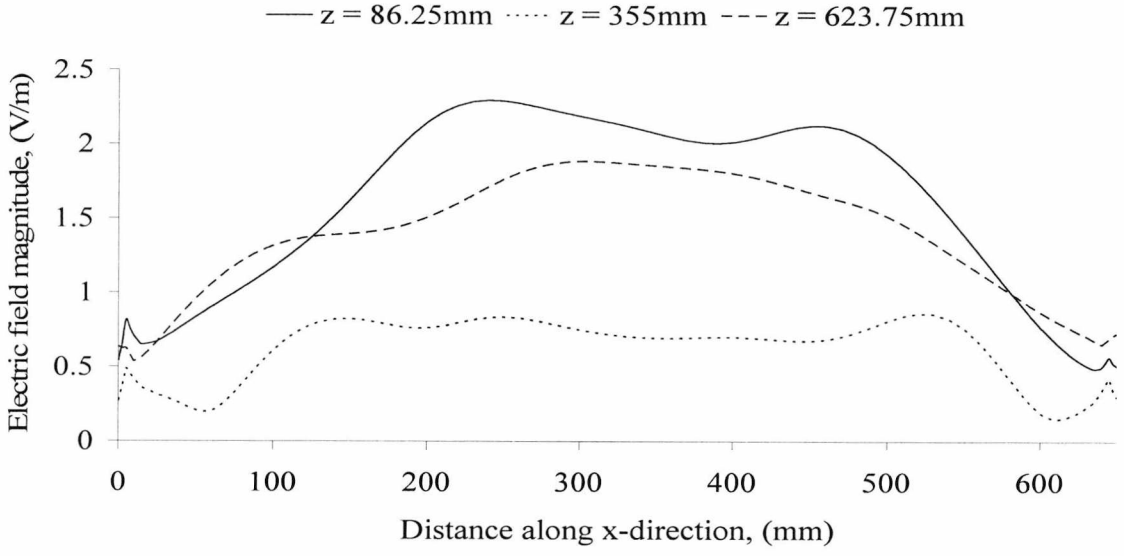

(b)

Figure 6.12: Comparison of the variation of the field in the ***x***-direction for different planes at ***z*** for the roll cage encountered in section 6.2 with mesh sizes of 50 mm at the coordinate: ***y*** =600 mm, ***z*** =86.25 mm, 355 mm and 623.75 mm and ***x*** = 0 – 650 mm for the frequencies of (***a***) 868 MHz and (***b***) 2450 MHz.

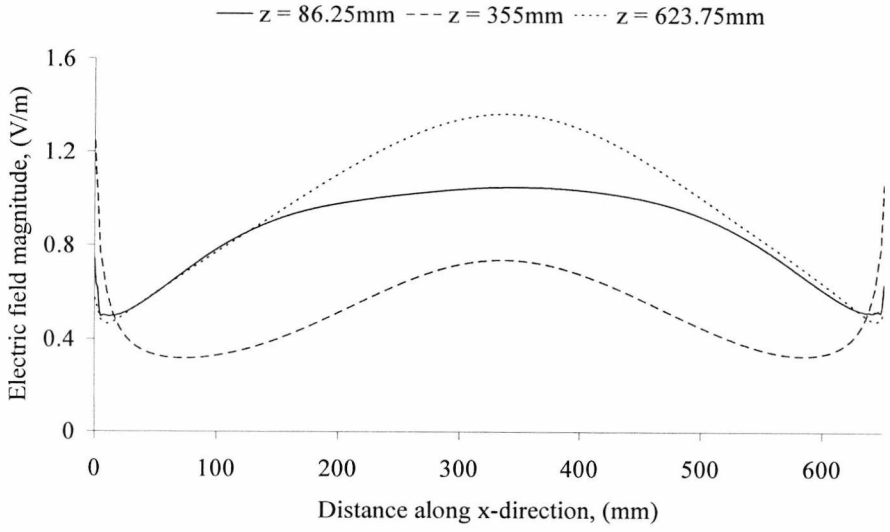

(a)

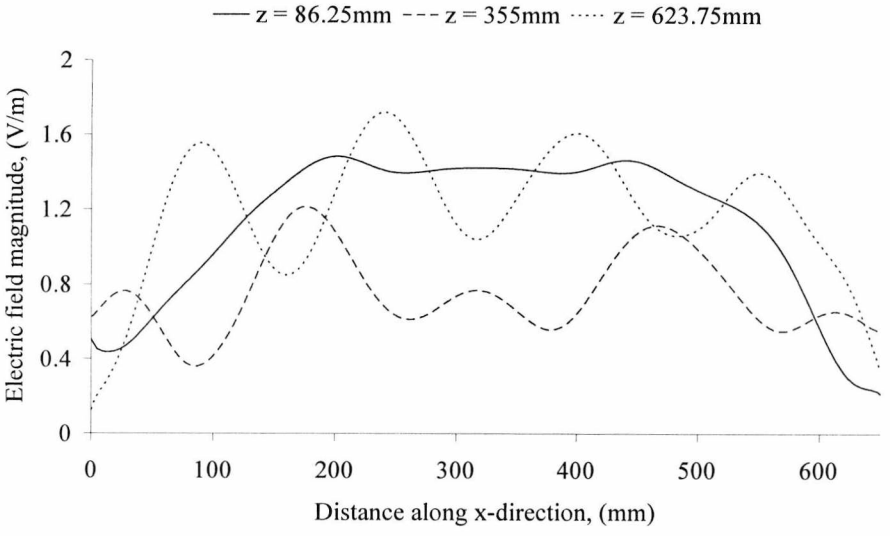

(b)

Fig. 6.13: Comparison of the variation of the field in the x-direction for different planes at z for the roll cage encountered in section 6.2 with mesh sizes of 75 mm at the coordinate: y=300 mm, z=86.25 mm, 355 mm and 623.75 mm and x = 0 – 650 mm for the frequencies of (a) 868MHz and (b) 2450MHz.

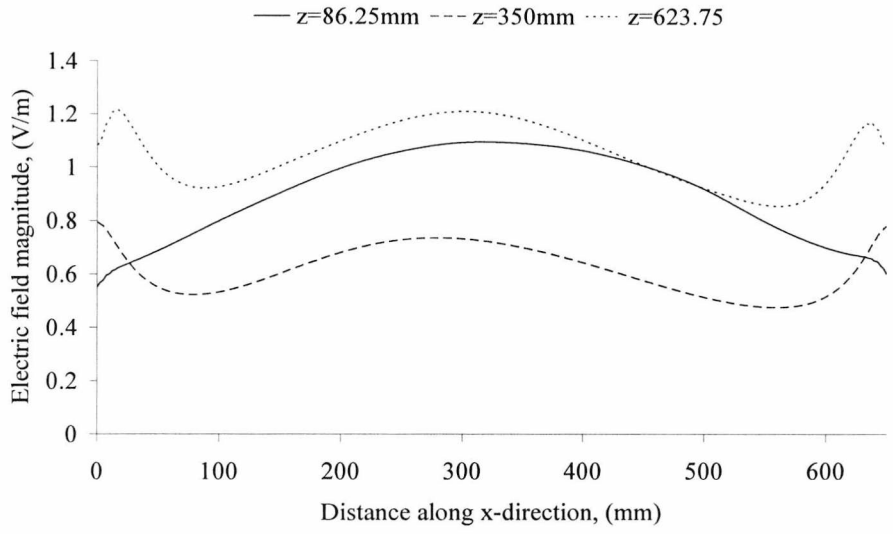

(a)

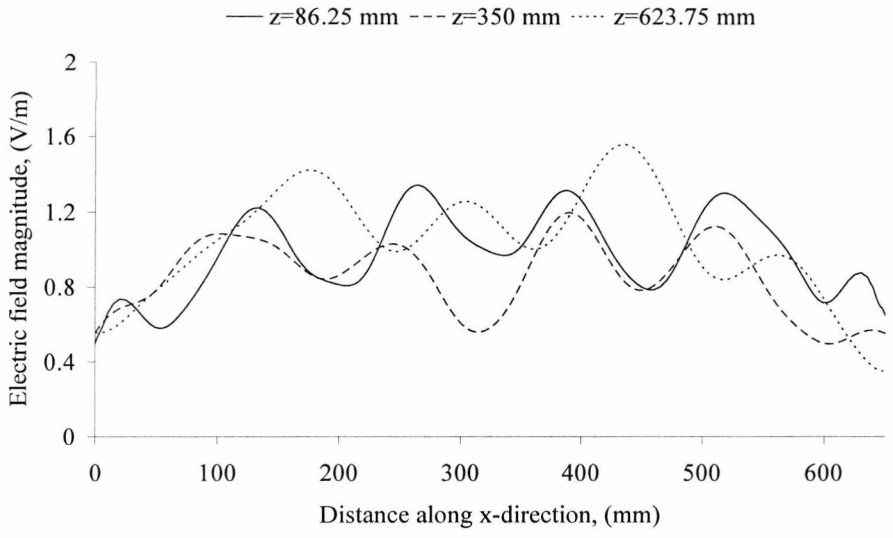

(b)

Fig 6.14: The variation of the field in the x-direction in the roll cage encountered in section 6.2 with mesh sizes of 100 mm through the coordinates y = 600 mm, z = 650 mm and for x ranging from 0 to 650 mm at the RFID frequencies of (a) 869 MHz and (b) 2450 MHz.

6.5 Read field of roll cages

This section explores the readability of an RFID tag at various locations in a roll cage. To establish the area where tags are likely to be detected, a partial height cage was fabricated with mesh sizes of: 50 mm, 75 mm and 100 mm (as specified in Table 6.1).

An EM4222 tag integrated with 869 MHz half wavelength dipole was positioned at 5 mm spacing around the plane under measurement. The sampling was carried out by positioning a tag, attached to a low dielectric constant plastic, at periodic points across different planes. The plastic ensured that no significant field distortion was introduced inside the cage and also that the tag was not skewed during measurement. The interrogator, which consists of a circularly polarized IPICO Reader operating at 869 MHz, was positioned 6λ from the centre point of the cage. It has not been possible to measure tag performance at 2.45 GHz due the single read frequency limitation of the Reader. An audio speaker was used to sense and approximately quantify the intensity of the backscattered signals. The measurement set-up is illustrated in Fig. 6.15.

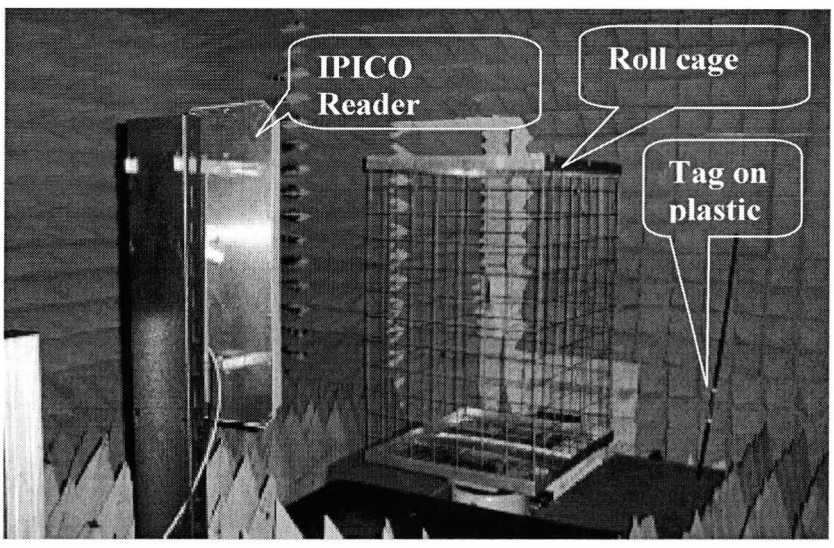

Fig. 6. 15: The roll cage read measurement set-up inside the anechoic chamber of a metallic roll cage when empty

The backscattered field for when these cages were either empty, fractionally-filled with four cartons of paper reams or with pieces of metal are examined. These perturbations were introduced in a controlled manner so that it was possible to associate specific fields with particular defects. The objective here is to create an equivalent to the situation within the roll cage for a commercial supply chain.

The Reader attempted to read the tag located at positions throughout the $x-y$, $x-z$ and $y-z$ planes; maps were used to show the active zones in which tags are detected. The measurement was carried out inside the anechoic chamber at the University of Kent.

6.5.1 The read field of an empty roll cage

The read zone in an empty cage is presented in this section. The contours of the read field were obtained for different planes and mesh sizes specified in Table 6.1. Figure 6.16 shows a map of where the tag was successfully read for the x-z plane at the height, y = 300 mm of the cage having a mesh sizes of 50 mm. A cavity standing wave distribution described in section 6.4, with peaks separated by a half wavelength is clearly seen. Also visible, were the troughs were the tag was not read.

Additionally, other mesh sizes cages had been tried for further investigation of their read fields. In Fig. 6.17 is presented the read field inside an empty roll cage having mesh sizes of 75 mm while Fig. 6.18 is for the case of 100 mm mesh sizes. These plots show a progressive increase in the read field compared to the 50 mm mesh sizes (shown in Fig. 6.16) albeit with correspondingly lower intensity. Clearly demarcated nulls are noticeable in this structure when it is empty. A tag located just outside the edges of the cage along the x–direction exhibits significant backscatter intensity (due to the contribution of edge diffraction) which tend to decrease with increasing mesh sizes [6.17] Such reduction is attributable to increased transparency of the cage as the mesh sizes increases.

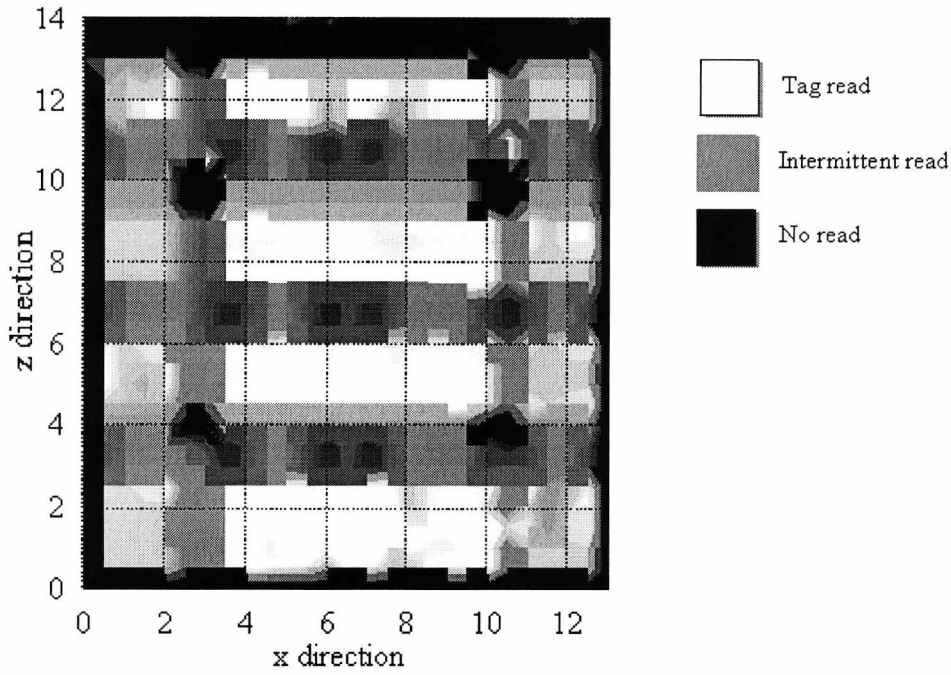

Fig 6.16: Normalised read zones inside an empty cage with 50×50 mm mesh for the plane at $y = 300$ mm.

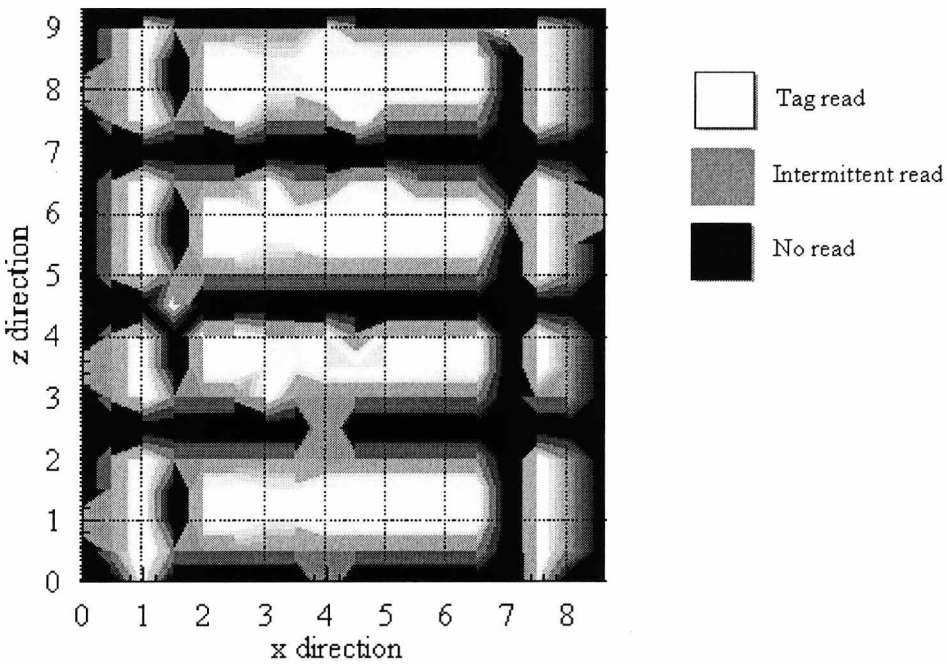

Fig: 6.17: Normalised read zones inside an empty cage with 75×75 mm mesh for the plane at $y = 300$ mm.

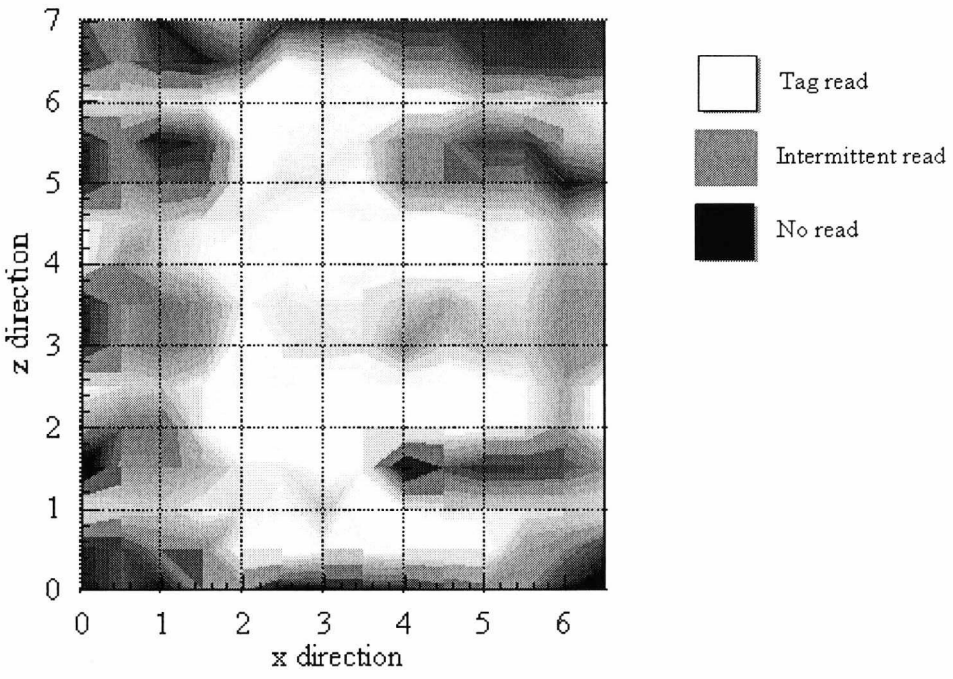

Fig. 6.18: Normalised read zones inside an empty cage with 100 × 100 mm mesh for the plane at y = 300 mm.

The spatial dependence of backscattered fields inside an empty roll cage has been demonstrated. In particular, a roll cage of 50 mm mesh sizes has been found to exhibit the highest backscatter sensitivity, although with deepest nulls at every half wavelength interval. The intensity of the backscattered signals decreases as the cage mesh sizes increase to 75 mm and then to 100 mm. The effect of incomplete nulls became progressively evidenced in the increased read area as the mesh sizes increases. An increase in mesh sizes are also related to an increase in the travelling wave inside the cage. The read fields for empty cages is clearly demarcated in a way reminiscent of the standing wave encountered in Section 6.4. This shows that the null is intrinsic to the structure of the roll cage.

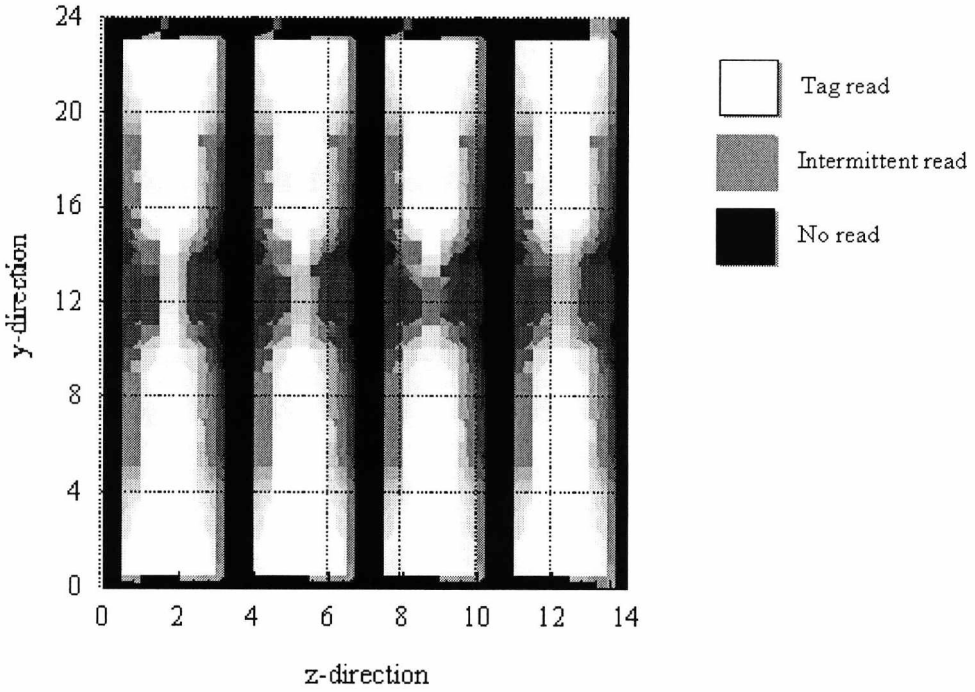

Fig. 6.19: Normalised read zones inside an empty cage with 50×50 mm mesh for the plane at $x = 325$.

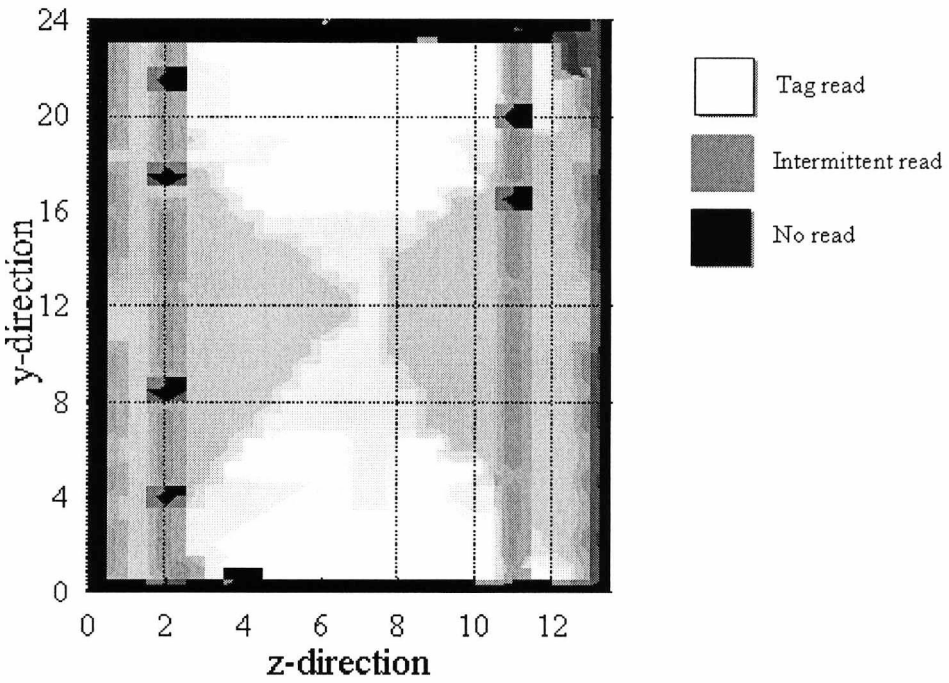

Fig 6.20: Normalised read zones inside an empty cage with 50×50 mm mesh for the plane at $x = 86.25$ mm.

The read field in the x and y planes are presented in figures 6.19 and 6.20 for x = 325 mm and x = 86.25 mm respectively. The effects of adding objects such as paper reams and pieces of metal into an empty roll cage will be presented in the following sections.

6.5.2 The effect of paper reams on the tag reading range inside roll cages

The variation in the read field for the case when the cage is perturbed in a systematic manner is presented in this section. For this case, cartons containing paper reams, as shown in Fig. 6.21 were added inside the roll cage to investigate the disruption of the RF link. The cartons each have the dimensions: 300 x 220 x *250* mm^3 and represent a volume filling fraction of 0.21, which is measured as a fraction of the total volume of an empty cage. For convenience, the read field here will only be investigated at ***x-z*** plane for y = 280 mm, which is close enough to the cartons to reveal the effect of the disruption.

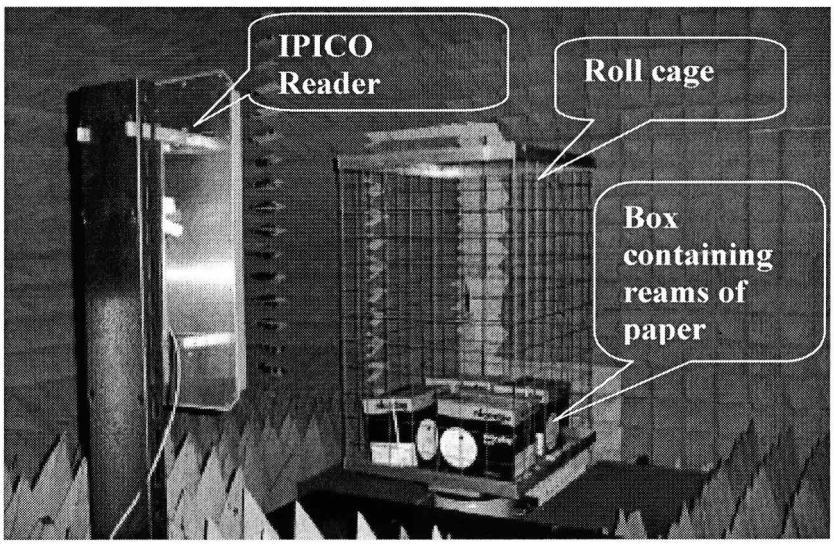

Fig. 6.21: The roll cage read measurement set-up inside the anechoic chamber of a metallic roll cage when fraction-loaded with paper reams

Figures 6.22, 6.23 and 6.24 correspond to the read field for cages with mesh sizes 50 mm, 75 mm and 100 mm and indicate a progressive decrease in both the intensity of the

backscattered signals (using audio response from a loud speaker) and the coverage. The nulls observed in the case of an empty cage are no longer clearly defined. It can be seen that the peaks, where they occur, are now located outside the area of perturbations.

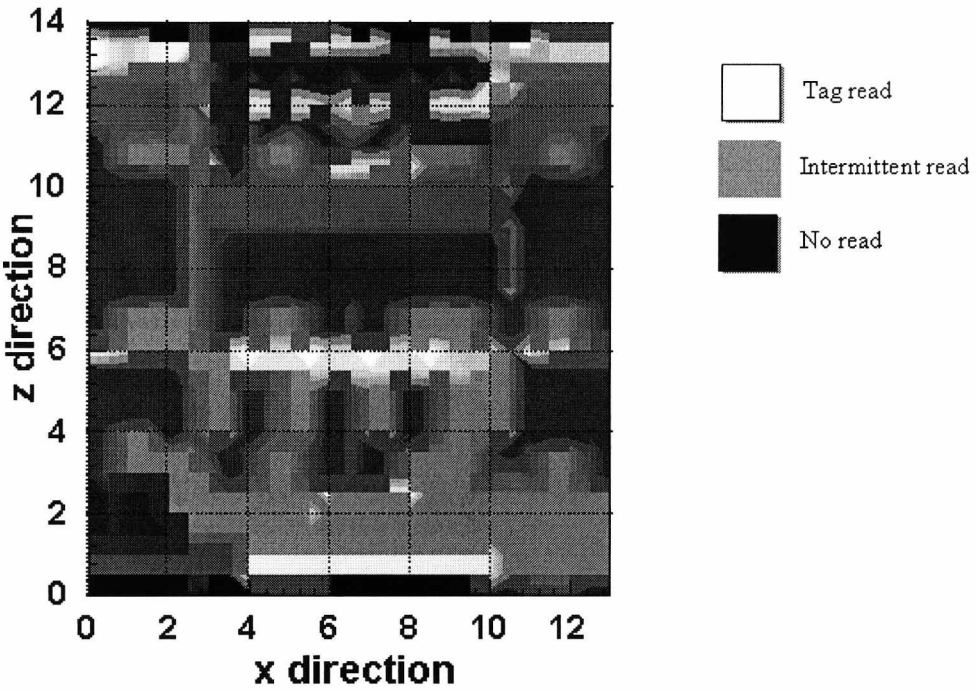

Fig: 6.22: Normalised read zones inside a fractionally-filled cage with 50 × 50 mm mesh with boxes of paper ream for plane at y = 300 mm.

The read field variation compared with the case of an empty cage was significantly reduced which indicates the strong EM absorption properties of paper materials. In other words, the backscattered field due to the paper ream is extremely weak. This explains the persistence of additional nulls in the areas away the paper. By monitoring the intensity of the backscatter signals when the position of the cartons is shifted in small increments of 25 mm, it is possible to associate these nulls with the position of the cartons.

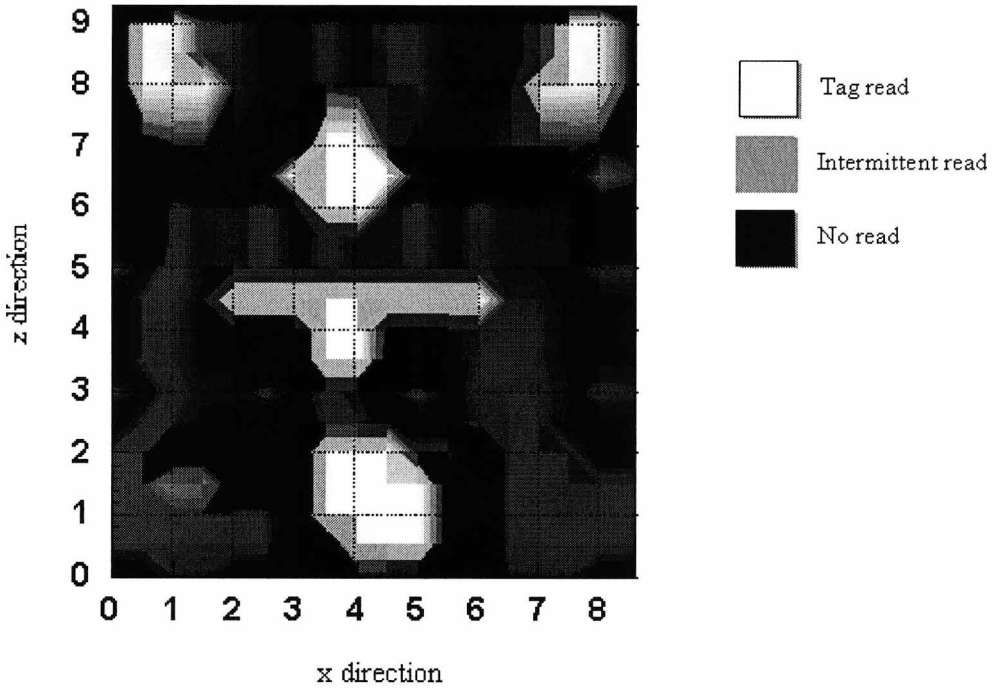

Fig. 6.23: Normalised read zones inside a fractionally-filled cage with 75 × 75 mm mesh with boxes of paper ream for plane at y = 300 mm.

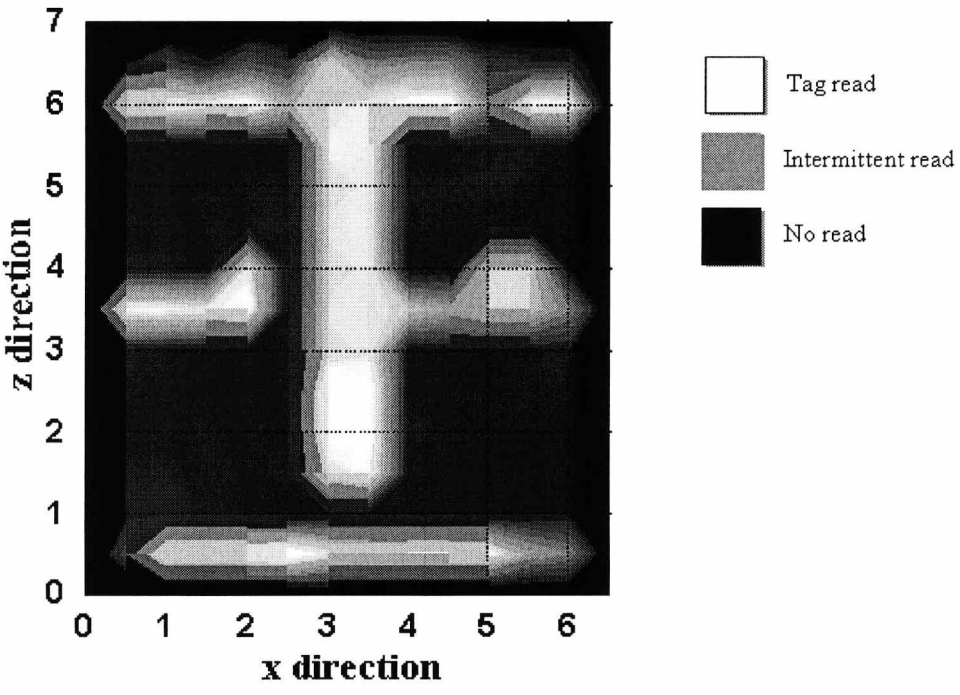

Fig: 6.24: Normalised read zones inside a fractionally-filled cage with 100 × 100 mm mesh with boxes of paper ream for plane at y = 300 mm

6.5.4 The effect of scatterers on the tag reading range inside the roll cages

When the paper reams as shown in Fig. 6.21 were replaced by pieces of metallic objects (horn antennas), transmission peaks appear sporadically in the immediate vicinity of these objects. As in the previous section, the measurements were carried out at *x-z* plane for y = 280 mm and at a volume filling fraction of 0.21. A typical backscatter field for a cage of mesh sizes 50 mm is shown in Fig. 6.25. Furthermore, the strength of backscattering field was compared with those of other mesh sizes cages: 75mm and 100mm and the results are presented in Fig 6.26 and Fig 6.27 respectively.

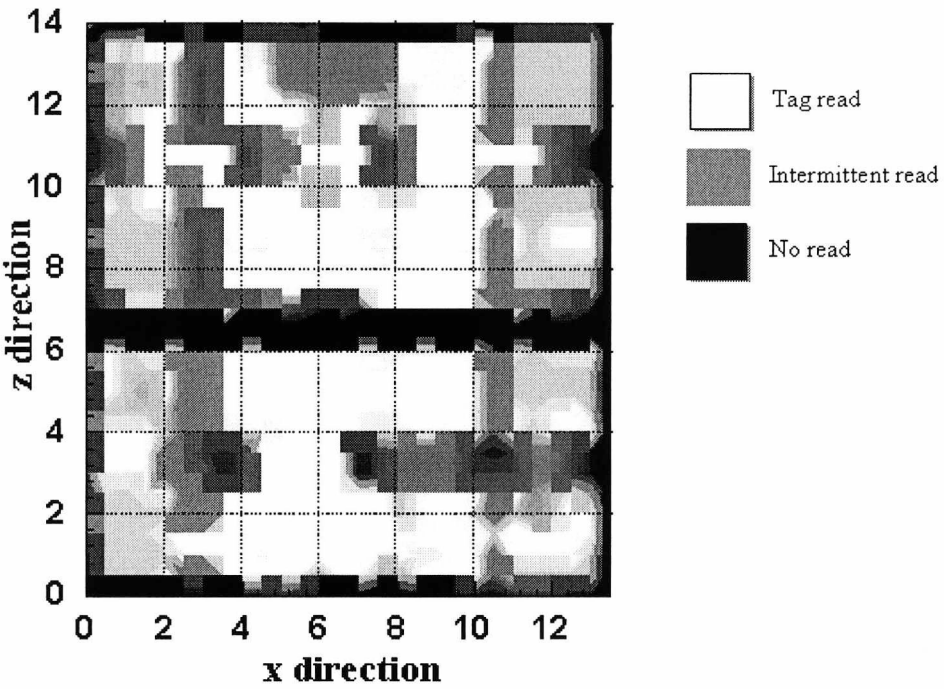

Fig. 6.25: Normalised read zones inside a fractionally-filled cage with 50 × 50 mm mesh with boxes containing pieces of metallic scatterer for plane at y = 300 mm.

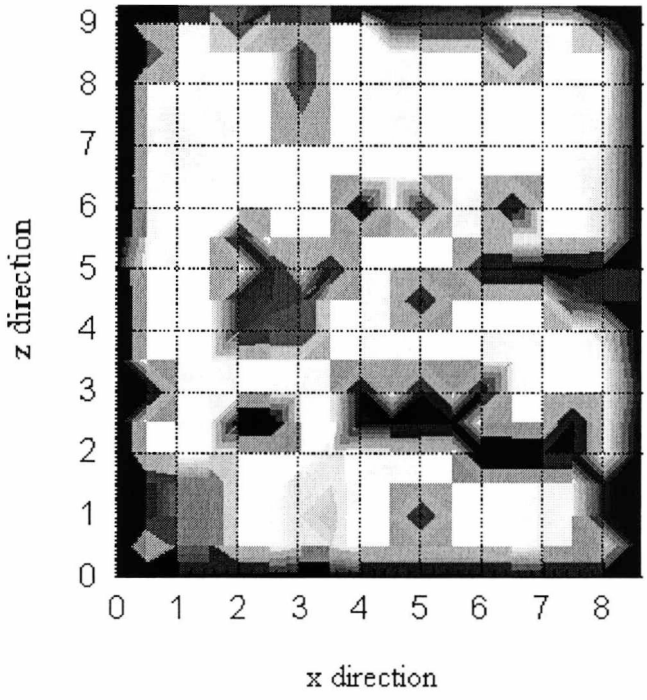

Fig. 6.26: Normalised read zones inside a fractionally-filled cage with 75×75 mm mesh with boxes containing pieces of metallic scatterer for plane at $y = 300$ mm.

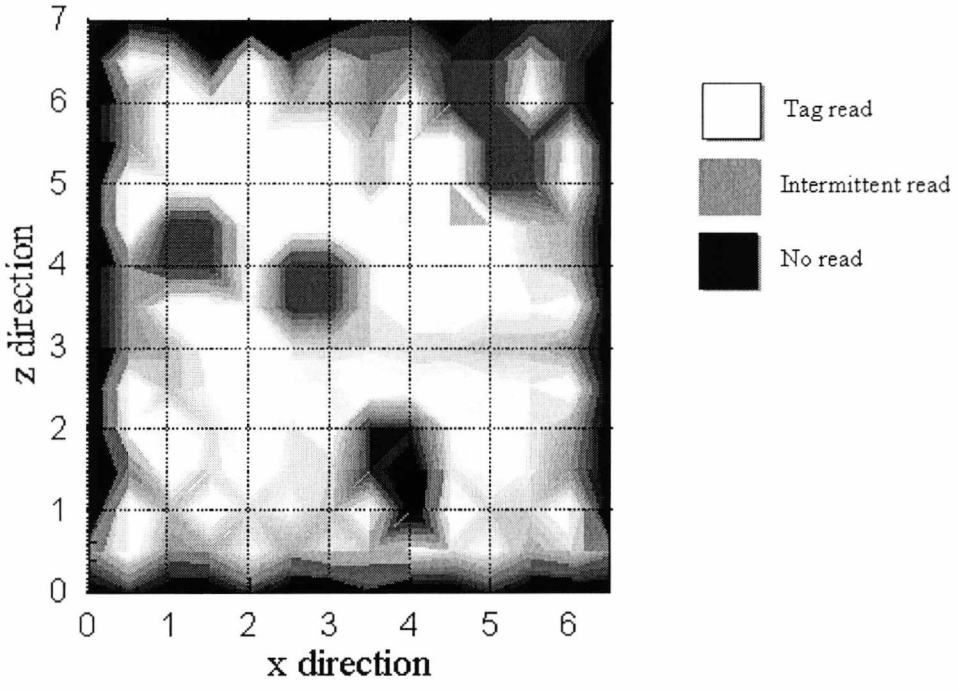

Fig. 6.27: Normalised read zones inside a fractionally-filled cage with 100×100 mm mesh with boxes containing pieces of metallic scatterer for plane at $y = 300$ mm.

The lengths of the individual scattering objects inside the cartons is at least of the order of magnitude smaller than the wavelength but were densely packed. Hence, the transmission peaks observed in the preceding diagrams were more likely associated with the random configurations of these metallic objects rather than with an individual scatterer. As a result, the nulls are now less pronounced. On average, the field is broadened relative to the case when the cage is empty or when partially filled with paper ream products. The broadening is associated with scattering from a random distribution of scatterers. More growth in the read field is observed along the z-axis. In the x-direction, just outside the edge of the cage, the diffracted wave did not increase the strength of the backscattered significantly as compared to the case for a 50 mm cage. As in previous sections, such reduction is also associated with an increased travelling wave.

6.6 Conclusion

The transmission response of a wire mesh roll cage and the spatial distribution of the emitted electromagnetic field for a plane wave source (which represents an RFID Reader) have been studied numerically. Interaction between the interrogating and reflected waves causes a half wavelength standing wave inside the cavity. In addition, measurement of the read field inside a wire-mesh roll cage has been taken for the cases when empty, fraction-filled with paper reams and scatterers. It was found that readability of tags located within one-half wavelength (and at the interval of 0.5λ) from the surface was not possible when the cage as empty. However, those within the vicinity of one-quarter wavelength (and at the interval of 0.5λ) attracted sufficient electromagnetic energy to backscatter.

The effects of loading the roll cage with different objects have been investigated by adding paper reams and pieces of metal. While the read range in the former case was on average significantly suppressed, the later showed detection spread covering the areas earlier classifieds as nulls. The roll cage loaded with pieces of metal showed an increase in backscattered signals. The fractional shifts in the various read field were the same for the all mesh sizes considered.

Generally, the detection of RFID tags within a metallic roll cage is difficult and depends on their spatial location within the enclosure. One interesting outcome here is that multiband tags could improve detection rates by employing frequency diversity. To this end, novel multi-frequency antennas have been proposed in Chapters 4 and 5. Future work will be to establish field distributions within roll cages populated with many tags. Furthermore, this research points to the development of surfaces which will increase the transparency of an enclosure at the desired RFID frequency.

The potential for improved readability by using frequency diversity in multi-frequency tags is noted. Frequency diversity for multi-frequency tags is proposed as a method of reading within standing wave nulls.

6.7 References

[6.1] Christos G. Christodoulou and Frank J. Kauffman, "On the Electromagnetic Scattering from Infinite Rectangular Grids with Finite Conductivity," *IEEE Trans. Antenna. Propag*, vol. AP-34, no. 2, February 1986

[6.2] T. W. Ebbesen, H. J. Lezec, H. F. Ghaemi, T. Thio & P. A. Wolff, "Extraordinary optical transmission through sub-wavelength hole arrays," NATURE - *Letters to Nature* Vol. 391,12 February 1998, Macmillan Publishers Ltd., 1998

[6.3] H. Wen, "Resonance-induced wave penetration through electromagnetic opaque object," Optics Express, Vol. 13, No.18, September 2005.

[6.4] M. Berute et al., "Enhanced Milimeter Wave transmission through Quasioptical Subwavelength Perforated Plates", *IEEE Trans. Antenna. Propag.* vol 53, no.6 June 2005, p.1897-1903

[6.5] H. Park, "Electromagnetic penetration into a rectangular cavity with multiple rectangular apertures in a conducting plane," *IEEE Trans. on EMC*, Vol. 42, No 3, August, 2000, pp.303-307

[6.6] C.A. Diugwu, J.C. Batchelor, and M Fogg, "Field distribution and RFID

reading within metallic roll cage," *Electr. Letters*, Vol. 42 No. 23, 2007

[6.7] J.D. Kraus, "A small but effective flat top beam antenna", Radio, no. 213, 56-58, March 1937 and no. 216, 10-16, June 1937

[6.8] E. A. Parker and B. M. Cahill, "Field switching in an enclosure with active FSS screen," Electronic Letters, Vol. 37, No. 4, February, 200, pp. 244-245.

[6.9] Butler, C., Rahmat-Samii, Y. Mittra, R, "Electromagnetic penetration through apertures in conducting surfaces", Antennas and Propagation, IEEE Transactions on [legacy, pre - 1988] Publication Date: Jan 1978, Volume: 26 , Issue: 1, On page(s): 82 – 93, ISSN: 0096-1973

[6.10] Charles Bunting and Shih-Pin Yu, "Field penetration in a rectangular box using numerical techniques: an effort to obtain statistical shielding effectiveness,"

[6.11] Robert Collin, "Foundation for microwave engineering," McGraw-Hill Inc., 2nd ed., 1992, p.500

[6.12] A.C. de Lima and E.A. Parker, "Fabry-Perot approach to the design of double layer FSS," *IEE Proc.-Microw. Antenna Propag.*, Vol. 143, No. 2, April 1996, pp.157-161.

[6.13] Zhi Liang Wang, Kozo Hashimoto, Naoki Shinohara, and Hiroshi Matsumoto, "Frequency-Selective Surface for Microwave Power Transmission," IEEE Transactions on Microwave Theory and Techniques, Vol. 47, No. 10, October 1999 pp.2039-2042

[6.14] Petr Beckmann and Andre Spizzichino, "The scattering of electromagnetic waves from rough surfaces," Artech House Inc., Norwood, 1987, Chapter 4, p.32

[6.15] John D. Kruas, "Electromagnetics," McGraw-Hill Inc., 4th Ed. 1992, pp.541 – 547

[6.16] S. J. Orfanidis, "Electromagnetic Waves and Antennas," Rutgers University June 2004, p.109

[6.17] H.A Bethe, "Theory of diffraction by small holes," *Phys. Rev*, vol. 66, pp. 163-183, Oct. 1944

CHAPTER 7

CONCLUSION AND FUTURE WORK

A full wave electromagnetic simulator, the CST Microwave Studio has been used to study different antenna configurations. The devices consisted of patch (electric dipole and Complementary Patch Antennas, CPA) and slot (magnetic dipole and Slot Patch Antenna, SPA) elements. The CST has also proved useful in the study of the field distribution inside electrically large wire mesh roll cages and hence was able to predict the corresponding read range. The field distributions in all planes of the enclosure have been presented. The CST tool allows the user to model devices on a commercial graphic interface with Visual Basic Application (VBA) micros that enables post design modification. The algorithm is capable of discretizing the problem space even for irregular shaped objects, using the Perfect Boundary Approximation and Thin Sheet Techniques.

The basic concepts concerning the behaviour of an antenna have been outlined, and the condition necessary for maximum power transfer between an antenna and its on-board chip has been defined. A set of concepts suitable for describing the communication link between a tag and an interrogating Reader in a Radio Frequency Identification (RFID) system have been defined. Some of the influences of the various antenna load conditions on the tag ability to receive power have been identified. The theoretical read distances from which a tag can be detected have been demonstrated with a linear dipole and in the case when the antenna was with and without an inductive matching loop. The variation of Read range as a function of antenna length has been analysed. Measurements demonstrate that constructing a loop around the antenna feed produces a substantial (ten times) improvement in detection range. The input impedance of the antenna was significantly reduced when the loop was added as it essentially short circuited the feed point. The results of experimental measurement of the read range indicate a complete detection and

location in all cases of tags within an average distance of 0.4 metres from a circularly polarised Reader with output power of 0.5 Watts.

One of the main thrusts of the investigative work was to extend the range of options in the tag antenna design by using the principle of complementarity for application with RFID tags. The starting point of this was to analyse a single linear dipole, which offers the possibility of obtaining the complementary slot configuration that in turn can be manipulated to excite higher order modes at 869 MHz and 2.45 GHz. Thus, a parametric study was made to identify the impact of coupling slots of various sizes to a conventional slotline in order to excite other frequencies. To achieve higher RFID operating frequencies, the SPA antenna was also scaled in terms of frequency. An important outcome here was that reducing the size of the antenna by half excite higher frequencies – 2.45 GHz and 5.8 GHz, which are also allocated for RFID.

Additional work was done on the SPA to establish the dominance of the slots as tuning elements. The targeted frequencies were within the RFID specified frequencies and hence the contributions of the slots offered significant tuning ability at the relevant frequencies. The slots proved additionally useful in tuning the resonant frequencies within the globally specified RFID frequencies.

Further optimisation techniques such as studying the effect of the substrate thickness and permittivity have on the operating frequencies were explored. It was found that both parameters can substantially impact on the performance of the antenna. The dependence of the antenna size on the substrate was confirmed. A broader slot width or a lower substrate permittivity increases the antenna size. However, it was noted that an increase in the antenna size led to an increased bandwidth and hence a decrease in the antenna quality factor. In comparison with a thinner substrate, the resonant frequencies of antennas fabricated on thicker substrates decreased faster. Furthermore for a given substrate relative permittivity, higher value of substrate thickness implied lower resonant frequency.

Passive tags were constructed of the different antennas studied in the thesis by integrating them with either Micro Electronics EM4222 or BiStar 3891-3 ASIC chips. The tags operate in the UHF frequency bands and typically modulate the backscattered radiation reflected from the tag antenna by load modulation. The SPA and CPA have the additional capability to extend operation up to the microwave frequencies but, it has not been possible to test tags in this regime due to the limitation of the IPICO Reader, which was only equipped for operation at 869 MHz. The surveillances of the tags made from patch elements (electric dipole and complementary patch antenna) were superior to those of their slot counterparts. However, the geometry of the slot antennas (magnetic dipole and slot patch antenna) are attractive choices, especially in application involving thin metallic sheet, e.g. where embedding a simple slot onto a foils surface would be sufficient to create a tag antenna. A useful consequence of the various tuning stubs was the ability to excite two planes of polarisation owing to their orthogonal arrangements. This meant that the resulting tags were able to be read in any arbitrary planes.

Another primary objective of this work was to provide the options of selecting tag antennas based on compatibility with the objects to which they were attached. Thus, having established the suitability of the SPA for the application, the feasibility of increasing the options of antenna configuration was carried out using the complementarity principle. Hence, the regions of the perfect electric conductor space and slot were interchanged, to give the required CPA. Indeed, this option proved useful both in simplicity of design and superiority of range performance in contrast to the SPA. Clearly, an option on antenna configurations that, at certain selected frequency bands, give optimum interaction with the objects to which the tag is attached has been achieved.

The other factor that affected read ranges, namely RCS was studied numerically for each antenna. The main difference between an electric dipole and its complementary slot was that while the RCS value increases with increasing patch width, the opposite was the case for increasing slot width. The effect of incident angles on the dipoles differs from that of the patches. While the RCS value in the case of the dipoles peaks at 90^{o}, which corresponds to when the antenna is in a straight line with the direction of the plane wave

propagation (for a horizontally polarised electric field), that for the patch antennas peaks at 0^{o} and 180^{o}.

The ranges of a tag on various materials including foam (approximately the same dielectric constant as free space), paper, wood, plastic, glass and metal (solid thin and wire mesh sheets) were tested. These materials provide a variety of complex permittivities and conductivities typical of an RFID environment. Only the tag made of CPA could be read attached at close proximity to metal surfaces; a read range of up to 2.5 metre was achieved when attached to wire mesh surfaces and 0.05 metre when directly attached to a flat sheet of metal. By using a foam 5 mm spacer to separate the tag and the metal, a read range of 0.5 metre was achieved. Thus, the antenna is recommended for high level tracking of large objects of the size of a metallic roll cage.

Furthermore, the feasibility of reading tags through wire meshes such as those on a roll cage was investigated. For various mesh sizes, the cage exhibits transmission responses characterised by frequency gaps of approximately half the first resonant frequency. The insertion loss of a cage side was simulated and found to decrease with increasing mesh size. Also, the standing waves inside the cage exhibited nulls whose voltage standing wave ratio (v.s.w.r.) decreases with increasing mesh size.

The above observations have been substantiated by experimentation. Various read measurements were taken and mapped for the different planes inside a physical cage. As expected, the distance, or range, over which the tag operates, was approximately in proportion to the amplitude of the standing wave at the position of the tag, with peaks and nulls occurring at every half wavelength. Frequency diversity for multi-frequency tags is proposed as a method of reading within standing wave nulls.

In the context of roll cages, the intensity of the backscattered signals due to the electromagnetic absorption affects of paper reams was found to increase as the distance from the source of perturbation increases. On the other hand, when the paper reams were substituted with pieces of metal (scatterers), spurious fields, and hence, random read

ranges, appeared due to the contributions of the random scatterers. It has not been straightforward to characterise the affect of distance on the spurious field due to the unpredictable nature of randomly distributed scatterers. The immediate inference here is that spurious fields would not only depend, to a large extent, on the reflection and transmission properties of the scatteres but also on the proximity to the roll cage surface.

The following may be of interest for future work. In chapter 3, the sensitivity of the dipoles with respect to different attached materials has been used as a figure of merit which combines the effects of antenna gain and decreasing beam width into a single consideration. The variation in the sensitivity has been used to predict the likelihood of either increasing antenna gain or decreasing beamwidth of the tag antenna on the overall RF tag performance. The knowledge of these variations in sensitivities will be useful, when as an option for future work, the free space RF tag sensitivity can be adjusted to its actual value when attached to objects by considering the differential in evaluating the power received by the tag.

The present construction of roll cages commonly used in supply chains do not take in account the requirement for radio frequency (RF) signal to penetrate through them. Typically, these roll cage are constructed of wire mesh which severely alters the propagation variables such as power and polarisation. Future work will include designing roll cages which specifically address the problems of RF propagation. Also, the case for large volume roll cages will be studied.

It has been demonstrated that the detection of RFID tags within a metallic roll cage depended on their spatial location throughout the enclosure. In particular, dead zones which resulted from the standing wave within the roll cages have been observed irrespective of the cage size. As a method of reading within standing wave nulls, the study of multiband tags that can improve detection rates by employing frequency diversity of multi-frequency antennas is proposed as a future work.

There were several techniques that have been developed, which allows selective penetration of RF signal and in particular Frequency Selective Surfaces (FSS). Future work is envisaged in the area of designing roll cages that are not only frequency selective but also allows their complementary designs to be equally explored.

Finally, the behaviour of tag populations both in free space and inside enclosures will be investigated in future.